Advanced Fluorescence Methods for the Investigation of Biological Membranes

Niall David Geoghegan

A thesis submitted to

The School of Engineering

College of Science and Engineering

The University of Glasgow

In fulfilment of the requirements for

The Degree of Doctor of Philosophy

Table of Contents

Contents

List of Tables

List of Figures

Publications and Conference Proceedings

M. Dent, I. Lopez-Duarte, **N. Geoghegan** et al., "*Imaging phase separation in model lipid membranes through the use of BODIPY based molecular rotors*," Physical Chemistry Chemical Physics, vol. 17, pp. 18393-18402, 2015

N. Geoghegan, M. Dent, D. Paterson, A. Glide, N. Brooks, M. Kuimova, J. Cooper "*TIRF-FLIM imaging of membrane viscosity using artificial membranes and molecular rotors*", Conference proceedings, Optics Infobase, Optical Molecular Probes, Imaging and Drug Delivery (OMP) – Vancouver April 2015

Acknowledgement

I would firstly like to thank Professor Jon Cooper for providing me the opportunity to perform this research within his group. Without his guidance, support, expertise and unwavering optimism this thesis would not have been possible. Thanks also to Dr Andrew Glidle for his guidance and expert knowledge on all matters and the many invaluable lessons I have learned from him.

I would like to thank all the members of the group who have helped with the development of this thesis through their contributions, both directly and indirectly. Dr Rab Wilson, Dr Julien Reboud and Dr Manlio Tassieri were all instrumental in the successful completion of this work both through practical guidance and picking me up when the science was uncooperative. Their, seemingly, bottomless combined knowledge is a credit to the group and will continue to develop brilliant researchers in the coming years. Thanks to my fellow PhD students who, through shared emotional toil, helped immensely in ensuring I made it to the finish line. Thanks to Dr Dave Paterson for his knowledge on all things lipids, Ellie Pulleine for her AFM wizardry, Mark Bennett for his craft of lipid vesicles, Ya Hua Chim for her help with cell culture and to all others who have contributed. Thanks go to everyone in the group, of which there are too many to list, who have helped in making these four years an incredible experience.

A special mention must be made to all external collaborators who enabled me to complete this work. I would like to thank Professor Gwyn Gould and his group members, Kamilla, Cassie, Alex and Silke, for their knowledge and guidance in the art of cell culture. Thanks to Michael Dent and Dr Marina Kuimova, from Imperial College London, for providing me with the opportunity to work with their exciting molecular rotor molecules.

This work would not have been possible without the funding of the EPSRC who I would like to thank immensely for ensuring that I was fed and housed for the duration of this PhD. In addition I would like to thank all the members of the Proxomics project for providing me with countless opportunities and connections which I will take with me through my career.

My penultimate acknowledgement must go to those most important to me, namely, my friends and family. To my parents for providing me with every possible opportunity to succeed in life and make it to where I am today, for encouraging me, and for your unwavering love and support. To my brother Patrick, or Dr Patrick Geoghegan to honour his full title, his fresh knowledge of the toils of a PhD degree were invaluable in making it this far. Through his helpful proof reading of this thesis he managed to demonstrate a surprising level of wisdom of which I'm greatly appreciative. My love and gratitude to you all exceeds expression. I must also thank the newest members of my family: David, Felicite and Sam, for your encouragement and support through these years. For all of my friends, of which there are too many to thank individually, I thank you. In particular, the wonderful Blakes for providing an escape from the constant presence of the PhD and reminding me of the world outside of the Rankine building.

Finally, to my wife Laura, I owe you everything. Your constant support, drive and love have pushed me, not only to finish my research, but to be the person I am today. You picked me up when times were hard, and celebrated in them when they were good. You made these last four years the immensely enjoyable times that they were and I can't wait to take on whatever the next challenge is with you by my side.

Author's Declaration

"I declare that, except where explicit reference is made to the contribution of others, this thesis is the result of my own work and has not been submitted for any other degree at the University of Glasgow or any other institution"

Niall Geoghegan

Definitions/Abbreviations

ACF	Auto-Correlation Function
ADC	Analogue to Digital Convertor
AFM	Atomic Force Microscopy
ASC	Adipose-derived Stem Cells
BODIPY	Boron-dipyrrin
CFD	Constant Fraction Discriminator
DMEM	Dulbecco's Modified Eagle Medium
DOPC	1,2-Dioleoyl-sn-glycero-3-phosphocholine
DPPC	1,2-dipalmitoyl-sn-glycero-3-phosphocholine
ESR	Electron Spin Resonance
FCS	Fluorescence Correlation Spectroscopy
FLIM	Fluorescence Lifetime Imaging Microscopy
FRAP	Fluorescence Recovery After Photobleaching
FRET	Förster Resonance Energy Transfer
GLUT	Glucose Transporter
GLUT4	Glucose Transporter 4
GSV	GLUT4 Storage Vesicle
GUV	Giant Unilamellar Vesicle
HA-GLUT4-GFP	HA-epitope tagged-GLUT4-Green Fluorescent Protein
HRI	High Rate Imager
IBMX	3-isobutyl-1-methylxanthine
ICCD	Intensified Charge Coupled Device
IR	Infra-Red
IRF	Instrument Response Function
ITO	Indium Tin Oxide
Ld	Liquid Disordered
Lo	Liquid Ordered
LUV	Large Unilamellar Vesicle
MSC	Mesenchymal Stem Cell
NA	Numerical Aperture
ND	Neutral Density
NMR	Nuclear Magnetic Resonance
OME	Open Microscopy Environment
OTF	Optical Transfer Function
PALM	Photo-Activated Localisation Microscopy
PBS	Phosphate Buffered Saline
PDT	Photo Dynamic Therapy
PMT	Photo Multiplier Tube

POPC	1-palmitoyl-2-oleoyl-sn-glycero-3-phosphocholine
PSF	Point Spread Function
ROI	Region Of Interest
SIM	Structured Illumination Microscopy
SLB	Supported Lipid Bilayer
SNOM	Scanning Near-field Optical Microscopy
SNR	Signal to Noise Ratio
SPAD	Single Photon Avalanche Diode
STED	Stimulated Emission Depletion
T2DM	Type-2 Diabetes Mellitus
TAC	Time to Amplitude Convertor
TCSPC	Time Correlated Single Photon Counting
TICT	Twisted Intramolecular Charge Transfer
TIR	Total Internal Reflection
TIRFM	Total Internal Reflection Fluorescence Microscopy
Vpp	Peak to Peak Voltage
WHO	World Health Organisation

Abstract

This thesis explores the use of advanced fluorescence imaging and spectroscopic methods for investigating various properties of biological membranes. The cell membrane is a complex environment comprised of a variety of important molecules all necessary for maintaining cellular function. The dynamics of processes involved in membranes are typically over very short time and spatial frames. Advanced fluorescence imaging and spectroscopic methods present an opportunity for probing the dynamic nature of this environment due to their high levels of both spatial and temporal resolution. The following thesis consists of three biological problems centred on the cellular membrane, investigated through high resolution techniques. The first area of investigation focusses on the insulin regulated metabolism of glucose in fat and muscle tissue. Traditional experiments are performed using either isolated rat adipocytes or differentiated fibroblasts which both required lengthy and expensive culturing procedures. A new modified HeLa cell line was investigated to determine its efficacy as a homologue to the well characterised adipocyte model as a method for investigating factors affecting glucose metabolism. A direct comparison of the dynamic recruitment of the molecule Glucose Transporter 4 (GLUT4) to the plasma membrane was undertaken using a custom built Total Internal Reflection Fluorescence Microscopy (TIRFM) system. Utilising TIRFM the time dependant translocation of GLUT4 to the plasma membrane under insulin stimulation was investigated in the two cell lines. This was achieved through analysis of the increase in normalised fluorescence signal found within the 110 nm illuminated region of the TIRFM system. It was found that in the HeLa cell line responsiveness to insulin stimulation was present but with a significant difference in GLUT4 levels to the imaged adipocytes. It was also seen that this observed response occurred over a significantly longer time frame than in adipocyte cells with a half rise time in fluorescence intensity taking, on average, 5 minutes longer. In addition, the dynamic mobility of GLUT4 Storage Vesicles (GSVs) within the vicinity of the membrane was assessed through image analysis techniques. The abundance of mobile and stationary vesicles was assessed. In the adipocyte cells a sharp increase in mobile GSVs was observed over the initial 5 minutes after insulin stimulation. The amount of immobilised GSVs was seen to increase at a constant rate over the time course of experimentation. In the HeLa

cell line, a similar rate of mobile GSV activity was observed, however, a decline in stationary GSVs was found. The increased accumulation of mobile vesicles at the plasma membrane is in accordance with previously proposed models of GSV recruitment. However, the reduction in stationary vesicles at the membrane surface in the HeLa cell line suggested differences in the machinery associated with vesicle fusion.

The second area of study focussed on the analysis of the environmentally sensitive class of fluorophores known as molecular rotors, in particular the meso-substituted BODIPY rotor. Molecular rotors are said to report on the viscosity of the environment in which they reside but questions still remained over their efficacy of assessing viscosity in complex environments such as lipid bilayers. A combined Fluorescence Correlation Spectroscopy (FCS) and fluorescence lifetime system was optimised to simultaneously probe the lateral mobility and viscosity sensitive fluorescent lifetime of the dye in artificial bilayer systems. The diffusion coefficients measured directly through FCS were compared with those inferred from the lifetime values by conversion through the Saffman-Delbruck model. Those measured by FCS were found to be similar to previously simulated values suggesting a well working experimental system. The values found through lifetime analysis were of the same order to those measured by FCS but differed by as much as a factor of 2 in some cases. The reasons for this most likely lie through the inherent assumptions made using the Saffman-Delbruck model. In addition, the probes were assessed in bilayers of differing degrees of phospholipid saturation. It was observed that the viscosity of the environment increased with decreasing saturation in the hydrocarbon tail regions of the lipids. This was noted through the diffusion coefficients measured with both methods.

The final chapter focussed on the creation of a system to increase the resolution of Fluorescence Lifetime Imaging Microscopy (FLIM) by implementing a TIRFM illumination scheme. The focus of this work was to increase resolution for imaging of membrane viscosity through the use of molecular rotors. Molecular rotors in cellular systems are susceptible to endocytosis over certain time frames, limiting their use in physiologically relevant studies in vitro. A gated FLIM system was constructed through the combination of pulsed laser diodes and

a gated Intensified Charge Coupled Device (ICCD) camera. To investigate the abilities of the system to selectively image a surface localised signal relating to membrane viscosity, Supported Lipid Bilayers (SLBs) were used. It was found, through both lifetime and FCS, that the substrate on which the bilayer was deposited reduced the mobility of the probe and the measured fluorescence lifetime. The effect was a change in diffusion coefficient by a factor or 2-3 which was taken into account when assessing the viscosity measured through FLIM of SLBs. The TIRF-FLIM principle was then demonstrated through imaging of SLBs containing the molecular rotor BODIPY against a highly fluorescent background of the fluorophore FITC. FITC provided a background with a distinctly longer lifetime to that of the rotor in the bilayer. The system was able to resolve the surface localised lifetime signal over a range of concentrations of background signal from nano-molar to micro-molar. The critical point, where the bilayer lifetime became indistinguishable from the background, came at a fluorophore ratio of 2:1 BODIPY to FITC.

1. Chapter 1: Introduction

1.1. Model of the cellular membrane

In just over a century the concept of the cell membrane has, and continues, to evolve. The initial assertion that the cell membrane was of a lipid nature came in the 19th century when Heinrich Quincke postulated that the cell membrane was a 100 nm fluid layer of fat [1]. A more complex understanding began to take shape as a result of work undertaken in the field of anaesthetics by Hans Meyer and Ernest Overton between 1895 and 1899 [2]. By looking into the osmotic properties of cells [3–5] Overton noted that molecules permeable to the cell had a particular partition coefficient between water and oil leading to the assumption that the membrane was comprised of a combination of lipids and cholesterol [6], known as their 'lipoid theory of narcosis'. The initial work to determine that the membrane is of a bilayer structure came in 1925 as a result of the work by Evert Gorter and Francois Grendel [7]. Through extraction of lipids from red blood cells and the use of 'Langmuir's trough' they were able to determine the area covered by a monolayer of lipids extracted from a known number of erythrocytes and measure its size. Their findings suggested it to be twice what was expected leading them to the conclusion that the membrane comprised a bilayer of polar molecules. In 1935 the model was extended to include proteins by Hugh Davson and James Danielli [8]. The model suggested by Davson and Danielli inferred that the lipid bilayer was located between two sheets of globular proteins in a sandwich structure. With the advent of the electron microscope J. David Robertson, in the 1950's, was able to empirically determine that the membrane was indeed a bilayer with a thickness of 75 A [9]. Observations by Robertson supported the theories proposed by Gorter and Grendel and by Davson and Danielli and he coined the term of the 'unit-membrane' to describe the protein incorporating bilayer model.

It wasn't until 1972 when the next major step in the development of the membrane model occurred when Seymour J. Singer and Garth L. Nicholson published their paper on the 'Fluid Mosaic Model' of the plasma membrane [10]. The key components of the model were that the membrane was a complex lipid bilayer with proteins residing at its surface or as integral components embedded

through bilayer. The Fluid Mosaic model developed as technologies [11] improved in Nuclear Magnetic Resonance (NMR) and electron spin resonance, leading to data suggesting the bilayer was a quasi-2D fluid constantly in motion. It was through Singer and Nicholson's stated distinction between integral and peripheral proteins which offered the largest paradigm shift for the model of the membrane to date. This is represented in Figure 1.

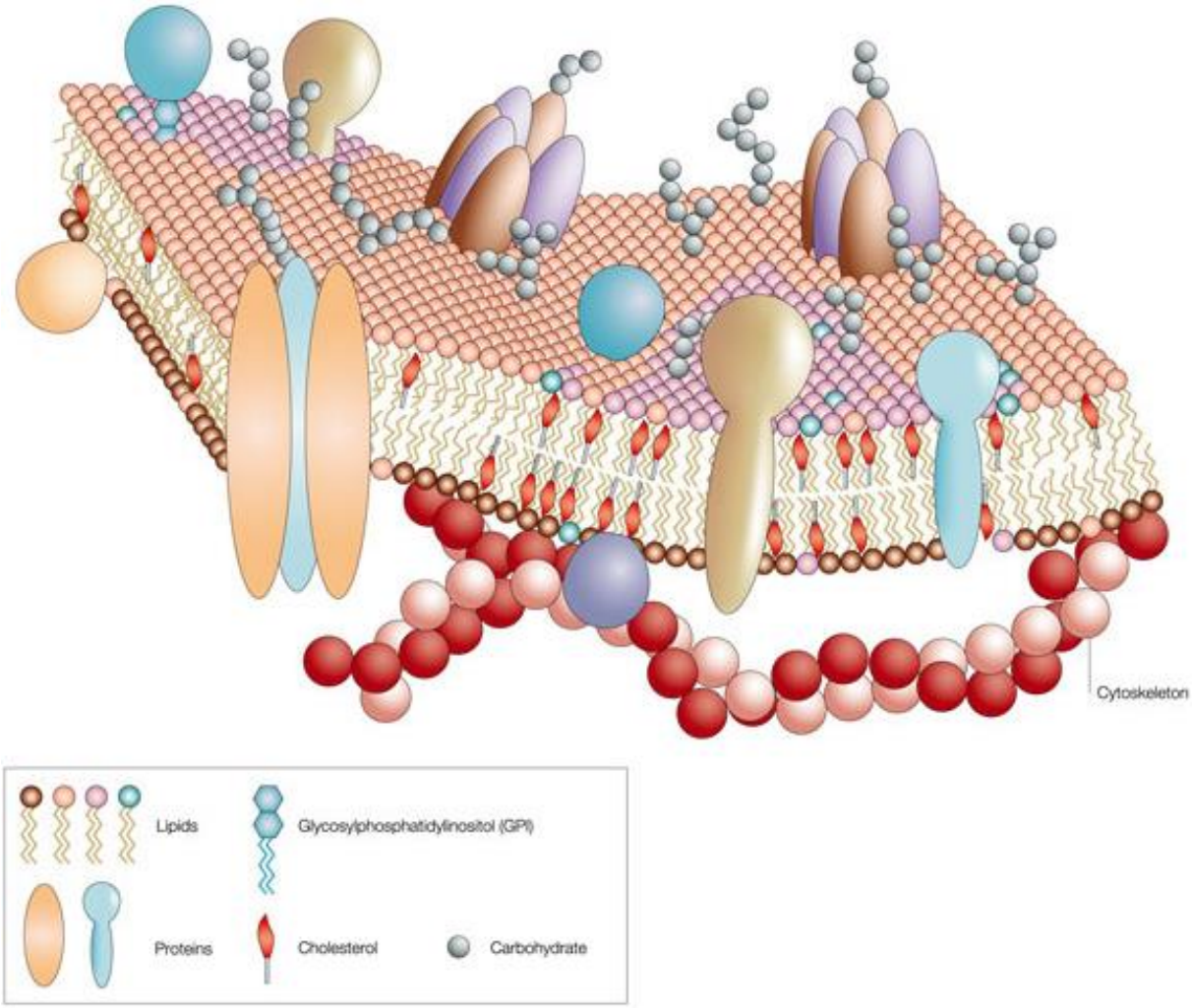

Figure 1: Schematic of the fluid mosaic model for the cellular plasma membrane. Cholesterol enriched rafts of different lipids exist alongside an array of integral and surface membrane associated proteins [12].

Beyond this the picture becomes even more complex as into the 1990's the concept of membrane domains was beginning to take shape [13]. It is now suggested that rafts of lipids, cholesterol and proteins exist within the plane of the bilayer offering specific functionality instrumental in maintaining overall cellular homeostasis [14–18]. However, there is yet much to be discovered with

regards to the biophysical and functional nature of the cell membrane with regards to its role in health and disease. As a result there is a significant requirement for high resolution microscopy and spectroscopic methods to probe this complex environment.

1.2. Biomedical Imaging

The information provided through methods of biomedical imaging has determined our ability to diagnose, investigate and treat illnesses throughout history. The diverse range of imaging methods available provides large data sets on any known ailment with varying degrees of resolution. While techniques such as MRI, CT, Ultrasound, X-ray, and Endoscopy are all fundamentally critical in terms of modern medicine, their focus is on large scale whole tissue or organ based information [19]. With the understanding of disease, both in terms of diagnostics and treatment, entering the realm of individual cells and individual molecule [20–22], a higher degree of both spatial and temporal resolution is required. In the context of investigating the role of the plasma membrane, numerous single molecule and optical microscopy and spectroscopy methods are widely employed [23]. Figure 2 outlines various imaging techniques and their relative resolution and penetration abilities with regards to biological samples.

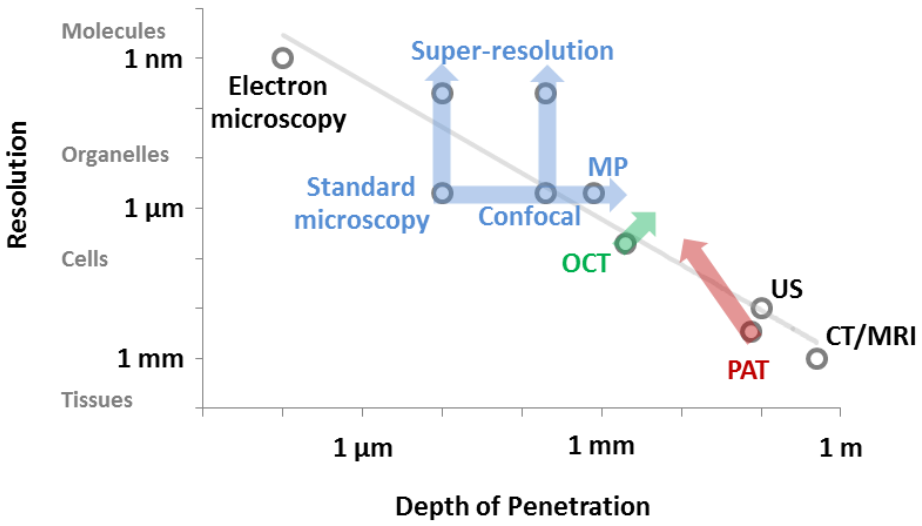

Figure 2: Plot of resolution against depth of penetration for a variety of biomedical imaging techniques. MP – Multi-Photon fluorescence microscopy. OCT – Optical coherence tomography. PAT – Photo-acoustic tomography. US – Ultrasound. CT/MRI – Computed Tomogrpahy/Magnetic Resonance Imaging.

In addition to resolution, depth of penetration is an important consideration when utilising a particular biomedical imaging technique. Figure 2 outlines the relative strengths of various imaging techniques in terms of both penetration depth and resolution. It can be seen from Figure 2 that optical microscopy methods, outlined by the blue arrows, fall perfectly within the necessary resolution range for cellular imaging. As technologies progress in terms of super-resolution techniques these methods are become ever more powerful in their ability to resolve smaller and smaller structures. For in-vitro and ex-vivo cellular studies deep sample penetration is not a pressing requirement making these techniques the ideal solution for investigating the dynamic processes at the plasma membrane.

1.2.1. Optical microscopy

Optical imaging techniques provide contrast based on a particular property of the illuminating light such as: scattering, absorption, reflection, and fluorescence. Depending on the application, light based microscopy offers the ability to image and measure aspects of biological samples based on changes to their chemical, biological or physical properties. One of the most important methods in light microscopy is fluorescence imaging, where either intrinsically fluorescent molecules or exogenous fluorophores are illuminated to provide contrast [24]. Fluorescent based techniques offer the possibility to observe and measure processes ongoing in various cellular compartments through the controlled labelling and imaging of specific molecules [25], [26]. With high specificity and selectivity, fluorescence based methods are ideal for examining disease from the single cell to single molecule level due to high levels of spatial and temporal resolution offered through modern instrumentation.

1.2.2. Fluorescence

Ever since Sir John Frederick William Herschel first observed a celestial blue hue emanating from his tonic water as it sat in the sunlight back in 1845 [24], the phenomena known as fluorescence has become a fundamental element of biomedical imaging [25]. Upon the absorption of a photon of light numerous photophysical processes occur within certain molecules, commonly known as fluorophores. Some of these processes are demonstrated in the Jablonski diagram in Figure 3.

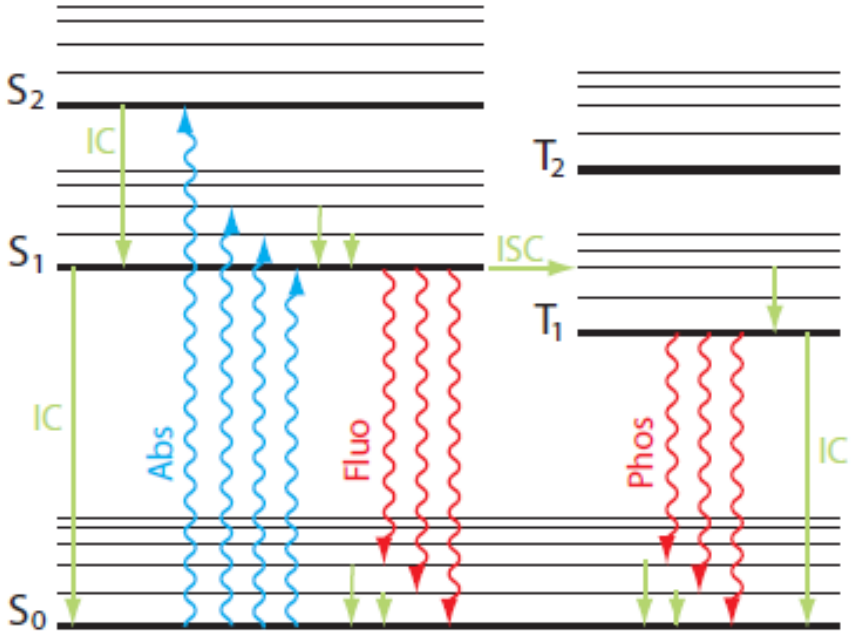

Figure 3: Jablonski diagram depicting energy conversion in fluorescent molecule. IC – internal conversion, Abs – absorption, Fluo – fluorescence, Phos – Phosphorecence, ISC – Intersystem crossing. S – Singlet excited energy states, T – Triplet excited energy states.

When a photon is absorbed, orbital electrons in fluorescent molecules are promoted to higher energy states. In the diagram the thick black lines depict the electronic states and the thinner lines show the vibrational states. Quickly following excitation the majority of the electrons quickly relax from higher electronic and vibrational states to the lowest excited singlet energy state, S_1, through internal conversion usually over the time frame of 10^{-12} seconds. The excited electrons occupy this lowest energy state for a period of time before becoming unstable and relaxing to the ground state, S_0. This is achieved either through non-radiative relaxation, e.g. through heat, or by radiative pathways to the ground state that are accompanied by the emission of a photon of light.

Electrons decaying directly from S_1 to S_0 emit energy in the form of fluorescence, however transitions to triplet excited states can sometimes occur through intersystem crossing. When occupying an excited singlet state an electron's spin is paired with the ground state electrons but when occupying an excited triplet state it is no longer paired to the ground state electrons and, as such, is allowed to occupy the excited state for a longer period of time. Upon decaying from the exited triplet state the emitted photon is of the form of phosphorescence and usually occurs over a time frame of 10^{-8} – 10^{-3} seconds in comparison to the 10^{-9} second time frame that occurs for fluorescence, known as the fluorescence lifetime. Excitation to an excited triplet state is far less probable than to an excited singlet state as it involves a forbidden electron spin transition.

All resultant radiative emission is of a lower energy than the incident excitation, due to the energy lost through the involved conversion processes, and is of a longer wavelength as a result. This shift in wavelength is known as the Stokes shift and is demonstrated in Figure 4.

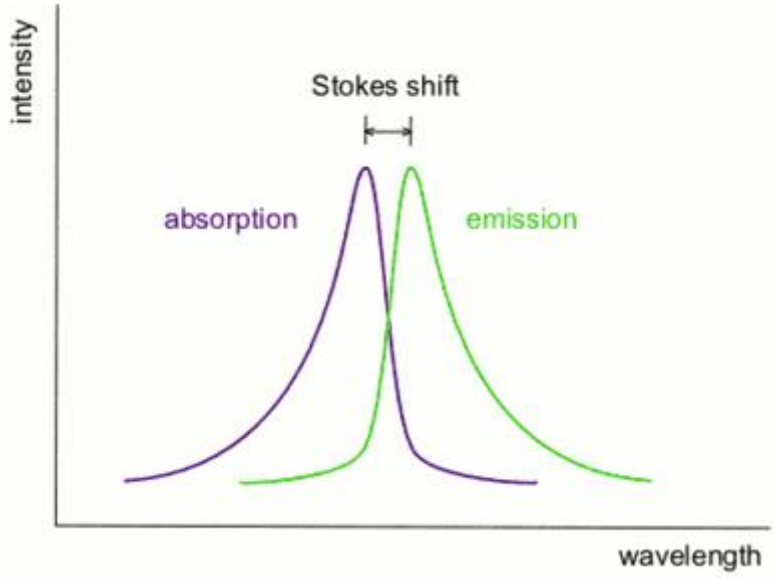

Figure 4: Stokes shifted spectra. Shift in absorption/emission spectra due to energy loss through competing radiative and non-radiative decay paths

This shift in emitted wavelength is the basis for any technique deriving information as a result of fluorescence. The ability to selectively detect light based on its wavelength enables systems to separate the emitted fluorescence photons from the incident excitation photons.

Three of the fundamental fluorescence properties of a fluorophore are the quantum yield, φ, the fluorescence lifetime, τ_L and the extinction coefficient. The quantum yield simply put, is the ratio of emitted photons to absorbed photons. This value is always less than one, due to the competing radiative and non-radiative decay pathways accounting for the expenditure of absorbed energy. The quantum yield, φ, is dependent on the radiative, k_r, and non-radiative, k_{nr}, rate constants, shown in Equation (1.1).

$$\varphi = \frac{k_r}{k_r + k_{nr}} \tag{1.1}$$

The fluorescence lifetime is theoretically described as the average time a fluorescent molecule remains in an excited state before relaxation and subsequent fluorescence emission. This is typically of the order of a few nanoseconds and is inversely proportional to the sum of the radiative and non-radiative rate constants.

$$\tau_L = \frac{1}{k_r + k_{nr}} \tag{1.2}$$

The radiative decay rate is an intrinsic property of the fluorescent molecule; however, the non-radiative decay rate can be influenced by the environment in which the molecule resides. Various processes are known to alter this pathway such as: Internal quenching, dynamic quenching, and energy transfer [27]. Internal quenching can arise as a result of internal molecular rotation driven by changes in temperature, viscosity and polarity. Collisional quenching occurs when the fluorescent molecule has a physical interaction with a quenching ion, e.g oxygen, resulting in increased rates of non-radiative decay. Energy transfer is more commonly referred to as Forster resonance energy transfer (FRET) where energy from a donor molecule is non-radiatively coupled to an acceptor molecule resulting in reduced lifetime and quantum yield values.

The third key parameter relating to a molecule's fluorescence is the extinction coefficient, or cross-section of absorption. This value relates to the probability that the fluorophore will absorb a photon of light and is denoted commonly as, ε, with units of $M^{-1}cm^{-1}$. The extinction coefficient is defined for a particular molecule at the wavelength corresponding to the maximum absorption. Typical values can range between, 20,000 to 200,000, with higher values relating to a more efficient absorber of radiative energy.

1.2.3. Fluorescence Microscopy

Utilising fluorescence as a contrast agent enables a microscopy technique with the ability to distinguish between separately labelled molecules. The technique exists in various forms and configurations with numerous advantages and potential drawbacks depending on the desired application. Investigations at the single cell level require a high degree of both spatial and temporal resolution to determine molecular dynamics.

The most commonly employed form of the fluorescence microscope is the epi-fluorescence configuration where a sample is illuminated and detected through the same objective lens. Excitation light is directed to the sample via an objective lens which also acts as an image forming light collector focussing the resultant fluorescence to either a camera or detector. The basic configuration can be seen in Figure 5.

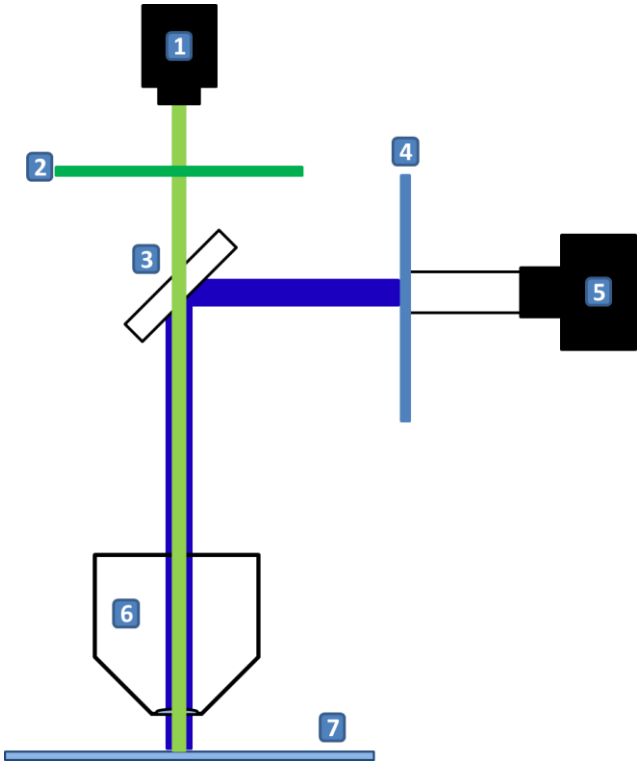

Figure 5: Epi-fluorescence microscope. 1 – Detector which is typically a CCD, EMCCD or ICCD. 2 – Emission filter passing fluorescence light only. 3 – Dichroic mirror separating excitation light from fluorescent signal. 4 – Excitation filter. 5 – light source typically a mercury arc light source. 6 – objective lens, 7 – sample.

While epi-fluorescence microscopy has numerous benefits, such as ease and cost of set up along with rapid image acquisition, fluorescence originating out with the focal plane is also collected by the detectors resulting in blurred images. This becomes problematic when viewing samples thicker than around 2 μm which are highly fluorescent throughout, such as fluorescently labelled cells. Confocal microscopy is a technique developed originally in the 1950's offering the ability to image optical sections of biological specimens. This is achieved through spatial light filtering with the use of a small pinhole placed in the detection path, just before the detector.

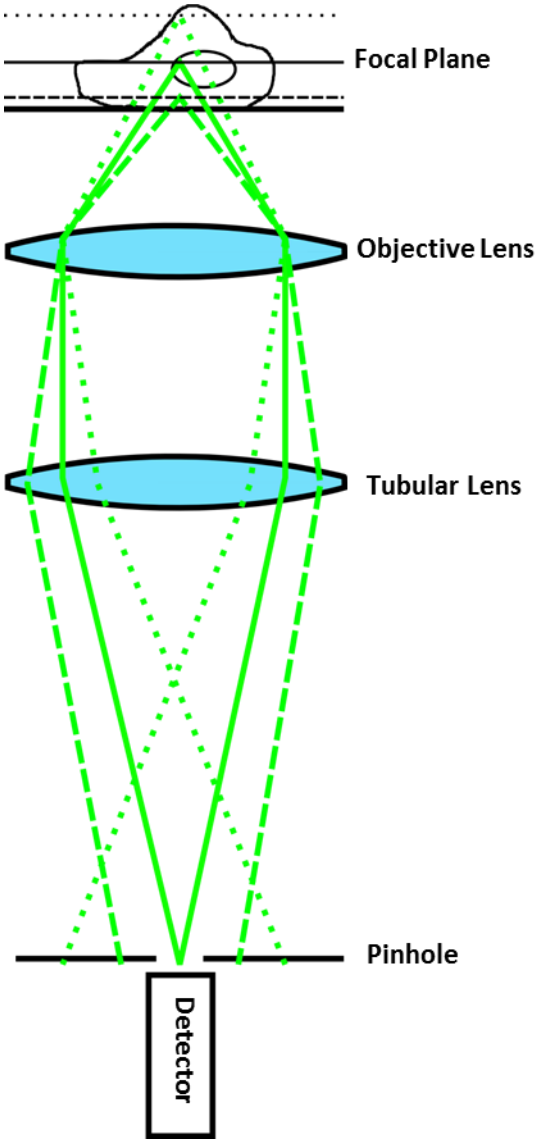

Figure 6: Principle of confocal detection optics. Fluorescence light is collected by the objective lens and directed to the detector via a small pinhole. The pinhole rejects light that does not originate from the focal plane creating a thin optical section. The dotted and dashed lines represent fluorescence originating from out of focus regions due to excitation from a Gaussian profiled laser beam,

The result is a well-defined Gaussian Point Spread Function (PSF) extending along the optical axis depending on the width of the detection pinhole. The width of the PSF is defined by the Numerical Aperture (NA) of the objective lens, with a higher value corresponding to a smaller PSF. The dimensions of the ideal PSF for a confocal configuration can be approximated by the following relationships.

$$R_{xy} = \frac{0.4\lambda}{NA} \tag{1.3}$$

$$R_z = \frac{1.4\lambda n}{NA^2} \tag{1.4}$$

R_{xy} and R_z denote the lateral x-y radius and the axial z radius, respectively. Both are defined in terms of the wavelength of incident light, λ, the numerical aperture of the objective lens, NA, and in the case of R_z, the refractive index of the immersion medium, n.

The most common form of the confocal microscope is the laser scanning confocal whereby a coherent light source is rastered across the focal plane of the image either by means of galvanometer driven mirrors or a piezo driven stage. Secondary fluorescence originating above and below the image plane is rejected by the pinhole resulting in the detection of an optically thin, typically 1 – 2 μm, section of fluorescence. The thickness of the section depends both on the NA of the objective lens and the size of the pinhole. Whilst the observational volume is significantly smaller than compared to widefield techniques, in the context of membrane investigations it is still 2 – 3 orders of magnitude larger in size.

1.2.4. Total Internal Reflection Fluorescence Microscopy (TIRFM)

While confocal microscopy has become one of the most important developments in imaging technology for the field of cell biology, in the context of the cell membrane it still falls short in terms of axial resolution. TIRFM offers an alternative illumination scheme exploiting the phenomena of total internal reflection (TIR). Utilising TIR the ability to selectively image thin optical sections, 10's to 100's of nanometres, at an interface is realised [28]. TIR is realised as a plane wave front propagates between media of differing refractive indices at an angle exceeding the critical angle. Light enters the sample in the

form of an exponentially decaying evanescent wave which propagates perpendicularly to the sample/substrate interface. The evanescent wave selectively excites fluorophores in close proximity to the sample/substrate interface. Figure 7 demonstrates the relative illumination regions created through epi-fluorescence, (a), confocal microscopy, (b), and TIRFM, (c).

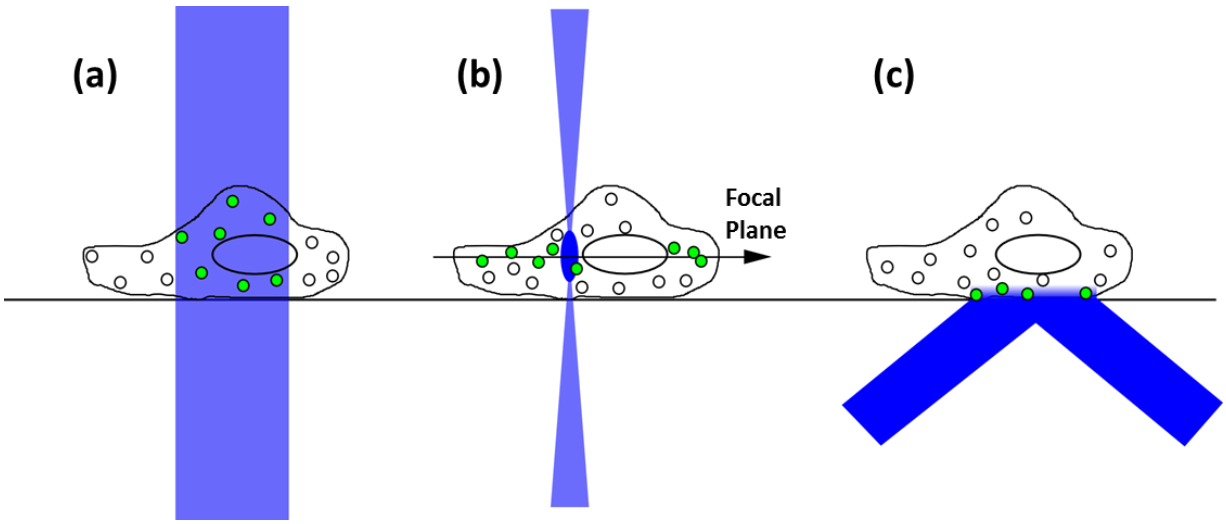

Figure 7: (a) – Epi-fluorescence configuration where all fluorophores throughout the sample are illuminated in the field of view. (b) confocal configuration where 1 – 2 μm sized focal volume is rastered through the sample along the focal plane. Only fluorophores within this plane are detected by the system. (c) – TIRFM configuration where small 100 nm evanescent wave excites molecules in close proximity to the substrate.

TIRFM has become a key experimental approach for elucidating processes occurring at the membrane region of adherent cells [29]. In recent years it has also become an essential technique for the investigation of membrane regulated processes such as endocytosis [30–33], exocytosis [34–36], cell adhesion [37–40], cytoskeletal dynamics [41–43] as well as investigations into the fundamental biophysical nature of lipid membranes.

An important area of research enabled by TIRFM is the analysis of the trafficking of intracellular vesicles. The technique was previously utilised to investigate the mechanisms involved with stress-induced ATP efflux in lung epithelial cells [36]. TIRFM enabled the ability to directly image single ATP-loaded vesicles and assess their recruitment and fusion to the plasma membrane during stimulated ATP release. In the field of diabetes research TIRFM has been widely used to investigate the role that vesicle trafficking plays in insulin stimulated glucose

metabolism [44]. Vesicles rich in glucose transporter 4 (GLUT4) molecules were individually imaged and analysed in terms of their dynamics near the plasma membrane.

1.2.5. Fluorescence Lifetime Imaging Microscopy

Standard fluorescence imaging techniques create contrast in images purely through the detection of the emitted fluorescent light offering the ability to observe and measure the location of the fluorescently tagged molecules under investigation. When observing complex biological samples, such as cells and tissue, data is obtained through analysis of the distribution of fluorescence intensity within the image. However, in most cases numerous assumptions are made based on the imaged systems providing qualitative results. For example, in cell biology intensity based measurements are at risk of misinterpretation due to factors such as photobleaching and the inability to precisely control the degree of labelling within a heterogeneous system.

Fluorescence Lifetime Imaging Microscopy (FLIM) is an imaging modality where pixel-wide contrast is determined by measuring the fluorescent lifetime of a fluorescent molecule at each point within the field of view. A component of a fluorophore's lifetime is an intrinsic property, different for most fluorescent molecules, and is typically of the order of a few nanoseconds. What makes the fluorescence lifetime such a useful property to measure is the fact that it is independent of fluorophore concentration and photobleaching. This makes FLIM an attractive method for imaging intricate systems where control over fluorophore distribution is difficult. Depending on the fluorophore under observation certain environmental parameters can be monitored due to the sensitivity of fluorescence lifetime values to various physical, chemical and biological elements. Oxygen concentrations [45], pH [46], and molecular binding events [47] have all been quantified through FLIM due to the quenching of particular fluorophores. FLIM is also emerging as a potential clinical tool in terms of cancer diagnosis and enhancing the search for new cancer drugs and therapies [48–51].

The fluid-mosaic understanding of membranes suggests they are comprised of smaller micro-environments, known as ‘rafts’, varied in terms of molecular composition and biophysical parameters. FLIM is increasingly being used as a tool to explore this diverse environment [52]. A combination of FLIM and FRET has been previously utilised to investigate lipid-lipid and lipid-protein interactions by monitoring the lifetime of the donor molecule which, under resonance energy transfer, is diminished [53–56]. In addition, environment sensitive dyes are available which display variations in fluorescence lifetime based on successful incorporation into different lipid domains [57].

A particular class of fluorophores known as ‘molecular rotors’ are emerging as promising tools for elucidating the physical nature of biological membranes [58]. Molecular rotors exhibit viscosity sensitive photophysical properties with alterations to both their fluorescent lifetime and quantum yield [59]. A more extensive review and summary of molecular rotors will be discussed in chapter 4.

1.2.6. Fluorescence Correlation Spectroscopy

The plasma membrane is a dynamic fluid environment and, as such, information relating to the mobility of single molecules is of great interest. Fluorescence Correlation Spectroscopy (FCS) is a sensitive technique with the ability to probe mobility constants for a very low number of fluorescent molecules. Using a small illuminated volume, traditionally via a confocal microscope, fluctuations in detected fluorescence intensity are time correlated to provide information on the dynamic processes driving them. The technique was developed in 1972 by Madge et al. to determine chemical reaction kinetics [60] and in 1974 diffusion coefficients [61]. Through the development of the confocal microscope [62], increasingly sensitive detection sources and cost effective illumination sources the technique became a powerful tool for investigating single molecule dynamics [63].

The technique is highly suited to membrane studies due to its relative sensitivity and the characteristic time scales over which it operates [64]. FCS has been

frequently used to determine diffusion coefficients of lipids, cholesterol, membrane proteins and various other membrane associated molecules [65].

1.3. Thesis Aims

The core objectives of this thesis were to construct and optimise versatile platforms consisting of TIRF, FLIM and FCS to explore various biological questions central to the plasma membrane. The first key research area investigated was in TIRFM imaging of insulin regulated glucose metabolism in adipose tissue and a simplified HeLa cell model. The second area of research focussed on the analysis of molecular rotors as reporters for membrane viscosity. To this end the following steps were undertaken to probe these issues.

1. Construction and characterisation of a TIRFM system capable of resolving single vesicle dynamics in single cells.

2. Development of image analysis procedure to analyse efficacy of HeLa cell line as a homologue for adipocyte cells to investigate insulin regulated glucose metabolism

3. Optimisation of a combined FCS-FLIM system to determine ability of BODIPY based molecular rotors to report on membrane viscosity

4. Development and characterisation of combined TIRF-FLIM system for the imaging of membrane viscosity in conjunction with molecular rotors.

1.4. Thesis Outline

Chapter 2 outlines the fundamental theory for the three advanced fluorescence techniques used in: Fluorescence Correlation Spectroscopy, Fluorescence Lifetime Imaging Microscopy and Total Internal Reflection Fluorescence Microscopy.

Chapter 3 details work relating to the construction and characterisation of an objective based TIRFM system and its application to live cell time-lapse imaging of insulin stimulated glucose metabolism in adipocyte cells and a modified HeLa cell line.

Chapter 4 describes the optimisation of a combined FCS-FLIM system to perform combined measurements on the molecular rotor BODIPY in artificial lipid bilayers.

Chapter 5 outlines the development of a combined TIRF-FLIM system to provide increased resolution for measurements of membrane viscosity using molecular rotors.

Chapter 6 summarises the presented work and discusses future directions for both the systems implemented and the biological questions raised in the preceding chapters.

2. Chapter 2: Theory of Techniques

2.1. Total Internal Reflection Fluorescence Microscopy (TIRFM)

2.1.1. Total Internal Reflection (TIR)

The fundamental theory of Total internal Reflection Fluorescence Microscopy (TIRFM) originates from the manipulation of an evanescent wave front created as light propagates between two media of differing refractive indices. When a plane wave of incident light travels from an optically denser medium to an interface with a less dense medium it becomes both refracted and reflected. The angle at which the light is refracted is governed by the wavelength of the incident light, the respective refractive indices of the two media and the angle of incident illumination. This is characterised by Snell's law.

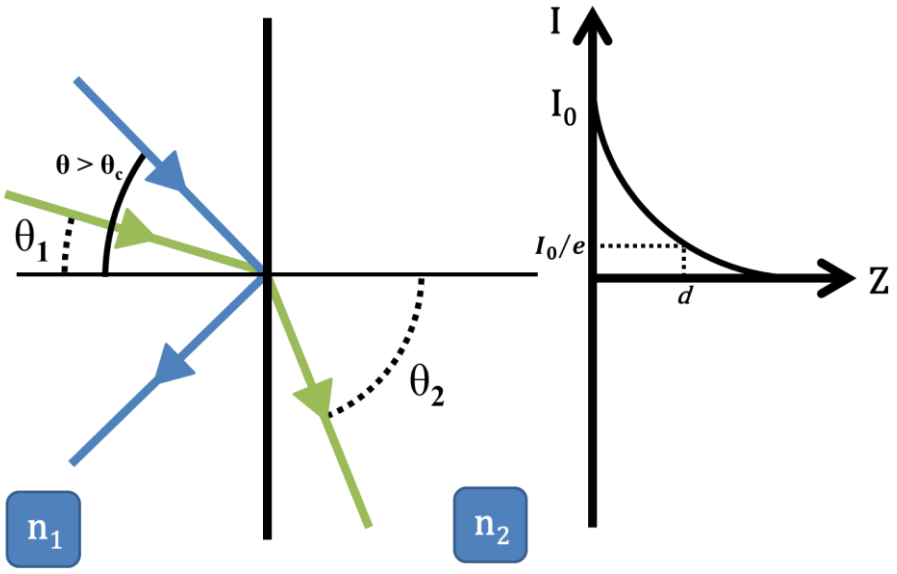

Figure 8: TIR representative schematic. X and Y axis' represent intensity, I, and position, Z, along the optical axis. Refractive indices n_1 and n_2 correspond to high, e.g glass, and low, e.g water/cells, values of refractive index. Green arrows represent plane wave incident on the interface at an angle, θ_1, lower than the critical angle, θ_c, which is refracted at an angle, θ_2. Blue arrows depict incident plane wavefront under TIR conditions, i.e incident angle, θ, higher than the critical angle, θ_c. I0 is the intensity of the resultant evanescent wave at $z = 0$ and the corresponding penetration depth, d, where the field has decayed to a point of I_0/e.

$$n_1 \times sin\theta_1 = n_2 \times sin\theta_2 \quad (2.1)$$

In the case of TIRFM n_1 represents the higher refractive index of the substrate and n_2 the lower index of the sample. θ_1 is the angle between the incident light and the normal to the reflecting interface, and θ_2 the angle of the refracted beam to the normal. TIR occurs when the angle of incidence, θ_1, is greater than the critical angle, θ_c, at which point $\theta_2 \geq 90^o$. A critical angle exists only when $n_1 > n_2$ and is defined by the relationship:

$$\theta_c = sin^{-1}\left(\frac{n_2}{n_1}\right) \tag{2.2}$$

At angles above θ_c all incident light is reflected except for a small amount of light which propagates perpendicularly to the interface creating a confined electromagnetic field. This is an evanescent field which decays exponentially from the interface. The intensity of the field decays such that:

$$I(z) = I_0 e^{\left(\frac{-z}{d}\right)} \tag{2.3}$$

In this instance, I_0 is the intensity of the field at the interface and I_z is the intensity at some distance, z, from the surface in the axial direction. d represents the point at which the intensity has decayed to 37% of its maximum value and is termed the penetration depth. This depth is dependent on the two refractive indices, the wavelength of the illuminating light and the angle at which it approaches the interfacial region.

$$d = \frac{\lambda}{4\pi} \times \left(\frac{1}{\sqrt{n_1^2 sin^2\theta_1 - n_2^2}}\right) \tag{2.4}$$

Typical values of d, are of the order of a few 10's to 100's of nm and this

exponentially decaying evanescent wave has the ability to selectively excited fluorescent molecules located within this surface localised region. The simplest way to decrease the depth of penetration is to adjust the angle of illumination further from the critical angle. Typical TIRFM experimental setups will consist of a solid/liquid interface consisting of glass, refractive index = 1.52, and water/cells, refractive index = 1.33.

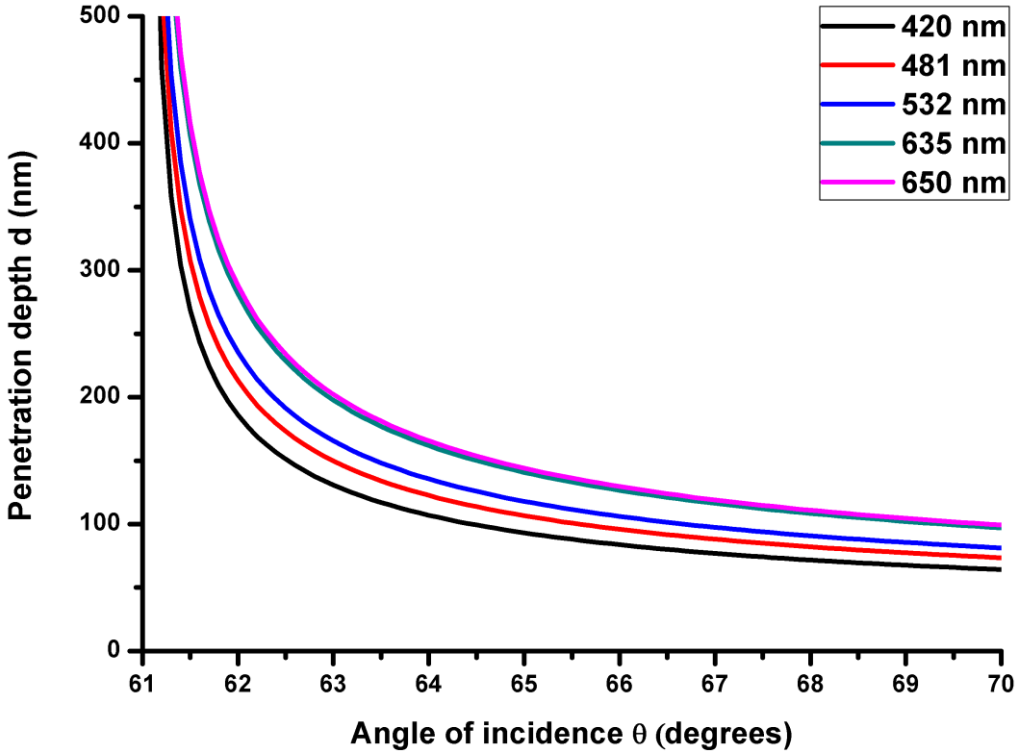

Figure 9: Plot of penetration depth vs. angle of incidence for a variety of common incident wavelengths. Simulated as outlined in equation (2.4) where n_1 = 1.52, glass, and n_2 = 1.33, water.

The solutions to Maxwell's equations for a plane wave front above the critical angle at the sample/substrate interface yields the following amplitudes for the electric field components of the evanescent wave at the point $z = 0$ [66].

$$E_x = \left(\frac{2cos\theta\sqrt{sin^2\theta - n^2}}{\sqrt{n^4cos^2\theta + sin^2\theta - n^2}}\right) A_{\parallel} e^{-i(\delta_{\parallel}+\pi/2)} \tag{2.5}$$

$$E_y = \left(\frac{2cos\theta}{\sqrt{1-n^2}}\right) A_{\perp} e^{-i\delta_{\perp}} \tag{2.6}$$

$$E_z = \left(\frac{2cos\theta sin\theta}{\sqrt{n^4 cos^2\theta + sin^2\theta - n^2}}\right) A_{\parallel} e^{-i\delta_{\parallel}} \tag{2.7}$$

The corresponding amplitude components for the magnetic field are as follows.

$$H_x = \left(\frac{2cos\theta\sqrt{sin^2\theta - n^2}}{\sqrt{(1-n^2)}}\right) A_{\perp} e^{-i(\delta_{\perp} - \pi)} \tag{2.8}$$

$$H_y = \left(\frac{2n^2 cos\theta}{\sqrt{n^4 cos^2\theta + sin^2\theta - n^2}}\right) A_{\parallel} e^{-i(\delta_{\parallel} + \pi/2)} \tag{2.9}$$

$$H_z = \left(\frac{2cos\theta sin\theta}{\sqrt{1-n^2}}\right) A_{\perp} e^{-i\delta_{\perp}} \tag{2.10}$$

For the above expressions $n = n_2/n_1$and is referred to as the relative refractive index. The amplitude components for the incident electric field vector for s-polarised (perpendicular) and p-polarised (parallel) incident light are given by $A_{\perp}$and $A_{\parallel}$ respectively. The phases of the perpendicular and parallel field vectors are given by $\delta_{\perp}$ and $\delta_{\parallel}$.

$$\delta_{\perp} = arctan\left(\frac{\sqrt{sin^2\theta - n^2}}{cos\theta}\right) \tag{2.11}$$

$$\delta_{\parallel} = arctan\left(\frac{2n^2 cos\theta}{n^2 cos\theta}\right) \tag{2.12}$$

The intensity, I_0, located at the interface, $z = 0$, is dependent on both the angle of incidence and the polarisation of the illuminating light. Two polarisation states are possible known as s-polarisation (perpendicular) and p-polarisation (parallel), with the corresponding intensities at $z = 0$ denoted as $I_0^{\perp}$and $I_0^{\parallel}$ respectively.

$$I_0^{\perp} = I_{\perp} \frac{4cos^2\theta}{1 - n^2} \tag{2.13}$$

$$I_0^{\parallel} = I_{\parallel} \frac{4cos^2\theta(2sin^2\theta - n^2)}{n^4cos^2\theta + sin^2\theta - n^2} \tag{2.14}$$

The intensities for both polarisation states are shown in Figure 10 for a range of incident angles from the critical angle to 90°.

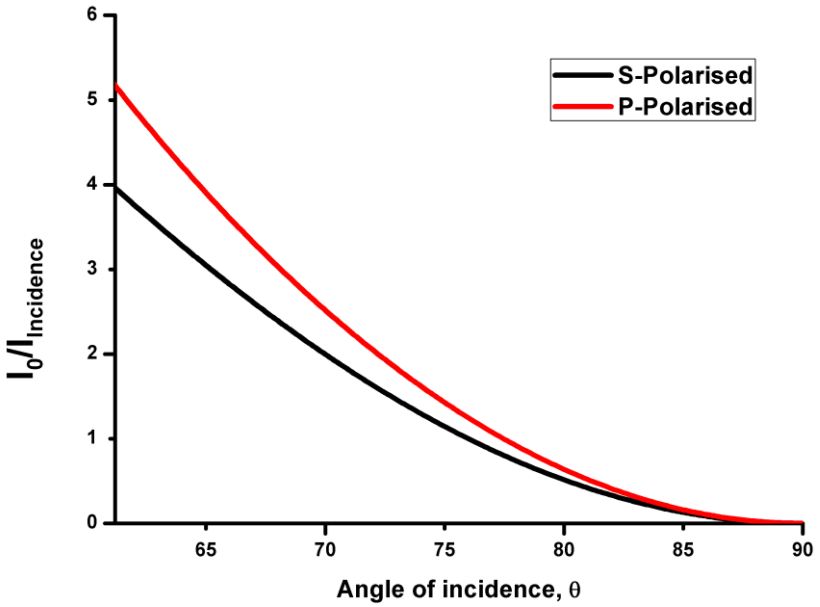

Figure 10: Plot of the ratio of I_0, the intensity of the evanescent field at z = 0, against I, the incident intensity, for both p-polarised and s-polarised light. Simulated over angles from the critical angle for a glass/water interface to 90°.

Figure 10 demonstrates the interesting properties of the evanescent field intensity at $z = 0$ where it can be seen to be stronger than the incident intensity for some angles above the critical angle. The reason for this increase is due to a surface polarisation induced by the incoming plane wave [67].

The energy flux at the interface is determined through the real component of the Poynting Vector, $\boldsymbol{S}$, given in equation (2.15) Where c , is the speed of light [66].

$$\boldsymbol{S} = \frac{c}{4\pi}\boldsymbol{E} \times \boldsymbol{H} \tag{2.15}$$

By substituting in the electric and magnetic field components outlined in (2.5)-(2.10) the z-component of the Poynting vector is found to be finite and when time averaged vanishes. As a result there is no energy flowing across the interface into the second medium [67]. However, when considering the energy transport along the interface, i.e. the x-component, a non-zero result is found meaning that the evanescent wave transports energy along the surface. For s-polarised light the electric field propagates perpendicularly respective to the interface in the x direction. Whereas for p-polarised incident light the electric field 'cartwheels' at the surface with a period of$\lambda_0/(n_1 sin\theta)$. This is due to the fact that for p-polarised light there is a non-vanishing z-component resulting in the electric field, $\boldsymbol{E}$, becoming elliptically polarised along the plane of incidence.

Exploiting the generated evanescent wave leads to a system whereby a small number of fluorescent molecules are excited at a surface. This forms the basis of the technique known as TIRFM.

2.1.2. Total Internal Reflection Fluorescence Microscopy (TIRFM) configurations

To enable TIRFM practically there are four key requirements: an ability to manipulate the angle of the incident excitation light, typically a laser, the refractive indices of the sample substrate interface, and the wavelength of the excitation light. The value of n_2 is an intrinsic value related to the sample to be observed, in the case of membrane studies is typically 1.33 – 1.37 as has been shown previously to be the values for cells [68]. This, fortunately, is similar to the refractive index of water, or most physiological buffers, so refractive mismatches in the sample are often avoided. The value of n_1 depends on the substrate chosen which, for most cellular experimentation, is the 1.52 value of common microscope coverslips. The most important variable to determine is the

angle of incidence which can be adjusted in two configurations for microscope systems: objective based TIRFM and prism based TIRFM.

2.1.2.1. Prism Based TIRFM

Figure 11 demonstrates one possible variant of a prism based TIRFM system.

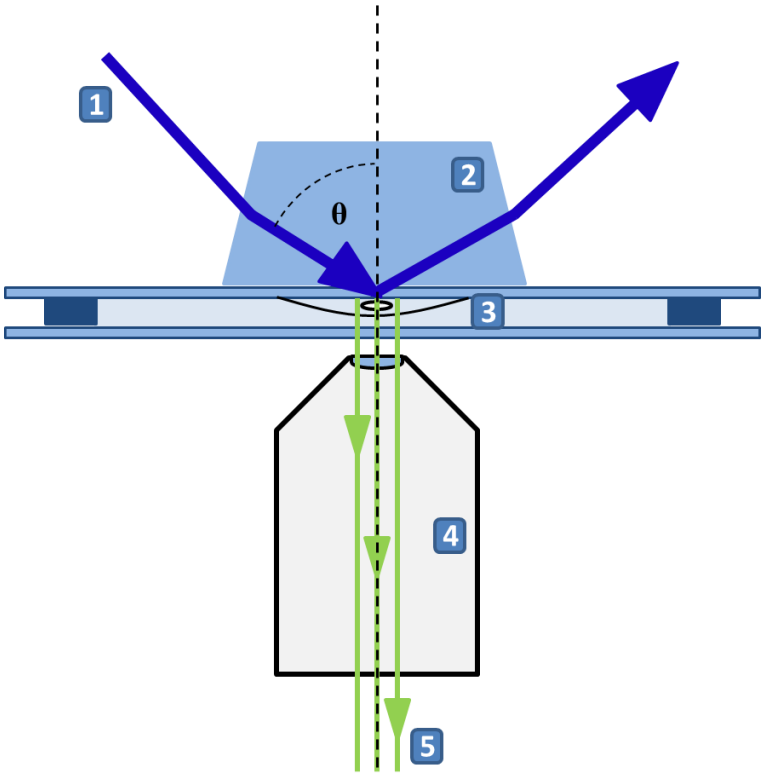

Figure 11: Prism based TIRFM system with an inverted microscope setup. 1 – Excitation light coupled to sample/substrate interface via trapezoidal prism. 2 – Prism. 3 – Sample of adherent cells on coverslip in buffered media wedged between a second coverslip. 4 – Objective lens. 5 – Resultant fluorescence originating from evanescent excitation.

Presented above is an example of a prism system implemented on an inverted microscope configuration. Excitation light is optically coupled to a coverslip via a prism of similar refractive index and immersion fluid. With an inverted microscope setup the sample is held upside down from a second coverslip via some spacers. The resultant fluorescence emission is collected by an objective lens below the sample.

Prism based TIRFM systems are relatively modular and can be combined with both inverted and upright microscopes. This approach offers many benefits in

terms of the use of lower magnification and numerical aperture objectives, however, the implementation of the prism itself can impose restrictions on the compatibility of some samples. To an extent the decoupling of the excitation and emission light can reduce the amount of background light in the system due to the fact that the intrinsic auto-fluorescence of certain optical elements, objective, prism, coverslips etc. is excluded from the detection path. There are also no restrictions imposed on the available incidence angles that can be achieved meaning that any theoretical penetration depth is possible. Utilising an inverted sample configurations places limitations on the use of high magnification, high NA lenses as the working distances can be very short, for NA = 1.45 the working distance is only 170 μm. With some prism configurations the lack of compatibility with high NA lenses restricts the achievable spatial resolution. As a result this type of microscopy may not suit some studies of membranes where high levels of lateral resolution are required, for example in the case of imaging diffraction limited vesicles related to endocytosis.

2.1.2.2. Objective based TIRFM

The alternative to a prism based system for achieving the angles necessary for TIRFM is to use an objective lens of high NA, greater than 1.4. The NA of a lens is defined by the relationship outlined in equation (2.16). In this case n is the refractive index of the medium between the lens and the sample and θ is one half of the angular aperture of the lens, i.e corresponding to the maximum of light propagation.

$$NA = n \times sin\theta \tag{2.16}$$

For the example of air between the objective and sample the refractive index would be 1, therefore a maximum NA of 1 would be possible due to the theoretical largest angle of 90°. To achieve a higher NA, corresponding to angles suitable for TIR, specialised immersion fluids are necessary to provide a high refractive index between the objective and the sample. Figure 12 demonstrates the objective TIRFM principle.

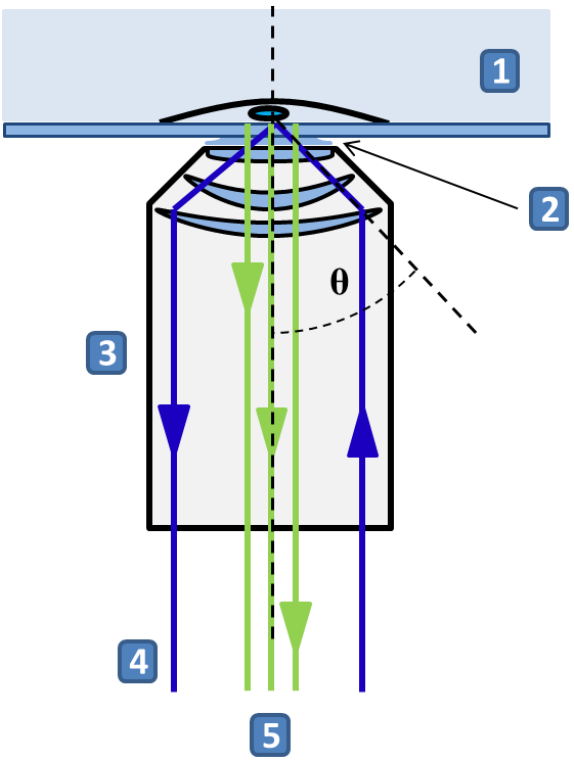

Figure 12: Objective based TIRFM system. 1 – sample of adherent cells and buffered media on appropriate coverslip, thickness 0.17 mm. 2 – Refractive index matching immersion fluid. 3 – High NA objective, >1.4. 4 – Excitation light adjusted to angle, θ > θc, by positioning beam to the far aperture of the high NA lens. 5 – Resultant fluorescence from evanescent field collected by same objective.

For most configurations of objective based TIRFM the illuminating excitation light is coupled to the high NA objective via a specialised TIRFM condenser with the ability to position the beam to the far aperture of the objective. This gives a fixed range of available angles, depending on the lens, over which the light can be focussed to the sample/substrate interface. The resultant fluorescence light is collected by the same objective and passed to the detection unit, e.g CCD, via a filter set that excludes any reflected excitation light and generated auto-fluorescence in the optical path. The range of angles that can be provided through and objective based setup is determined by the relationship $\theta_{max} = arcsin\, NA/n_2$ and for a typical setup, 1.45 NA objective coupled to a glass coverslip, this value is roughly 75°.

2.2. Fluorescence Lifetime Imaging Microscopy (FLIM)

2.2.1. Time-Domain FLIM

Fluorescence lifetime imaging microscopy (FLIM) is a method which unlocks information about the molecular environment that is not apparent in steady-state spectra. This is achieved through the measuring of a property of a fluorescent molecule known as the fluorescence lifetime. This value differs between fluorophores and is independent of the excitation intensity, concentration and unchanged through photobleaching. Depending on the molecule under investigation the fluorescence lifetime can respond to changes to temperature, pH, viscosity, polarity, proximity to other molecules and surfaces. Theoretically the fluorescence lifetime is defined as the average time a fluorescent molecule occupies an excited state and this is characterised practically by the decay of fluorescence intensity upon excitation. This decay takes the form of a simple exponential and is defined below.

$$I(t) = I_0 e^{\left(\frac{-t}{\tau}\right)} \tag{2.17}$$

In equation (2.17) I_0 represents the intensity of the fluorescent signal at time $t = 0$ initially after excitation and τ represents the fluorescent lifetime.

Commonly employed are two methods by which FLIM can be enabled with frequency-domain FLIM and time-domain FLIM. Outlined in this section will be the fundamental theory of the possibly implementations of time-domain FLIM as these will be the techniques used later in this thesis. In time domain-FLIM the rate of decay is measured through the use of high repetition rate laser sources often in the MHz ranges. There are two technological solutions to measuring the nanosecond fluorescence decays with up to picosecond resolution: Time Correlated Single Photon Counting (TCSPC) and the time-gated principle.

2.2.1.1. TCSPC

TCSPC based FLIM systems are incredibly sensitive with the ability to provide reliable fluorescence decay data from even just a few hundred photons [69]. Excitation is provided using high repetition rate laser sources via commercially available, inexpensive laser diode sources now offering repetition rates up to 100 MHz with incredibly short pulse widths, ~ 100 ps. The resultant fluorescence is detected by a highly sensitive single photon avalanche diode (SPAD) or photomultiplier tube (PMT) each with the ability to detect individual photon events. The TCSPC principle is based on the detection of individual photons, their point in time relative to the periodic light source and finally the rebuilding of the fluorescence decay waveform [70]. Figure 13 demonstrates the detection of photon events relative to the pulsed excitation source.

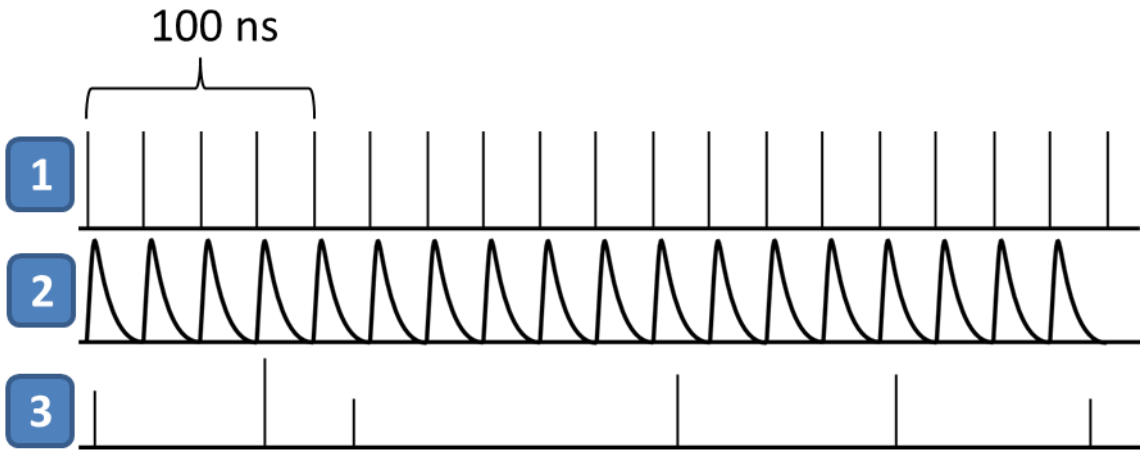

Figure 13: Demonstration of detection of individual photon events. 1 – stream of excitation pulses at rate of 40 MHz. 2 – Expected decay waveform representing fluorescence decay. 3 – Stream of recorded individual photon events representative of a realistic system with an average count rate of 10^7 photons per second.

Figure 13 (1) shows the stream of excitation pulsed from a highly repeating laser diode, in this case 40 MHz. It can be seen in Figure 13 that the recorded photon stream, (3), differs greatly from the expected signal of individual decays from each pulse of illuminating light, (2). The displayed photon detection events are representative of a count rate of, roughly, 10^7 photons per second, which is at

the limit of most photon counting systems. This means that the resultant fluorescence decay signal should be thought of as a probability distribution of detecting a photon event at a particular time point after an individual pulse of laser light.

This concept is demonstrated in Figure 14. Trace (1) demonstrates the desired output waveform detected within the sample period defined by the repetition rate of the laser. Trace (2) shows a representative distribution of detected photon events within each sample period continuing for the duration of the acquisition. Trace (3) reveals the actual distribution of photon events detected in each time channel within the laser period for all periods over the experimental acquisition.

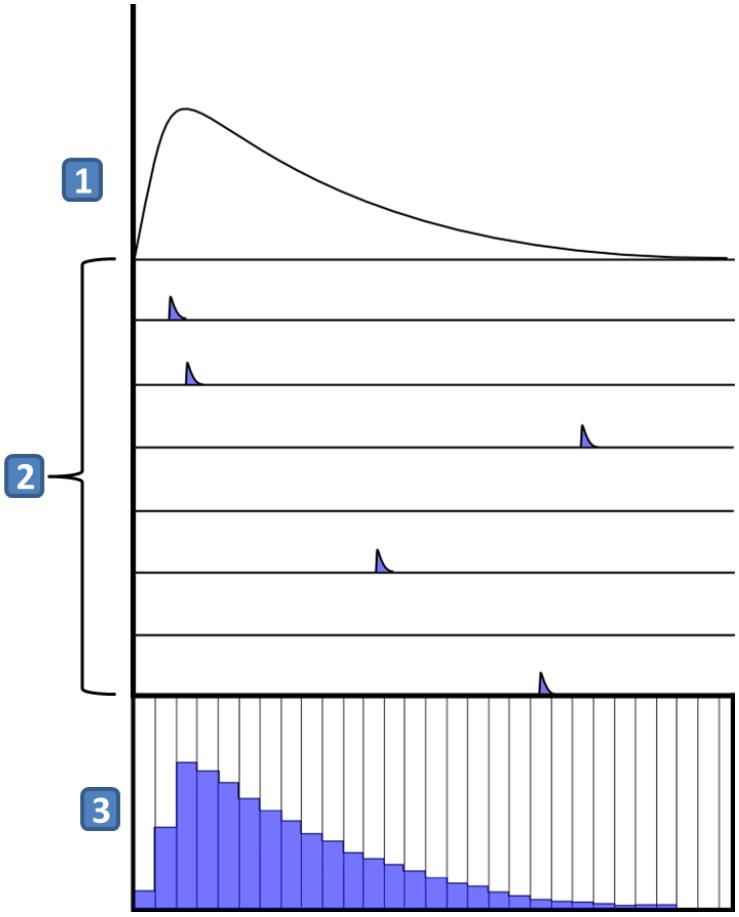

Figure 14: TCSPC principle. 1 – Original decay profile representative of the distribution of photon probability. 2 – Individual periods defined by the pulse of a repeating laser source. 3 – build-up of all detected photon events for a number of time bins after numerous repetitions of the laser pulsed detection period.

The TCSPC principle exploits the fact that the probability of detecting more than one photon per light pulse is negligible due to the low levels of light recorded in such a short time frame, e.g for 40 MHz a time frame of 25 ns. Even at the lowest levels of light there is no real limit in detection due to the single photon sensitivity of the system, however, there is a conceivable upper limit of detection. To ensure that the probability of detecting more than one photon per signal period is minimised a detected count rate of 0.1 photons per signal must not be exceeded. With modern high MHz repetition light sources this is equivalent to several 10^7 photons per second. Exceeding this upper limit of detection results in photon pile-up effects at the detector; however, for modern light sources with limits upward of 10^6 photons per second this is, in most cases, sufficient light signal to overload the most sensitive of detectors.

The general architecture of a high repetition rate TCSPC system can be seen in Figure 15.

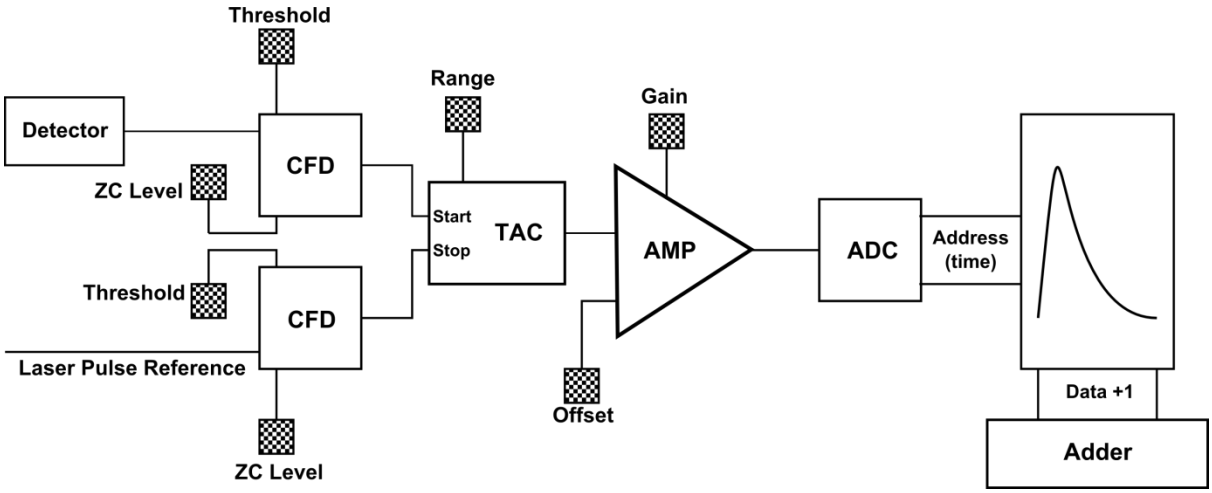

Figure 15: General architecture of reverse start-stop TCSPC system. ZC level – Zero Cross Level CFD – Constant Fraction Discriminator, TAC – Time to Amplitude Convertor, AMP – Amplifier, ADC – Analogue to Digital Convertor. Chequered squares indicate controllable elements.

Upon detection of individual photon events a detector, usually a PMT or SPAD, sends a pulse to a fast discriminator. These pulses tend to have considerable differences in amplitude due to the random nature of the detectors amplification. A Constant Fraction Discriminator (CFD) is used to trigger at a defined fraction of the overall pulse height to remove any timing errors

implemented due to the differences in pulse heights. The lower CFD is used to determine the reference of the excitation light pulse relevant to the particular detected photon. For modern systems capable of operating at laser repetition rates of 50 – 100 MHz a reverse start-stop principle is employed. In older systems the start signal for the detection period was defined by the laser pulse and the stop signal was provided by the detection of a photon event at the detector. This was deemed inefficient with highly repeating systems that observe numerous pulse periods where no photons are detected resulting in several start pulses with no corresponding stop pulses. The result was that the Time to Amplitude Convertor (TAC) required resetting every 10 to 20 ns. Using the detection of a photon as the start signal and the following excitation pulse as the stop signal increases the overall efficiency of the TAC which now only operates at the rate of photon detection. The TAC then converts the time between the reference laser pulse and the detected photon to a signal with proportional amplitude. The output voltage is delivered via a biased amplifier to an Analogue to Digital Converter (ADC). The corresponding digital output provides the detection time of the individual photons with respect to the corresponding excitation laser pulse. The ADC works with high precision resolving the TAC output signal to thousands of individual time channels of equal width. The ADC addresses a memory location for each detected photon corresponding to the time it was recorded in a word. The contents of the stored data are incremented over the course of the experimental acquisition providing the final photon distribution corresponding to the measured fluorescence decay profile. The ADC, TAC and CFD contain parameters which can be optimised to ensure that the overall detection period is synchronised to the repetition rate of the illuminating laser.

2.2.1.2. Time-Gated Principle

Where scanning laser microscopy may not be a viable option an alternative time-domain based FLIM method exists in time-gated FLIM, compatible with wide-field and TIRF illumination. The key difference between time-gated and TCSPC systems is in the detection hardware where, instead of a PMT or SPAD, an intensified gated CCD is used. Unlike TCSPC confocal based scanning methods,

the time-gated approach builds a lifetime image where each pixels value is determined simultaneously. This is achieved through synchronisation of the pulsed laser source with the read-out of the gated image intensifier. The principle is demonstrated in Figure 16.

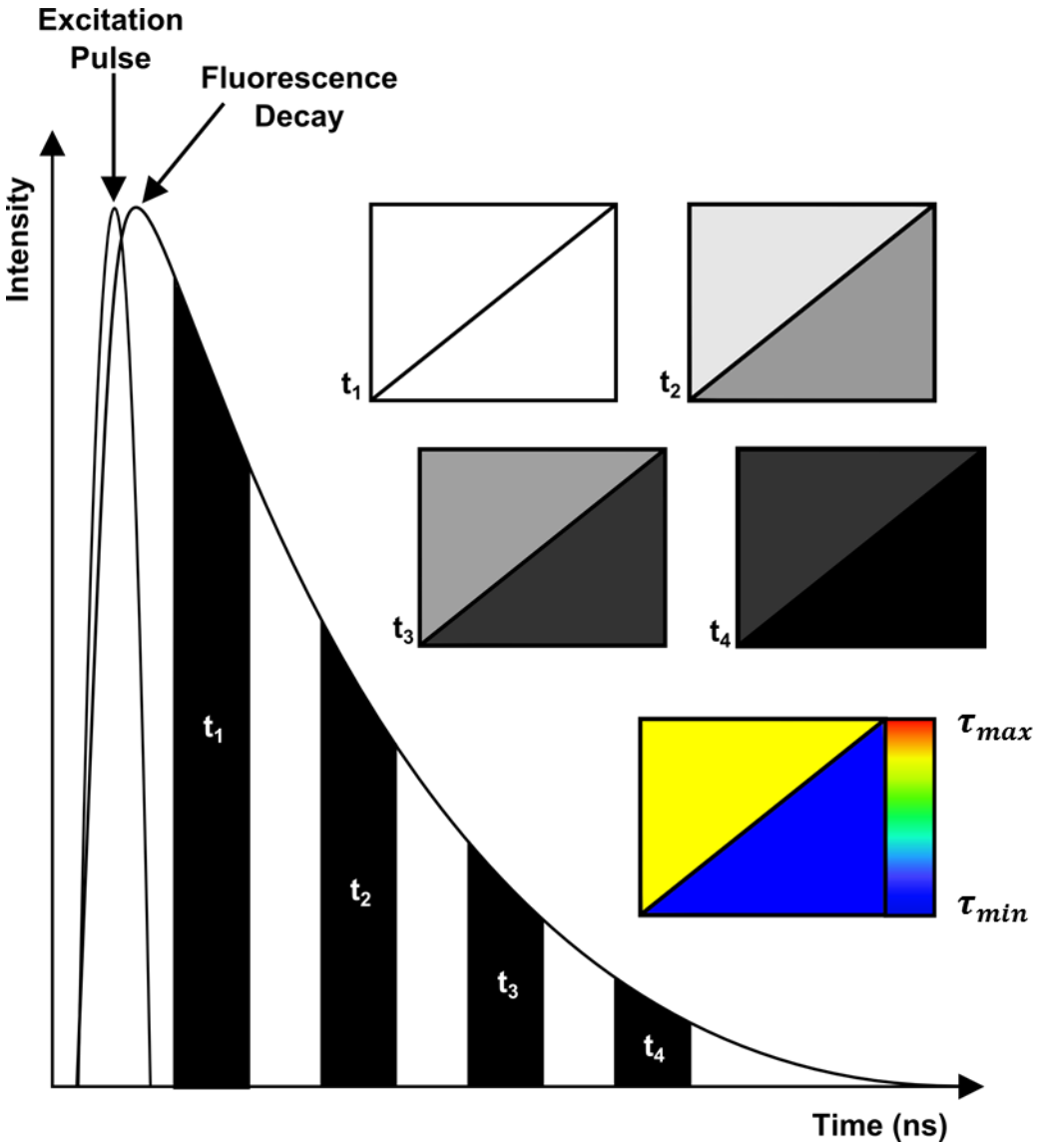

Figure 16: Simplified Time-Gated FLIM principle. Gated images are recorded at defined time intervals after a pulse of excitation. The decay of signal intensity is recorded for each pixel and assigned a lifetime value and corresponding colour.

Figure 16 demonstrates the principle of a time-gated FLIM system where upon excitation from a pulsed illumination source the decaying signal is recorded in a series of images. The gated ICCD camera is synchronised to the repetition rate of the laser and at defined nanosecond periods after a laser pulse, an image is recorded for a defined gate-width. The length of signal accumulation for each

image is defined by the exposure time of the camera with a longer exposure resulting in greater recorded signal. The width of each gate defines the resolution of the recorded decay analogous to the ADC resolution of a TCSPC system. Typical gate widths can be as low as 10's of picoseconds [71] providing high temporal resolution. In Figure 16 the example images show two regions of differing decay rates denoted by the upper left and lower right grey-scale image representations. Each section, after a measurement, is then assigned a colour corresponding to a particular lifetime value.

The benefits of such a system lie in the simultaneous recording of all positions in an image resulting in faster image acquisition. Some systems have been reported to record lifetime images up to a framerate of 100 Hz [72]. Other advantages lie in its versatility in use with various illumination configurations as there is no need for sample scanning [73]. The time-gated principle has previously been employed for use with wide-field endoscopy, structured illumination whole-field and TIRF microscopy [74–77] to expand the information retrievable via these microscopy methods.

2.2.2. Data Analysis

2.2.2.1. Exponential Curve Fitting

For all time-domain based FLIM methods, once the data has been recorded the information is interpreted through fitting of exponential decay functions. For a homogenous sample where all fluorescent molecules within are observed under the same physical conditions a single exponential of decay is observed. For more complex samples, such as biological specimens, the fluorescent molecules may experience multiple decay pathways within the same spatially resolved location manifesting itself as a sum of multiple exponential decays. The fitted decay functions for a single, double and triple exponential system are shown below.

$$f(t) = e^{-t/\tau} \tag{2.18}$$

$$f(t) = a_1 e^{-t/\tau_1} + a_2 e^{-t/\tau_2}$$

(2.19)

$$f(t) = a_1 e^{-t/\tau_1} + a_2 e^{-t/\tau_2} + a_3 e^{-t/\tau_3} \quad (2.20)$$

For the above expressions the τ values correspond to the measured lifetimes for each component of decay. The values of a represent the fractional contribution of each component to the overall fluorescence decay signal. The majority of modern FLIM image analysis software packages have the ability to fit up to 3 or 4 exponential decay components. Attempting to fit more than 4 components would need significant signal and analysing data of such complexity is difficult to interpret with any great deal of accuracy.

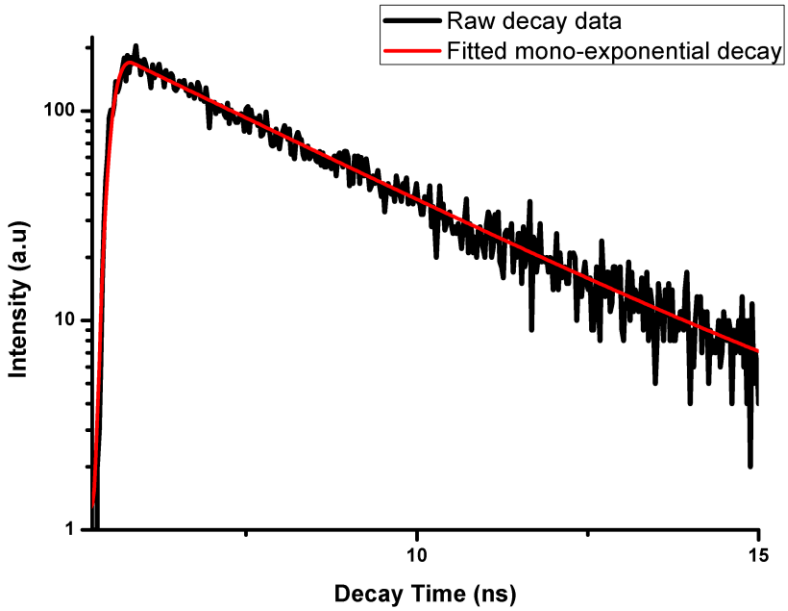

Figure 17: Example mono-exponential fluorescence decay plotted with a logarithmic intensity scale

Figure 17 demonstrates that a mono-exponential decay can clearly be determined when plotted against a logarithmic intensity scale. A more complex decay is demonstrated in figure where there are two components of fluorescence decay.

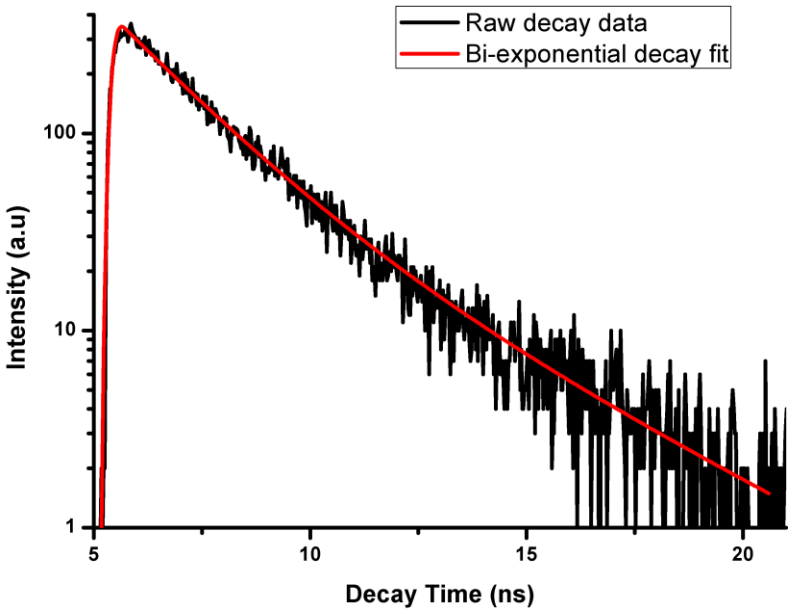

Figure 18: Example Bi-exponential fluorescence decay plotted with a logarithmic intensity scale.

The appropriate number of exponential components is traditionally determined through analysis of the reduced chi^2, χ^2, value, relating to the goodness of fit between the raw data and the model. Typical values between 1 and 2 suggest an overall good agreement between the model and the data.

2.2.2.2. The Instrument Response Function (IRF)

The measured decay function is more complex than simple decay functions in any real FLIM system. Due to the fact that the pulse width of the laser is not negligible and the detectors have a temporal response of a non-zero width these elements must be considered when analysing decay functions. To compensate for these properties in practical terms they are grouped to one Instrument Response Function (IRF). The IRF takes into account anything that will alter the shape of the measured fluorescence decay function from the detector and laser profiles to any optical reflections in the system. The recorded decay function is actually a convolution of the IRF with the decay function, $f(t)$, measured from the fluorescent molecules. This can be expressed mathematically as shown in equation (2.21).

$$f_m(t) = \int_{\tau=0}^{\tau} f(\tau) IRF(t-\tau) d\tau \quad (2.21)$$

In the above expression $f_m(t)$ is the measured fluorescence decay function and $f(\tau)$ is the true fluorescence decay. Unfortunately, due to various factors such as systematic noise in photon detection $f_m(t)$ is unknown. It is for this reason that fitted function is a convolution of both the IRF and a model exponential decay function outline in equations (2.18) - (2.20). The perfect IRF would be an infinitely short pulse having no effect on the overall shape of the fluorescence decay, however, this is often not the case. With modern pulsed laser diodes and fast single photon detection the IRF can be minimised to a width of only a few tens of picoseconds. This function is found experimentally through detecting a pulse directly from the illuminating source with the detector to be used. Modern software packages for FLIM analysis offer the possibility of using a recorded IRF that can be de-convoluted from the recorded fluorescence decay offering precision in lifetime recording.

2.3. Fluorescence Correlation Spectroscopy (FCS)

The theory of FCS is based on Poisson statistics [78] whereby the probability of a particular event occurring within a defined region of space, or time, can be determined if these events occur with a known average and independently of each other. For FCS the defined region in space is the effective confocal volume in which the number of occupying of molecules fluctuates around an average. Changes in the number of molecules in this space give rise to seemingly random fluctuations in fluorescence intensity. The physical processes that govern these fluctuations define the basis for the derivation of the autocorrelation function (ACF) from which physical constants can be extracted.

2.3.1. Confocal Volume

The standard for an experimental FCS system is based around a confocal microscope as illustrated in Figure 19.

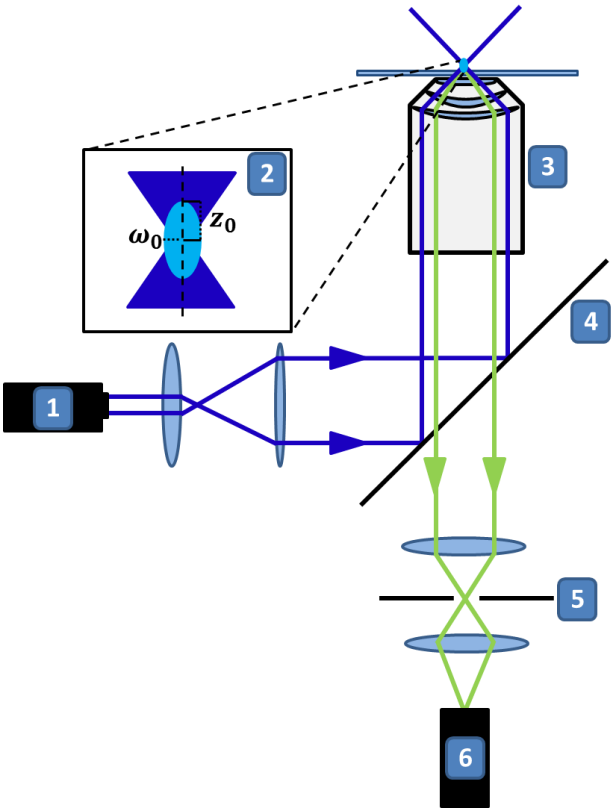

Figure 19: Confocal FCS system setup. 1 – Excitation laser source coupled to objective via series of optics. 2 – Defined confocal volume where ω_0 is the lateral radius and z_0 is the axial radius. 3 – Objective with NA > 0.9, typically a 40x 1.2 NA water immersion objective. 4 – Dichroic mirror. 5 – Confocal pinhole to restrict out of focus light and define the axial radius of the confocal volume. 6 – Detector, typically a photo multiplier tube (PMT) or avalanche single photon diode (APD).

One of the key aspects of FCS is the definition of the observed confocal volume which is achieved through the utilisation of a confocal optical configuration. The Gaussian beam profile of an excitation light source is focussed to the sample via a high NA lens, greater than 0.9, to create a tightly focussed spot radius. The resultant fluorescence is collected via the same objective and focussed to the detectors through a confocal pinhole rejecting out of focus light creating a thinly illuminated region. The dimensions of the observed area are typically 1 μm in width and 2 μm in height with a volume of roughly 1 fL. The result is an observational volume which takes the form of an ellipsoid and is demonstrated in Figure 19 (2). The implementation of a Gaussian beam results in the following detection profile for the observed region.

$$p(r) = I_0 e^{-2\left(\frac{x^2+y^2}{\omega_0^2}\right)} e^{-2\left(\frac{z^2}{z_0^2}\right)} \tag{2.22}$$

This defines the region where the excitation intensity decays to e^{-2} of its peak intensity, I_0, over all points r. The effective volume does not possess explicitly defined boundaries due to a number of factors [78] so the expression for V_{eff}differs slightly to that for the volume of a geometric ellipsoid.

$$V_{eff} = \pi^{3/2} \omega_0^2 z_0 \tag{2.23}$$

2.3.2. The Auto-Correlation Function (ACF)

The fluorescence signal in the focal region is recorded with single photon sensitivity and fluctuations in intensity around an average are noted. Auto correlation as a function of time of this signal produces the intensity based auto-correlation function (ACF). A combination of the ACF with knowledge of the detection profile gives rise to the information provided on the physical parameters driving the fluctuations in fluorescence intensity. The ACF is defined in equation (2.24).

$$G(\tau) = \frac{\langle I(t) I(t+\tau) \rangle}{\langle I \rangle^2} \tag{2.24}$$

$$G(\tau) = \frac{\langle \delta I(t) \delta I(t+\tau) \rangle}{\langle I \rangle^2} + 1 \tag{2.25}$$

These two expressions both hold valid for the definition of the auto-correlation function. The first expresses it purely in terms of the measured intensity at times (t) and$(t+\tau)$, normalised by the average intensity. The second expresses the function in terms of the fluctuations around the average intensity such that: $\delta I(t) = I(t) - \langle I \rangle$. This gives rise to the first physical parameter which can be noted from the auto-correlation function.

Due to fluctuations arising from random processes, such as diffusion, in a system at equilibrium the average of the square of the fluctuations in intensity, known as the sample variance, equals the average that value i.e. $\langle (\delta I)^2 \rangle = \langle I \rangle$. This holds true for any parameters which fluctuate around a mean resulting in intensity fluctuations as there are as many fluctuations above the average as there are below. Take N to be the number of particles in the focal element at a given time, this means that: $\langle (\delta N)^2 \rangle = \langle N \rangle$. The same can be said for concentration since the intensity is directly proportional to both the concentration and number of fluorescing particles in the observed space. Looking back at the auto-correlation function for the initial correlation time, such that $\tau = 0$, this then gives:

$$G(0) = \frac{\langle \delta I(t) \delta I(t+0) \rangle}{\langle I \rangle^2} = \frac{\langle \delta I(t)^2 \rangle}{\langle I \rangle^2} \tag{2.26}$$

Due to the proportional relationship between intensity, concentration and particle numbers it can be deduced that:

$$\frac{\langle \delta I(t)^2 \rangle}{\langle I \rangle^2} = \frac{\langle (\delta C)^2 \rangle}{\langle C \rangle^2} = \frac{\langle (\delta N)^2 \rangle}{\langle N \rangle^2} = \frac{1}{\langle N \rangle} \tag{2.27}$$

This shows that at time interval $\tau = 0$ the amplitude of the correlation function is inversely proportional to the average number of fluorescing particles. For a large number of fluorescing particles, i.e. a high concentration, the amplitude of the trace would be incredibly low and difficult to deduce from any sort of noise, hence why FCS experiments yield best results from monitoring low concentrations of fluctuating fluorophores.

There are numerous physical processes that can be determined using FCS such as diffusion in 3D and 2D, anomalous diffusion, active transport, reaction rates, molecular binding, and molecular rotation. Originally the technique was used to observe chemical reaction rates [60] but is now more commonly used to investigate rates of diffusion. Figure 20 demonstrates some example systems whereby fluctuations in fluorescence intensity are driven by different means.

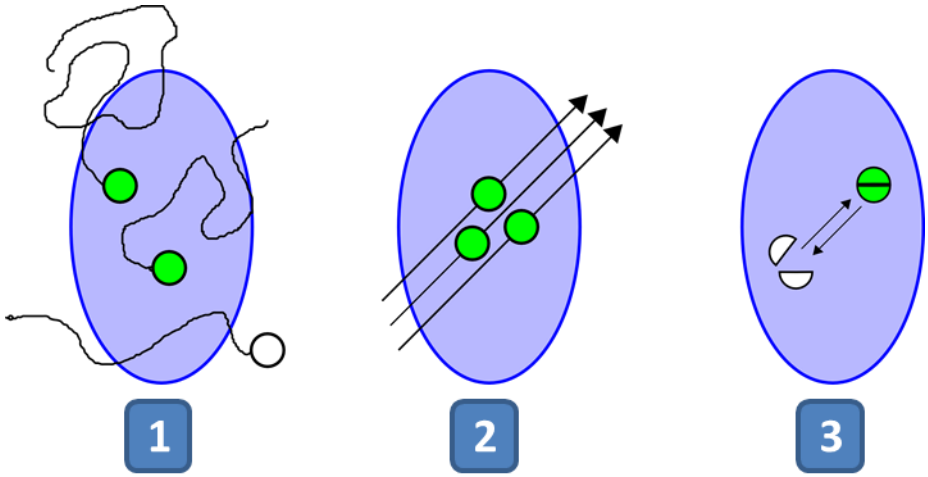

Figure 20: Mechanisms of fluorescence fluctuations within the boundaries of the confocal volume. (1) – Diffusion, (2) – Flow, (3) – Chemical reactions

Figure 20 (1) shows a commonly investigated system where the thermal motion in a fluid mobilises the fluorescent molecules through the focal region. FCS can also be used to investigate systems under flow conditions as shown in (2). Finally fluctuations that are independent of the focal volume can also be observed such as particular chemical reactions where the fluorescence of the molecule is activated and deactivated within the focal volume.

Below the auto-correlation function relating to a system influenced by thermal diffusion will be derived. To determine physical data from correlation measurements, in terms of kinetics, a suitable model needs to be fit to the auto-correlation function relating. The fitted model relates the dimensions of the optical system and the processes driving intensity fluctuations. This To begin with an arbitrary parameter called the brightness, B, is defined: $B = q\sigma Q$. Coupled within the brightness are the parameters of the quantum efficiency of

the detector, q, the cross-section of absorption of the fluorescent molecules, σ, and the quantum yield of the fluorophore, Q. This is a way of grouping all immeasurable values that will later be cancelled by normalisation. Expressing the intensity in terms of the system parameters, i.e. the optical system and the parameters of the fluorophore:

$$I(t) = B \int S(r)I(r)C(r,t)dV \tag{2.28}$$

$S(r)$ refers to optical transfer function (OTF) for the optical system determining the spatial collection efficiency over all points, r, within the observable space. $I(r)$ and $C(r,t)$ are the intensity and the concentration of fluorescent molecules, respectively, at any given point in the detection region and at any point in time, t. This is integrated over the entire observational volume, V, for all points, r. The OTF and intensity values can be grouped together to provide the detection profile which was defined earlier in equation (2.22), $p(r) = S(r)I(r)$. The ACF can now be re-written as:

$$G(\tau) = \frac{B^2 \int\int p(r)p(r')\langle \delta C(r,t)\delta C\big(r',(t+\tau)\big)\rangle dV dV'}{\left(B\langle C\rangle \int p(r)dV\right)^2} \tag{2.29}$$

The denominator for the above expression denotes the average intensity squared, as in equation (2.24), as the product of the average concentration of fluorescent molecules and molecular brightness over all points in the focal volume. The numerator gives the product of fluctuations in the intensity at time, t, and time, $t + \tau$, at all points in the system. For the fluctuations taken at a point in time, $t + \tau$, the position will most likely have also changed which is denoted by r' and then integrated against dV'. The brightness term is independent of position so is grouped outside of the integral and is cancelled since the function is normalised by the average intensity squared. It is at this point where the model of the auto-correlation function may be defined relative to the kinetic processes under observation.

The concentration of fluorescent molecules within the observational volume can be considered in terms of their local concentration, $C(\vec{r},t)$, their ensemble average, $\bar{C} = \langle C(\vec{r},t)\rangle$, and the concentration fluctuation, $\delta C(\vec{r},t) = C(\vec{r},t) - \bar{C}$. Fluctuations of concentration relax according to Fick's second law denoted in (2.30).

$$\frac{\partial \delta C(\vec{r},t)}{\partial t} = D\nabla^2 \delta C(\vec{r},t) \tag{2.30}$$

In the above expression D represents the diffusion coefficient. Solving the partial differential with the Fourier transform provides the following expression:

$$\delta C(\vec{q},t) = \delta C(\vec{q},0)e^{(-Dq^2t)} \tag{2.31}$$

This now provides the ability to calculate the autocorrelation of the concentration fluctuations. For a system where particles are diffusing freely in 3-dimensions the term $\langle \delta C(r,t)\delta C\big(r',(t+\tau)\big)\rangle$, the number density auto-correlation term, can be derived as:

$$\langle \delta C(r,t)\delta C\big(r',(t+\tau)\big)\rangle = \langle C\rangle \frac{1}{(4\pi D\tau)^{\frac{-3}{2}}} e^{\frac{-(r-r')^2}{4D\tau}} \tag{2.32}$$

This expression can then be substituted back into (2.29) to provide the following expression:

$$G(\tau) = \frac{1}{\langle C\rangle (4\pi D\tau)^{\frac{-3}{2}}} \frac{\int\int p(r)p(r')e^{\frac{-(r-r')^2}{4D\tau}} dVdV'}{\left(\int p(r)dV\right)^2} \tag{2.33}$$

Integrating this function over the respective volumes and remembering the convention for the effective volume, shown in (2.22), provides an expression for the auto-correlation function in terms of 3D diffusion.

$$G(\tau) = \frac{1}{V_{eff}\langle C\rangle}\frac{1}{(1+\frac{\tau}{\tau_D})}\frac{1}{\sqrt{1+\left(\frac{\omega_0}{z_0}\right)^2\frac{\tau}{\tau_D}}} \tag{2.34}$$

For the above expression V_{eff} is the effective confocal volume in which fluctuations are measured as denoted in (2.23). The auto-correlation function gives rise to the characteristic diffusion time τ_D which can be related to the diffusion coefficient of the fluorescent species as follows:

$$\tau_D = \frac{\omega_0^2}{4D} \tag{2.35}$$

The first part of auto-correlation function can be used to determine the dimensions of the focal volume. This occurs by calculating the amplitude of the correlation function at time $\tau = 0$ so that the other elements of the expression are reduced to 1. Through using a fluorophore of known concentration and with a defined diffusion coefficient (2.35) and (2.36) can be used to calculate both ω_0 and z_0 [79].

$$G(0) = \frac{1}{\langle C\rangle V_{eff}} = \frac{1}{\langle N\rangle} \tag{2.36}$$

Examples of the measured auto-correlation function can be seen in Figure 21.

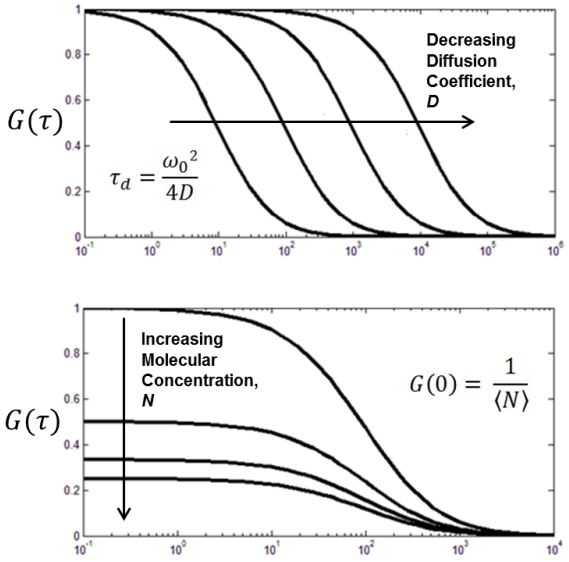

Figure 21: Simulated Auto-correlation functions for systems of increasing diffusion coefficients and increasing particle concentration

As can be seen in upper simulated auto-correlation functions, as the diffusion coefficient decreases $G(\tau)$ is shifted to higher values. As the number of molecules in the observational volume increase, the amplitude of $G(\tau)$ is decreased, suggesting that lower concentrations are desirable for FCS measurements.

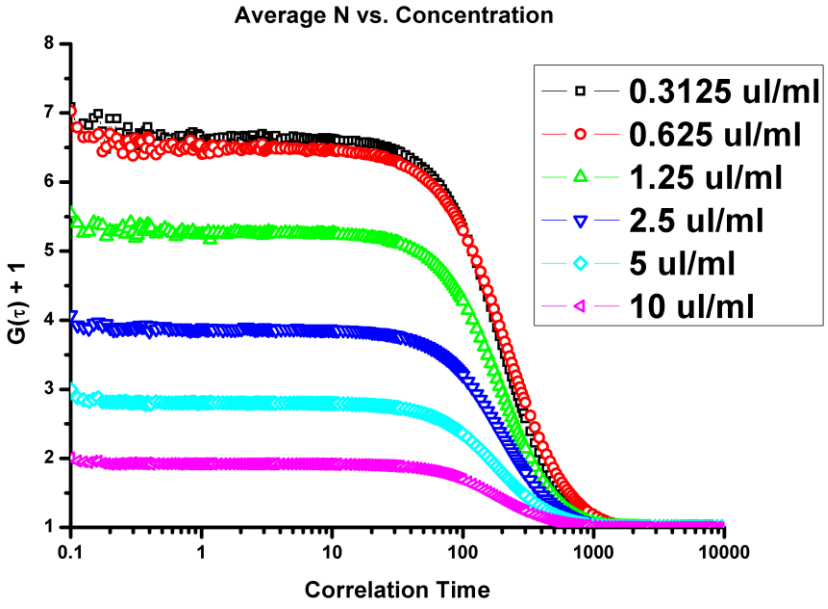

Figure 22: Measured auto-correlation functions for diffusing 100 nm microspheres with increasing concentrations. Concentrations are volumes of 100 nm microsphere stock solutions per ml of water.

Taking the values of N taken from the amplitude of the auto-correaltion function and plotting them against the concentration of microspheres per ml of water is shown in Figure 23.

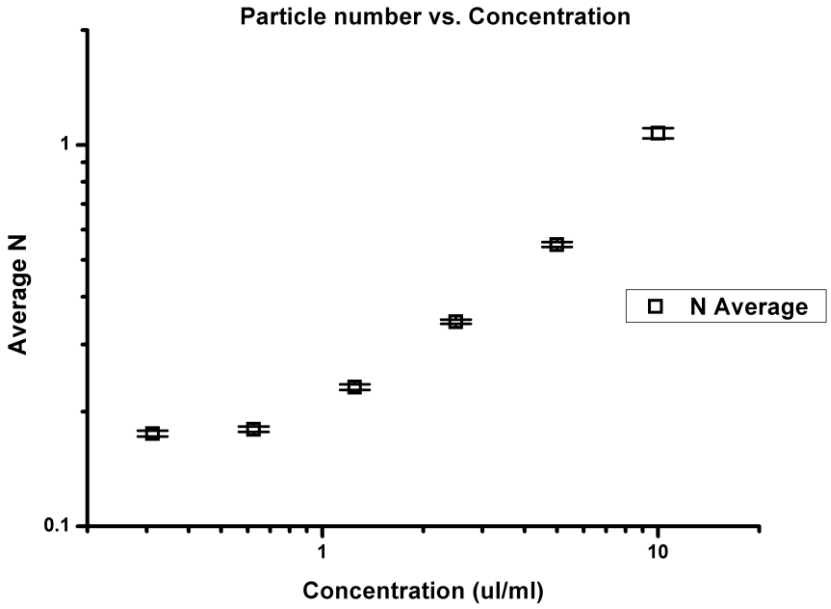

Figure 23: Average number of particles in focal volume against concentration of 100 nm microspheres per ml of water

As can be seen in Figure 23 the average number of particles follows a linear relationship with the concentration of particles in water until low concentration, roughly 1 – 2 μl/ml. The reason for this is as the average signal of fluorescence reduces close to the intrinsic background count rate of the system, it becomes difficult to obtain valuable information about particle concentration. A correction exists for incredibly dilute samples in the pico-molar range [79].

As mentioned earlier, FCS measurements can be utilised to determine dynamics other than those driven by 3D-diffusion. Translational 2D diffusion coefficients can be extracted by fitting a model very similar to (2.34).

$$G(\tau) = \frac{1}{V_{eff}\langle C\rangle}\frac{1}{(1+\frac{\tau}{\tau_D})} \tag{2.37}$$

It is also possible to analyse more complex systems where there are more than a singular diffusing species. This may be due to fluorescent particles of differing sizes or where a fluorescent probe is used to observe molecular binding to larger molecules. When bound to a target molecule the probe will exhibit a reduced coefficient of diffusion. If there exists two possibilities where there is a fraction of both bound and unbound fluorescent probe in the observational volume the following model can be used.

$$G(\tau) = \frac{1}{\langle N \rangle}\left(\left\{\frac{1-y}{\left(1+\frac{\tau}{\tau_{fast}}\right)}\frac{1}{\sqrt{1+\left(\frac{\omega_0}{z_0}\right)^2\left(\frac{\tau}{\tau_{fast}}\right)}}\right\}+\left\{\frac{y}{\left(1+\frac{\tau}{\tau_{slow}}\right)}\frac{1}{\sqrt{1+\left(\frac{\omega_0}{z_0}\right)^2\left(\frac{\tau}{\tau_{slow}}\right)}}\right\}\right) \quad (2.38)$$

The fractional contribution to the auto-correlation function for a secondary slower component of diffusion is given by the variable y and the two respective diffusion times are denoted by τ_{fast} and τ_{slow}. For the case of molecular binding the fast component would be attributed to unbound fluorescent probe diffusing freely in the system, whereas, the slow component represents bound probe molecules. Theoretically any number of diffusing species can be extracted from $G(\tau)$ [80], however, in systems of more than two components the exponential decays become indistinguishable. The smallest possible difference in diffusion coefficient that can be determined between two species is roughly 1.6 [81].

Models for auto-correlation functions determining kinetics such as flow, chemical reaction rates have been previously derived [63]. Flow speeds can be determined using the following model:

$$G(\tau) = \frac{1}{\langle N \rangle} e^{-\left(\tau/\tau_V\right)^2} \quad (2.39)$$

In this instance $\tau_V$represents the characteristic flow time and is related to the dimensions of the focal volume via:

$$\tau_V = \frac{\omega_0}{V}$$

(2.40)

Where, V, represents the relative flow speed. Note that since the this is a volumetric measurement no information is provided in terms of directionality and as a result $G(\tau)$ does not provide a measure of velocity. However, previous works describe a dual focus system where both speed and direction are measured with two confocal volumes positioned at a known distance apart and performing cross-correlation of the two recorded auto-correlation functions [82].

In complex systems where both convective flow and diffusion occur a summation of the two models can be employed to distinguish diffusion coefficients and flow speeds simultaneously.

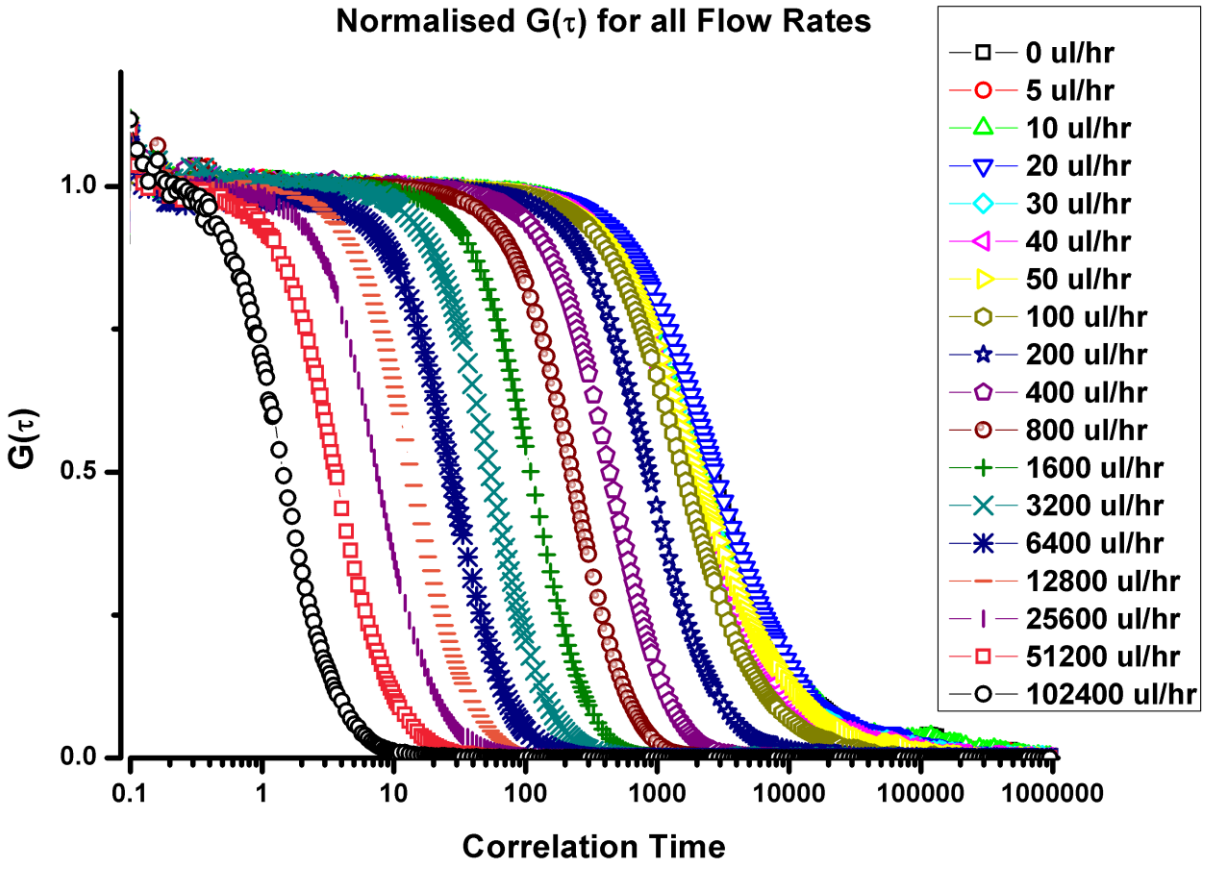

Figure 24: Auto-correlation functions measured for 100 nm fluorescent microspheres flowing in a 250 μm glass capillary channel. Confocal volume positioned to centre of channel and flow speed gradually increased.

Figure 24 shows measured data of 100 nm fluorescent microspheres flowing within a 250 μm glass capillary. By positioning the confocal volume to the mid-point of the channel and adjusting the flow rate, by means of a syringe pump,

the auto-correlation functions were recorded. As the flow rate decreases to < 100 μl/hour the auto-correlation function ceases to increase any further. It is at this point where diffusion becomes the dominant physical force.

3. Chapter 3: TIRF investigation of Glucose Metabolism in HeLa cell line

3.1. Introduction

3.1.1. Diabetes

The negative impact of diabetes mellitus on the health and wellbeing of the world's population is increasing as the number of diagnosed cases, in particular type 2 diabetes mellitus (T2DM), continues to rise sharply. In 1985 it was estimated by the World Health Organisation (WHO) that, worldwide, 30 million people suffered from the condition with the number rising to 135 million by 1995 [83]. According to the International Diabetes Foundation by 2014 this figure was said to top 387 million people [84] with 90% of present cases taking the form of TD2M. The financial cost of the disease was estimated to be roughly [85] $245 billion in the U.S alone in the year 2012 with a global cost closer to $600 billion dollars contributing to up to 5 million deaths per year.

Type 1 diabetes is characterised by a failure in the body's ability to produce sufficient insulin. Whilst the pathogenesis of Type 1 diabetes is still a topic for debate and exploration [86] it is categorised as an autoimmune condition where there is widespread destruction to the insulin producing pancreatic β-cells resulting in a need for exogenous insulin [86]. Type 2 diabetes, however, occurs as a result of the inefficient utilisation of naturally produced insulin [84], [87]. This is either through resistance to the action of the insulin or due to a disorder in insulin secretion. In all instances of the disease the result is an imbalance in circulating blood glucose levels. Elevated blood glucose levels, hyperglycaemia, and reduced blood glucose levels, hypoglycaemia [88] can result in a variety of conditions such as cardiovascular disease, ketoacidosis, coma and even death. T2DM is the most prevalent form of the condition throughout the world and can arise due to numerous factors such as inactivity, poor diet or age but the molecular pathways through which it propagates are a present matter for investigation.

3.1.2. Adipose Tissue and GLUT4

In adipose and muscle cells the rate at which glucose is transported, and hence metabolised, is governed by a series of molecules known as the glucose transporters (GLUT) with the predominant form being GLUT4 [89], [90]. The levels of GLUT4 located at the plasma membrane govern the rate of cellular glucose transport, and thus, metabolism [91] contributing to the overall whole-body glucose homeostasis. GLUT4 is synthesised in the endoplasmic reticulum before being transported to the Golgi network where it experiences various post-translational modifications [92]. Following this GLUT4 is inserted to storage vesicles (GSVs) which are located intracellularly under basal conditions. Upon insulin stimulation GSVs are recruited to the plasma membrane where they are tethered, docked and fused. Once fused with the plasma membrane the GLUT4 content of the GSVs is dispersed through the membrane ready to transport glucose to the cell. GLUT4 molecules present at the plasma membrane are endocytosed and recycled. If insulin is still present the GLUT4 is recycled back to the plasma membrane, otherwise, it is sent back to GSVs to be re-used once insulin is again presented.

A model, presented in [93], suggested that GLUT4 exists in four states in adipose and muscle tissue: as monomers or clusters in the plasma membrane, as endosomes and in GSVs displayed in Figure 25.

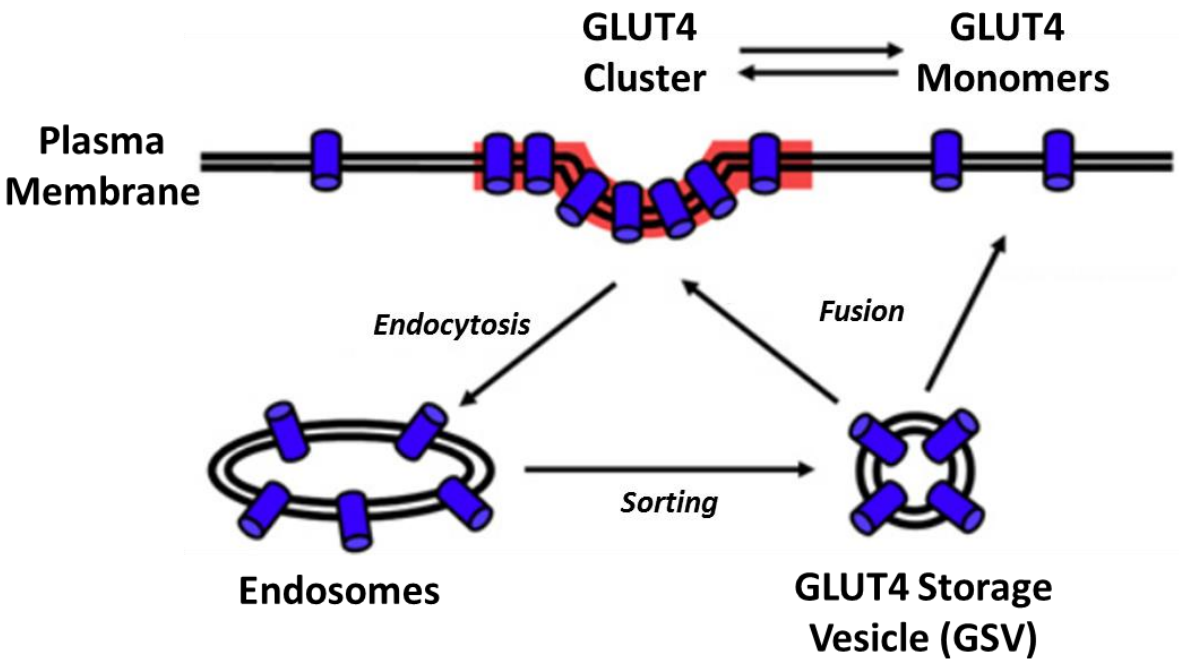

Figure 25: GLUT4 exists in four states: As monomers and clusters at the plasma membrane, as internal endosomes and GLUT4 Storage Vesicles (GSVs). Insulin stimulation increases recruitment of internal GSVs to the plasma membrane whilst regulating the dispersal of the GLUT4 enriched GSV content to the membrane. Image modified from [93].

The majority of GLUT4 (~95%) is localised to intracellular GSVs in the absence of insulin, which traffic to and from the plasma membrane at a slow rate. Under non-insulin stimulated conditions the majority of vesicles fuse to the membrane without releasing their contents, i.e. fusion with retention. Upon insulin stimulation the recruitment of GSVs to the plasma membrane increases and the vesicles now disperse their contents into the membrane, i.e. fusion with release. Importantly, insulin is suggested to govern the spatial distribution of GLUT4 now present in the membrane ready for glucose metabolism [93]. With knowledge of the trafficking of GLUT4 in adipose tissue, the mechanisms by which this processes occurs can be examined and the external stresses that affect it [94-96]. Post-translational modifications of GLUT4 have also been shown to affect its subcellular localisation and translocation [92]. Deficiencies to the insulin stimulated translocation through post-translational modifications, as well as deficient machinery, are fundamental to insulin resistance and T2DM [97].

3.1.3. Adipocytes

All present investigations of the dynamics and signalling processes involved in insulin regulated GLUT4 dynamics are carried out in differentiated 3T3-L1 fibroblasts or isolated rat adipocytes [91], [93], [98–100]. Adipocytes (fat cells) are characterised by the presence of one or many large lipid droplets. These cells have a particularly difficult and lengthy isolation and culturing procedure [101–103] making them a complicated system for experimentation due to their slow growing nature, low yield and large size. The use of isolated rat adipose tissue has the advantage of providing an ex-vivo small animal homologue for investigating numerous human diseases and exposure to particular toxins but suffer from significant experimental restrictions. One critical draw-back being the need for controlled laboratory regulations and instrumentation when working with small animals for tissue extraction. Isolated rat adipocytes are often derived from a type of mesenchymal stromal stem cell (MSC) known as the adult adipose-derived stem cells (ASCs). Numerous factors contribute to variations in derived ASCs such as donor age, type and location of adipose tissue, method of harvesting, proliferation rate, differentiation capacity etc. [103]. Once isolated the ASCs require various differentiation stages: Adipogenic, Osteogenic and Chondrogenic. Each stage takes significant time and care to ensure a successful resultant yield. In most cases the entire process can take upwards of 3 weeks before functional isolated adipocytes are available for experimentation.

Another commonly employed cell line for investigations in adipocytes is the preadipose mouse fibroblast 3T3-L1 cell line originally isolated from non-clonal Swiss 3T3 cells [104], [105]. The 3T3-L1 line is commercially available so isolation from an animal model is unnecessary. Once acquired, the cells are differentiated from their fibroblastic phenotype to adipocytes through the use of pro-differentiative agents following growth arrest [102]. Commonly used agents such as: insulin [105], dexamethasone [106] and 3-isobutyl-1-methylxanthine (IBMX) [107] have all previously shown varying levels of success. Differentiation with such agents typically occurs after 4 - 6 days, characterised by the accumulation of lipid droplets of varying sizes as well as markers of fat cell differentiation [108]. The sensitivity of the differentiation process can be seen in the work of Mehra et al. in 2007 [108] where it was shown that the

differentiation rate was dependent on the type of culture dish used. They found that the type of dish material, processing of the plastic surface and also the style of dish used greatly affected differentiation. Zebisch et al. developed an improved method for differentiation [102] through the addition of rosiglitazone to the first differentiation medium providing virtually complete differentiation of the fibroblasts to adipocytes. While they demonstrated a successful protocol, the overall length of the procedure was greater than 12 days.

3.1.4. HeLa Cells

The majority of current investigations of GLUT4 activity and recruitment to the plasma membrane suffer from a low throughput due to the lengthy isolation and culturing of adipocytes. In addition, adipocytes are particularly difficult to genetically manipulate, e.g. by transfection or siRNA approaches. As a result a need is seen for a more robust experimental cellular model expressing similar GLUT4 activity for more statistically sound data sets. Such a system would provide the perfect platform for high throughput investigations into factors involved in disrupting insulin regulated glucose metabolism. The HeLa cell line is an immortal cervical cancer cell line, originally acquired in 1951 [109], and is the most widely investigated cell model [110]. The cell line has gained particular success due to its rapidly growing nature and a significant lack of contact inhibition [111]. It is even claimed that due to the robustness and ubiquity of HeLa cells in laboratories world-wide they account for nearly 25% of all cross-contamination events [112]. The strengths of the HeLa cell line make it an ideal model to work with experimentally. While HeLa cells do not contain any endogenous GLUT4, they do possess insulin sensitivity [92]. In 2011 Haga et al. investigated the role that N-Glycosylation plays in the trafficking of intracellular GLUT4 in a modified HeLa cell line expressing both wild-type GLUT4 and a GLUT glycosylation mutant [113]. GLUT4 located at the cell surface was shown to increase within the modified HeLa cell line under normal conditions, but was reduced upon glycosylation. They followed this work up in 2012 with a transmembrane FRET based investigation into visualising protein glycoforms [114]. This was demonstrated using the HeLa cell model with GFP tagged GLUT4.

The modified HeLa cell lines show promise in acting as a homologue to the GFP tagged GLUT4 adipocytes in investigating insulin stimulated glucose metabolism in adipose tissue. However, at this point in time there has been no direct comparison in the rate of GLUT4 recruitment to the cell membrane surface between adipocytes and HeLa cells to the best of this author's knowledge.

This chapter presents a comparison of the insulin stimulated GLUT4 recruitment to the plasma membrane in both differentiated 3T3-L1 fibroblasts and a modified HeLa cell line. This was achieved through the use of live cell TIRF microscopy illuminating GFP tagged GLUT4 molecules within the evanescent region of the plasma membrane. Comparisons were drawn from the time dependent increase in the average signal originating from the GFP-GLUT4 located at the plasma membrane as well as the dynamic rates of recruitment of GSVs.

3.2. Materials and Methods

3.2.1. TIRFM system construction

3.2.1.1. Illumination and detection

Illumination was provided using a series of interchangeable pulsed laser diodes (HORIBA) with available wavelengths of 420 nm, 481 nm and 654 nm. For GFP tagged GLUT4 excitation the 481 nm laser line was used. Attached to the front of each laser is a condenser lens which focuses the collimated laser light to the 0.1 NA aperture of a multi-mode fibre optic cable. The fibre is coupled to the back of the specialised TIRF condenser via a standard FC fibre coupler. For imaging the LaVision Picostar intensified CCD (ICCD) camera was employed offering single photon sensitivity.

3.2.1.2. TIRF Alignment

The fundamental theory of TIRFM was outlined in chapter 2 where it was explained that there are two possible practical configurations that can enable TIR: in prism and objective based systems. An objective based system was constructed due to the favourability of the system for live single cell imaging

experiments. Achieving total internal reflection with an objective based orientation requires two components: an objective of high numerical aperture (>1.4) and the ability to position the laser at the far aperture of the lens by mechanical means. This was achieved using a Zeiss 1.45 NA oil immersion lens and the TILL photonics TIRF condenser unit. The condenser was coupled to the back of a Zeiss Axiovert 200m microscope containing a micrometre screw gauge for precise lateral manipulation of the beam position.

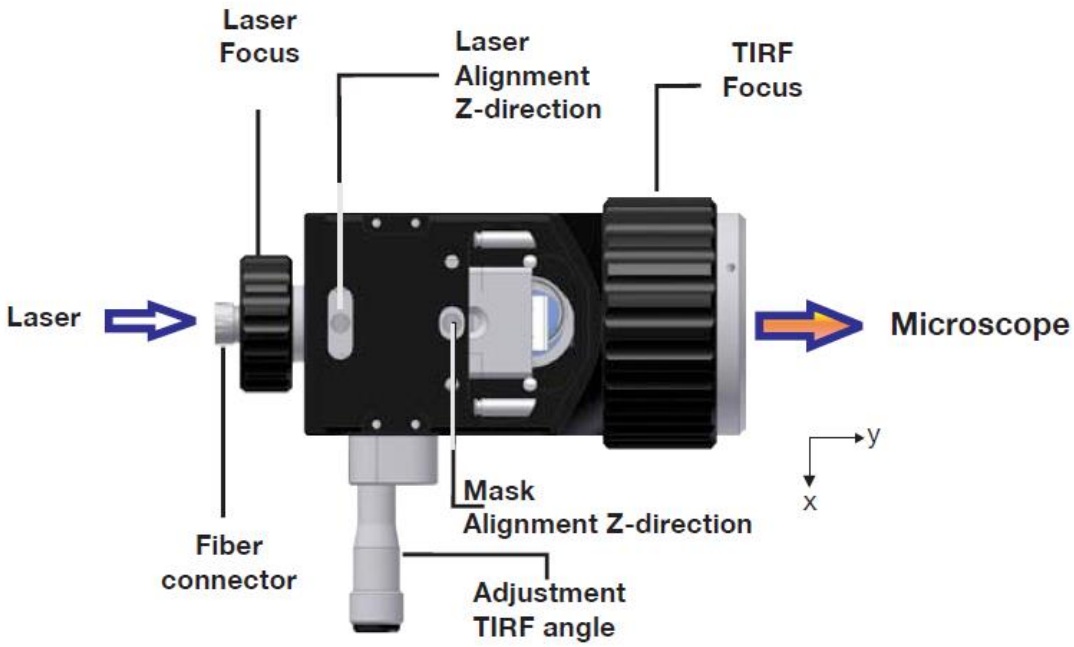

Figure 26: TIRF condenser. Micrometre at bottom controls the position of the beam relative to the optical axis of the microscope. The laser is coupled to the back of the condenser via a 0.1 NA multi-mode fibre. The TIRF focus adjusts the image to the back focal plane of the objective lens.

The light was focused to a mask in the condenser containing two slits for TIRF and a central pinhole for alignment, demonstrated in Figure 27. The two slits correspond to the optical path relative to the far aperture of the objective lens. Positioning the laser spot through these slits offers a small range of illumination angles enabling TIR illumination.

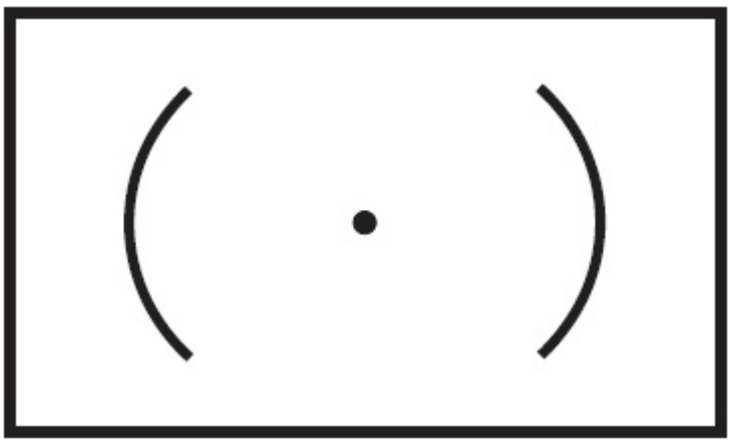

Figure 27: Mask for TIRF alignment containing central pinhole and two slits. The two slits correlate to the position in the optical path at the far aperture of the objective lens. The size of the slits allows for some adjustment of the angle of illumination for angles below, at and above the critical angle.

To align the condenser firstly the laser spot is aligned to the central pinhole of the mask then the mask and laser spot are aligned relative to the optical axis of the microscope. This is achieved using an alignment tool inserted into an empty objective slot.

3.2.1.3. Alignment Testing

To test the alignment a droplet of solution containing 100 nm fluorescent microspheres was deposited to a coverslip. The droplet is allowed to rest for a few moments to allow a number of the microspheres to adhere to the surface with a large concentration remaining in the bulk solution above. This offers a contrast between the assumed TIRF illumination region at the surface, and the bulk solution.

Initial alignment revealed astigmatism in the optical path due to misalignment of the TIRF condenser unit relative to the dichroic mirror of the microscope. This was noted when focussing the laser through the centre of the objective, along what was assumed to be the optical axis, to a surface a few feet above the microscope. When moving the objective through the optical axis the spot was noted to drift away from the centre of alignment. Astigmatism is severely detrimental to an objective based TIRF system causing uneven alignment of the

laser at the sample substrate interface resulting in areas of varying evanescent field depth and also angles under that needed for TIRF. The issue was rectified through means of mechanical adjustment of the condenser position by attaching coiled spring washers to the screws connecting the condenser to the microscope. This gave the ability to manually counteract the misalignment originating from the condenser.

Once the astigmatism was corrected the alignment was confirmed by imaging the 100 nm fluorescent microsphere adhered to the surface of a coverslip. Figure 28 demonstrates the system where the laser is positioned just under the critical angle so that TIRF is not achieved. In this configuration a large background is seen from the bulk solution of freely diffusing fluorescent microspheres and from the resultant profile no information can be drawn from the features imaged at the surface.

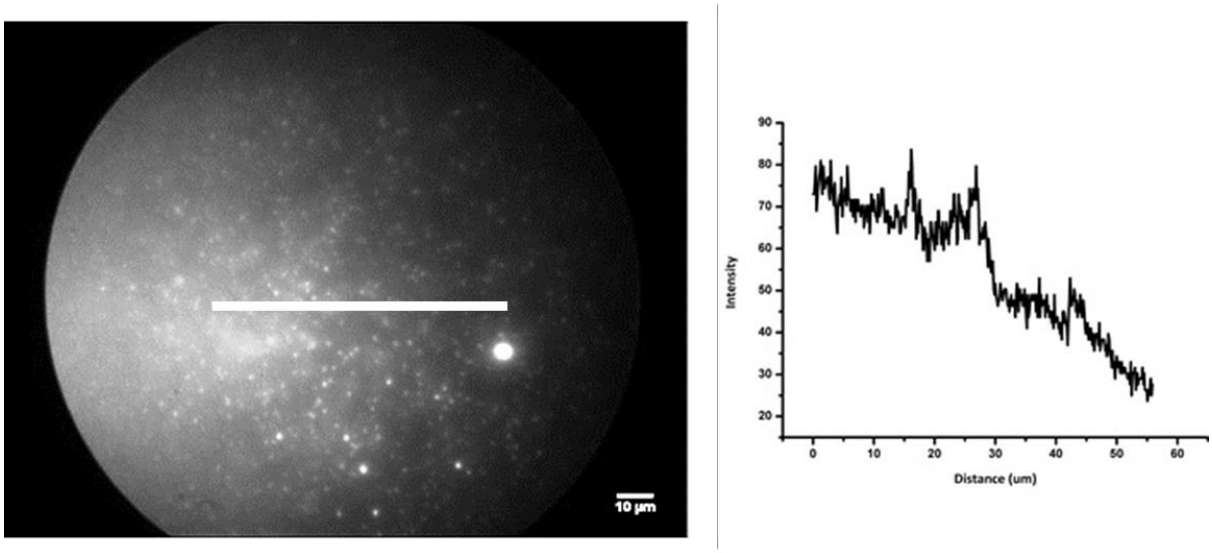

Figure 28: Fluorescence intensity image of 100 nm beads adhered to a coverslip while also freely diffusing in the bulk solution above. The Illumination angle was positioned just below the critical angle to provide 'off-angle' illumination. Configuration provides no depth resolution resulting in no ability to distinguish between beads at the surface and those in the solution as seen in plotted profile. Scale bar 10 µm.

Figure 29 shows the system in a TIRF configuration. A signal resulting solely from microspheres immobilised at the substrate surface can be seen with the features present along the intensity profile.

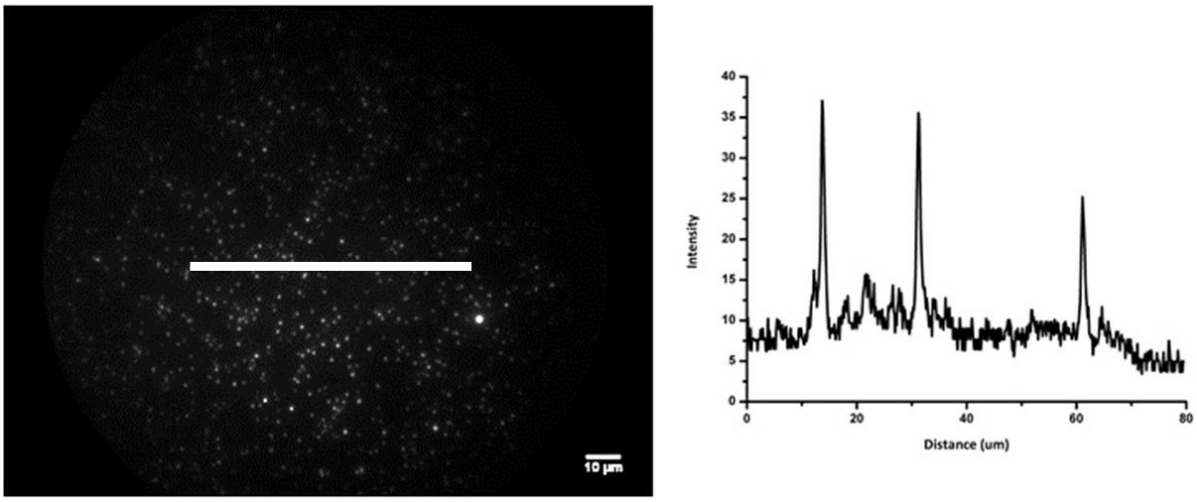

Figure 29: TIRF intensity image of 100 nm beads adhered to a coverslip. Illumination angle set higher than the critical angle resulting in a signal from the beads at the surface only. The plotted profile shows the ability to resolve the surface features from the background signal. Scale bar 10 µm.

3.2.1.4. Penetration depth calibration

With the system now seemingly able to achieve TIRF illumination the characterisation of the evanescent field was required to quantify the penetration depths achievable by the system. A procedure presented in [1] was employed where fluorescently labelled large, 10 µm silica particles were utilised to determine the evanescent field profile. The area of the bottom surface of the particle imaged corresponds to the penetration depth using the following geometrical relationship.

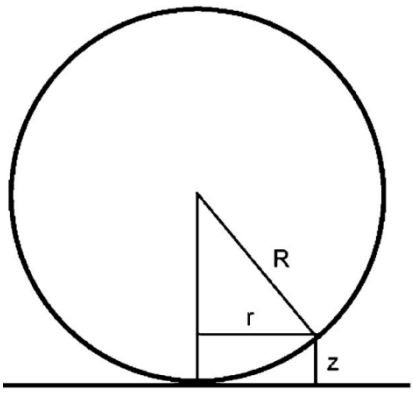

$$R^2 = r^2 + (R - z)^2$$

Figure 30: Relationship between the radius of spot imaged by TIRF and the penetration depth.

The critical angle necessary for TIRF was found by adjusting the micrometre screw gauge of the condenser using the 100 nm fluorescent microsphere calibration solution. The corresponding position on the micrometre was noted and used as the start point for the depth calibration measurement, found to be at 5 μm. In increments of 1 μm turns of the screw gauge an image was taken of the bottom surface of a fluorescently tagged silica microsphere. The images are shown below.

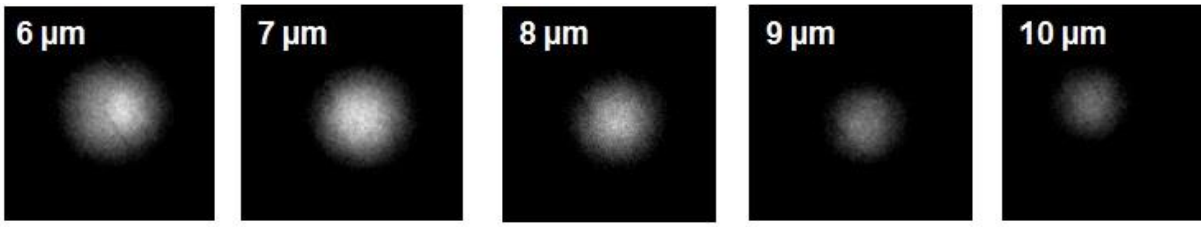

Figure 31: TIRF images of 10 μm fluorescently tagged silica microsphere on a coverslip. Values correspond to position of micrometre gauge on the condenser unit. The radius of the imaged spot decreases as the penetration depth is reduced by positioning the laser further from the optical axis and closer to the far aperture of the objective lens. This increases the angle of illumination further from the critical angle.

The size of the imaged region was determined using the pre-defined measuring routines of the image analysis software ImageJ. A centre point of peak intensity was located then an average was taken of the intensity profiles along varying points from the centre. The corresponding measured penetration depths were as follows.

Position of screw gauge	6 μm	7 μm	8 μm	9 μm	10 μm
Measured penetration depth	358 nm	275 nm	204 nm	140 nm	118 nm
Corresponding Angle of Incidence	61.39°	61.63°	62.09°	63.31°	64.25°

Table 1: Measured penetration depth at different positions of the lateral beam position indicated by position on micrometre gauge Angle of incidence calculated using measured penetration depth.

3.2.2. Cell Preparation

3.2.2.1. HeLa Cells

Cells were kindly provided by the lab of Dr Gwyn Gould of the cell biology department at the University of Glasgow. Cells arrived adhered to the surface of a sealed culture flask and were transferred in this state immediately to an incubation chamber to provide appropriate climate control, 5 % CO_2 and a temperature of 37°C. The cell line provided was a HeLa cancer cell type transfected with HA-epitope-tagged-GLUT4 fused to Green fluorescent protein (HA-GLUT4-GFP).

All cell handling took place in a class II fume hood cupboard sterilised with 70% ethanol before each use. HeLa cell cultures were maintained in DMEM (Gibco) supplemented with 10% (v/v) FCS (Foetal Calf Serum) (Gibco), 1% glutamine (Gibco) and 1% penicillin/streptomycin antibiotic (pen/strep) (Gibco). Dulbecco's phosphate buffer saline (PBS), trypsin and all media were warmed in a water bath to 37°C before use to ensure no heat-shock damage to the cells. Existing media in the flask was removed and cells were rinsed twice with 5 ml of PBS. Following this 5 ml of trypsin solution was added to the flask and incubated at 37°C to encourage cell detachment from the surface of the flask. 5 ml of fresh media was added to the flask and the solution was used to rinse any remaining cells from the surface. The 10 ml trypsin/media solution was passed to a sterile plastic container and placed in the centrifuge. Cells were recovered by centrifugation at 1400 rpm for 4 minutes. The cells were then re-suspended in 10 ml of fresh media. 1 ml of cells was finally added to 15 ml of fresh media to provide an adequate coverage over the surface of the flask. This process was repeated every 2 -3 days when the cells were 80 – 90% confluent.

At the point of re-suspension, post centrifugation, the cells were counted using a haemocytometer. Cells were plate on a special TIRFM compatible observation chamber (Ibidi) which contained a 170 µm coverslip base. HeLa cells were plated to a density of 4 $x10^{23}$ cells per chamber to distinguish single cells from the

population for observation. Cells were left to attach to the surface of the coverslip overnight. Before all experimentation, HeLa cells expressing HA-GLUT4-GFP were serum starved in serum free media for two hours to bring them to a resting state and maximise the response to insulin as outlined elsewhere [93], [98], [115].

For insulin stimulation 100 nM insulin was added to the chamber whilst on the microscope stage to allow time-lapse imaging of individual cells.

3.2.2.2. Adipocytes

3T3-L1 pre-adipocytes expressing HA-GLUT4-GFP were differentiated over the course of 7 days by culture with a supplemented DMEM containing 10% FBS, 170 nM Insulin, 1 mM rosiglitazone, 0.25 mM dexamethasone and 2mM methyl-isobutylxanthine. Cells were maintained in standard DMEM once differentiated. For imaging of adipocytes 3T3-mouse fibroblasts were differentiated to provide a 70% confluent layer. Similar to the HeLa cells the adipocytes were serum starved for 2 hours prior to experimentation.

3.2.3. Live Cell Imaging

3.2.3.1. Temperature Control and Sample Stability

A temperature of 37^{o}C was maintained for all experiments utilising a heated microscope stage insert (PeCon). The stage was compatible with the sample chambers and maintained positional stability with four screw pins. This mitigated the effects of the sample drifting relative to the field of view. The sample was allowed to adjust to the temperature of the stage for 15 minutes before imaging commenced to minimise the effects of focal drift due to temperature changes. A temperature of 55^{o}C from the stage control unit was deemed to be sufficient to bring the media to a value of 37^{o}C as measured using a K-type thermocouple and compared to images obtained using an Infrared (IR) camera.

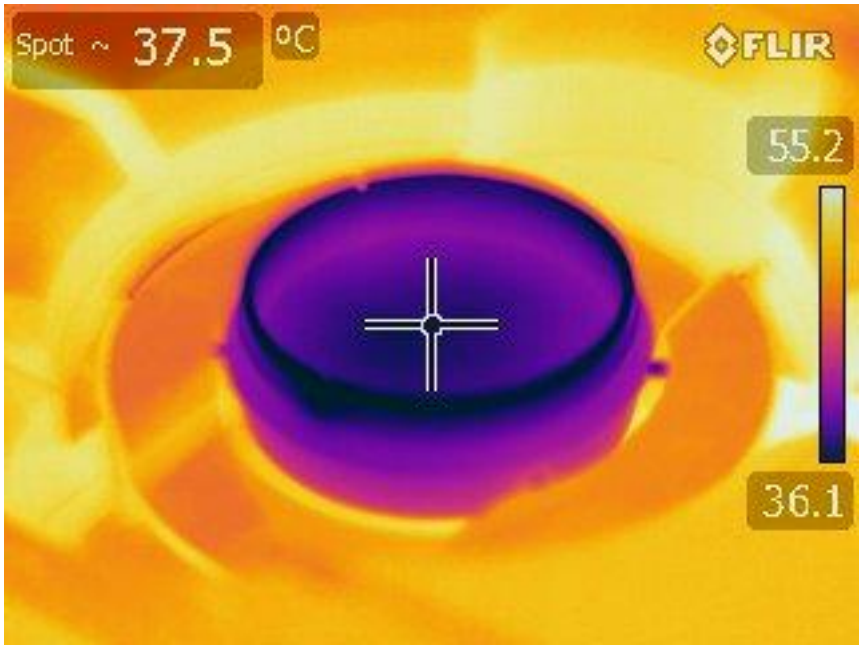

Figure 32: IR image of μSlide chamber containing HeLa cells in serum free media. Temperature at crosshair corresponds to 37.5°C with overall stage insert set point set to 55°C as noted by highest temperature on scale.

3.2.3.2. Media Buffering

In the absence of CO_2 control it was noted that over the time frame of one hour the cells began to detach from the substrate. This was mitigated by buffering the media with 25 mM HEPES for the time course of the time-lapse imaging. Under these conditions the majority of HeLa cells remained attached to the substrate for the duration of experimentation. To maintain continuity the HEPES buffered media was also used for adipocyte imaging even though no detachment was noted.

3.2.3.3. Imaging Parameters

All images in this chapter were taken using a pulsed 481 nm laser line set to a repetition rate of 10 MHz, to minimise the effects of photobleaching. For all imaging the exposure time was set to 400 ms. For time lapse image series a frame rate of 2 Hz was used to visualise vesicle dynamics.

3.3. Image Analysis

To determine data relating to the recruitment of GLUT4 to the membrane under insulin stimulation, various image analysis techniques were employed. Using a

range of algorithms available through the open source software platform of ImageJ various aspects of the molecular environment were analysed.

3.3.1. Membrane Intensity

To analyse the level of GLUT4-GFP intensity within the TIRFM region, an area relating to the perimeter of the cell at the point of insulin stimulation was drawn. The contrast for all images in an image sequence was optimised for the initial image corresponding to the time t = 0 at the point of insulin stimulation. This resulted in the normalisation of the contrast for all subsequent images in an sequence providing a clear indication of increased membrane intensity. The average intensity for all pixels within the defined boundary for a cell was then plotted for all discrete points, image, following t = 0. All values of intensity were normalised by the value at the point of insulin stimulation, t = 0, to provide a value for the increase in membrane intensity from GLUT4-GFP at the membrane. This process was repeated for image sequences of cells under non-insulin stimulated conditions as a comparison.

3.3.2. Vesicle Definition and Identification

To determine the kinetics of GSVs in HeLa cells compared to the previously characterised adipocytes, image analysis techniques were required to define, identify and analyse dynamic and static GSVs. Subroutines readily available through ImageJ were combined to form a custom designed macro to provide automated image analysis. Algorithms such as the rolling-ball background subtraction, despeckle, Gaussian blur, FindFoci and image projection methods were utilised. The exact parameters used for the different techniques are outlined later in this chapter.

3.4. Results

3.4.1. TIRFM imaging of Adipocyte membrane GLUT4-GFP signal

Initial experiments were performed to determine the effect of insulin stimulation on the recruitment and dispersal of GFP tagged GLUT4 molecules around the membrane region of adipocytes. It has previously been demonstrated that upon the addition of insulin to adipocytes a marked rise in GLUT4-GFP fluorescence at the membrane can be seen [100]. Presented here, differentiated 3T3-L1 adipocytes expressing HA-GLUT4-GFP were imaged at discrete time intervals every five minutes with an exposure time of 500 ms in the presence of media both with and without insulin. Figure 33 demonstrates an image sequence captured of an adipocyte stimulated with 100 nM insulin for 25 minutes.

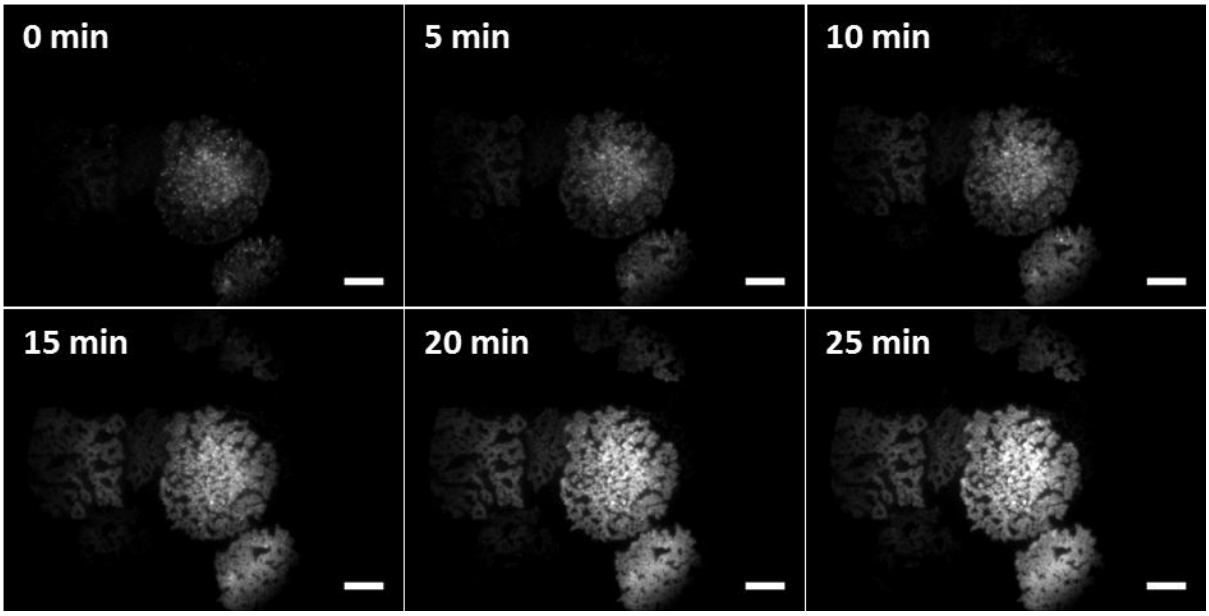

Figure 33: TIRFM image sequence of 100 nM insulin stimulated 3T3-L1 adipocytes expressing Ha-GLUT4-GFP. Excitation wavelength 481 nm, images acquired at 5 minute intervals with an exposure time of 500 ms. Scale bar – 20 μm.

It can clearly be seen visually that the intensity of the signal originating from the illuminated TIRF zone, corresponding to the cell membrane region, increases upon stimulation. This suggests a dynamic shift of the internal HA-GLUT4-GFP molecules from intracellular compartments to the plasma membrane. The dark

regions within the footprint of the cell likely correspond to internal lipid droplets resting in the bottom region of the cell. Insulin stimulation was achieved through replacing 50% of the media with media containing 200 nM insulin to provide an overall concentration of 100 nM. The media was added gently to ensure no movement of the cell for comparative single cell imaging.

To determine whether the observed fluorescence increase was due to the added insulin, and not the act of exchanging the media, control images of adipocytes under non-stimulated conditions were obtained. This can be seen in Figure 34 which demonstrates a typical adipocyte imaged with no insulin stimulation, but with half of the media exchanged.

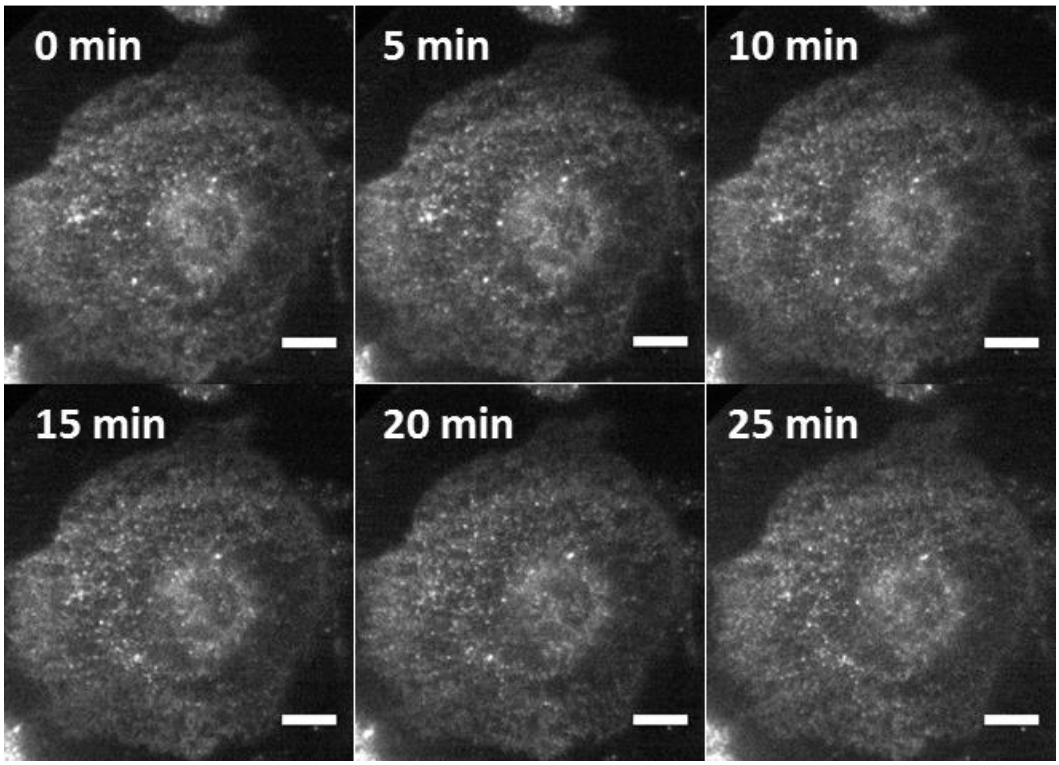

Figure 34: TIRFM image sequence of transfected 3T3-L1 adipocyte expressing HA-GLUT4-GFP without insulin stimulation. Excitation wavelength 481 nm, images acquired at 5 minute intervals with an exposure time of 500 ms. Scale bar – 10 μm.

It can be seen that there is no significant rise in fluorescent signal in the illuminated region. This demonstrates that the increase in fluorescence intensity observed in Figure 33 is as a direct result of the insulin stimulation as opposed to the act of exchanging media.

To qualitatively assess the rise in fluorescence signal a perimeter was drawn for each cell using the outlining tool in ImageJ. This was drawn for the first image at a point before insulin stimulation, t = -2 minutes, and held at the same position for each following image as demonstrated in Figure 35.

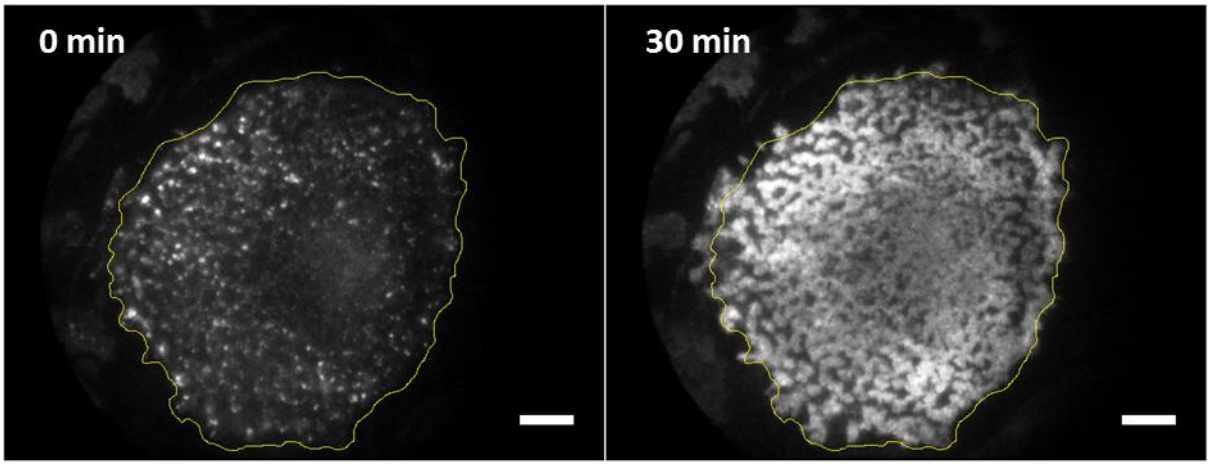

Figure 35: Definition of cell boundary to measure average intensity signal. Yellow outline corresponds to boundary defined before insulin stimulation. Images of adipocyte stimulated with 100 nM insulin at time 0 and 30 minutes. Scale bar – 20 μm.

The initial boundary is defined so that the measured intensity value at each time point corresponds to the area of the cell footprint. This takes into account slight increases in the size of the illuminated membrane region due to the spreading of the cell over time. This is apparent in Figure 35 where at 30 minutes some bright fluorescence can be seen outside the defined perimeter. Due to minimal perturbation of the cell through adding insulin cell movement over the time course of the experiment is negligible.

TIRFM image sequences were gathered for a number of cells, N = 15, that exhibited a minimum 10% increase in average intensity within the measured region. These values were then normalised against the intensity value measured before insulin stimulation. Each cell was insulin starved for 2 hours before stimulation to maximise the response. A plot of the normalised fluorescence intensity signal increase for insulin-stimulated adipocytes can be seen in Figure 36.

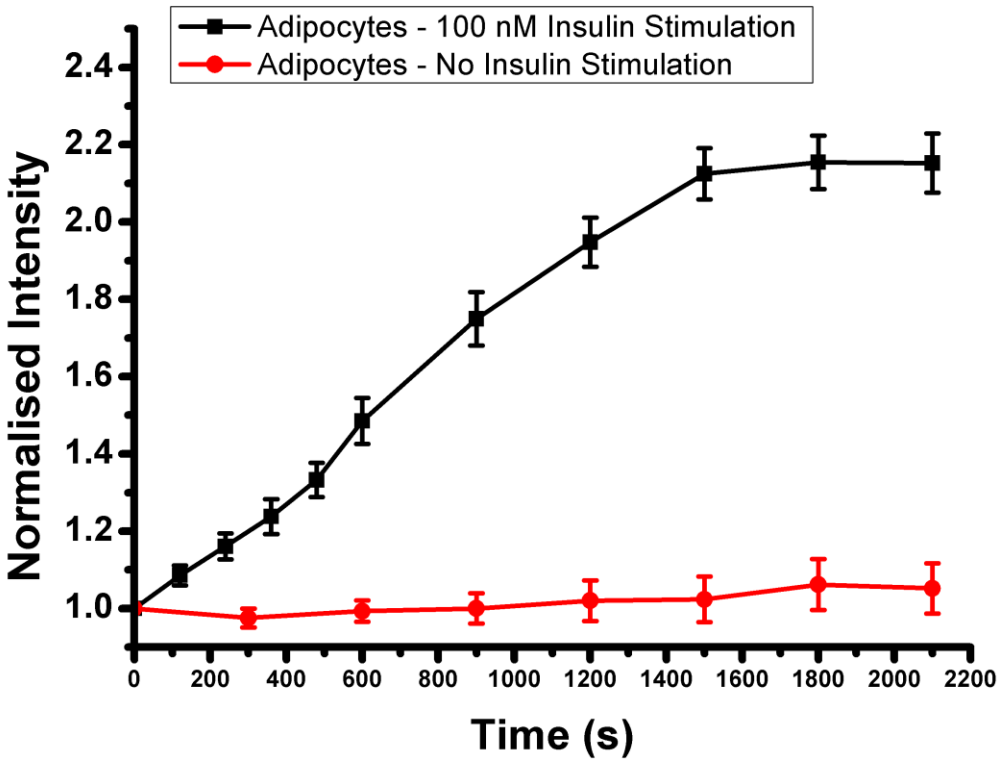

Figure 36: Normalised intensity vs. time for 3T3-L1 adipocytes under both insulin stimulated and non-stimulated conditions. Plots normalised to the average value of the intensity prior to addition of media with either 100 nM insulin for stimulated conditions, or no insulin for non-stimulated conditions. Error bars represent SEM from the mean measured intensity for each time point. N = 15 for the stimulated cells and N = 5 for the non-stimulated cells.

The measured average intensity values from the TIRFM images display a dramatic rise in the signal originating from membrane localised GLUT4 molecules. Typically a 2 – 2.5 fold increase in normalised fluorescence intensity was observed. These values are consistent with previously reported values of 1.5 – 3 fold increases in GFP-GLUT4 fluorescence signal at the plasma membrane [91], [100]. The control experiments demonstrate that the exchanging of media did not contribute to the measured fluorescence increase and is likely as a result of insulin stimulation. A distribution of the final intensity increases for the imaged adipocytes can be seen in Figure 37.

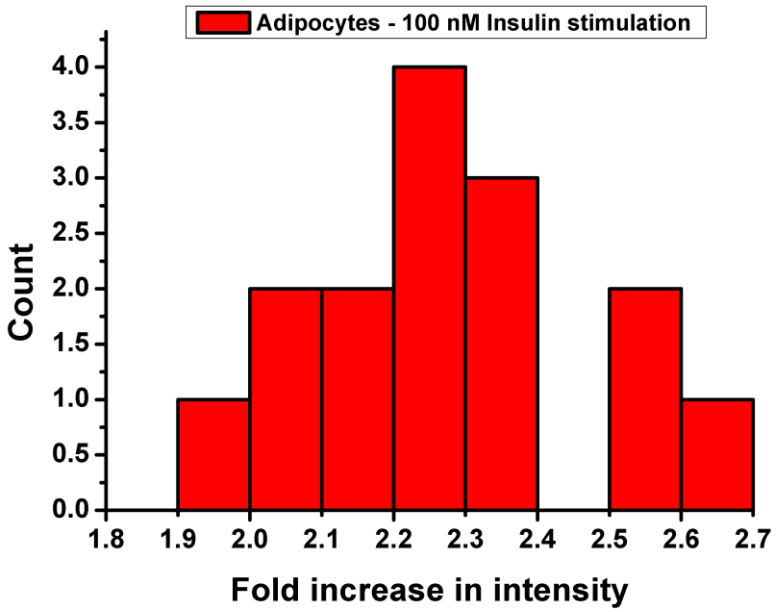

Figure 37: Histogram of TIRFM measured intensity fold increase for adipocytes stimulated with 100 nM insulin for 25 minutes. Bin width for each bar is 0.1.

Figure 37 demonstrates the distribution of final intensity fold increases for all the imaged cells. It was noted that every cell analysed produced at least a 1.9 fold increase in intensity under stimulated conditions.

3.4.2. TIRFM imaging of HeLa cell membrane GLUT4-GFP signal

An example of the observed intensity increase in the HeLa cell line can be seen in Figure 38 where images taken from t=0 and t=60 are compared.

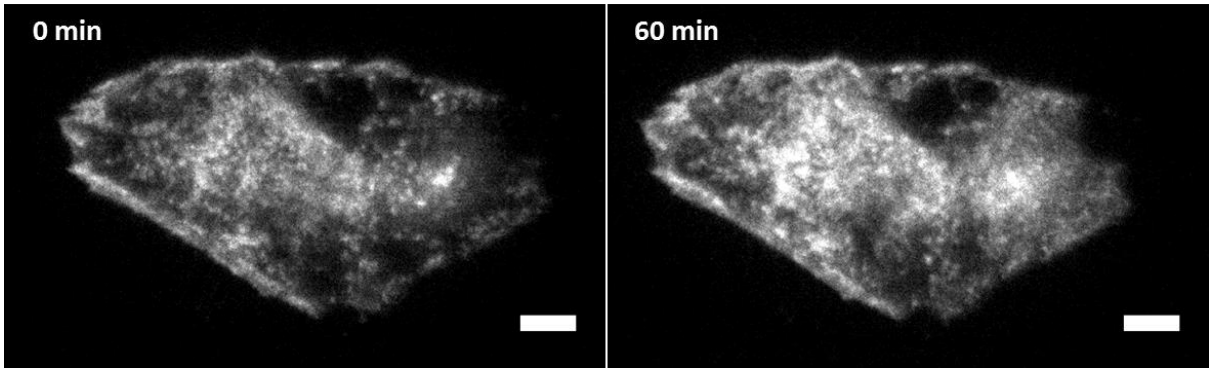

Figure 38: TIRFM images of 100 nM insulin stimulated GLUT-GFP transfected HeLa cells. Excitation wavelength 481 nm, images with an exposure time of 500 ms collected one hour apart. Scale bar – 10 μm.

TIRFM images of HeLa cells display a slight increase in membrane associated fluorescence intensity; however, compared to the previous images of adipocytes, under similar conditions, the total increase was visibly lower. Due to the unknown dynamics of the HeLa cell line, cells were imaged over a time course of one hour as opposed to the 30 minutes for adipocytes. Data was taken from cells that demonstrated a minimum 10% rise in measured fluorescence intensity as shown in Figure 39.

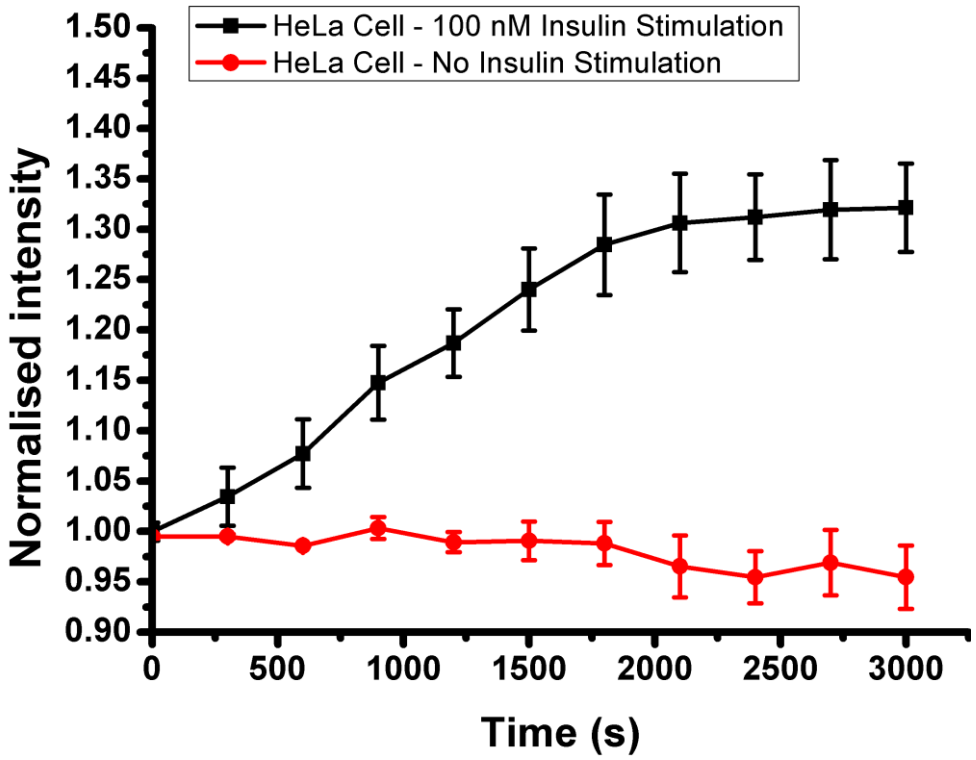

Figure 39: Normalised average fluorescence intensity vs. time for HeLa cells expressing GFP-GLUT4 under both insulin stimulated and non-stimulated conditions imaged with TIRFM. Plots normalised to the average value of the intensity prior to addition of media with either 100 nM, for stimulated conditions, or no insulin for non-stimulated conditions. Error bars represent SEM from the mean measured intensity. N = 12 for stimulated cells and N = 5 for non-stimulated cells.

Figure 39 demonstrates the normalised intensity changes for the HeLa cells under both stimulated and non-stimulated conditions. It can be seen that the increase is significant compared with the control, however, the typical increase was between 1.3 – 1.5 fold increase in fluorescence intensity. This is significantly lower than the minimum measured 2 fold rise for the adipocytes.

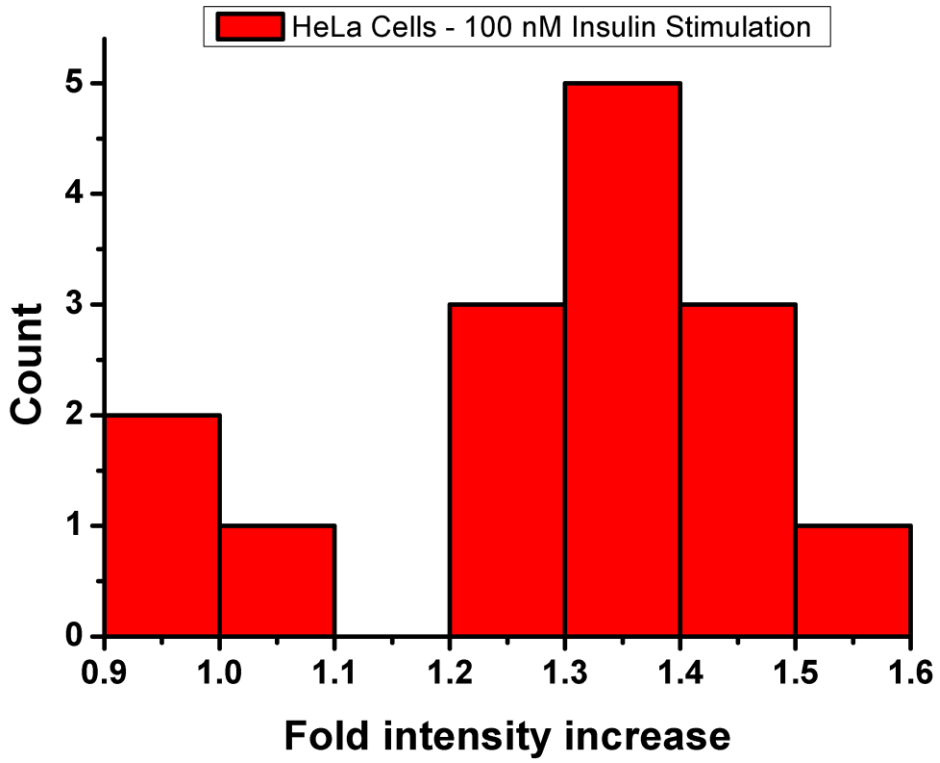

Figure 40: Histogram of TIRFM measured intensity fold increase for HeLa cells stimulated with 100 nM insulin for 25 minutes. Bin width for each bar is 0.1.

Upon inspection of the histogram for the final intensity fold increase for the imaged cells, it can be seen that a small percentage exhibited no significant rise in intensity. Figure 41 provides a direct comparison between the two cell lines in terms of rates of membrane localised fluorescence intensity increase.

3.4.3. Comparing Adipocyte and HeLa membrane intensity increases

Figure 41 outlines the relative rates of increasing fluorescence intensity between the HeLa and adipocyte cell lines under stimulated conditions compared with the non-stimulated HeLa cells.

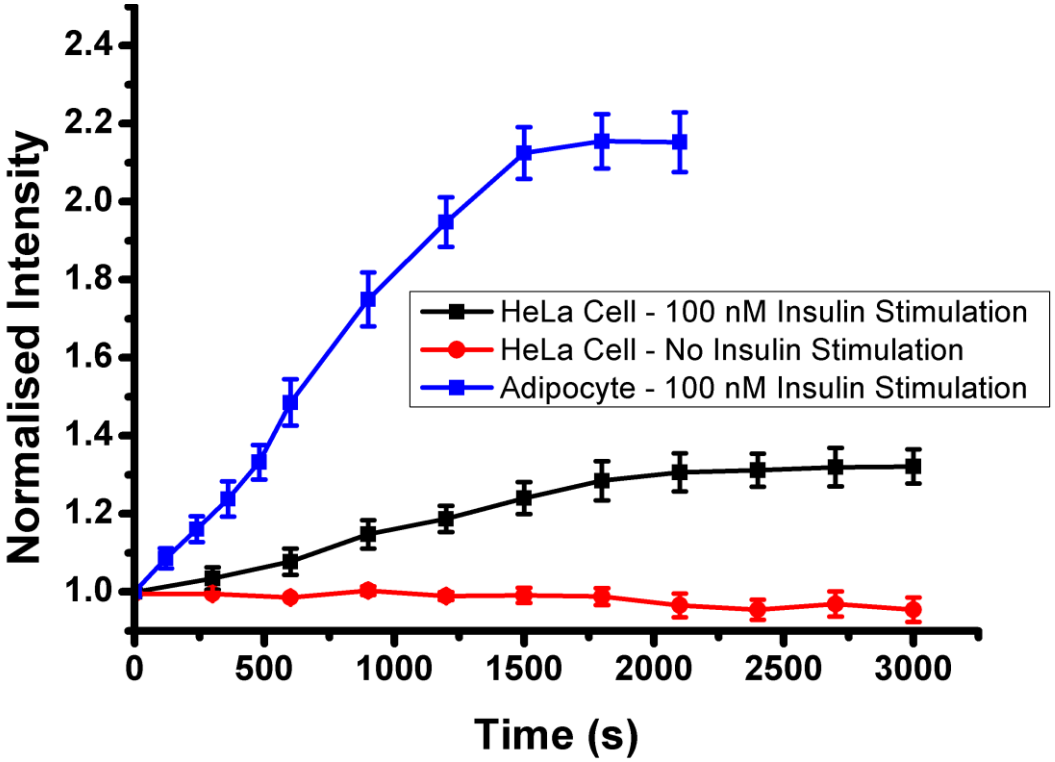

Figure 41: Comparison of average TIRFM fluorescence intensity increase between the adipocyte and HeLa cell lines under insulin stimulated conditions. Adipocytes imaged over time course of 25 minutes before intensity signal plateaus and HeLa cells imaged for one hour. Error bars represent standard deviation of mean measured fluorescence intensity

Figure 41 demonstrates that the final plateau region of intensity increase is significantly reduced in the HeLa cell line. In addition, the time course over which it achieves maximum signal is increased. This is highlighted through investigation of the half rise time, $\tau_{1/2}$, of the measured intensities.

Cell Type	Max fold increase	Half rise Time, $\tau_{1/2}$, (Minutes)	N
Adipocytes - GLUT4-GFP	2.15 ± 0.2	12.25 ± 2.18	15
HeLa - GLUT4-GFP	1.34 ± 0.1	17.13 ± 6.32	12

Table 2: Comparing the intensity increase and half rise times for the insulin stimulated Adipocyte and HeLa cell lines expressing GLUT4-GFP. Error indicates the standard deviation for each value taken from N cells. Two-tailed t-test applied to half rise time values provided a p value of 0.0078 indicating statistical significance, i.e. < 0.05.

The observed half-rise time for adipocytes occurred within 12 minutes to eventually reach a plateau of a 2.15 fold intensity increase after 25 minutes. For the HeLa cell line the rise in fluorescence intensity was not only lower in magnitude but took, on average, 17.13 minutes to reach the half-rise point before plateauing after 35 minutes. The difference between the half rise times for the two cell lines was found to be statistically significant through application of a two-tailed t-test yielding a p value < 0.05.

It has previously been shown numerous times that in adipocytes expressing GLUT4-GFP a significant rise in fluorescence intensity can be detected within the plasma membrane region [91], [98], [115]. In general the observed increase is between 1.5 – 3 fold in normalised fluorescence intensity but the half rise time, $\boldsymbol{\tau_{1/2}}$, over which this is achieved can vary between 6-10 minutes [91], [100]. The values obtained in this study fall close to these previously reported values, suggesting the devised experimental system provides consistent information on the dynamic recruitment of GLUT4-GFP to the plasma membrane in adipocytes. The slightly increased $\boldsymbol{\tau_{1/2}}$ value of 12.25 minutes may be due to the method by which the insulin is added to the cells. Instead of replacing the entirety of the media in the observation chamber only half of the media was exchanged resulting in a potential lag in insulin stimulation due to diffusion. However, in comparing the two cell lines the method was held consistent allowing a direct comparison.

Haga et al. [113] have previously demonstrated, using western blotting, that ectopically expressed GLUT4 in HeLa cells migrates to the plasma membrane under insulin stimulation. They found a near 2-fold increase in surface expressed wild type GLUT4 at the plasma membrane under insulin stimulation. The levels found here through TIRFM imaging reveal an average 1.3-fold increase in fluorescence signal at the membrane resulting from translocation of the GLUT4-GFP. While this rise appears to be due to the 100 nM insulin stimulation, it is significantly lower than that found elsewhere. A potential source for this discrepancy may be the levels of over-expression of the GLUT4-GFP in the different laboratories. The capacity of HeLa cells to sequester GLUT4 in GSVs is limited; hence at lower levels of expression, a great fraction of the total may be expected to exhibit insulin-dependent movement to the cell surface.

Unfortunately, it was not possible to compare levels between those employed by Haga et al. and those here due to the inherent differences between assays. Confocal imaging of HeLa cells expressing GLUT4 show a relatively large background fluorescence signal of GLUT4 located outside of GSVs. For the TIRFM images this may contribute to a higher background value of GLUT4 located near the plasma membrane before stimulation. Normalising all subsequent images against the pre-stimulation images could explain the lower observed rise in normalised fluorescence intensity. However, this method does provide a quick and simple approach for qualitatively investigating translocation of GLUT4 to the plasma membrane in a robust HeLa cell model. A significant rise in intensity was observed in just 30 minutes with extremely simple data handling.

3.4.4. GSV identification

To determine the kinetics of GSVs in HeLa cells compared to previously characterised adipocytes, image analysis techniques were required to define, identify and analyse dynamic and static GSVs. To begin with the signal from GSVs versus the diffuse fluorescent background was enhanced through the implementation of a rolling ball algorithm. The rolling ball method was inspired by the work of Sternberg [116] and is used to enhance the signal of small bright spots from an uneven diffuse background signal. GSVs are, for the most part, represented by diffraction limited punctate due to their sub-diffraction size, typically 50 - 70 nm [92]. The algorithm subtracts an average value for each pixel defined by the number of pixels within a set radius around the original pixel. The radius value must be at least as large as the largest object which is not deemed to be part of the background. In the case of membrane localised GSVs in adipocytes this is demonstrated in Figure 42.

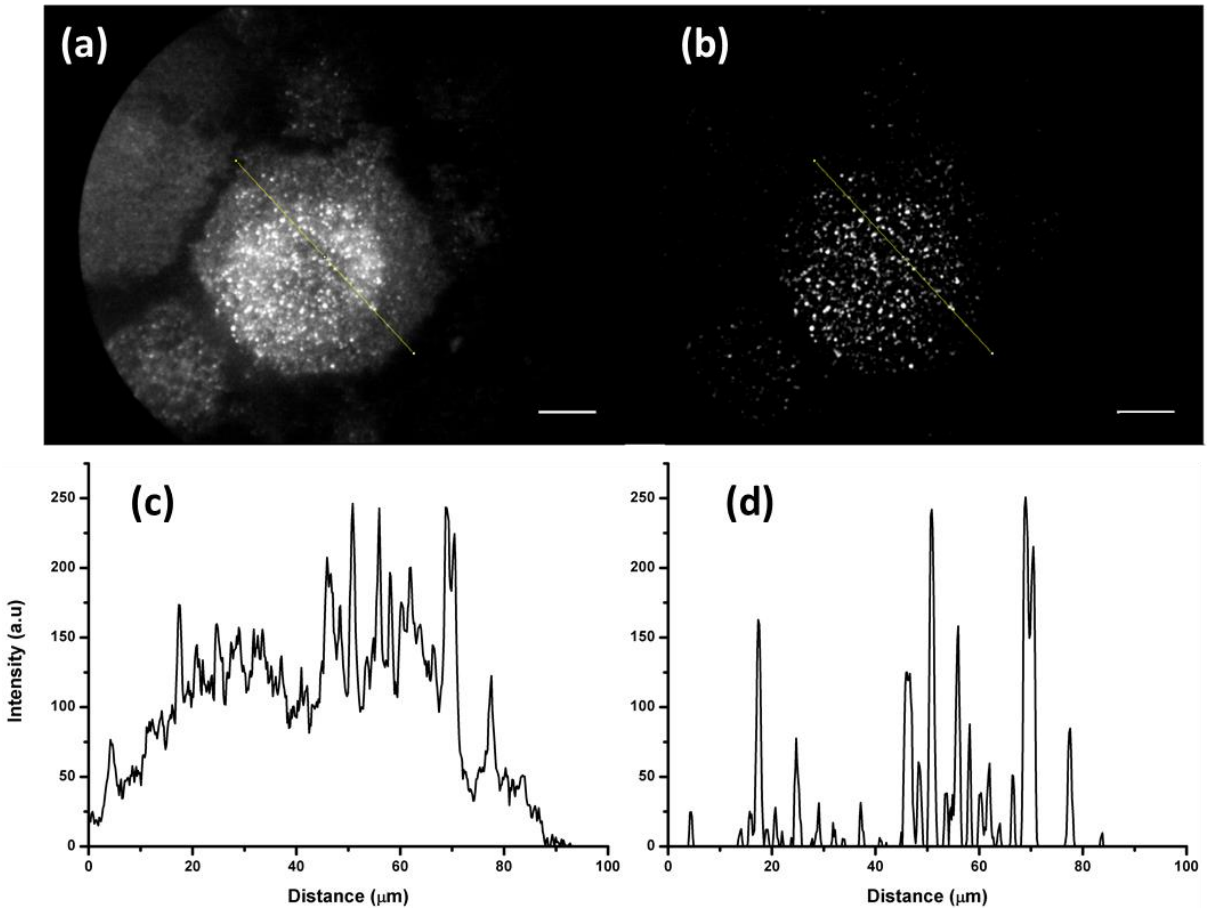

Figure 42: (a) Raw 8-bit grey scale TIRFM image of adipocyte expressing GLUT4-GFP with corresponding plot (c) representing intensity profile plotted along yellow line. (b) same image as (a) with rolling ball background algorithm implemented with a ball radius of 5 pixels. Corresponding plot (d) represents intensity along yellow line.

In Figure 42 (a) an adipocyte was imaged in the TIRF mode and signal can be seen originating from both bright small punctate spots and a broader background region. The reason for this most likely is due to GLUT4 molecules residing within or close to the plasma membrane that are not contained within GSVs. The corresponding intensity plot along an arbitrary line, (c), demonstrates that these features can be determined but are, in places, dominated by the background signal. implementing the rolling ball background subtraction with a ball radius value of 5 pixels the background signal is eliminated as seen in Figure 42 (b) and in the plot (d).

Post-background subtraction, noise was then removed through the use of the 'despeckle' and 'outlier removal' subroutines of imageJ. Despeckle removes any single pixel noise from the image based on the median of a 3 x 3 region around

the original pixel. Removal of outliers subtracts all particles of a particular radius which is deemed to be lower the minimum expected for GSVs. Individual vesicle events were defined as outlined in previous studies of GSV recruitment in adipocytes [93] following three important criteria (1) that the fluorescent point had a local maxima value, (2) 75% of the peak intensity was contained within a 5 pixel radius and (3) the point was larger than a minimum 2 pixel radius. This was achieved through the use of the FindFoci algorithm developed on the ImageJ platform at the University of Sussex [117]. Figure 43 demonstrates the ability of the algorithm to pinpoint the locations of the isolated GSVs based on their local maxima values.

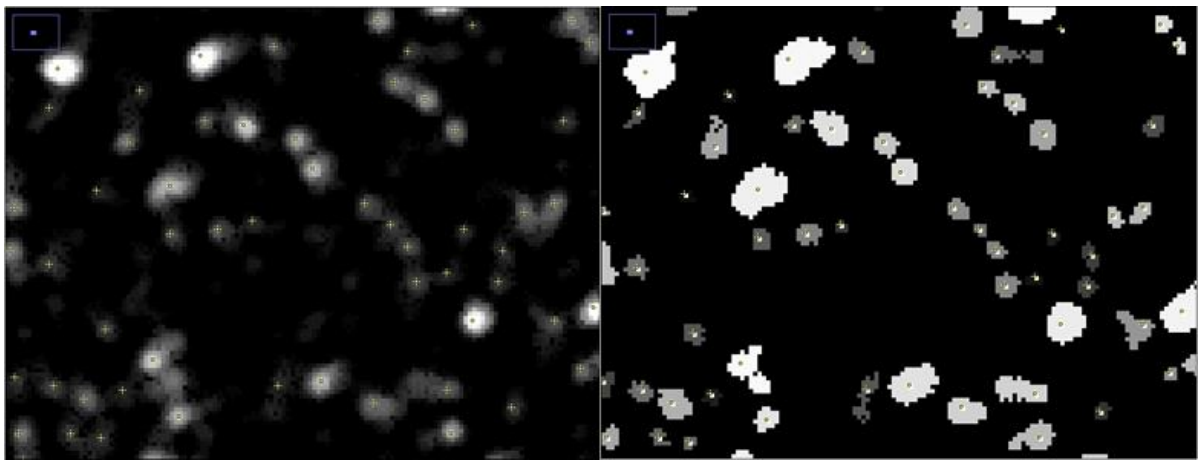

Figure 43: Magnified region of TIRFM images adipocyte from Figure 42 (a). Rolling ball algorithm applied with noise and outliers removed. Crosshairs correspond to local maxima points. (b) the resultant mask of detected GSVs excluding all points which do not conform to the three definitions for GSVs.

The use of this particular algorithm possesses numerous benefits over manual focal spot counting methods [117]. GSVs that overlap in terms of intensity can be separated, to a certain degree, even if they share a common background value. Areas potentially corresponding to localised pools of GLUT4-GFP, which may appear to be diffraction limited spots, are eliminated as they do not contain a local maxima value.

3.4.5. Comparing mobile GSVs to stationary GSVs in Adipocytes

With knowledge of the rate of increase in membrane localised GLUT4-GFP signal it was determined that the probable time window over which GSV recruitment,

fusion and dispersal takes place is within the initial 15 minutes of insulin stimulation. To investigate the dynamics of GSVs within the membrane region time-lapse live cell TIRFM was utilised. Images were acquired at a rate of 2 frames per second for 2 minutes prior to insulin stimulation and for 15 minutes after the addition of insulin.

To determine the ratio of mobile to stationary GSVs located at the membrane region with respect to time, time-projection image stack methods were used. Stacks of time-lapse images were separated into 1 minute segments to determine the time dependent nature of vesicle dynamics. To begin with, the average projection of the image stack was subtracted pixel by pixel from each image in the stack. The result was a secondary image stack consisting purely of moving vesicles, with stationary GSVs and other static GLUT4 signal removed from the images. This secondary image stack was then subtracted frame by frame from the original image stack. The resultant image stack provided a sequence of images relating to only stationary vesicles located within the membrane region.

An image was taken from the beginning of each image stack for every recorded one minute segment providing comparative images of mobile and stationary GSVs at the plasma membrane surface. GSVs were then identified as outlined earlier and the time dependent vesicle dynamics were obtained for both cell lines. These values were measured for three individual cells within ten different 100 μm^2 regions of interest (ROI).

Figure 44 demonstrates the time dependent dynamics of GSVs in adipocytes as measured through TIRFM. At the point of insulin stimulation, t = 0, a notable increase in mobile GSVs within the illuminated membrane region was observed. The period of increased activity lasted, on average, 5 minutes before returning to a rate similar to that prior to insulin stimulation. The number of stationary GSVs over the time course of insulin stimulation was found to increase gradually at a consistent rate over the analysed 15 minutes. Prior to insulin stimulation it can be seen that larger quantities of membrane localised GLUT4 signal is confined to GSV spot regions. Through insulin stimulation the signal becomes more homogenous over the area of the membrane. This is consistent with the

theory that insulin not only recruits GLUT4 to the membrane, but also controls its dispersal and spatial distribution [93].

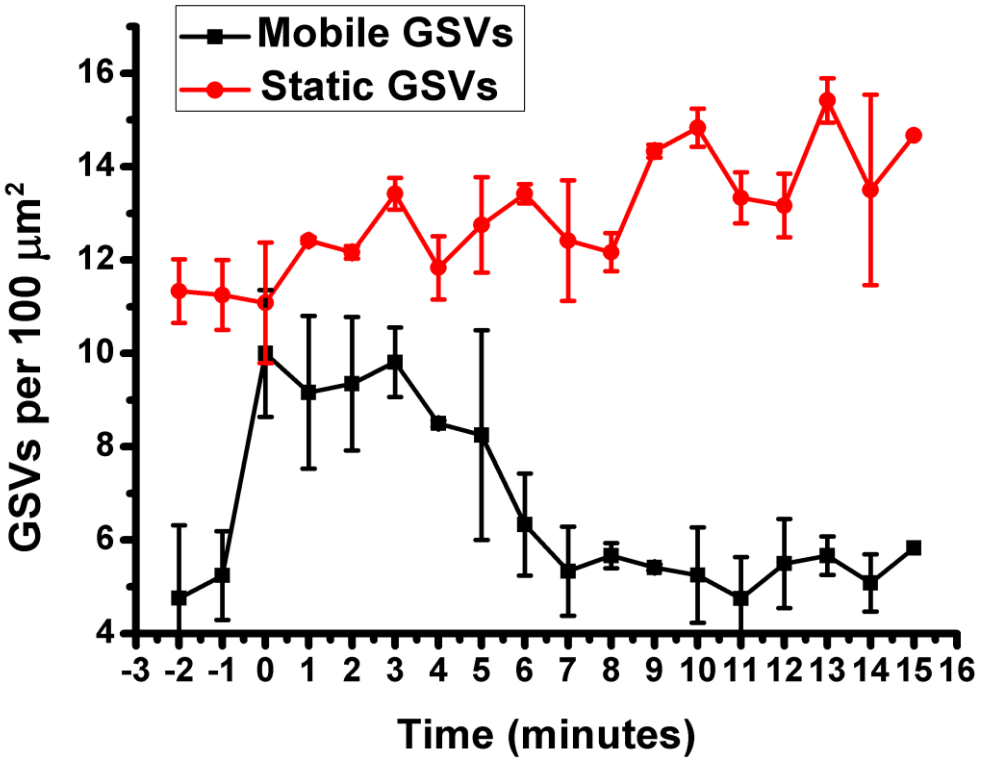

Figure 44: Counts of mobile and stationary vesicles for adipocytes stimulated by 100 nM insulin. N – 3 cells where 10 individual ROI of 100 µm² were analysed. Error bars correspond to standard deviation for 30 measured ROIs. Images recorded at a frame rate of 2Hz for 15 minutes where time point 0 corresponds to point of insulin addition.

In 2010 Stenkula et al. [93] devised a kinetic model detailing the rate of GSV fusion with the plasma membrane in Adipocytes using TIRFM. They found a very distinct region of activity between 1-5 minutes post insulin stimulation where there was a 60-fold increase in the rate of vesicle fusion to the plasma membrane. The observed increase in dynamic GSVs, over a similar time frame, in this study would suggest vesicle activity in line with the previously presented kinetic model. The gradual increase in stationary GSVs would be expected as the vesicles continue to tether and fuse to the membrane upon stimulation.

3.4.6. Mobile vs. stationary GSV analysis in HeLa Cells

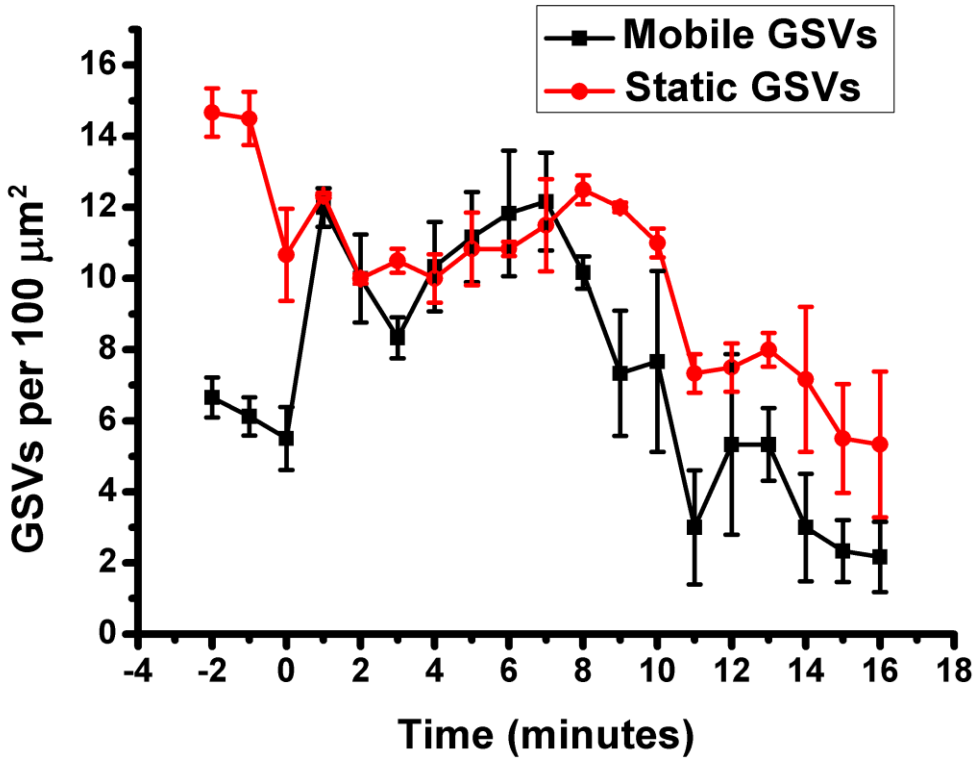

Figure 45: Counts of mobile and stationary vesicles for HeLa cells stimulated by 100 nM insulin. N – 3 cells where 10 individual ROI of 100 µm² were analysed. Error bars correspond to standard deviation for 30 measured ROIs. Images recorded at a frame rate of 2Hz for 15 minutes where time point 0 corresponds to point of insulin addition.

Under insulin stimulated conditions the quantity of mobile GSVs in HeLa cells underwent a similar increase to the imaged adipocytes as seen in Figure 45. The duration of this increased activity was observed to last 8 minutes after insulin stimulation. After the increase in activity the number of mobile GSVs returned to a density of roughly 2 per 100 µm^2. The increase in vesicle activity is over a very similar time frame to that observed in the adipocyte cell line. The slightly lengthy duration, and slightly lower final density, could be responsible for the extended $\tau_{1/2}$ noted in Table 2. The density of GSVs immobilised at the membrane surface underwent a constant reduction from an, initially, high volume of 15 per 100 µm^2. This was in stark contrast to the measured increase in static GSV density observed in the adipocyte cells. The reduction in GSVs tethered at the plasma membrane, in HeLa cells, could be the reason for the lower fold increase in measured fluorescence intensity presented in Figure 41.

3.5. Conclusions

An experimental system was devised to analyse the translocation of GFP tagged GLUT4 molecules using TIRFM. Investigating the measured increase in membrane associated fluorescence intensity revealed that upon stimulation with 100 nM insulin, the measured fluorescence intensity increase in adipocytes was consistent with previously reported values. In addition, using a series of image analysis techniques, identification and analysis of GSVs was performed. It was found that in adipocytes a significant rise in mobile GSVs was observed immediately upon insulin stimulation. This was in accordance with the previously proposed kinetic model of GSV recruitment presented in [93]. This provided the basis of data to which a novel HeLa cell model expressing GLUT4-GFP could be compared. It was found that, while a degree of insulin responsiveness was present, the final increase in membrane GLUT4-GFP signal was significantly lower than that for the adipocytes. In addition, the time taken for the measured membrane GLUT4-GFP intensity to increase to the final value was significantly longer in the HeLa cells compared with the adipocytes. Upon inspection of the GSV dynamics for the HeLa cell model it was observed that the mobile fraction of GSVs appeared to follow a similar trend to the adipocytes. However, the fraction of stationary GSVs at the membrane surface underwent a reduction over the course of the image accumulation as opposed to the observed increase in the adipocytes. The results presented here suggest that under insulin stimulated conditions there is a similar recruitment of GLUT4 molecules to the membrane surface but over a longer time period. This indicates that the HeLa model does respond to the insulin stimulation in terms of GLUT4 membrane localisation. Also, the recruitment of GSVs to the membrane under stimulated conditions increases, however, the fraction stationary at the membrane over the experimental time frame decreases. This may imply differences between the two cell models in terms of the post-fusion dispersal of GLUT4 to the membrane and the related machinery involved in the endocytotic process. The implications of these results is a robust cellular model with similar insulin sensitivity but differences in the fusion processes involving GSVs. Further investigation is required to determine the exact kinetics of vesicle fusion to the plasma

membrane. However, these results present a promising homologous system that may be used for higher throughput experimentation when investigating factors affecting the insulin mediated metabolism of glucose.

4. Chapter 4: FCS-FLIM study of viscosity measurements with molecular rotors

4.1. Introduction

4.1.1. Membrane Fluidity

The cellular plasma membrane is a complex fluid-like environment principally constructed from various phospholipids, proteins and cholesterol [12]. It is increasingly understood that the physical properties of the plasma membrane are involved in a series of important cellular functions such as endocytosis, exocytosis and cell signalling. One of the key physical parameters of the membrane is its fluidity which represents the reciprocal of the viscosity of this 2D-fluid bilayer [118], [119]. The fluidity of a membrane determines the ease at which key molecules are able to travel within the plane of the phospholipid bilayer. Alterations to this intrinsic property have been linked to a number of diseases [120] such as: Alzheimer's disease [121], [122], stroke [123], cardiovascular disease [124], cancer [125–128], atherosclerosis [129] and many more. As well as indicating the pathogenesis of a variety of diseases, determining the fluidity of the plasma membrane can show the efficacy of particular treatments and therapeutics [130–132].

4.1.2. Measurement Methods

Various methods for determining the membrane fluidity exist, which determine this intrinsic property by either probing the rotational or lateral mobility of a tracer molecule. Commonly employed is the method of deuterium Nuclear Magnetic Resonance (NMR) spectroscopy were deuterated lipids are incorporated into a membrane [133], [134]. Specifically, with ^{2}H-NMR the residual quadrupolar couplings are related to the segmented order parameters of the flexible phospholipid molecules in a liquid-crystalline membrane system [135]. The measured order parameters coupled with the nuclear spin relaxation rates provides information on the molecular mobility of the deuterated lipids. While NMR is beneficial in that it can provide both structural and dynamic information

simultaneously, non-invasively and with atomic precision it lacks any degree of spatial resolution which is of great value in the heterogeneous and dynamic membrane environment. Similar to NMR, Electron Spin Resonance (ESR) spectroscopy, has been historically applied to the investigations of biological membranes [136]. ESR utilises stable nitroxyl radicals as probe molecules (spin probes) to investigate the dynamic nature of the bilayer by determining the rotational correlation time of the probes [136]. ESR offers a high resolution method for determining quantifiable micro-viscosity values in biological membranes which is of great use in the studies of vesicles for drug delivery [137] and various other applications [138]. For the case of investigating the heterogeneous nature of biological membranes ESR suffers, as NMR does, in the fact that it is a spectroscopic method offering no insight into lateral differences in membrane viscosity values. These techniques also suffer due to the high level of expertise, expensive and complex equipment necessary, along with a reduced applicability to studying living cells and tissues.

Fluorescence based methods offer a diverse set of tools through the incorporation of a dynamic array of suitable probes spanning a variety of wavelengths [57]. Fluorescence Recovery After Photobleaching (FRAP) has frequently been used to determine the lateral diffusion coefficients of fluorescent lipids or tracer probes in biological membranes [121]. For FRAP a membrane is fluorescently labelled where a small region, of known dimensions, is photobleached using a source of powerful excitation light. The bleached area is then imaged, using significantly reduced excitation light, over a period of time as the fluorescence signal recovers due to lateral diffusion of the lipid molecules. From the rate of the increasing signal, the diffusion coefficient of the fluorescent lipid or probe in the membrane can be determined and related to the lateral mobility within the bilayer region. FRAP is an ideal technique for the analysis of larger membrane associated proteins and molecules as it can provide information on immobile fractions of molecules and there is no lower limit on the diffusion coefficients that can be probed [139–141]. Whilst FRAP is instrumentally and theoretically simpler to NMR and ESR, it remains unable to resolve localised differences in viscosity and, at times, requires lengthy acquisition. Another powerful fluorescence based method for determining diffusion coefficients can be found in Fluorescence Correlation Spectroscopy

(FCS). Like FRAP, FCS determines the lateral mobility of fluorescent molecules within the bilayer however, only a diffraction limited spot defined by a confocal microscope is analysed. As discussed earlier in this thesis, FCS time correlates fluctuations in fluorescence intensity within the defined confocal volume to provide information on molecular dynamics. Positioning the observed area to the plane of the bilayer enables direct measurement of the diffusion coefficient of a low concentration of fluorescent tracer molecules [142]. FCS operates with a spatial resolution of roughly 500 nm, although methods are available that go beyond this limit [143], and over a temporal resolution ranging from 10's of ns to 10's of seconds. The result is a technique highly suited to determining the viscosity of fluorescent membranes as has been demonstrated numerous times [64], [144–147].

4.1.3. Molecular Rotors

Molecular rotors have emerged in recent years as promising tools in constructing images based on local microviscosity values [148]. Molecular rotors are a class of fluorescent molecules with viscosity dependent photophysical parameters, specifically their quantum yield and fluorescence lifetime [27]. This sensitivity to viscosity arises due to internal molecular rotation resulting in quenching of fluorescence. Rotation of sections of the molecules related to fluorescence emission is one of the key pathways of non-radiative decay for certain fluorescent molecules. Upon excitation, double bonds associated with fluorescence decrease in bond order resulting in an equivalent single bond with rotational ability. In an unrestricted system, such as an isotropic solution, the rate of rotation can be denoted via the Stokes-Einstein Debye relationship.

$$k_{rot} = \frac{1}{\theta_r} = \frac{k_B T}{4\pi r^3 \eta} \tag{4.1}$$

Where $k_{rot}$is the rate of rotation, $\theta_r$is the rotational correlation time, T is the temperature, r is the radius of the molecule in metres, and η is the solvent viscosity in $N\ s/m^2$. Outlined in chapter 1 the fluorescence lifetime is related to

the rates of radiative and non-radiative rate constants. For the particular class of rotors with Twisted Intramolecular Charge Transfer (TICT) excited states the dominant source of non-radiative decay arises from the rotational ability of the molecules. Assuming $k_{nr} = k_{rot}$ equation can be re-written by incorporating equation (1.1) resulting in the following.

$$\tau = \frac{1}{k_r + \frac{k_B T}{4\pi r^3 \eta}} \tag{4.2}$$

In the above relationship τ is the fluorescence lifetime and k_r relates to the radiative decay rate constant. The non-radiative decay rate constant, k_{nr}, has been replaced with equation (4.1) relating the lifetime to values of temperature, hydrodynamic radius and viscosity. A more practical relationship between viscosity and fluorescence lifetime is realised through the Förster-Hoffman model given below [27], [149].

$$\tau = C_m \times \eta^{\gamma} \tag{4.3}$$

Where C_m is the concentration-temperature dependent parameter and γ is the dye dependent molecular parameter which is calculated from the slope of a log vs log plot of viscosity vs. lifetime. These values are determined empirically by measuring the lifetime of the rotor in solutions of varying viscosities such as methanol-glycerol mixtures of increasing glycerol content. There are a variety of molecules which express such viscosity dependent lifetime changes such as retinol palmitate [150], Hoechst 33258 [151], DCVJ[152] and di-4-ANEPPDHQ [153]. A similar molecule which has attracted a great deal of interest is the meso-substituted boron-dipyrrin (BODIPY) dye which exhibits strong dependencies on viscosity with sharp changes in its fluorescence quantum yield and lifetime [59]. Utilising the viscosity dependent fluorescence lifetime of these molecules with the capabilities of Fluorescent Lifetime Imaging Microscopy

(FLIM) offers the ability to map membrane microviscosity values with high degrees of spatial resolution as previously demonstrated [58], [59], [148].

Questions still remain, however, as to its effectiveness as a probe of quantifiable viscosity when incorporated into more complex environments such as sub-cellular locations and, in the context of this thesis, biological membranes.

4.1.4. Giant Unilamellar Vesicles and Supported Lipid Bilayers

Due to the complexities of naturally occurring plasma membranes, simplified lipid systems are traditionally used to investigate the physical nature of membranes. Bilayers in the form of liposomes and surface supported lipid bilayers provide controlled systems for investigation. Using methods such as electroformation, gentle hydration, lipid extrusion and microfluidics, unilamellar and multi-lamellar vesicles of various sizes can be manufactured. Numerous types of phospholipids and cholesterols are commercially available, which can provide environments of various physical states depending on the ratios of the components use. Phospholipids are amphipathic molecules and, as such, self-assemble into a variety of structures under certain conditions depending on the solvents and buffers used. A typical lipid molecule can be seen in Figure 46.

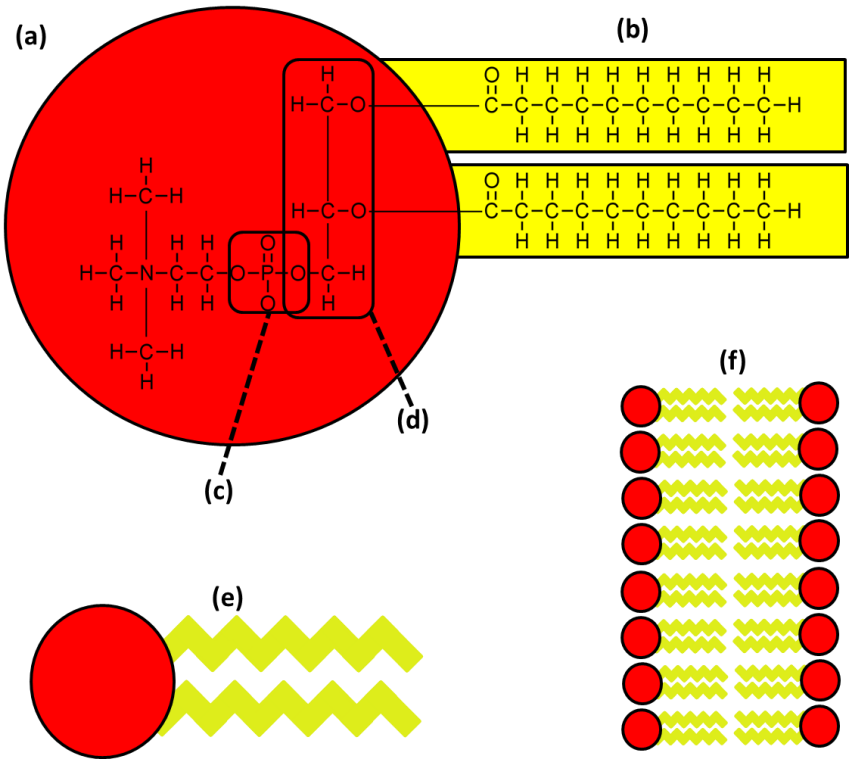

Figure 46: Typical phospholipid molecule made of two core sections the polar (hydrophilic) head region (a) and the hydrophobic non-polar tail region (b). The head region consists of a phosphate group (c) and glycerol backbone (d). (e) depicts a simplified phospholipid molecule which represents a saturate lipid molecule. (f) Depicts a resultant lipid bilayer consisting of self-assembled phospholipid molecules with a hydrophobic core.

Phospholipids consist of two key sections, the polar head group and the non-polar tail region. The head group contains choline, phosphate and the glycerol backbone of the molecule and is hydrophilic in nature. The tail region consists of hydrocarbon chains, varying in length depending on the lipid, and forms the hydrophobic core of the lipid bilayer. Depending on the degree of saturation in the hydrocarbon tail region, phospholipids can form bilayers of varying viscosities. DOPC contains a double bond in each of the tails resulting in an unsaturated lipid which forms a fluid phase bilayer with a very low viscosity. Saturated lipids, such as DPPC, contain completely single bond oriented tail regions and take on the form of a rigid (Gel phase) bilayer at room temperature. Phospholipids have an intrinsic phase transition temperature, T_m, where the phase of the formed bilayer transitions from a rigid gel phase to the dynamic fluid phase. For DPPC this temperature is 41^{o}C and for DOPC it is -17^{o}C, providing two very useful systems for investigations at room temperature.

In more complex systems containing more 2 or more phospholipids or one phospholipid plus various concentrations of cholesterol, phase coexistence may occur in the form of liquid ordered (Lo) and liquid disordered (Ld) phases. This has excited interest into the study of lipid domains which are suggested to influence a diverse range of cellular processes. In artificial systems these are of the order on microns as opposed to the hypothesised nano-domains found within the plasma membranes of living cells. Fluorescent probes that show distinct variations in their photophysical responses as a result of incorporation into different lipid domains are of great importance [57].

Giant Unilamellar Vesicles offer an analogous system on the order of the size of an individual cell, i.e 10's to 100's of microns.

4.1.5. Combined FCS-FLIM study of molecular rotors

Due to the questions that remain over the efficacy of molecular rotors, and in particular the meso-substituted BODIPY rotor, in providing quantifiable viscosity values, a combined FCS-FLIM system has been utilised. By combining the ability of FCS to probe lateral lipid diffusion and FLIM to image micro-viscosities, a study has been devised to compare viscosities measured by both methods. Such a study has never been performed for these particular molecules and offers a comparison of measurements of bulk bilayer viscosity measured by FCS to the apparent micro-viscosities of FLIM.

4.2. Materials and Methods

4.2.1. Phospholipids

All lipids used for experimentation were from stock samples purchased from either Avanti Polar Lipids or Sigma Aldrich. 1,2-Dioleoyl-sn-glycero-3-phosphocholine (DOPC), 1,2-dipalmitoyl-sn-glycero-3-phosphocholine (DPPC), 1-palmitoyl-2-oleoyl-sn-glycero-3-phosphocholine (POPC) and cholesterol were all purchased either dissolved in chloroform at a concentration of 25 mg/ml or as lyophilised powders and subsequently dissolved in chloroform at 50 mg/ml. All

chloroform solutions were stored in cleaned glassware with a special Teflon covered screw top as to avoid contaminants.

4.2.2. BODIPY based molecular rotors

The molecular rotors used were a kind gift from Dr Marina Kuimova, Dr Nicholas J. Brooks and Mr Michael Dent, all of Imperial College London. The molecules were synthesised as outlined in previous work by Dr Kuimova and Dr Brooks' group [58], [154]. Three variants of the meso-substituted BODIPY molecule were investigated containing three different tail molecules.

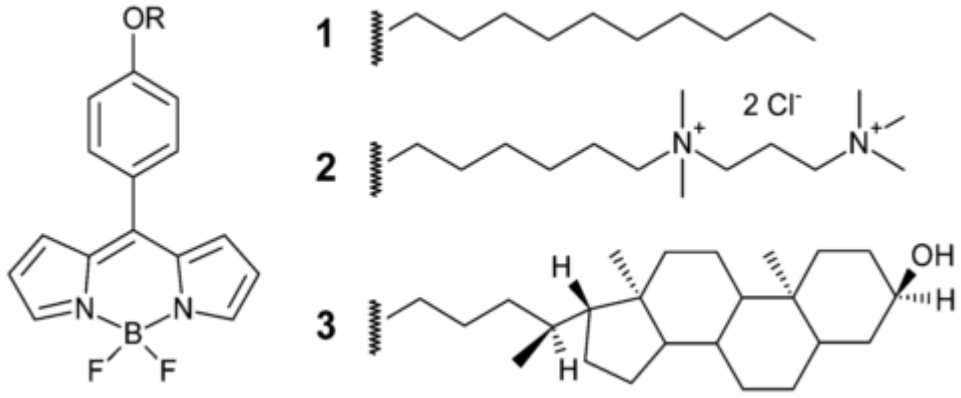

Figure 47: Meso-substituted BODIPY rotor with three different tail molecules. (1) – BODIPY C10 (2) – BODIPY ++ and (3) – BODIPY Cholesterol

4.2.3. LUV production

Large Unilamellar Vesicles (LUVs) were made through the extrusion method outlined in [155]. Firstly, a solution of DOPC and BODIPY C10 in chloroform at a concentration of 10 mg/ml was dried under N_2 in a glass vial to provide a lipid cake on the vial surface. Following this 1 ml of 100 mM sucrose buffer was added and vortexed for 2 minutes. The resultant solution containing vesicles and micelles was freeze-thawed using liquid nitrogen and a heated water bath, set to 37^{o}C, 10 times. This provided a solution containing single lipid bilayer vesicles over a range of sizes. To ensure a mono-dispersed range of vesicles, roughly 100

nm in size, the solution was extruded through a polycarbonate porous membrane 5 times and then decanted to an Eppendorf tube.

4.2.4. GUV Electroformation

Electroformation was utilised for the creation of GUVs using a modified procedure to that originally outlined by Angelova et al. [156]. Using a spin coating system [157] for uniform lipid coating of indium tin oxide (ITO) electrodes the procedure used is as follows. Clean Indium Tin Oxide (ITO) slides for electro formation were prepared by attaching one wire using conductive silver paint to provide electrical contact. These were then rinsed with methanol and dried using compressed nitrogen to remove any dust. For every lipid mix used the solution was made up to a total concentration of 3.75 mg/ml which was optimal for uniform lipid coating. The lipids were initially diluted at a concentration of 25 mg/ml in a solution of chloroform. The mixture was made up to a 1 ml solution using 95% chloroform to 5% Acetonitrile. At this stage, solutions were stored in the freezer for a few days before spinning. The ITO slides were prepared for lipid coating with a short rinsing of methanol and dried using N_2. A 250 µl volume of the lipid mixture was then pipetted to the ITO slides to provide ample coverage for spinning. This was preferably achieved without introducing any bubbles to the surface. The slides were then spun for 30 seconds at a speed of 400 rpm. These were then dried down under vacuum in a desiccator for at least 2 hours to remove any residual solvent present within the lipid layers.

To control values of pH and osmotic concentration and to provide a density gradient between the inner and outer GUV regions two buffers were used. An internal buffer consisting of 100 mM sucrose was used and an external buffer of 90 mM Glucose and 10 mM HEPES was added to provide a sugar density gradient. The differences in density ensured that the vesicles settled to the coverslip surface for investigation by optical microscopy. The ITO slides, now coated with lipid sheets, were used as the base to form a sealed chamber for electroformation. A rubber gasket was sealed to the coated ITO slide using vacuum grease and then 300 µl of sucrose buffer solution was added to the chamber. Following this a final piece of ITO, uncoated, was sealed to the top of

the chamber. For both single and multi-phase GUV electroformation the two ITO electrodes are connected to the output terminal of a signal generator running at 10 Hz and 100 mVpp (peak to peak). The voltage is then ramped to 1.5 Vpp over varying time frames depending on the required size of the GUVs needed for investigation. For the sake of all experiments GUVs of sizes 10 – 100 μm was deemed to be sufficient and required the following ramping procedure. Table 3 outlines the electroformation parameters used for different lipid compositions.

Signal	DOPC			POPC			DPPC			DOPC:DPPC:Cholesterol		
	f	V	T	f	V	T	f	V	T	f	V	T
Sine	10	0.1	10	10	0.1	10	10	0.1	10	10	0.1	10
Sine	10	0.5	20	10	0.5	20	10	0.5	20	10	0.5	20
Sine	10	1	30	10	1	30	10	1	30	10	1	30
Sine	10	1.6	60	10	1.6	60	10	1.6	60	10	1.6	60
Square	3	2	60	3	2	60	3	2	15	3	2	60

Table 3: Electroformation parameters f – Frequency (Hz), V – voltage (Vpp) T – time (Minutes) Sine wave signal used for growth phase and square wave signal used for detach pulse to remove vesicles from ITO surface

Due to the use of transparent ITO the vesicles could be observed as electroformation took place which enabled analysis of the size and yield of vesicles. If the yield is deemed sufficient then the chamber can be set for detachment through application of a square wave signal at a lower frequency. To detach the vesicles from the surface the system is set to 2 Vpp at a frequency of 3 Hz for 1 hour. For pure DPPC vesicles and ternary phase vesicles a cooling procedure was implemented at a rate of 1 ^{o}C/minute at the end of electroformation.

Once detached the GUVs are then decanted into the glucose buffer at a ratio of 300 μl of sucrose to 1 ml of glucose. This gave adequate distribution of GUVs over the surface of a coverslip to investigate single GUVs without interaction with other vesicles.

For investigation of GUVs using FCS the vesicle solution was gently transferred to a coverslip which had been treated with a 10 % solution of poly-l-lysine in PBS for 1 hour at 37^{o}C. This was to ensure that the GUVs remain as spherical structures for the duration of experimentation. This coverslip was then sealed to a dished microscope slide to ensure no evaporation of the buffer and to remove any movement resulting from convection.

In the case of supported lipid bilayer structures investigated using FLIM; GUVs were allowed to burst on the surface of a coverslip over the course of 3-4 hours.

4.2.5. Surface treatments

For combined FCS-FLIM analysis of the BODIPY rotors in GUVs it was imperative that the vesicles remain stationary at the coverslip surface for the duration of the measurements. This was achieved through a surface treatment of 0.01% Poly-l-lysine in water, previously demonstrated to hold liposomes at the coverslip surface [158]. Coverslips were sonicated in methanol then acetone for 10 minutes followed by drying under N_2. PLL treatment was applied for 30 minutes at 37^{o}C followed by 5 minutes rinsing in water. Vesicle adhesion was investigated through timelapse confocal imaging of DOPC vesicles containing 0.05 mol % of BODIPY C_{10}.

4.2.6. FCS-FLIM System

To perform simultaneous FCS and lifetime measurements a Becker and Hickl DCS-120 confocal scanning system was used. Combined measurements were performed using the 473 nm picosecond diode laser line in beam parked mode with the laser set to pulsed mode at frequencies of 20 MHz and 50MHz. Using the laser in this configuration allowed for simultaneous FCS and lifetime measurements. Single photon detection was provided through the use of the hybrid photo-multiplier tube (PMT) HPM-100-40 detection unit. An excitation filter, 480 nm, and emission filter, 535 nm, were placed in front of the confocal pinhole to enable detection of the resultant BODIPY fluorescence. The pinhole was set to 0.25 mm equivalent to 0.5 Airy units to provide the smallest possible

confocal volume suitable for FCS. A Zeiss 1.2 Na 40x C-Apochromat objective lens was used to determine a tightly confined focal region.

4.2.7. Afterpulsing effects

For FCS measurements of small molecules in a lipid bilayer a high degree of signal to noise ratio is required due to the low fluorescent count rate per molecule. There are various sources of noise in an optical FCS system with one of the main contributors being afterpulsing originating in the single photon detectors. Afterpulsing occurs when a real detected photon is followed, almost immediately, by a false recorded photon event [159]. In terms of the ACF this manifests itself as a sharp peak for short correlation times, $< 1\ \mu s$. A common solution to this issue is to split the signal between two different single photon detectors and cross-correlate the individually measured auto-correlation functions [160]. Since the afterpulses found in one detector will not match those in the second detector no distortion to the measured auto-correlation function is seen. Recently, a solution for a single detector system free of afterpulsing has been realised through the use of hybrid PMTs. This is demonstrated in Figure 48 where $G(\tau)$ was recorded for a dilute solution of 100 nm fluorescent microspheres diffusing in a water solution using two detectors: the H7442P-50 PMT and a hybrid HPM-100-40 PMT.

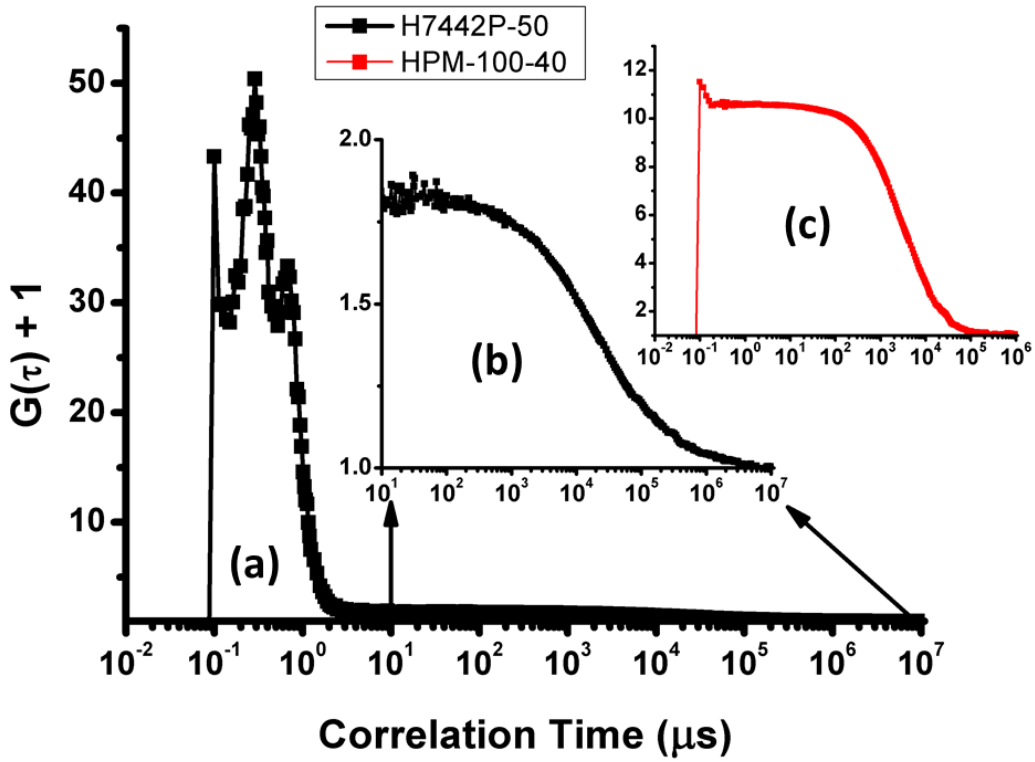

Figure 48: Auto-correlation functions relating to 100 nm fluorescent microspheres diffusing in a solution of water recorded by two detectors: H7442P-50 PMT and a hybrid HPM-100-40 PMT. (a) G(τ) measure with the H7442P-50 detector with large correlation at short times due to afterpulsing. (b) region of signal corresponding to diffusing microspheres. (c) G(τ) recorded using the hybrid PMT detector shows correlation down to sub microsecond times free of afterpulsing.

Figure 48 (a) and (b) demonstrate that with the H7422P-50 detector afterpulsing dominates the signal for short correlation times. Figure 48 (c) shows clear correlation to sub microsecond correlation times for the hybrid PMT detector demonstrating a single detector system free of afterpulsing effects.

4.2.8. Optical Alignment

Due to the single molecule sensitivity of FCS a perfectly aligned optical system was necessary; of particular importance is the alignment of the detected fluorescence relative to the pinhole. Misalignments in the optical path create distortions to the detected confocal region creating errors in the measured auto-correlation function. An improperly aligned system can even lead to no measured auto-correlation function and this is demonstrated in Figure 49.

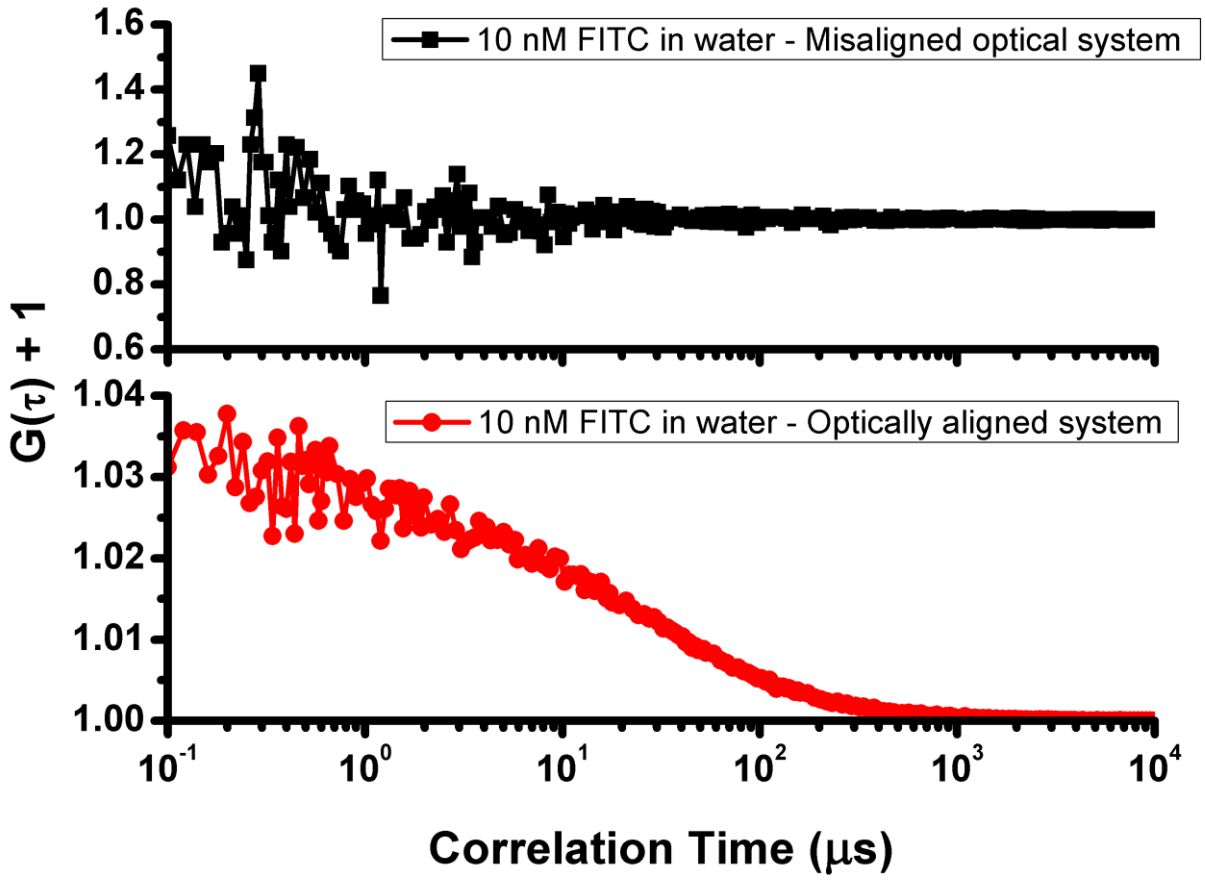

Figure 49: Auto-correlation functions measured for a 10 nM solution of FITC diffusing freely in water. The top graph corresponds to a measurement taken with the detected region moved relative to the confocal pinhole. The lower graph demonstrates that for a properly aligned system G(τ) can be measured for a dilute solution of a small diffusing fluorescent species.

Figure 49 demonstrates the importance of correct positioning of the detected confocal volume with respect to the PMT. Optimal alignment was achieved through positioning of the tube lens relative to the optical axis. The lateral position was first optimised as determined by the maximum throughput from a highly fluorescent sample. The axial position was optimised through use of bright field light and a transparent sample containing visible features, a fixed plant tissue sample, coupled with a low magnification objective. When an image of the sample was seen to be in focus at the pinhole this was taken as the start point for alignment. The position was then adjusted to a point where correlation of a 10 nM fluorescein in water was observed. There are numerous factors which may affect the shape of the observed focal region which can be damaging to extracting quantifiable values from the measured auto-correlation function

[161]. The thickness of the coverslip, through which a sample is viewed, plays a crucial role in proper definition of the confocal volume when using water immersion objectives. Using the C-Apochromat 1.2 NA 40x objective this effect can be counteracted through correct positioning of the coverslip correction collar. The effects of positioning of the coverslip correction collar were investigated using solutions of 200 nm fluorescent microspheres diffusing freely in water, varying the position of the collar. The coverslip used was measured to have a thickness of 140 μm using a micrometre screw gauge.

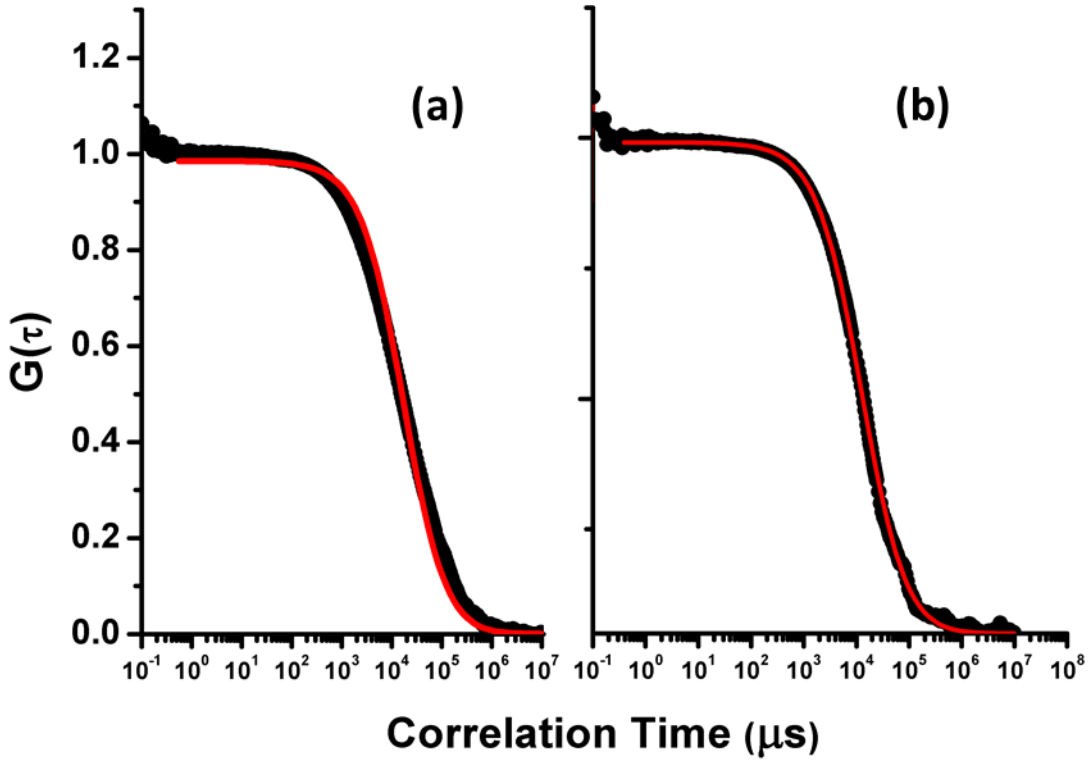

Figure 50: (a) – ACF measured for 200 nm fluorescent microspheres diffusing in water solution with objective correction ring positioned to 200 μm correction position. (b) – Correction ring positioned to 140 μm correction position corresponding to thickness of coverslip used.

Figure 50 demonstrates the effect of improper positioning of the objective lens coverslip thickness correction collar. A model for 3D diffusion was fit to the raw data measured for 200 nm microspheres diffusing in water. As can be seen from the fit and the resultant residuals in Figure 51 when the collar was positioned to the 200 μm correction position, a poor fit was observed. Optimising the position to correspond to the thickness measured via a micrometre screw gauge resulted in a better fit of the model to the data.

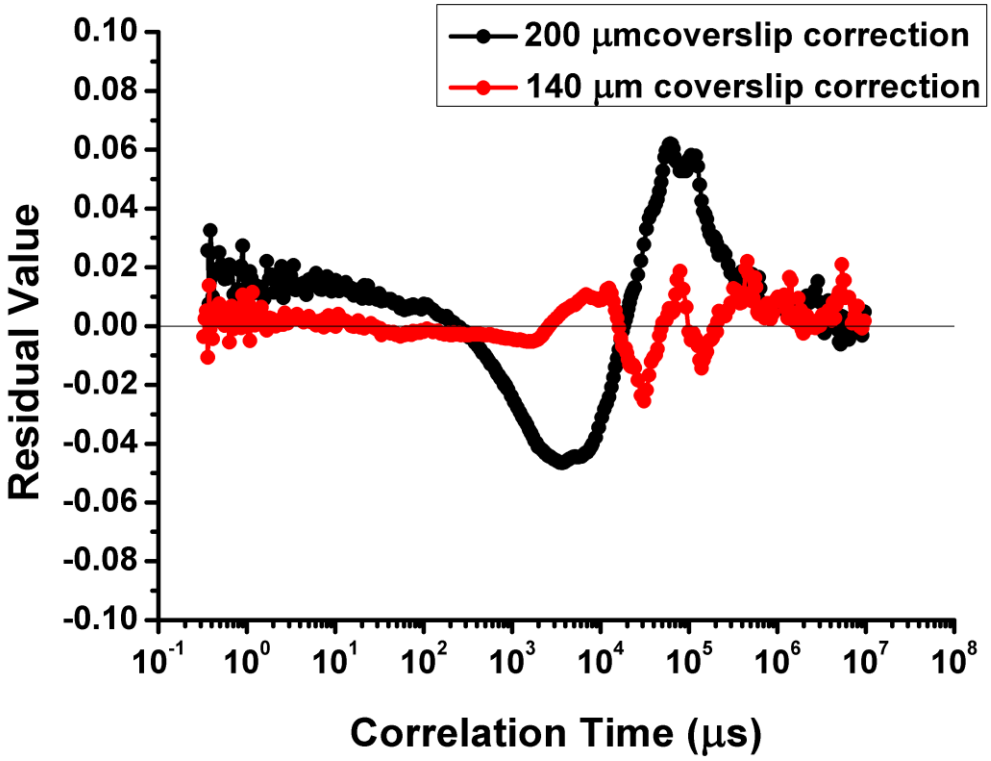

Figure 51: Residuals for single component fitting functions for ACFs relating to different positions on objective collar corrective ring. Position 140 μm corresponds to measured thickness of coverslip providing closer approximation to fitted function.

Both the position of the auto-correlation function and the amplitude, corresponding to the average number of particles, change dramatically with coverslip thickness. A 4-fold change to the number of particles and a, nearly, 2 fold difference in the diffusion times were observed, shown in Figure 52. As a result before each measurement the thickness of the used coverslip was measured and corrected for.

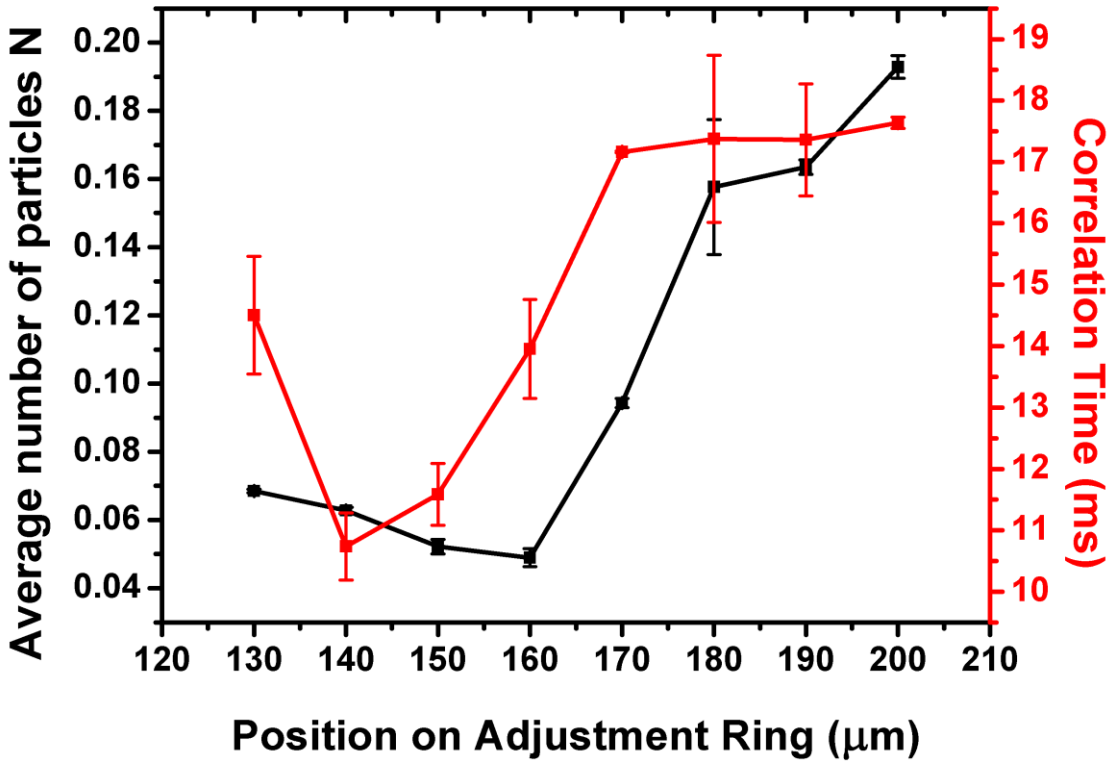

Figure 52: Average number of particles, N, and measured correlation time both exctracted from fitting procedure plotted against position of objective correction collar. Values correspond to ACF measured from 200 nm fluorescent microspheres diffusing in solution of water.

4.2.9. FCS Data Analysis

All recorded FCS decay curves were fit with suitable models outlined earlier in chapter 2. For diffusion of molecules constricted to a quasi 2D bilayer a model for 2D diffusion was fit to the raw data using the custom fitting functionality of Origin 8.

4.2.10. Focal volume positioning

The mid-point of the focal volume was positioned to the apical region of the vesicle determined by the maximum measured photon count. A common source of uncertainty in such measurements can be due to incorrect positioning of the focal volume with respect to the bilayer since this is achieved manually. The effects of miss positioning the focal volume were investigated by measuring the diffusion coefficient of the BODIPY C10 rotor in DOPC bilayers at varying z-positions. This is illustrated in Figure 53 and Figure 54.

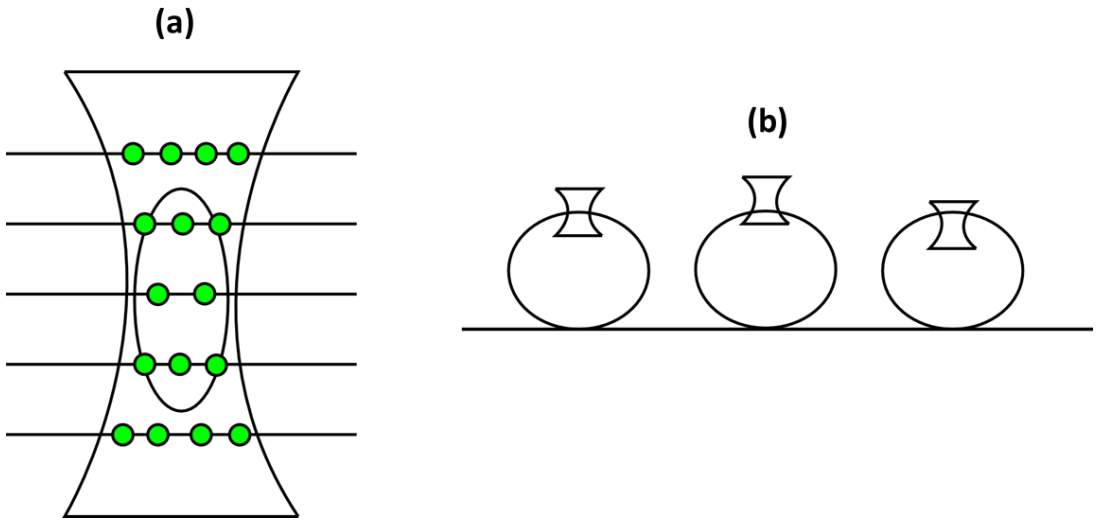

Figure 53: (a) schematic of focal volume where bilayer is positioned at varying heights with respect to central beam radius. At different heights the dimensions of the measured focal volume vary resulting in an increase in the number of detected particles. (b) Demonstration of miss positioning of focal volume with respect to apical region of GUV.

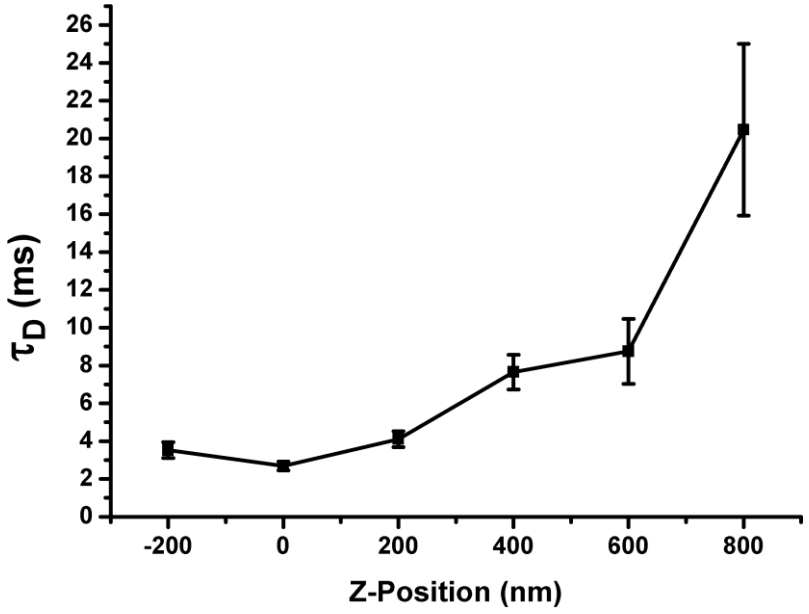

Figure 54: Measured diffusion time, τ_D, against position of focal volume with respect to centre of DOPC lipid bilayer with 0.05 mol% BODIPY C10 diffusing laterally. Diffusion times determined by fitting the auto-correlation function to a model for 2D diffusion

It can be seen from Figure 54 that the position of the bilayer with respect to the focal volume can greatly affect the measured diffusion time. A tenfold variation

in diffusion time can be seen moving less than 1 micron from the central position. The parabolic relationship stems from a widening of the apparent beam radius as the focal volume moves with respect to the bilayer.

The diffusion times from multiple data sets for a 0.05 mol% concentration of BODIPY C10 in a pure DOPC bilayer were collated to determine the variability in the measured value. On average a value of 2.1 ms was found with a standard deviation of 25% where N = 80 individual FCS correlation curves. The variability of 25% was deemed sufficient to consider the method of manually positioning the focal volume adequate for all following measurements.

4.2.11. Focal Volume Calibration – FCS

In order to determine quantifiable physical parameters using FCS the dimensions of the confocal volume are required. Various methods exist to determine the lateral and axial radii [79]. For 2D diffusion only knowledge of the lateral radius is required and was determined using fluorescent molecules of known diffusion coefficients. A 1 nM concentration of FITC in water was measured to provide a value of $\omega_0 = 262\ nm\ \pm 10\ nm$ and was confirmed by measuring 100 nm fluorescent microspheres in water. Both measurements were performed at a constant temperature of 20°C. This process was repeated before each data set was obtained in case of changes to the optical system.

4.2.12. Fluorescence lifetime data analysis

All fluorescence lifetime data for this chapter was analysed using the dedicated software package SPCImage from Becker and Hickl. All fluorescence decay traces were fit with either mono or bi-exponential decays with the goodness of fit determined by the reduced Chi squared, χ^2, test. For all images, χ^2 values between 0.8 – 1.4 for all pixels was used as an appropriate value for the fitted function and for all single point measurements values between 1 – 2 were used as a measure of goodness. For lifetime imaging all images were gathered until a maximum signal in the peak channel of 100 counts was recorded, and for single point measurements a peak signal of 100 – 1000 counts deemed sufficient.

4.2.13. IRF Recording - FLIM

The instrument response function (IRF) for a FLIM system accounts for any contributions to the decay function from the optical system. To obtain appropriate data from the measured fluorescence decay an IRF should be de-convoluted from each curve to account for any aberrations introduced by the optical system. Artificial IRFs can be used, however, these would not account for any unique aberrations originating from reflections or misshaping of laser pulses in the experimental system. Artificial IRFs also cannot be used to analyse data which may have a shorter lifetime than the provided IRF. Real IRF data was acquired through parking the laser beam through the centre of the optical axis and removing the selective filters before the detector. To protect the detector from damage neutral density (ND) filters were placed before the pinhole to reduce the optical density. All parameters relating to the ADC, TAC, CFD of the lifetime system and the optical components used, were held consistent for the IRF measurements and lifetime measurements. The electronic power slider for the laser was also maintained as this can affect the shape of the laser pulse. A fluorescent sample was replaced with a non-fluorescent scattering, e.g. Glass, silica, Ludox etc. and the resultant signal was recorded for one second with a maximum signal in the peak channel of 50,000 counts.

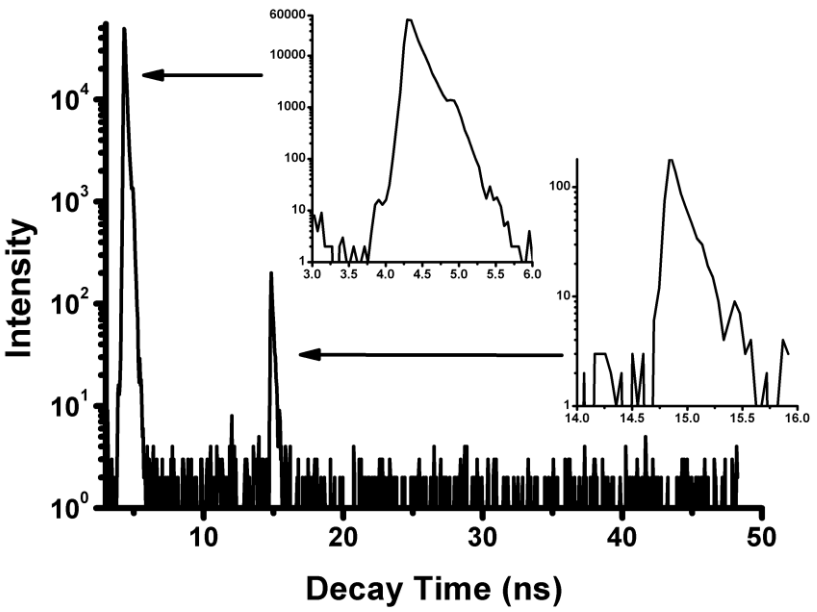

Figure 55: IRF recorded for 473 nm laser at a repetition rate of 20 MHz with a HPM-100-40 detector with an ADC resolution of 1024. 1st peak corresponds to initial laser pulse recorded from a glass scatterer sample and 2nd related to optical reflection.

Figure 55 demonstrates an example IRF recorded using the 473 nm laser line at a repetition rate of 20 MHz using glass as a scattering agent. Notably it can be seen that 10 ns following the original laser pulse exists a secondary pulse 2 orders of magnitude lower in intensity. The most likely source of this pulse is due to reflections within the optical path of the system. This could be mitigated by determining the optical surfaces responsible for this reflection and slightly tilting one of them. However, it was decided that this was not necessary due to the ability of the SPCImage analysis software to deconvolute the systems IRF from the measured decay. Also, any minor adjustment to the properly aligned optical system was seen to impact negatively upon the ability to perform sensitive FCS measurements.

To determine the impact of the secondary pulse on measured fluorescence decay curves, fluorescent calibration solutions of known lifetime were used [162]. FITC is known to have a fluorescent lifetime of 4.1 ns in a water solution with a pH of 7.4 and at room temperature. Rhodamine was also used as it possesses a lifetime value of 1.74 ns at room temperature. Both fluorophores hold fluorescence decays which are mono-exponential

The resultant lifetimes found for FITC in water were 4.05 ± 0.01 ns with a mono-exponential fit providing a χ^2 value of 1.1 ± 0.1. At the slightly longer lifetime value for FITC it could be visibly seen that the secondary pulse had minimal effect due to the high fluorescence signal at the corresponding time point. When analysing the decay profile for the Rhodamine B solution at room temperature it could clearly be seen that using the artificially generated IRF provided a poor fit to the data as indicated by the high χ^2 value of 6.89 with a corresponding lifetime value of 1.98 ns. The measured lifetime is greater than that expected for Rhodamine B and the exaggeration arises due to the artefact produced by the secondary pulse. When fitting using the measured IRF the results were significantly improved with a simple mono-exponential decay fit providing a lifetime value of 1.72 ± 0.02 ns with a χ^2 of 1.3 ±0.1. This can be seen in Figure 56.

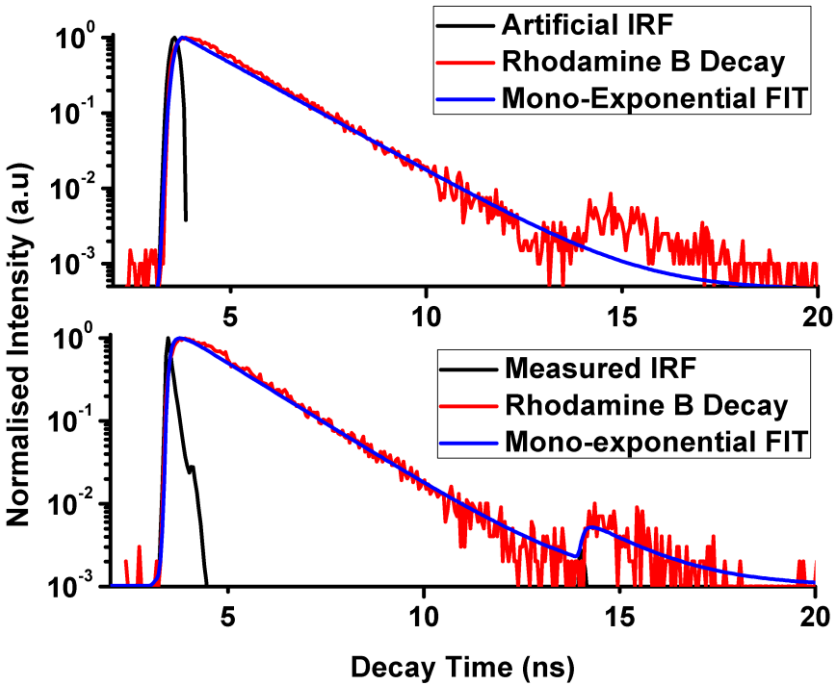

Figure 56: Fluorescence decay curves for Rhodamine B solutions in water at a temperature of 20°C analysed with both an artificially generated IRF and a measured IRF.

4.3. Results and Discussion

4.3.1. Molecular Rotor Calibration

Obtaining quantifiable information on micro-viscosity from molecular rotors is possible through calibration of the rotor in solutions of methanol and glycerol at varying concentrations of glycerol. The rotor BODIPY C10 was first dissolved in methanol at a concentration of 2.5 μM before adding glycerol. Concentrations from 50 % to 95 % w/w glycerol where measured at temperatures from 10°C to 60°C to determine the calibration curve. Temperature was controlled via a peltier heater coupled to a thermocouple controlled by a PID board to maintain constant temperature.

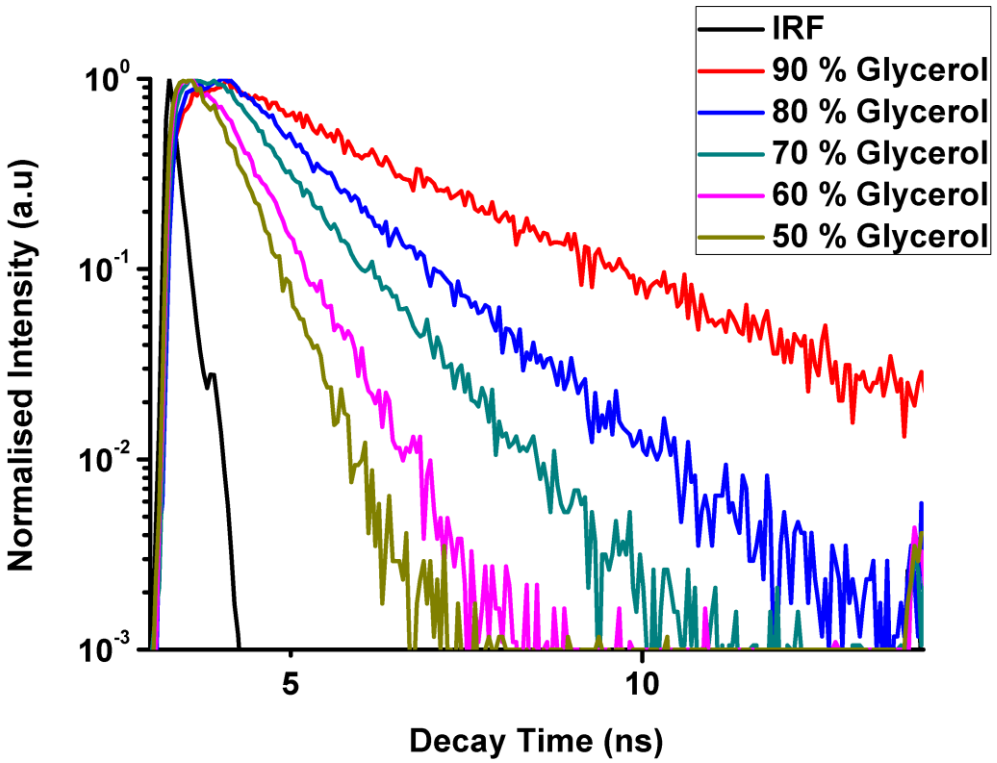

Figure 57: Normalised fluorescence decay curves for BODIPY C10 in methanol-glycerol mixtures with increasing glycerol concentrations.

As the concentration of glycerol increases the fluorescence lifetime of the rotor increases in accordance with the theory presented earlier. Importantly, decay curves for each solution were best fit with a mono-exponential function indicating only one population of the rotor in solution, as would be expected for an isotropic environment. Varying the temperature for each solution determined the calibration curve in Figure 58.

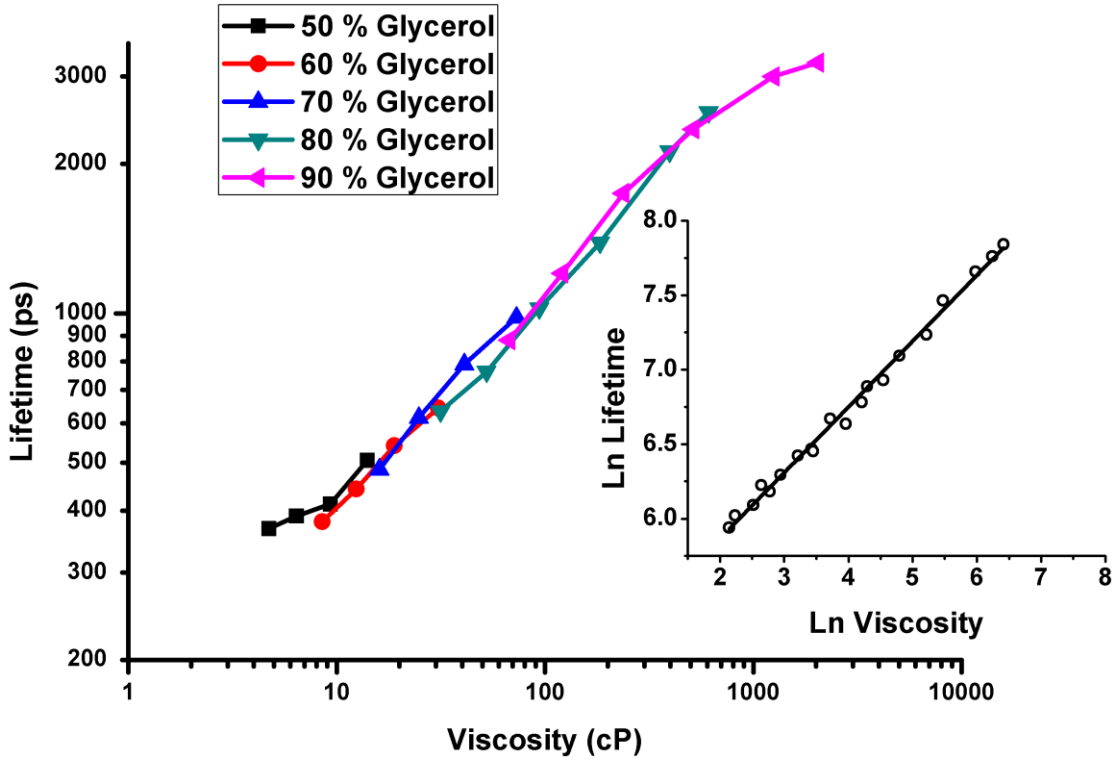

Figure 58: Calibration curve for BODIPY C10 rotor in methanolglycerol solutions over temperature range of 283 K – 333 K. Inset – Log-Log plot of lifetime over linear range of viscosities from 10 cP to 1000 cP with a gradient of 0.48.

The calibration plot shown in Figure 58 shows in linear relationship between the logarithm of lifetime vs the logarithm of viscosity over two decades of viscosity values. This is consistent with previously reported calibrations of similar rotors over the same viscosity range [58], [154]. Using this calibration plot the viscosity dependent constants, C_m and γ, relating to the Förster-Hoffman relationship were obtained by fitting a linear function to the plot of Ln lifetime vs Ln viscosity. The measured values of $C_m = 5$ and $\gamma = 0.5$, which are consistent with previously reported values [163]. The calibration plots for all three rotors overlap well within the viscosity ranges measured [164].

$$\ln(\tau) = C_m + \gamma \ln(\eta) \tag{4.4}$$

4.3.2. Diffusion measurements of BODIPY rotors in DOPC GUVs using FCS

The lateral diffusion coefficient for all three rotors was measured by FCS in a single component GUV system consisting of pure DOPC providing a fluid phase bilayer. Figure 59 shows an example data set taken of the BODIPY C10 rotor diffusing in a pure DOPC bilayer.

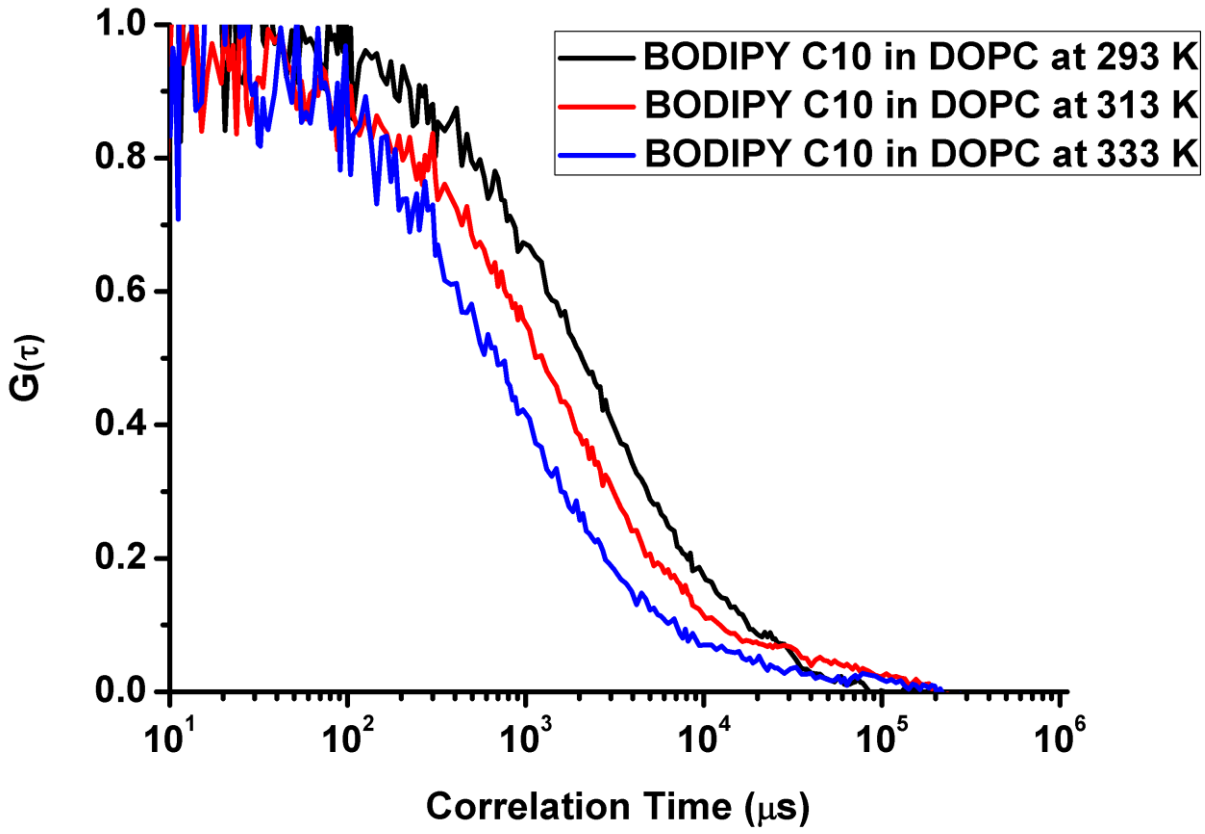

Figure 59: Measured autocorrelation functions for 0.05 mol% BODIPY C10 rotor diffusing in a pure DOPC bilayer at increasing temperatures. Raw data representative of individual GUVs of similar size, 10 – 20 μm. Data was accumulated for 10 x 10 s and averaged together for each temperature. Temperature was maintained using a thermoelectric peltier heater coupled to a thermocouple controlled by a PID control unit.

It can clearly be seen that as the temperature is increased the diffusion time reduces indicated an increase in the lateral diffusion coefficient for the rotor in the bilayer. The measured diffusion coefficients for all three rotors in a pure DOPC bilayer can be seen in Table 4.

Temperature (K)	BODIPY C10 ($\mu m^2/s$)	BODIPY ++ ($\mu m^2/s$)	BODIPY Cholesterol ($\mu m^2/s$)
293	10.522 ± 0.283	8.749 ± 0.471	7.253 ± 0.626
313	18.056 ± 2.311	12.317 ± 2.474	14.181 ± 1.334
333	22.654 ± 3.588	19.905 ± 4.093	21.178 ± 2.693

Table 4: Diffusion coefficients measured by FCS for three BODIPY rotors in pure DOPC GUVs. Number of measurements for each value N = 50. Error is equivalent to the SD between vesicles.

DOPC (Tm = 253 K) remains in the fluid phase over the experimental temperature regime. The diffusion coefficients for all three rotors increased by at least a factor of 2 between 293 and 333 K. For each value 10 individual measurements were performed on 5 different vesicles adhered to the coverslip surface. The sizes of the vesicles varied slightly but were all found to be between 10 to 50 microns which was deemed large enough to negate any curvature effects on lipid diffusion. The standard deviation for the measured diffusion coefficients increased from roughly 5 % on average to 18 % between the temperatures of 293 K and 333 K. This was most likely due to an increase in vesicle undulations at higher temperatures from the increase in the thermal energy. Undulations may move the bilayer relative to the focal volume causing variations in the measured diffusion time.

The diffusion coefficients measured by FCS were then compared to values obtained elsewhere by means of molecular dynamics simulations [164].

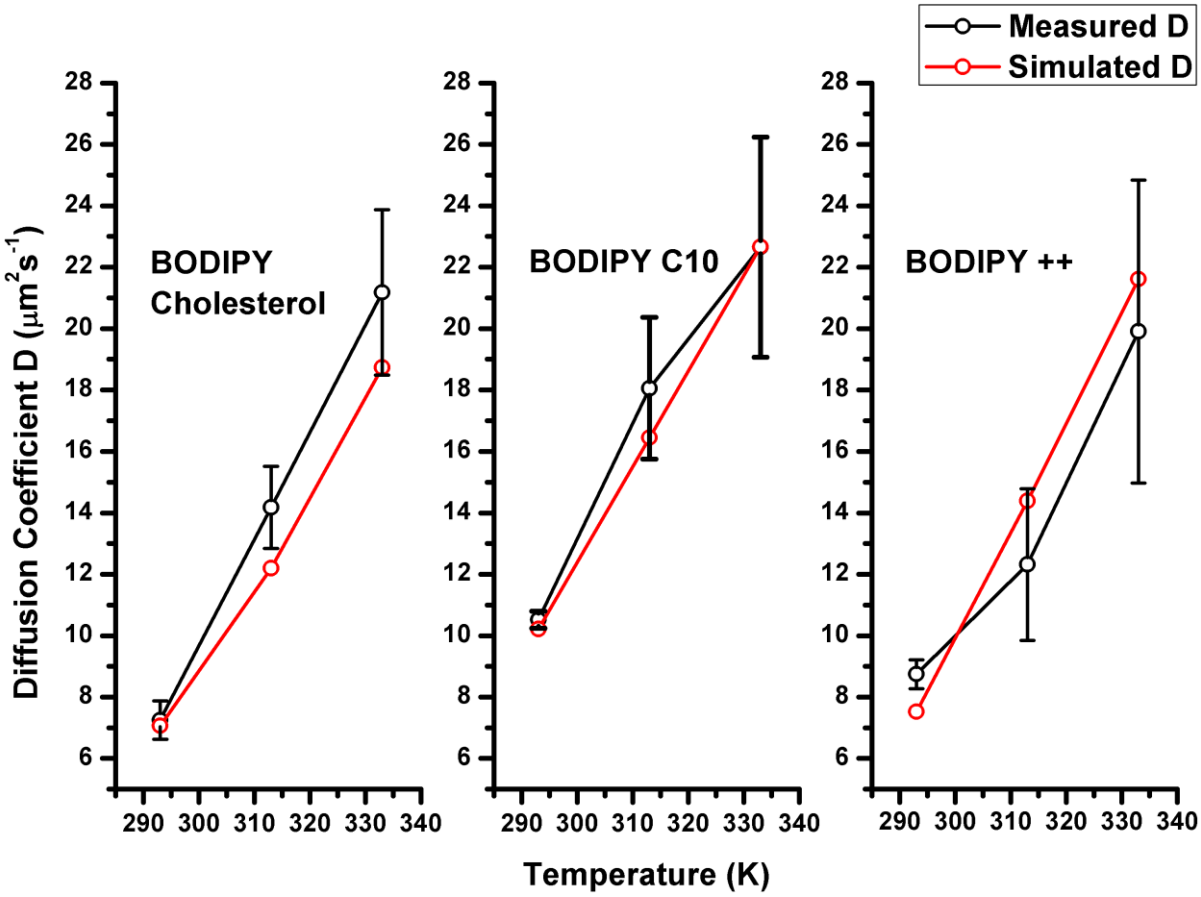

Figure 60: Comparison of D measured by FCS and Molecular Dynamic Simulations (MDS) for all three BODIPY rotors in bilayers of pure DOPC. Error bars represent the standard deviation between 5 individual GUVs each measured ten times.

Figure 60 displays the direct comparison for D measured by FCS and MDS displaying a good agreement between the measured data and simulated data for all three rotors. The measured values are typically within 1 $\mu m^2 s^{-1}$ of the simulated values with a particularly good agreement at lower temperatures, T = 293 K. This provides a strong argument that the values for D measured by single point FCS on a free standing bilayer are reliable.

4.3.3. The Saffman-Delbrück model

To provide a comparison between values of viscosity from the measured fluorescence lifetime of the molecular rotors to the diffusion coefficients from FCS the Saffman-Delbrück model was used. The model was originally outlined in [165] where the Brownian motion of molecules embedded in a viscous membrane environment was linked to the surrounding fluid medium. Originally developed

to describe protein mobility in membranes, the model relates the viscosity of the membrane to its height, and the viscosity of the surrounding bulk fluid. A simplified depiction of a molecule, which could be a protein or lipid, diffusing laterally within a membrane can be seen in Figure 61.

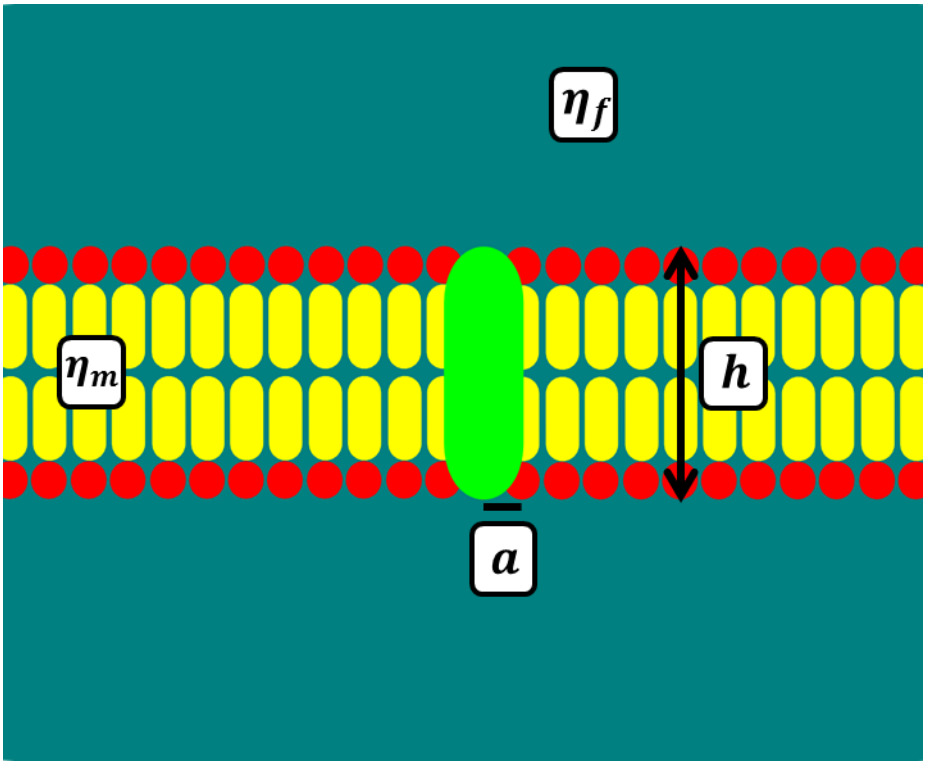

Figure 61: Schematic of a simplified lipid bilayer, viscosity η_m and a height h, with a laterally diffusing molecule of radius, a, surrounded by a bulk fluid with viscosity, η_f.

$$D_{sd} = \frac{k_B T}{4\pi\eta_m h}\left[ln\left({}^{2L_{sd}}/_{a}\right) - \gamma\right] \tag{4.5}$$

$$L_{sd} = \frac{h\eta_m}{2\eta_f} \tag{4.6}$$

Equation (4.5) presents the Saffman-Delbrück model in terms of the membranes viscosity, η_m, the membrane's height, h, the viscosity of the surrounding fluid, η_f, and the radius of the diffusing molecule, a. γ is the Euler-Mascheroni

constant. L_{sd} is the characteristic Saffman-Delbrück length with typical values ranging between 0.1 – 1 μm. the model holds true under the conditions where $a \ll L_{sd}$ which is appropriate for molecules such as proteins and lipids, however, for large lipid domains an extension of the Saffman-Delbrück model is required [166].

4.3.4. Determining membrane height

For accurate conversion of membrane viscosity to diffusion coefficient, knowledge of the height of the membrane was required. This was determined using Atomic Force Microscopy (AFM) spectroscopy which has been shown to be able to measure the height of lipid bilayers on a surface [167]. Fluorescent GUVs were burst onto a coverslip to provide identifiable single bilayers on the glass surface. These were located through widefield fluorescence microscopy before being measured by AFM. The general principle of measuring the thickness of a bilayer through atomic force spectroscopy is outlined in Figure 62.

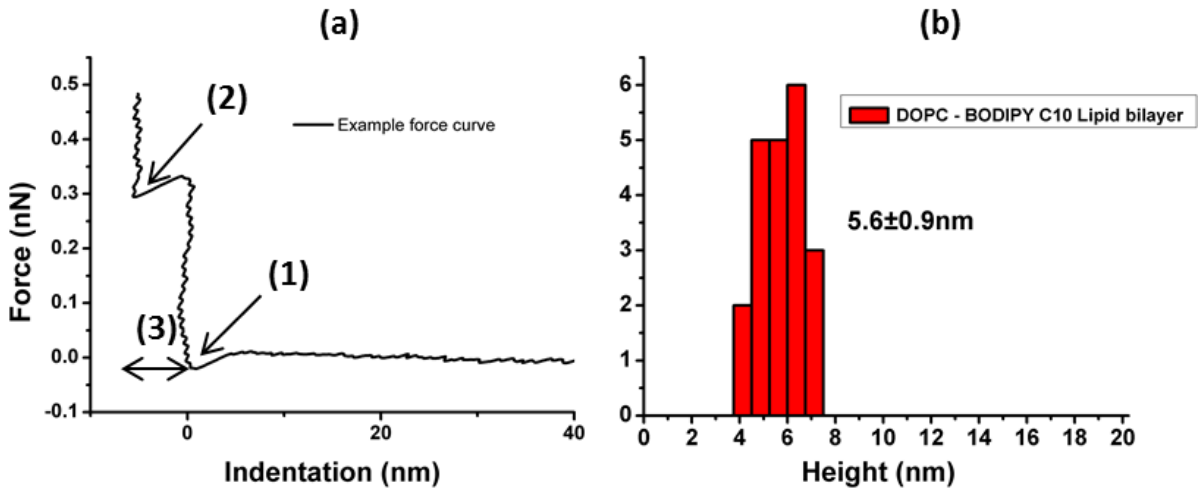

Figure 62: (a) – Example force curve as measured through AFM spectroscopy. (1) – point of contact with top of lipid membrane that is deposited on to a glass surface. (2) point of contact with substrate. (3) the difference in nm between the top and bottom regions of the membrane. (b) – distribution of values for the height of a DOPC membrane containing BODIPY C10. N = 21. Error represents SD.

AFM spectroscopy measures the nN forces experienced by a cantilever tip as it comes into contact with a sample, in this case a DOPC lipid bilayer on a glass

substrate. DOPC GUVs were allowed to burst on to a glass surface to form individual bilayers. At the point of contact with the bilayer a sharp rise in force was experienced as the tip was pushed through the membrane. After a short distance a second significant rise in force resulting from contact with the substrate below, was observed. The resultant distance is equivalent to the height of the lipid bilayer. For the fluid phase single component DOPC bilayer an average height of 5.6 ± 0.9 nm was measured. This is in accordance with previously reported values [168], [169]. The narrow distribution of measured values suggests that the created bilayers are unilamellar where multi-lamellar membranes would present themselves as integer value multiples of the unilamellar system. To confirm this, confocal microscopy was used to investigate the lamellarity of the electroformed vesicles. Positioning the focus to the equatorial region of GUVs resting on a glass surface, a thin optical section was imaged. Plotting a line through the centre of the images vesicle provided the peak intensities at both the north and south sides. This method has previously been shown to definitively group together bands of intensity values against the degree of lamellarity of the bilayer [170]. Plotting the intensity measured at the mid region of the vesicle against diameter revealed striking groups corresponding to 1-4 bilayers.

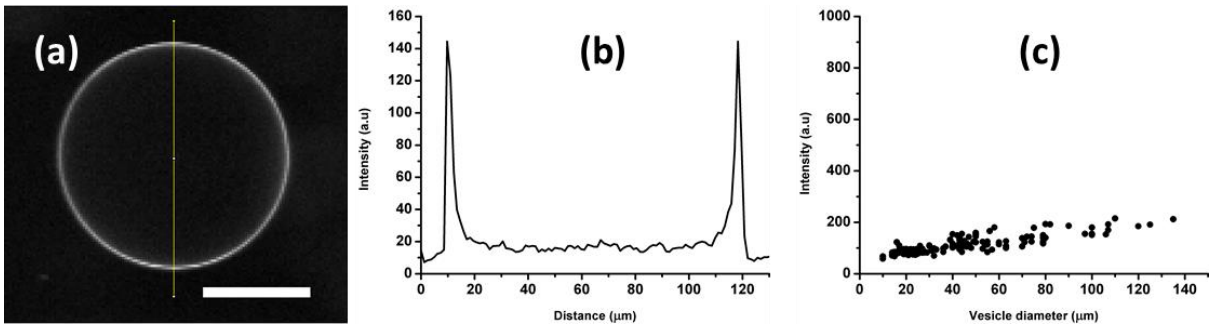

Figure 63: (a) confocal image of DOPC GUV at the equatorial region. Scale bar 50 μm. (b) plot along middle region of GUV displaying peak intensity values at the north and south points of the vesicle. (c) distribution of peak intensity values against diameter of vesicles measured.

Figure 63 (a) illustrates an example of a pure DOPC bilayer imaged by confocal microscopy. The intensity along a line plotted through the centre of the vesicle provides the corresponding plot in (b). The intensity values for 160 vesicles of

varying sizes were plotted against their diameters in (c). It can be seen from the plot in (c) that one distinct grouping of values is present, indicating that all the measured vesicles are unilamellar in nature. This confirms the previously obtained values through AFM spectroscopy.

4.3.5. Fluorescence lifetime measurements of BODIPY in DOPC bilayers – GUVs and LUVs

The fluorescent lifetime of the molecular rotor BODIPY C10 was measured in a lipid bilayer consisting of pure DOPC over a range of temperatures. It was first investigated through FLIM set to an imaging modality to investigate the rotor's lifetime response to increasing temperature.

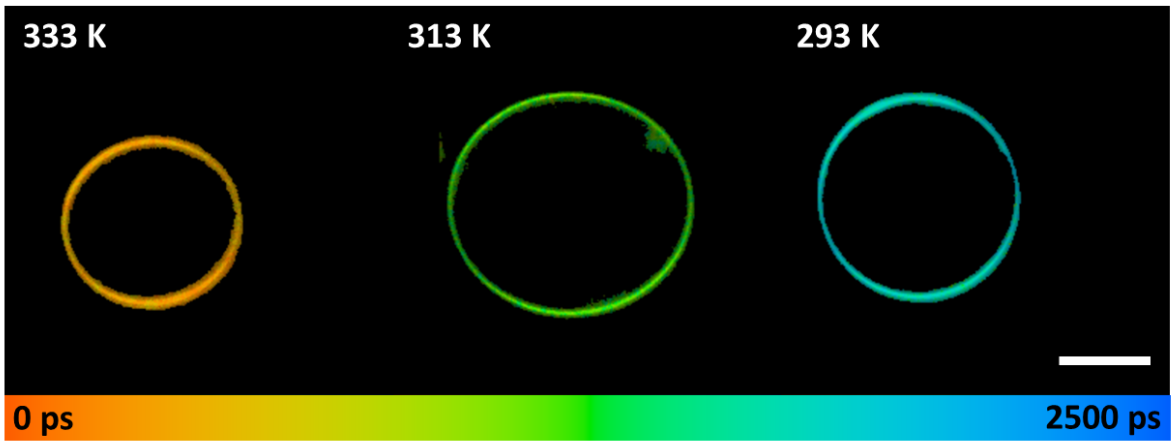

Figure 64: FLIM images of 3 different DOPC GUVs of varying size containing BODIPY C10 at a lipid dye ratio of 1000:1 imaged over a range of temperatures. Lifetime represented is the first component τ_1 for a bi-exponential decay function. Lifetime values found: 293 K – 1753.07 ± 20.05 ps, 313 K – 1059.36 ± 13.52, 333 K – 652.61 ± 11.35. Chi squared values of 1 – 1.3 for all images. Scale bar 20 µm.

It was found that when imaged over a range of temperatures the lifetime images for BODIPY C10 in DOPC were best fit to a bi-exponential decay. This is in contradiction to the widely reported mono-exponential decays in fluid phase bilayers for BODIPY based molecular rotors [58], [148], [164]. Figure 64 represents the first component of exponential decay, τ_1, which contributed to 80% of the fluorescence decay signal for each set of images. The values found for the first component were similar to those previously reported for a BODIPY rotor incorporated into a bilayer of DOPC, indicating this to be the viscosity sensitive

component of decay. This value was later corroborated when investigating the lifetime of the rotor in LUVs of pure DOPC. It was found that the decay profile was best fit with a mono-exponential decay when the rotor was incorporated into LUVs composed of pure DOPC.

DOPC-BODIPY C10 Vesicle Type	Temperature (K)	τ_1 (ps)	a_1 (%)	τ_2 (ps)	a_2 (%)
GUV	293	1753.07	79.95	2769.53	20.05
LUV	293	1725.84	N/A	N/A	N/A
GUV	313	1059.36	82.15	2856.31	17.85
LUV	313	1005.49	N/A	N/A	N/A
GUV	333	652.61	80.91	2827.51	19.09
LUV	333	589.18	N/A	N/A	N/A

Table 5: measured lifetime values of BODIPY C10 in DOPC bilayers in LUV and GUV formats. τ_1 and τ_2 represent the two exponential lifetime components found from a bi-exponential fit with the relative contributions of each denoted as a_1 and a_2 respectively. As the LUV data was fit to a mono-exponential only one lifetime value was present.

Table 5 demonstrates the measured lifetimes for the BODIPY C10 rotor in bilayers of pure DOPC in both LUV and GUV configurations. It can be seen that of the two components measured for the GUVs only τ_1 is altered as a result of increasing temperature. In addition the relative contributions of both components, a_1 and a_2, remains unperturbed indicating two populations of fluorophore that remain constant over the range of viscosities measured. The decrease in τ_1 over the measured temperature range is almost identical for both GUVs and LUVs suggesting that this value represents the viscosity sensitive component in the measured GUVs. BODIPY based molecular rotors of this type have been shown to have a dynamic viscosity sensitivity without any major temperature dependence suggesting that the measured lifetime change observed is due to the decrease in viscosity [171]. The source of the second decay component may originate from rotor aggregates which may form during the

electroformation process which have previously been shown to provide multiple-component exponential decays. The same behaviour was observed when analysing the decay profiles provided by the single point FCS-Lifetime combined measurements.

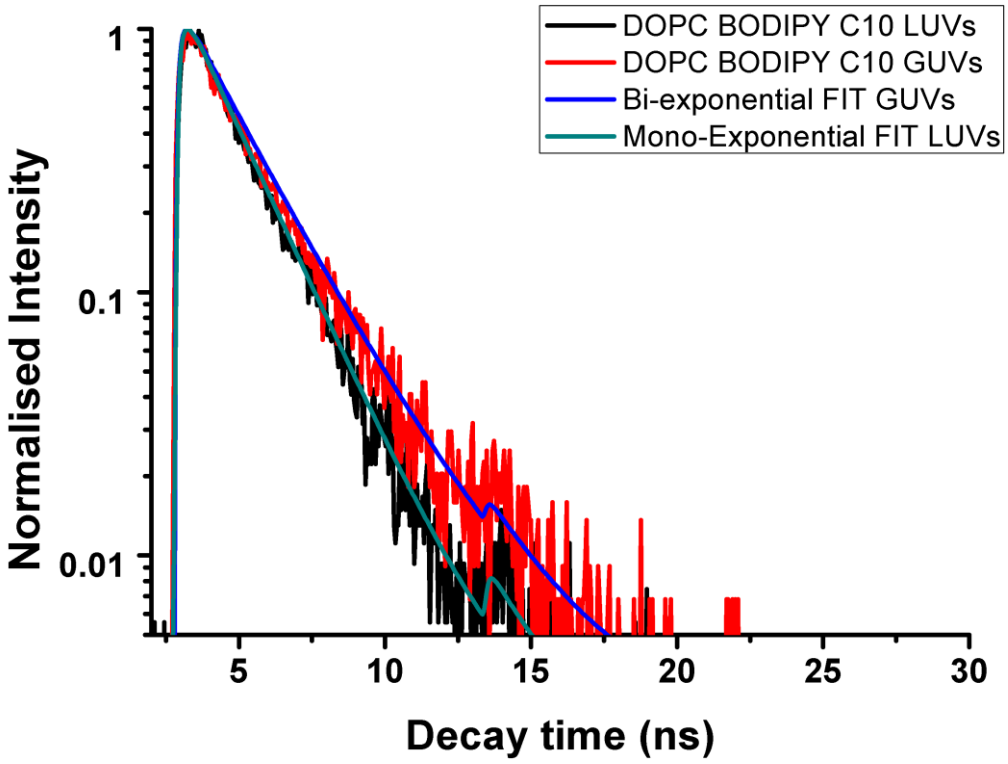

Figure 65: Normalised decay data for BODIPY C10 in a DOPC bilayer in both GUVs and LUVs taken at 293 K. The data for the DOPC LUVs fits well to a mono-exponential decay, however, the data for the DOPC GUVs fits better to a bi-exponential decay function.

Figure 65 demonstrates the differences between the measured decay profiles for the BODIPY rotor in DOPC GUVs and LUVs. It can clearly be seen that for the GUVs the data is suitably fit to a bi-exponential decay function but when in LUV form the data represents a mono-exponential decay. For this reason the values taken for the comparative viscosity measurements were from the first, and dominant, decay component, τ_1, for the combined FCS-Lifetime measurements.

4.3.6. Comparison of diffusion coefficients obtained by FCS-Lifetime combined measurements

Combined FCS-Lifetime measurements were performed on GUVs composed of purely DOPC with 0.05 mol % of each of the three BODIPY rotors. The diffusion

coefficients from the FCS measurements were compared to those obtained through conversion of the lifetime inferred viscosity via the Saffman-Delbrück model. Each value of D was taken as the average of 10 single measurements from 4 different GUVs.

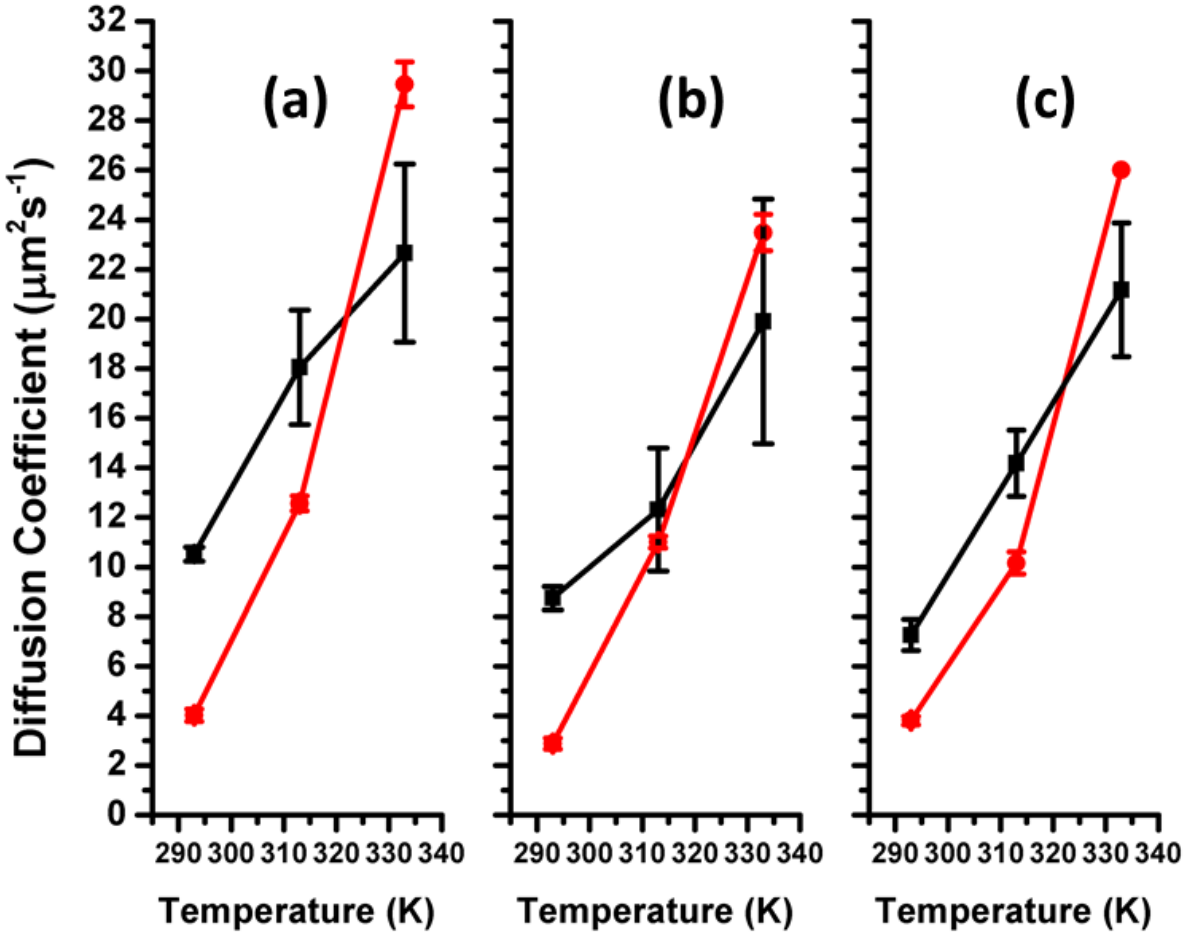

Figure 66: Comparison of diffusion coefficients measured by FCS (black data) and lifetime (red data) for the three BODIPY rotors: (a) – C10 (b) - ++ (c) – Cholesterol for temperatures of 293, 313 and 333 K

The diffusion coefficients measured by FCS were outlined earlier demonstrating a good agreement with molecular dynamics simulations. The diffusion coefficients calculated from the lifetime values using the Saffman-Delbrück model were of a similar order of magnitude compare with the FCS measured values. It can be seen from Figure 66 that the lifetime calculated diffusion coefficients were roughly 2 times lower for the lowest measured temperature, 293 K. As temperature increased a significant rise in D calculated from the lifetime values was observed with a closer agreement observed for 313 and 333 K. The standard deviation found for the lifetime values was significantly lower

than that of the FCS measurements. Since the measured lifetime is independent of fluorophore concentration, the position of the focal volume relative to the bilayer is inconsequential for lifetime based measurements resulting in more consistent results.

Fundamentally the two complementary methods are measuring a response to two different properties of the bilayer: the lateral mobility of lipids through FCS and the properties of the solvent with lifetime analysis. The diffusion coefficient measured by FCS is a direct measure of a physical value and can be directly related to the viscosity of the membrane via the Saffman-Delbrück model. The lifetime response of the rotor is slightly more complex and various properties of the solvent environment, i.e. the bilayer, must be considered. Firstly the temperature of the environment in which a fluorophore resides may have an effect on the photophysical properties such as the quantum yield and lifetime [27]. For a molecular rotor the environmental sensitivity is determined through a balance of emissive, bright, and non-emissive, dark, states. Typically the access to the dark non-emissive states for molecular rotors is suggested to be determined by molecular rotation. However, for some molecules the temperature of the environment itself may disrupt this balance [171]. For the BODIPY based molecular rotors this was found not to be the case and this can be seen through the calibration curve outline in Figure 58. The solvent viscosity was altered by increasing concentrations of glycerol and then measuring the lifetime over a range of temperatures. The overlap between different glycerol concentrations and different temperatures would suggest that the temperature has little or no effect on the relative balance of bright and dark excited states. Another component of the environment which may have a significant effect on the fluorescent lifetime is the polarity of the solvent. In a lipid bilayer this would change between residence of the probe nearer the hydrophilic head or hydrophobic tail regions. Dent et al. [164] investigated the localisation of the three molecular rotor probes through molecular dynamics simulations. It was outlined that for the three variants of BODIPY in a DOPC bilayer the orientation of the BODIPY head group was similar, locating itself towards the interface of the head and tail regions of the phospholipids. In the same study it was noted that at high viscosities the lifetime of the rotors were unaffected by solvent polarity, demonstrated through measuring the lifetime in castor oil. Castor oil

has similar viscosities to the methanol-glycerol calibration mixtures over a range of temperatures but differs in polarity. It should be noted, however, that at low viscosities a polarity dependency was observed but over a range of viscosities out with those found in most measured bilayers. With these considerations it is reasonable to assume that the measured fluorescent lifetime of the BODIPY rotor in artificial bilayers changes as the viscosity of the environment changes.

While the diffusion coefficients determined by both methods are similar in terms of magnitude, there are some discrepancies. The discrepancies between the diffusion coefficients measured by FCS and those calculated from the fluorescence lifetime values may arise due to a number of assumptions made through the Saffman-Delbrück model. The model assumes a cylindrical shaped membrane inclusion with a particular radius, a [165]. The radius used for the three molecular rotors were the hydrodynamic radii for each of the molecules which may not accurately represent the true shape and size of the rotors in the bilayer. Added to this the variability in reported heights for DOPC bilayers as well as the inherent inaccuracies for each method of measurement, the values reported here represent a reasonable agreement.

4.3.7. Effect of bilayer composition on membrane viscosity measured by FCS-lifetime

The composition of lipid membranes can affect the viscosity of the fluid bilayer [172]. GUVs are incredibly useful tools in investigating the physical nature of the plasma membrane by deconstructing it to its principle components, such as phospholipids and cholesterol. Phospholipids of differing degrees of saturation provide environments with varying degrees of viscosity. To investigate the efficacy of the combined FCS-lifetime technique in verifying viscosity values, three different phospholipids were investigated: DOPC, POPC and DPPC. Both DOPC and POPC at room temperature are in the fluid phase, however, POPC only contains one un-saturated double bond in one of its hydrocarbon tails. DPPC is a fully saturated phospholipid, containing no double bonds in its hydrocarbon tails. As a result, DPPC exists in the gel phase at room temperature, thus providing a significantly more viscous environment. The diffusion coefficients for the rotor

BODIPY C10 was measured at 20°C in GUVs containing purely DOPC, POPC or DPPC.

GUV lipid type	FCS Diffusion Coefficient ($\mu m^2 s^{-1}$)	Lifetime Diffusion Coefficient ($\mu m^2 s^{-1}$)
DOPC	10.52±0.28	4.02±0.25
POPC	8.12±0.84	3.34±0.51
DPPC	1.09±0.15	0.84±0.09

Table 6: Comparison of diffusion coefficients measured by FCS and calculated from fluorescence lifetime for GUVs composed of pure DOPC, POPC or DPPC. Each value represents the average of 10 measurements made on 4 different GUVs. Acquisition time for each individual measurement was set to 10 s to minimise photobleaching. Errors represent the standard deviation between the 4 measured GUVs.

Table 6 provides the FCS measured and lifetime calculated diffusion coefficients for BODIPY C10 in three different lipid types: DOPC, POPC and DPPC. It can be seen from the FCS measurements that the lateral diffusion of the probe is highest in the pure DOPC bilayer, reduced by 23% in the POPC bilayer and by 90% in DPPC. This would be expected as the degree of saturation is increased in POPC and further in DPPC resulting in a higher packing order in the lipid bilayer. The corresponding diffusion coefficients calculated from the measured lifetime values are lower compared to those measured by FCS but follow a similar downward trend from DOPC through to DPPC. It should be noted that for a BODIPY rotor in DPPC it has been shown that two orientations [164] of the molecule exist resulting in a bi-exponential decay. Of the two suggested orientations, one exists similar to that in a fluid phase bilayer with the head section of the molecule located at the interfacial region of the bilayer. This orientation is suggested to correspond to the second fluorescence decay component. For that reason the values presented here correspond to the viscosity values inferred by that second component.

4.4. Conclusions

Presented in this chapter is the optimisation and utilisation of a system capable of simultaneous FCS and fluorescence lifetime measurements to determine the

efficacy of molecular rotors as reporters of membrane viscosity. Diffusion coefficients of three different molecular rotors based on the molecule BODIPY were measured by both methods. A significant agreement between those measured by FCS and molecular dynamics simulations, presented elsewhere, was found indicating a good degree of experimental accuracy for single point FCS measurements. When compared with diffusion coefficients calculated from fluorescence lifetime measured viscosities, using the Saffman-Delbrück model, similar trends were found. However, it was discovered that the values varied by a factor of 2 compared to those measured by FCS, in some cases. This was potentially due to assumptions made using the Saffman-Delbrück method. It was also demonstrated that the molecular rotors were useful indicators of membrane order by measuring diffusion coefficients in three different lipid systems consisting of pure DOPC, POPC and DPPC. In a more saturated system, i.e. a lipid environment with no double bonds in the hydrocarbon tail regions, a measurable decrease in diffusion coefficient was measured. This was found both through direct measurement of lateral probe diffusion using FCS and through the calculated lifetime based diffusion coefficients. To the best of this author's knowledge this is the first simultaneous comparison of the lateral mobility of these molecular rotors to the viscosity values measured by their fluorescence lifetime. It stands to reason that in simplified bilayer systems, BODIPY based molecular rotors provide a reasonable means for quantifying the viscosity of the environment.

5. Chapter 5: A TIRF-FLIM System for imaging membrane viscosity

5.1. Introduction

5.1.1. Molecular rotors in live cells

The previous chapter demonstrated that molecular rotors may be used to report on viscosity values in synthesised lipid bilayers using a combined FCS-Lifetime system. Previous studies have reported on the use of BODIPY based molecular rotors in live cell systems reporting on viscosities in different cellular compartments. BODIPY C12 was previously used to image viscosity in SK-OV-3 cells determining the viscosity of two distinct regions [59], [173]. The first region of shorter lifetime was hypothesised to be internalised lipid droplets, represented by bright punctate, due to the hydrophobic nature of the probe. The second observed longer lifetime value was in an unknown cytoplasmic associated region. While the dyes used in this study were successful in illuminating the heterogeneous nature of intracellular viscosity, no information on the plasma membrane was offered. The reason for this could be found in the rapid internalisation of the dye from the plasma membrane to intracellular vesicles through some endocytotic pathway.

A modified version of the probe was presented in [154] containing a double positive charge located at the end of the hydrocarbon tail. The molecule, BODIPY ++, was based on the same motif as the previous variants, C10, C12 etc., but due to the positively charged tail region endocytosis was minimised. The result was a molecule that could, for a certain period of time, selectively stain the plasma membrane of cells. This was demonstrated in SK-OV-3 cells where a reasonable value for the average membrane viscosity of 270 cP was determined. The method of staining used with the charged rotor molecule was one previously used which required lowering the temperature of the cells to 4^{o}C. The dye was also added in magnesium and calcium free media to minimise endocytosis. This particular study found that, while there was a degree long term labelling of the

plasma membrane (> 50 minutes), after 30 minutes the dye was seen to internalise to other areas of the cell. Due to the charged tail region the rotor was partially water soluble and as a result the uptake to other cellular regions was not limited to hydrophobic lipid droplets. Over time a more diffuse background of fluorescence was observed.

Molecular rotors based on other fluorophores [148] have been explored for their use in measuring live cell viscosities. Haidekker et al. [174] used a modified DCVJ molecule, known as FCVJ, to investigate the effects of shear stress on membrane viscosity. The FCVJ molecule was relatively successful in staining the plasma membrane and displayed a dramatic intensity change upon exposure of the cells to high levels of shear stress. It should be noted, however, that in the reported study the determination of membrane staining was taken from stacked confocal images, and some doubt remains in how efficient the label is as a specific membrane target. It was observed that, as well as apparent membrane staining, significant labelling of the cytosol was also present. In addition, DCVJ based molecular rotors display significant changes in quantum yields, but their fluorescent lifetime responses aren't well characterised. As a result using these probes to quantify viscosity in a heterogeneous environment, such as the plasma membrane, would be difficult.

Peng et al. [175] presented a molecular rotor based on the short chain indocyanine dye structure cy3, called RY3. The RY3 dye was capable of dual mode fluorescence imaging through lifetime and ratiometric imaging. The molecule contained a meso-substitured CHO group resulting in low quantum yields, and fluorescent lifetime, in low-viscous media. The small molecule is water soluble, and as such not a suitable molecule for determining the viscosity of hydrophobic membrane regions. RY3 was successful in determining viscosities of cytoplasmic structures in living cells due to its high membrane permeability. The lifetime values measured for this particular dye lie within the 100's of ps to 1 ns time scales which are at the limit of some modern lifetime imaging systems. Cy3 molecules are, however, widely commercially available and extremely versatile in terms of conjugation to target molecules meaning they certainly should not be overlooked in terms of biological viscosity applications.

Ratiometric molecular rotors have also demonstrated promise in determining cellular viscosities [176–178]. Kuimova et al. [176] presented a porphyrin based dimer commonly used in Photodynamic Therapy (PDT) for cancer. The modified molecule remained functional as a PDT photosensitiser but was also an efficient fluorescent ratiometric molecular rotor. The dual-functional probe was used to investigate how the micro-viscosity of the cellular environment was altered during photoinduced cell death. The probe was successful in determining that viscosity did indeed increase through the process of cell death; however, what was reported was the overall viscosity of the internal cellular environment. The molecule itself has not been utilised in the study of the micro-environment of the plasma membrane. Some ratiometric rotors have been used to study artificial membranes and liposomes [177] but have yet to be applied to cellular membrane applications

It can be seen that the availability of specific membrane labels for complex heterogeneous samples is limited. Other than the modified rotor BODIPY ++, no molecules have demonstrated successful affinity for the plasma membrane. In the case of the charged BODIPY rotor limitations still exist in the time frame over which the probe remains located to the membrane. As the signal becomes more wide spread within the cell the contributions from the plasma membrane would reduce, limiting its long term viability as a membrane probe. It may be possible to improve upon the signal to noise ratio (SNR) of membrane signal against the diffuse cellular background through alternative imaging modalities.

5.1.2. Resolution enhancement for fluorescence microscopy

With molecular rotors presenting promising tools for determining membrane viscosity, limitations still exist in terms of specific labelling strategies. It stands to reason that optical techniques provide a supplementary method in the development of fluorescence techniques for exploring the physical nature of the thin 2D-fluid region of the plasma membrane. By restricting the illuminated region to the order of the size of a single bilayer, improvements can be made to the Signal-to-noise ratio (SNR) of detected fluorescence. Combining improved axial resolution with the functional imaging capabilities of FLIM may dramatically improve the use of BODIPY based molecular rotors in live cell

membrane studies. Common FLIM approaches involve either epi-fluorescence or confocal imaging systems. With epi-fluorescence discrimination between signals originating in different planes is unavailable. Confocal imaging is limited by the diffraction barrier in terms of both lateral and axial resolution resulting in dimensions significantly larger than that of the plasma membrane in the z-direction.

The fundamental limits imposed upon optical microscopy due to the diffraction limit have motivated researchers to find novel ways to exploit fluorescent phenomena to circumvent this barrier. Super-resolution optical techniques have developed over the last decade offering various levels of resolution, both laterally and axially, through the use of light manipulation or novel fluorescent probes. Discussed below are various modern optical imaging techniques which seek to view beyond this fundamental limitation.

5.1.2.1. Photo activated localisation microscopy

Photo activated localisation microscopy (PALM), developed by Betzig et al. [179], operates through the use of photo-activated fluorophores where a small subset of fluorescent molecules are activated using a low wavelength, high energy, light. The near UV activation energy ‘turns on’ only a small number of fluorescent molecules in a sample which can then be excited to higher energy states using a lower energy light source. This process is repeated until all the molecules have been imaged and the locations for each molecule are reconstructed to provide super-resolution images. The lateral resolution is only limited by the reliability in locating the central point of each imaged molecule offering a xy resolution down to 30 nm [180], much lower than conventional optics. The technique also has the ability to restrict the z-resolution to 100-200 nm when coupled with other techniques, such as TIRFM. These values are ideal for imaging cell membranes but the technique is severely limited in terms of fluorophore availability [181] and length of image acquisition. In the context of improving the resolution of FLIM measurements for membrane based studies PALM would not be a suitable choice in the context of molecular rotors.

5.1.2.2. Stimulated emission depletion microscopy

Stimulated Emission Depletion (STED) [182] microscopy emerged at a similar time to PALM as a super-resolution fluorescence based imaging modality. STED offers improved resolution in both the xy plane through manipulation of the Point Spread Function (PSF). This is achieved by overlapping two illuminating laser beams with the first exciting a diffraction limited region of fluorescence. A second laser, of longer wavelength, is overlaid to the original laser with a 'donut' shape returning fluorescent molecules within this region back to the ground state. The result is a lateral resolution of around 60 nm creating a PSF below the diffraction limit which is scanned across the focal plane of the image similar, as in a confocal microscope. While the xy-resolution is greatly improved, in the axial direction the dimension of the PSF are comparable to a confocal microscope, offering limited improvements to the SNR in imaging of a fluorescently tagged membrane.

5.1.2.3. 4 Pi Microscopy

A novel illumination scheme providing enhanced axial resolution was presented in 1994 [183] with 4Pi microscopy. 4Pi microscopy utilises two opposing identical objective lenses focussed to the same plane in the sample. Illumination light is split between the two lenses, with identical path lengths, coherently illuminating molecules in the overlapping focal region. The result is a PSF with a resolution of roughly 100-150 nm along the z-axis [184]. The technique is an alternative laser scanning technique compatible with the diverse set of available fluorophores. The principle limitation to such a technique is the increased complexity in system construction due to the necessity of two opposing objective lenses.

5.1.2.4. Structured Illumination Microscopy

Structured illumination Microscopy (SIM), in particular 3D-SIM, is a versatile super-resolution technique, improving both lateral and axial resolution. In SIM a sample is illuminated with a series of, high spatial frequency, sinusoidal patterns by passing light through an optical grating. The sinusoidal pattern interferes with

fine structures, below the diffraction limit, in the sample creating coarse moiré fringes. This process is repeated at various orientations of the overlaid illumination pattern and the subsequent images are reconstructed providing information beyond the diffraction limit. The resolution achievable through SIM does not extend to that of higher resolution imaging modes, such as STED or PALM, providing around 100-350 nm of xy-resolution, however, enhanced axial resolution is readily achievable down to as low as 100 nm. This is accomplished by introducing an additional light modulation in the z-axis through three beam interference. While the technique excels in terms of resolution and is also compatible with practically all modern fluorescent dyes, the technique requires significant image accumulation and post processing, resulting in lengthy acquisition times.

Perhaps more suited to the application of cellular membrane imaging are near-field based optical imaging techniques where illumination is localised to the interface between substrate and sample.

5.1.2.5. Scanning Near Field Optical Microscopy

Scanning Near Field Optical Microscopy (SNOM) was developed in the 1986 by Pohl et al. [185] as an imaging technique breaking the resolution barrier through exploitation of the properties of evanescent waves. Unlike most conventional optical approaches SNOM does not utilise objective lenses, instead a very small physical aperture at the tip of a conically tapered fibre provides a restricted PSF. The achievable resolution can be as low as 20 nm in the xy-plane and around 100 nm along the z-axis. SNOM falls under the class of scanning probe microscopy techniques providing super-resolution information on the surface characteristics of numerous materials, or biological tissues. However, the application of all scanning probe techniques provides unique challenges to live cell investigations and as such is not suited to investigating the nature of living cell membranes.

5.1.2.6. Total Internal Reflection Fluorescence Microscopy

The most common near-field imaging technique remains TIRFM with its simple experimental implementation making it a highly attractive technique for probing the membrane environment. The fundamental theory of the technique outlining that TIRFM can be implemented in either a prism of objective based configuration was outlined in chapter 2. With objective based TIRFM, high NA lenses are used to focus the light to the sample above the critical angle necessary for TIR. Detecting the resultant fluorescence through such lenses provides a lateral resolution that is still limited by diffraction; however, the exponentially decaying nature of the illuminating evanescent field provides a diffraction breaking 100 nm axial resolution. The improved z-resolution, coupled with the simple nature of the optical system, results in an attractive optical method for improving the resolution of FLIM for membrane applications. The relative resolution capabilities of all the discussed methods are presented in Figure 67 with respect to imaging of a lipid bilayer.

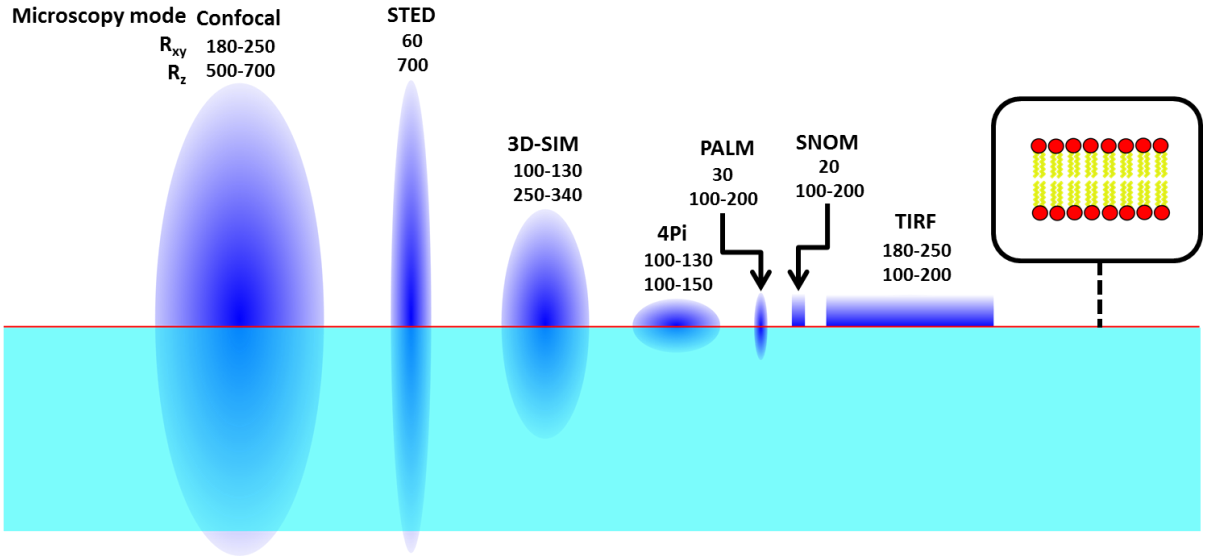

Figure 67: Comparison of PSFs for various optical microscopy methods for diffraction and sub-diffraction limited imaging. All representative PSFs are to scale with the red line representing a lipid bilayer on the surface of a microscope slide. All values are in nm representing the lateral and axial radii for each PSF.

Figure 67 demonstrates, to scale, the relative resolutions for the discussed optical microscopy methods. It is clear that, with respect to the size of a single lipid bilayer, many of the techniques are significantly larger. For fluorescence microscopy of living cells the result would be signal originating from both the membrane and a large amount of intracellularly located molecules. Methods such as 4Pi, PALM, SNOM and TIRF begin to approach an order of magnitude in axial resolution comparable to the dimensions of the imaged membrane resulting in an increase in the SNR of membrane localised fluorophores. The added benefit of the near field techniques, SNOM and TIRF, for membrane studies is the intrinsic location of the excitation region defined by the illuminating light.

The following chapter outlines the construction of a combined TIRF-FLIM system for the application of imaging membrane viscosity using molecular rotors. This was demonstrated through the use of artificial individual bilayers created through the process of vesicle adsorption and bursting on a glass substrate. The Supported Lipid Bilayers (SLBs) incorporated the molecular rotor based on the fluorophore BODIPY.

5.2. Materials and Methods

5.2.1. Fluorophores

Stock solutions of 1 mM of the fluorophores FITC (Sigma), Rhodamine B (Sigma) and Erythrosin B (Sigma) were dissolved in Millipore water for lifetime calibration measurements. Stock solutions were stored for no more than one week and for each calibration measurement performed a new dilute solution of 1 – 5 μM was prepared from stock.

BODIPY C10 was used in all membrane studies at ratios of 0.05 mol%, for spectroscopic measurements, and 0.5 mol% for imaging.

5.2.2. SLB formation

Lipids used for supported lipid bilayer (SLB) formation, DOPC and DPPC, were all purchased from Avanti Polar Lipids and stored at a stock concentration of 25 mg/ml in chloroform.

GUVs were formed by the electroformation method outlined in chapter 4 and were used to form SLBs. SLBs were formed through the bursting of electroformed GUVs on glass substrates. For each experiment all glass substrates were treated identically through sonication in acetone, IPA and methanol at 10 minutes in each solvent. The vesicles were deposited to the substrate surface at a low concentration, as not to cause bilayer overlap, resulting in defined spots of single, unilamellar, fluorescent bilayers.

5.2.3. TIRF-FLIM system

5.2.3.1. TIRF Illumination

TIR alignment was provided as outlined in Chapter 3 using the TILL photonics TIRF condenser coupled to a Zeiss Alpha-plan Fluor 100x 1.45 NA objective lens. The penetration depth used for all imaging was 110 nm by adjusting the micrometre screw gauge to the appropriate position.

5.2.3.2. Pulsed laser diodes

To enable simultaneous TIRF-FLIM imaging pulsed laser diodes were used, purchased from Horiba. The wavelengths available for imaging were: 420 nm, 481 nm and 650 nm; for imaging of BODIPY fluorescent bilayers the 481 nm laser line was utilised. The laser diodes were controlled by the DeltaDiode C1-controller, able to set the repetition rate of the laser between 10 kHz and 100 MHz. For the 481 nm laser line the peak power output for each pulse was 100 mW with an average power of 3 mW. The laser was coupled to a multi-mode fibre with, NA = 0.22, terminated at both ends via a FC connector via a small collimating lens. The power output from the end of the fibre to the TIRF condenser was optimised to 1.7 mW, at a repetition rate of 100 MHz, by careful adjustment of the collimating lens relative to the output of the laser. The

average pulse duration for the 481 nm laser was roughly 100 ps, suitable for high repetition FLIM applications. The C1-control unit provided a triggering signal output of 2 V via a BNC connection terminated by a 50 Ω load for synchronisation to a high rate imaging system.

5.2.3.3. Image intensified CCD

A gated image intensified CCD (LaVision Picostar HR 12) was used to enable combined TIRF-FLIM through gated lifetime imaging. The S25 cathode type was selected providing good quantum efficiency, >40%, for the wavelengths between 450 and 650 nm. The ICCD was capable of exposure times as low as 300 ps for fast imaging applications. For all acquired image sets exposure times between 100 – 1000 ms were used depending on the required signal. The image intensifier was triggered from the 2 V output signal from the pulsed laser diodes. This was achieved via the High Rate Imaging (HRI) triggered delay unit capable of triggering the ICCD from 20 MHz up to 100 MHz. For applications where longer lifetimes are to be analysed, i.e > 20 ns, the camera could be triggered via the P400 (Highland Technology) benchtop delay and pulse generator unit. The P400 was able to trigger the gated ICCD from Hz – 10 MHz. Both the camera and delay units were controlled remotely, via RS-232 connection, by the DaVIS acquisition software (LaVision). Values of gate width, gain, exposure time, timing and pixel binning were control via the software. For the imaging of SLBs gate widths of either 500 or 1000 were used to minimise the effects of photobleaching between sequential images. For measurements of calibration and the instrument response function (IRF) gate widths of 200, 500 and 1000 were used where appropriate. An simplified schematic of the optical and electronic system can be seen in Figure 68.

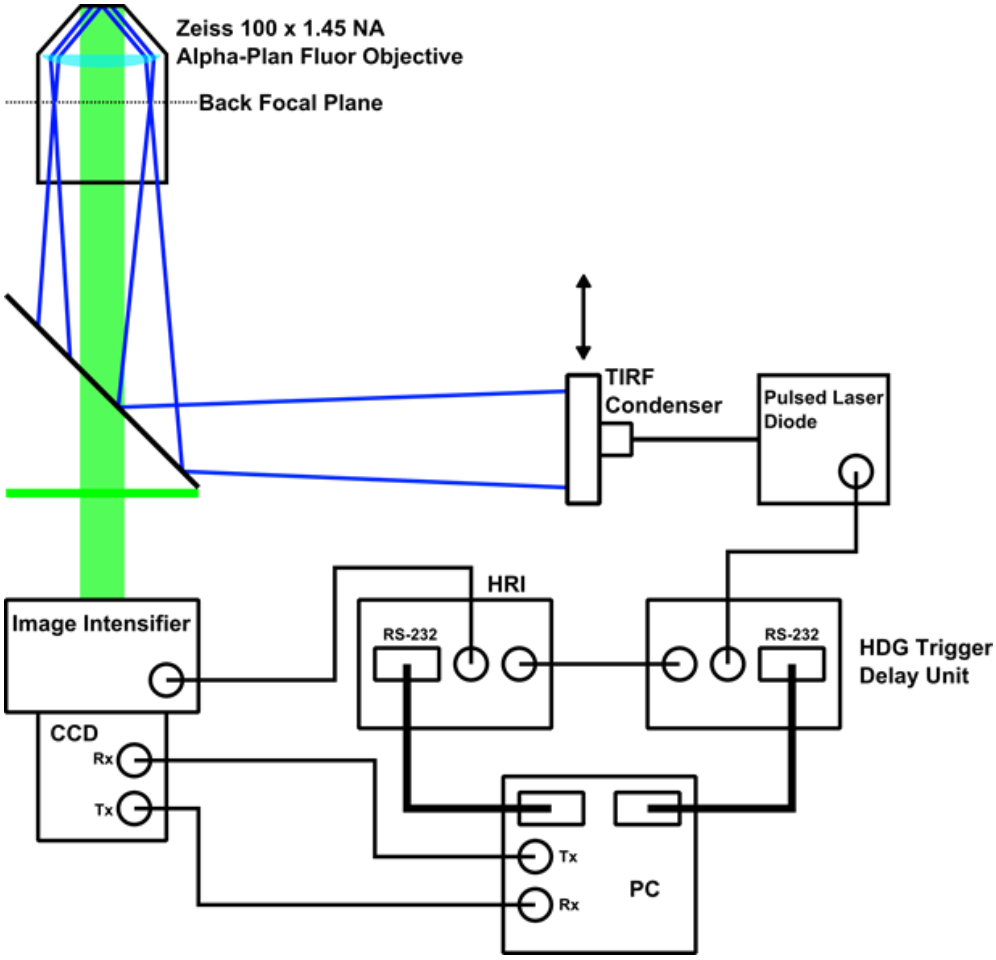

Figure 68: Schematic of TIRF-FLIM system. Illumination from a pulsed laser diode source is coupled to a 100 x 1.45 NA objective lens via a specialised TIRF condenser. Fluorescence is directed through an emission filter to an ICCD. The ICCD and pulsed laser diode are synchronised via the HRI unit. All circular connections are via BNC and the rectangular connections represent RS-232.

5.2.3.4. Data handling

All data was processed through the FLIMfit software package, an OMERO client, which is part of the Open Microscopy Environment (OME). FLIMfit, developed at Imperial College London [186], globally fits large datasets recorded from fluorescence lifetime systems from either TCSPC or gated FLIM methods. The analysis software offers the ability to fit mono and multi-exponential decay functions to the raw recorded lifetime data sets. The functions are fitted using a nonlinear least square fitting algorithm with a goodness of fit determined by minimising the reduced chi-squared value. The software also has the ability to account for the IRF profile recorded from a fluorophore with a known single

component of exponential fluorescence decay. For all measured decays the goodness fitting was deemed sufficient as indicated by a χ^2 value falling between 1 and 2 over all pixels. Mono and bi-exponential decays were fit where appropriate.

5.3. Results

5.3.1. Determining TIRF-FLIM system IRF using Erythrosin B

In order to determine reliable, and quantifiable, lifetime data it was imperative that the IRF was known for the TIRF-FLIM system. This was achieved through the imaging of a sample containing 10 μM Erythrosin B dye in a water solution. Erythrosin B is a fluorophore of known lifetime which is both short, 89 ps, and mono-exponential [162]. Such a short lifetime offers a means of directly measuring the IRF through analysis of the fluorophore's decay profile. Profiling the IRF in this way offers the benefit of truly representing the IRF of the system as all electronic and optical components are maintained in further lifetime measurements. This method has previously been employed with other systems including the use of the FLIMfit software [186]. Figure 69 demonstrates the IRF measured at two different gate widths of 200 and 1000 ps over a decay window of 21000 ps. Each gated image was exposed for 500 ms to accumulate a significant signal for the time period. No pixel binning was used in the accumulation of the IRF images.

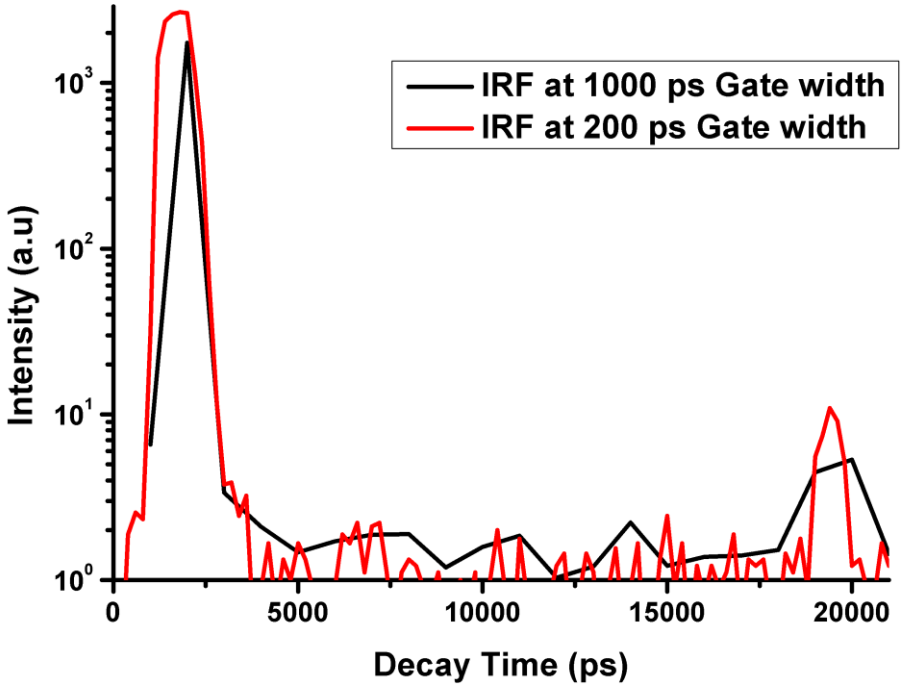

Figure 69: IRFs measured from 10 μM sample of Erythrosin B in water. IRFs measured with gate widths of 200 and 1000 ps over a decay window of 21000 ps.

It can be seen from Figure 69 that the shape of the IRF is dependent on the gate width of the imaging system. The gate width defines the temporal resolution of the FLIM images, analogous to the ADC resolution of a TCSPC system. With some imaging applications it was not possible to operate at a high temporal resolution, < 500 – 1000 ps, due to photobleaching found in subsequent gated images. A trade off was necessary between exposure time, ICCD gain, pixel binning and gate width to obtain images with suitable temporal and spatial resolution with a suitable SNR, i.e a peak intensity of >500 counts in the maximum image. Using the measured IRF provided an improved fit, as indicated by the reduced χ^2 value, compared with that of software generated IRFs for the same data. This can be seen from Figure 70 which demonstrates an example decay profile measured from 5 μM FITC in water excited at 481 nm. The decay is fitted with a mono-exponential decay model using an artificially generated IRF in the form of a delta function, provided by the FLIMfit software.

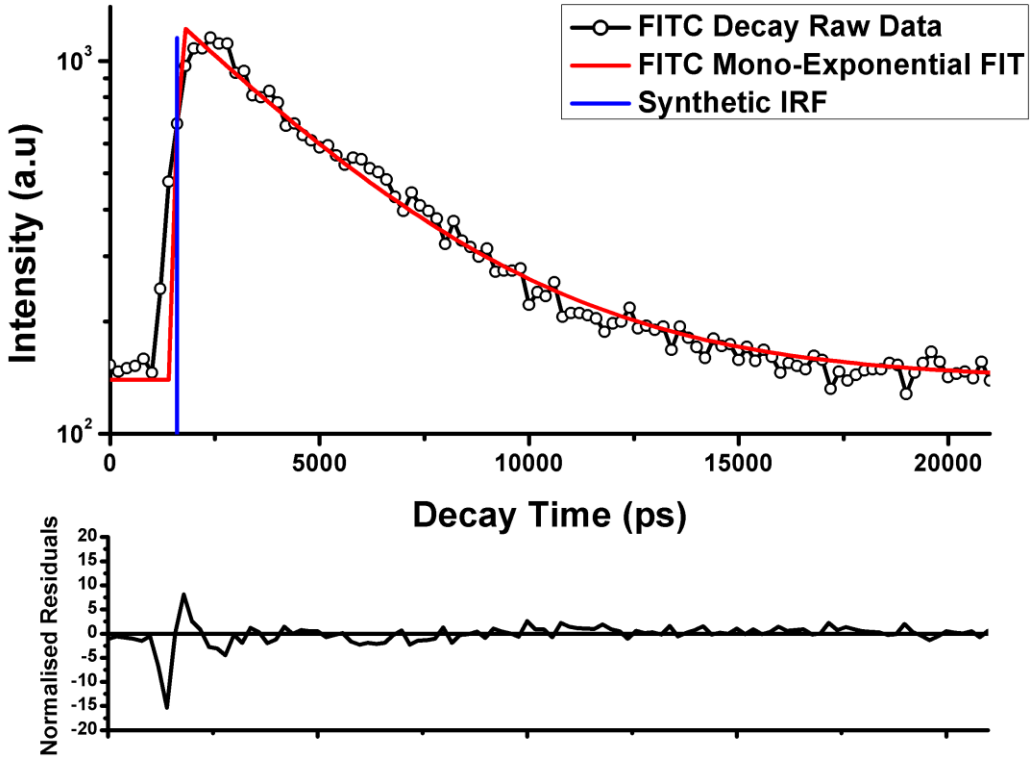

Figure 70: Decay profile for FITC in water excited at 488 nm. Data fit with, expected, mono-exponential model using artificially generated IRF function shift to 1600 ps.

It can be seen visually in Figure 70 that the function is poorly fit to the raw data over the selected decay window. The position of the delta function is optimised through iterative positioning along the data points and observing the effect on the reduced χ^2 value. The optimal position was found and the resultant χ^2 value was 4.94. This was further improved by fitting a bi-exponential model resulting in a value of 1.98; however, the raw data for FITC in water should be mono-exponential. The apparent multi-component decay arises due to the artificial IRF not taking into account the pulse width and response time of the laser diode and ICCD. The section of the data prior to the delta function is visibly miss-fitted to the data since the real response of the system takes some time to rise to the maximal intensity value. In addition, it was found through measuring the real IRF of the system in Figure 69 that decay times of around 21000 ps a secondary peak was observed. This was most likely due to reflections in the optical system and results in a skewed model fitted to the data. To rectify these issues it was imperative to measure the real IRF to be fit to the data for each measurement prior to experimentation. An example of a suitably fit model using a measured IRF can be seen in Figure 71.

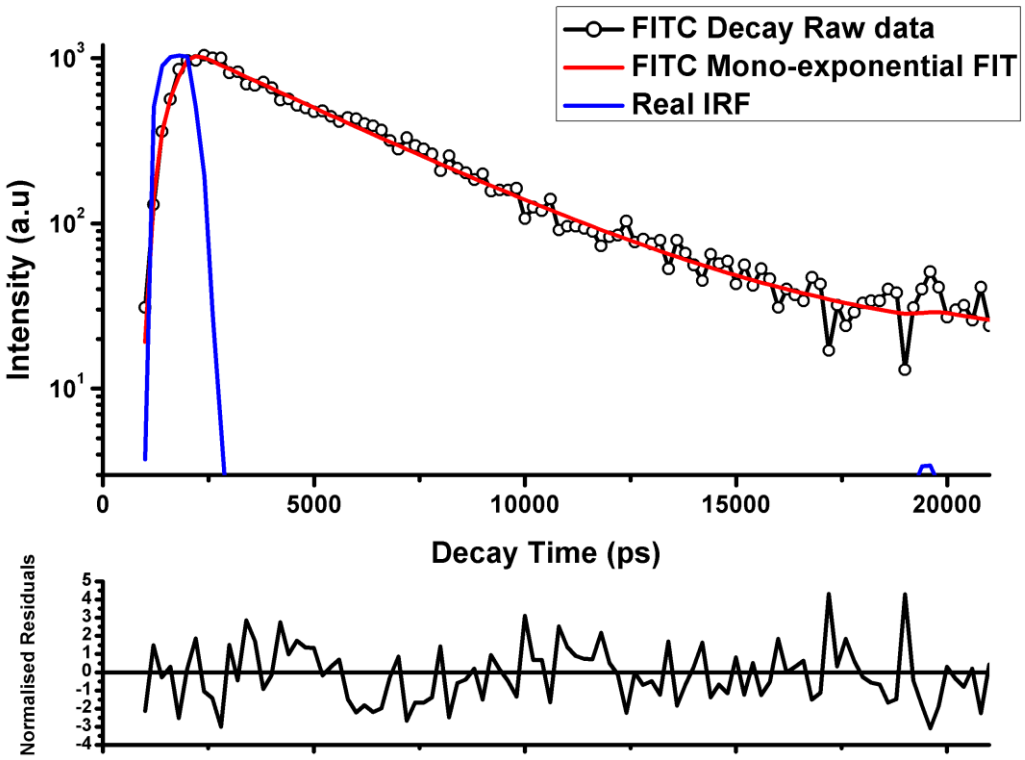

Figure 71: Decay profile for FITC in water excited at 488 nm. Data fit with mono-exponential function using IRF measured through imaging of Erythrosin B solution.

Using the same set-up and sample for Figure 71 as in Figure 70 the decay profile for FITC in water was fit using the Erythrosin B measured IRF. The resultant χ^2 value was found to be 1.22, well within a suitable range of 1-2 for FLIM measurements. The plot of the normalised residuals shows no significant deviation from the fitted mono-exponential model suggesting that using the IRF measured with the Erythrosin B value represents a true reflection of the systems response.

5.3.2. Comparison of TIRF-FLIM and confocal FLIM systems using standard fluorophores

To compare the systems performance to that of the previously presented TCPSC lifetime imaging system outlined in chapter 4, sample of standard fluorophores with known lifetimes were measured. Initially, images of a stock 5 μM FITC in water solution were taken on both a confocal and TIRF-FLIM system. For the confocal measurements the pinhole was set to the smallest setting, 0.5 airy

units, and excitation was provided through the 473 nm laser line at a repetition rate of 20 MHz. Figure 72 provides distributions based on the pixel-wide lifetime values measured by the two optical configurations of lifetime imaging.

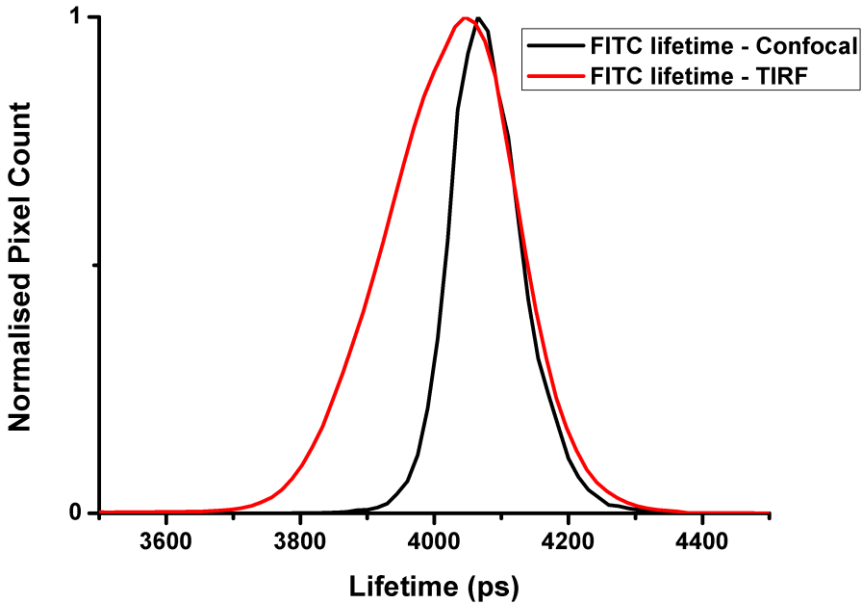

Figure 72: Normalised pixel histograms of lifetime values for FITC in water measured by confocal and TIRF lifetime imaging. Values normalised by maximum pixel count for comparison.

The subsequent lifetime values found were 4024.23 ± 239.38 ps for the TIRF illuminated lifetime image and 4074.65 ± 121.38 ps for the confocal imaged sample. Both measured values are similar to the previously reported lifetime of 4100 ps commonly found for FITC in a water solution of neutral pH. There was a wider distribution of lifetime values when measured in the TIRF configuration. This was due to the higher pixel count measured in the image window with a resolution of 1024 x 1024 compared with the 256 x 256 image of the confocal system. However, the similarity in the values with previously reported lifetimes suggest that the constructed gated lifetime system provides reliable and quantifiable values whilst utilising a TIRF illumination scheme.

5.3.3. Effect of surface on lifetime of SLBs

All previous studies of BODIPY based molecular rotors have been undertaken in freestanding bilayers through the use of either LUVS or GUVs. To demonstrate the abilities of the TIRF-FLIM system in resolving, surface localised lifetime values, Supported Lipid Bilayers were used. SLBs are formed through the deposition of a lipid bilayer on a solid support, e.g glass, mica etc. and the nature of the support is known to have an effect of the physical properties of the bilayer [187]. These effects were investigated through use of the combined FCS-lifetime system presented in the chapter 4. Initially the diffusion of BODIPY C10 was investigated at the apical and bottom, corresponding to the bilayer at the substrate surface, regions of GUVs made from pure DOPC. Figure 73 shows the normalised auto-correlation curves for the rotor BODIPY C10 diffusing laterally in a pure DOPC bilayer. It can be seen that there is a significant difference in diffusion time, corresponding to and decrease in diffusion coefficient D, between the top and the bottom of a GUV. This is evident in the shift to the right in the auto-correlation function.

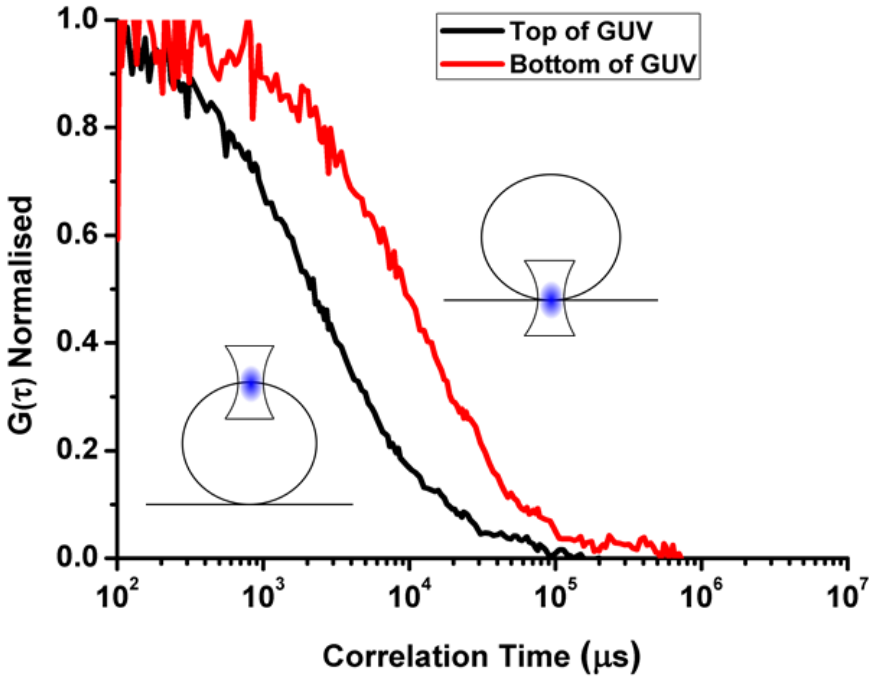

Figure 73: Normalised FCS auto-correlation curves for 0.05 mol% BODIPY C10 diffusing in a pure DOPC bilayer. FCS measurements taken at top and bottom regions of single GUV for 10 seconds. N – 10 for both cases.

The measured diffusion times for the top and bottom of the GUV were 2.68 ± 0.16 ms and 9.21 ± 0.79 ms respectively. The increase in diffusion time indicates that the effect of the substrate on the physical nature of the bilayer is significant and must be taken into account. As a result it was necessary to determine if this effect was replicated in the measured lifetime values. The corresponding lifetime values were taken from the same GUV as the FCS measurements, all taken at a temperature of 293 K. At the apical, free standing bilayer, region of the GUV the lifetime value found was 1765.44 ± 65.44 ps, which was similar to that presented in the previous chapter. At the bottom region of the vesicle the viscosity dependant component of lifetime was found to increase to 2016.88 ± 103.49 ps indicating an increased restriction on the rotor's rotational ability. This effect was seen in Figure 74 where the lower and middle regions of a vesicle were imaged using the confocal FLIM system.

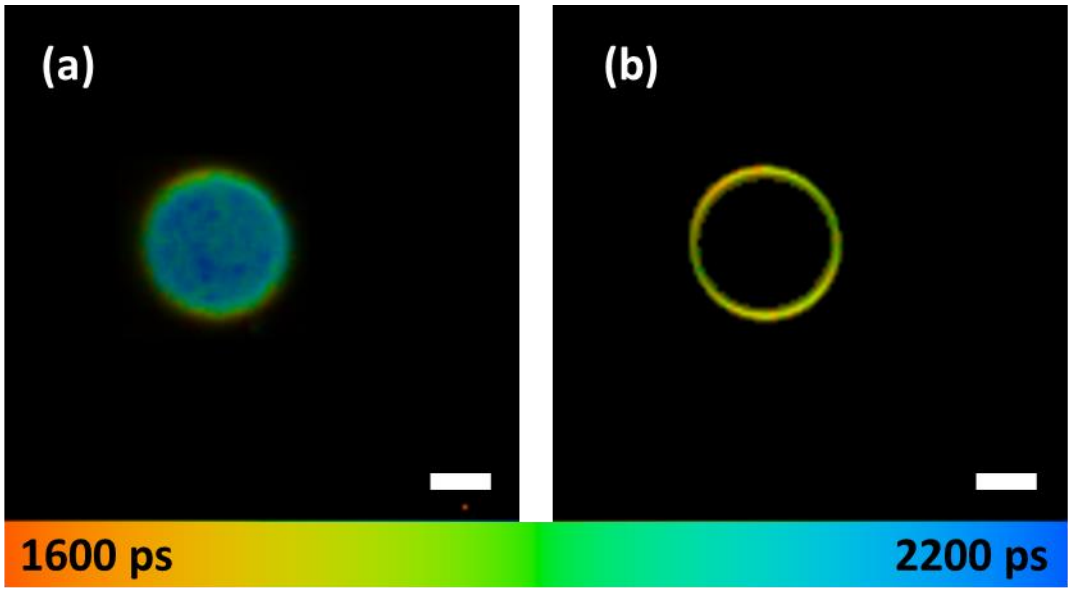

Figure 74: (a) Confocal FLIM image of BODIPY C10 in pure DOPC GUV at the bottom of the vesicle (interface between vesicle and substrate). (b) Confocal FLIM image of same vesicle taken from the mid-point of the GUV. Scale bar – 10 μm.

Figure 74 (a) presents a lifetime image of the region of the vesicle in contact with the glass substrate and (b) shows the lifetime values from the middle region of the same vesicle, corresponding to a free standing bilayer. It can clearly be seen from (a) that the lifetime of the BODIPY rotor in the bilayer is greater at the region in contact with the glass substrate. This indicates that the micro-

viscosity measured by the rotor is influenced by the properties of the supporting substrate. These values are consistent with those measured by FCS where an increase in lateral diffusion was observed at the bottom surface of the vesicle. Identical values were found when measuring the lifetime of the rotor in SLBs deposited to the glass surface by means of bursting GUVs. Figure 75 demonstrates a typical patch of a unilamellar bilayer deposited to a supporting surface through the bursting of a single GUV. The likely source of the increase in lateral diffusion is frictional coupling from the substrate to the bilayer. The increase in measured lifetime would suggest that the measured micro-viscosity is linked to the overall viscosity of the bilayer.

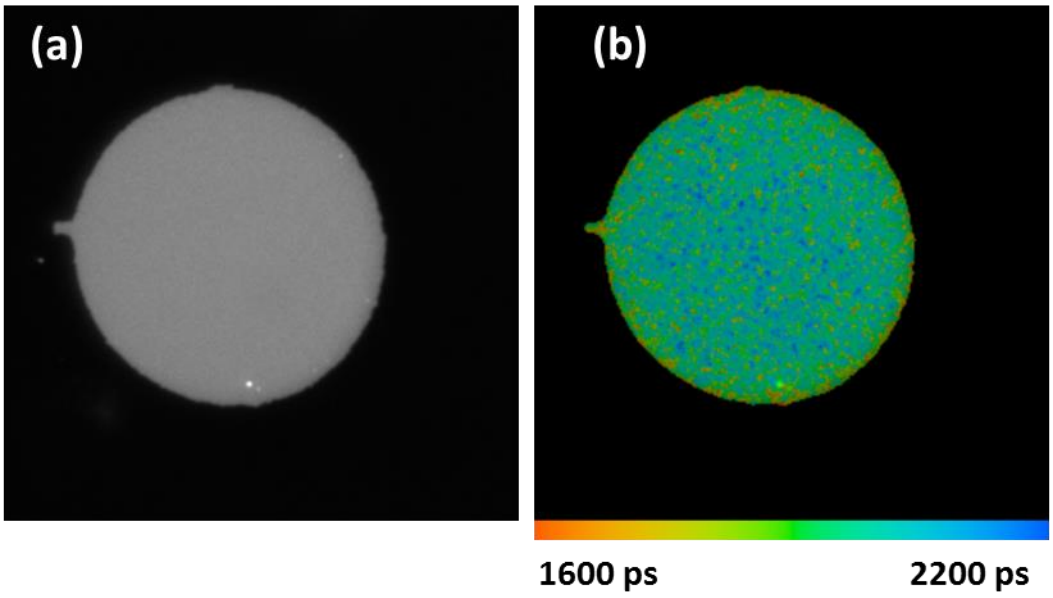

Figure 75: (a) 256 x 256 intensity image of pure DOPC SLB formed from bursting of GUV on glass support containing 0.5 mol% BODIPY C10. (b) corresponding lifetime image for same SLB

Figure 75 (a) and (b) provide both the intensity and lifetime images for a purely DOPC SLB containing 0.5 mol% BODIPY C10, imaged at a temperature of 293 K. The pixel-wide distribution of lifetime values gave an average of 2101 ± 105 ps. These values are similar to those found for the bottom region of the GUV imaged in Figure 74 (a) suggesting similarities in the physical nature between both forms of bilayer.

Using FCS and lifetime analysis simultaneously has demonstrated that the nature of the substrate surface affects both the lateral mobility of the lipids and the lifetime reported micro-viscosities of the rotors. As a result the lifetime values determined for SLBs were higher than the previously reported values for GUVs and LUVs. GUVs and LUVs represent freestanding bilayer systems where the mobility is less impeded by the surrounding environment. The effect of substrates on the bilayer's physical characteristics have been a source of debate [188] with great attention placed on the importance of the bilayer preparation and substrate cleaning methods [189]. While the exact degree to which the substrate affects bilayer mobility is still under investigation, the consensus appears to be that the overriding result is a significant reduction in fluidity [190], [191]. The results presented here through both lifetime and correlation analysis supports this claim. Furthermore, due to the fact the reported mobility restriction is in terms of lateral phospholipid diffusion the fact that a similar lifetime shift was observed adds strength to the claims that these molecular rotors report on bilayer viscosity.

5.3.4. SLBs imaged against a background of FITC

To demonstrate the TIRF-FLIM principle for determining membrane viscosity, SLBs of pure DOPC containing the molecular rotor BODIPY C10 were deposited to a glass substrate. Lifetime images were constructed of the SLB against a background of FITC in both a TIRF and non-TIRF illumination configuration. Non-TIRF illumination corresponded to adjusting the angle of illumination to below the critical angle so that the majority of the sample was illuminated. The result was an off-angle illumination with a non-uniform intensity profile due to the angled illumination. Using a fluorophore such as FITC provides a lifetime based contrast in imaging due to its longer lifetime, typically 4100 ps. Figure 76 demonstrates the principle through the intensity based images for both TIRF and non-TIRF configurations.

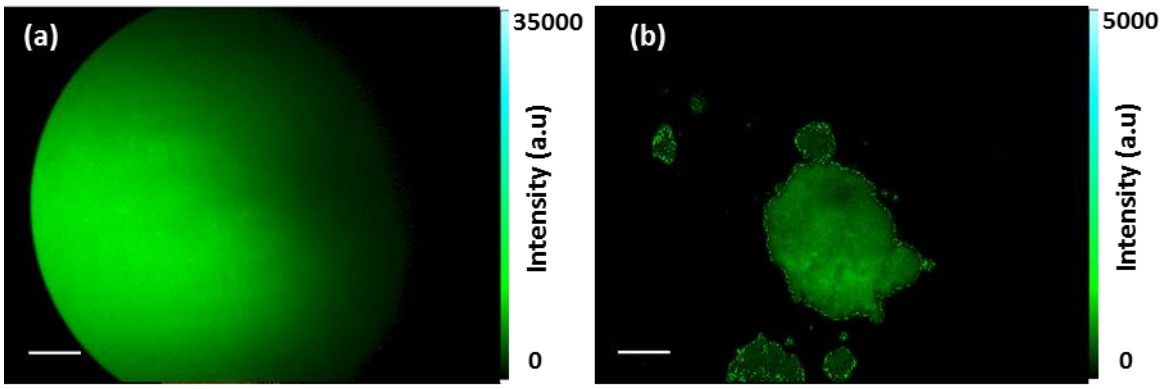

Figure 76: (a) Non-TIRF image of DOPC SLB against a background of 100 nM FITC. Dominant signal is that of the FITC with no resolvable image of the SLB. (b) TIRF image of same area showing SLB formed on the surface. Scale bars – 10 µm

In Figure 76 (a) a DOPC SLB containing BODIPY C10 was imaged in a non-TIRF configuration and it can clearly be seen that no information of the bilayer itself was resolved through the intensity images. The large observable signal was attributed to the bulk FITC solution above the bilayer. When switched to a TIRF illumination configuration, as shown in Figure 76 (b), the SLB itself was clearly imaged against the FITC background. The relative intensities of the two images show a 7-fold increase between the SLB imaged at the surface and the solution above. This suggests that even at relatively low concentrations of background fluorescence, 100 nM, information at the surface was obscured. Whilst it is clear from these images that TIRF illumination possesses the power to resolve information of the surface, intensity based imaging does not possess the power to determine information on the viscosity of the membrane. This was achieved through analysis of the corresponding lifetime images shown in Figure 77.

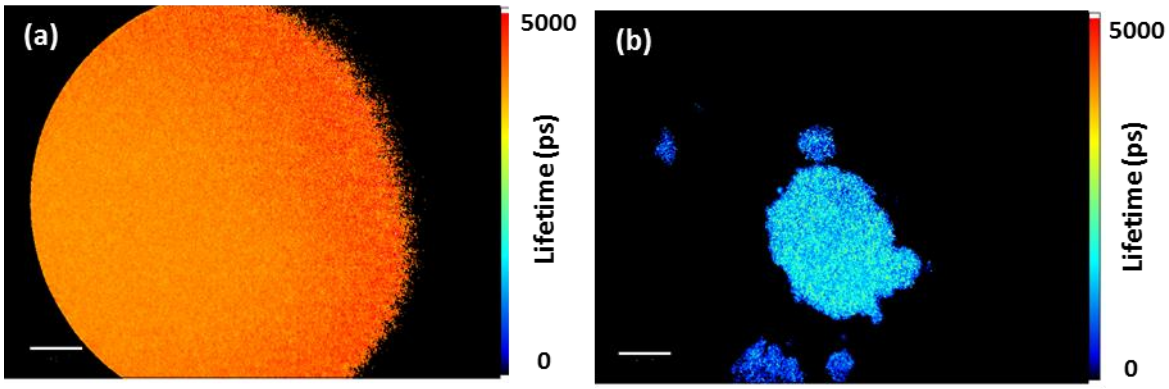

Figure 77: (a) Non-TIRF lifetime image of DOPC SLB against a background of 100 nM FITC. Dominant lifetime signal originating from bulk FITC solution above bilayer. (b) TIRF Lifetime image of same region where the lifetime of the SLB is resolvable against the bulk background solution. Scale bars – 10 µm.

Figure 77 (a) shows the corresponding lifetime image to Figure 76 (a) with an average pixel wide lifetime value of 4153 ± 102 ps. This value corresponds to FITC in the water solution above the bilayer on the surface in accordance with previously measured values. There was no significant deviation from this value over the field of view suggesting that fluorescence originating from the bilayer at the surface was unobservable when imaged in a non-TIRF configuration. Figure 77 (b) provides the corresponding lifetime image to Figure 76 (b) with an average pixel-wide lifetime value of 1931.81 ± 304 ps. These values were determined from the viscosity sensitive component of decay, τ_1, from a bi-exponential fit to all pixels with χ^2 values between 1-2. This value compares well with values previously determined for BODIPY in a pure DOPC SLB as determined by both confocal and TIRF-FLIM where no background of FITC was present. These results demonstrate that the TIRF-FLIM system has the ability to distinguish lifetime values from surface localised bilayers against a homogenous fluorescent background signal of a highly fluorescing solution.

To analyse whether the system can distinguish changes to the viscosity of the bilayer environment against a large fluorescent background, images were acquired for the rotor incorporated in SLBs of pure DPPC, an unsaturated gel phase bilayer at room temperature. This is demonstrated in Figure 78 where both images of DOPC and DPPC bilayers were imaged and compared.

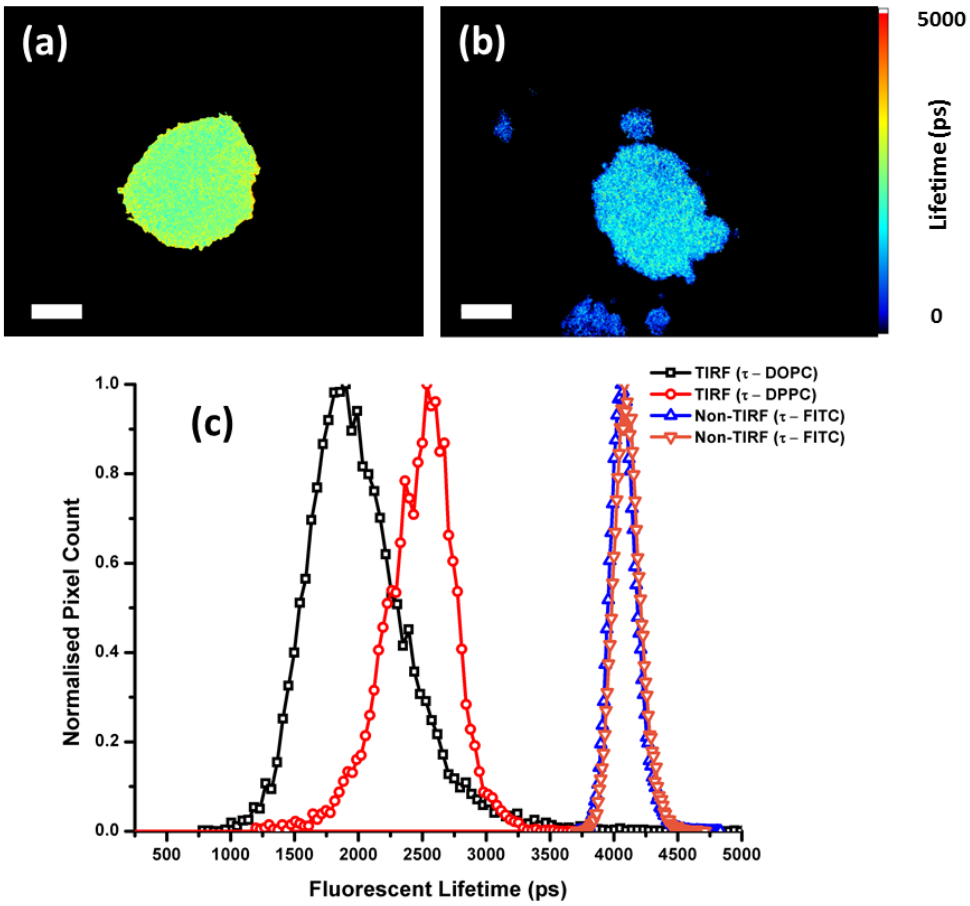

Figure 78: (a) TIRF-FLIM image of pure DPPC SLB containing BODIPY C10. (b) TIRF-FLIM image of pure DOPC SLB containing BODIPY C10. Both images taken at 293 K against a background of 100 nM FITC. (c) corresponding normalised pixel histograms for (a) and (b) and their corresponding non-TIRF images where the dominant lifetime is that of the FITC background (Not pictured). Scale bars – 10 µm.

Through analysis of the normalised pixel distributions of lifetime values it was observed that when incorporated in to the more rigid environment of DPPC the observed lifetime increased to 2514.02 ± 245.59. This can be seen in Figure 78 (c) where the values for images taken in a non-TIRF orientation are also plotted. Demonstrated is the system's ability to image based on the viscosity of the microenvironment localised exclusively at the substrate surface.

5.3.5. Lifetime imaging of SLBs against increasing background fluorescence

The images acquired in Figure 76 - Figure 78 were against a background of 100 nM FITC which significantly dominated the image when in a non-TIRF imaging

mode, however, with respect to most cellular staining procedures the concentration was low. To determine the effect of increasing concentration on the measured lifetime values for SLBs on a glass surface the same system was employed with increasing concentrations of FITC as a source of background, 100 nM – 5 μM. This is demonstrated in Figure 79 where six example data sets are presented for increasing concentrations in background fluorescence. For the measurements all images were best fit with a bi-exponential model for fluorescence decay with χ^2 values falling between 1 and 2. Pixels were fit if a minimum value of greater than 1000 was measured for the peak value of intensity in the decay curve. This was set by adjusting the integrated minimum value in the FLIMFit software to 5000 to disregard any pixels which did not meet this minimum requirement. All images were taken with 2 x 2 pixel binning, gate width of 500 ps and an exposure time of 500 ms to minimise any artefacts presented through photobleaching between sequential images. As a result the acquisition time for each decay curve was 21 seconds. For the sake of comparison the average lifetime value, τ_{avg}, was used which is determined by the respective ratios of both τ_1 and τ_2 to enable fitting and analysis of both the bilayer and the FITC background.

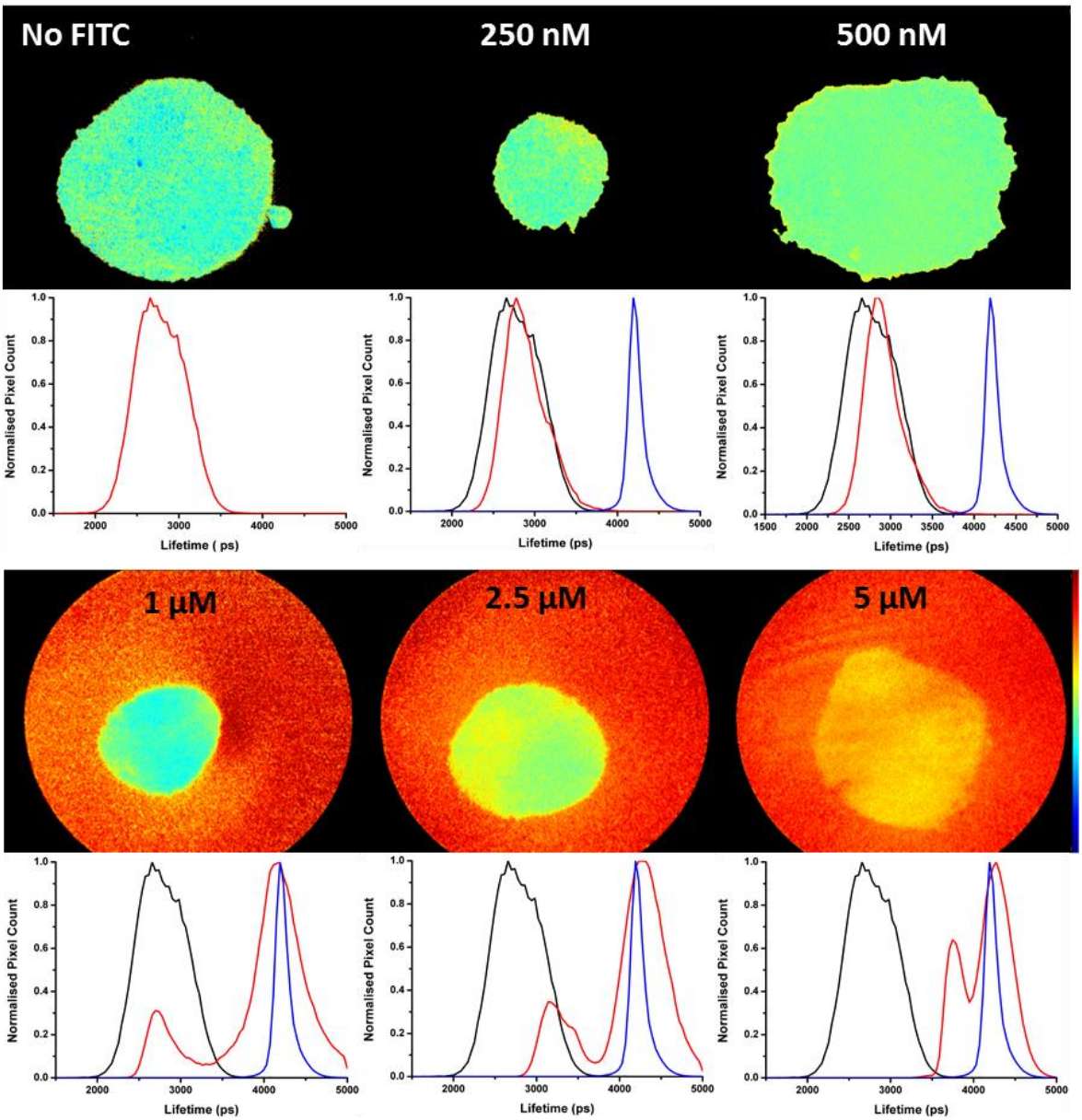

Figure 79: Lifetime images of DOPC SLB against background of FITC of increasing concentrations. Histogram red lines – distribution of pixel values for corresponding images, black lines – reference histogram for no FITC background, red lines – reference histogram for FITC background values only.

For all of the lifetime histograms shown in Figure 79 the red lines present the data corresponding to the related lifetime images. The black lines display an example histogram for when no background is present and the blue lines are equivalent to an image where only the fluorescent background was imaged. The two extra lines act as reference values to compare the pixel-wide lifetimes measured in each image. For the case of no fluorescent background the average lifetime value across all pixels was found to be 2770.32 ± 383.51 ps. The measured lifetime values for the imaged bilayers against concentrations ranging

from the nanomolar regime to at least 1 μM are within the range of the initial reference histogram. At 1 μM the histogram becomes bi-modal due to the background signal being significant enough to require fitting of the model to, i.e above an integrated intensity of 5000. The secondary peak of the histogram from 1 μM to 5 μM corresponds in value to that of the FITC background reference of 4174.65 ± 198.46 ps. This value remains constant for the higher concentrations as the lifetime of the background remains unchanged. However, the lifetime for the region corresponding to the SLB experienced an increase in lifetime from 1 μM onwards. Plotting the values of the initial peaks against concentration can illuminate the effect that increasing background concentration has on the measured SLB lifetime shown in Figure 80.

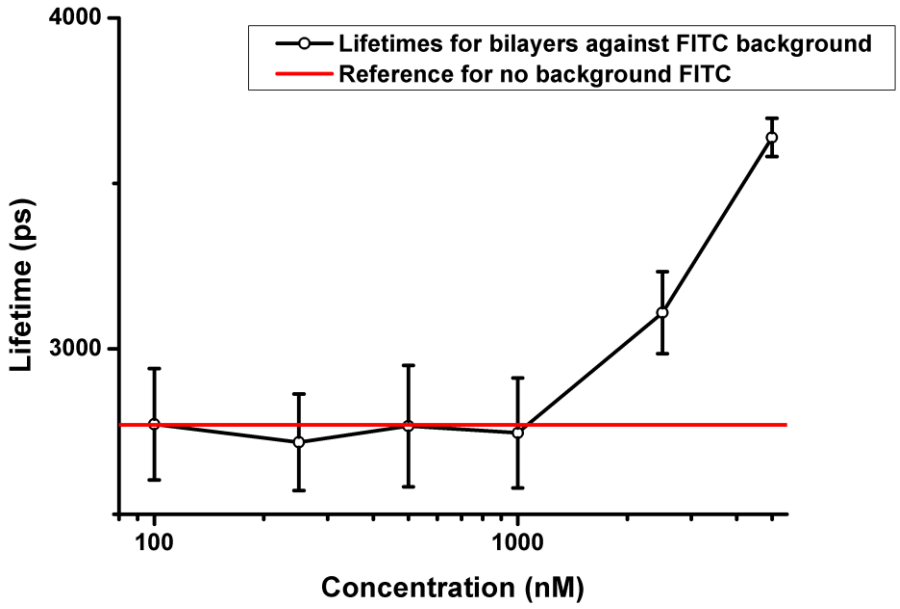

Figure 80: τ_{avg} values for imaged DOPC SLBs taken from the average of 3 imaged patches for each background FITC concentration. Red line indicates average value for SLB where no background FITC was present.

Figure 80 elucidates the relationship between the measured lifetime within the region of the bilayer and the effect of increasing background fluorescence. Up to concentrations of 1 μM there is no discernible effect was noted in the lifetime values, however, above this value the measured lifetime begins to increase. This is due to the fluorescence of the FITC solution, with a lifetime of 4 ns, contributing to the measured τ_{avg} of the bilayer. Even though the bilayer is still

visible, as evident in Figure 79, the measured lifetime value was no longer independent of the fluorescent background

Standard cell labelling protocols typically utilise micro-molar concentrations of dye to provide sufficient labelling of the cell [192], [193]. This is true for methods of selective staining of membranes, as with the BODIPY ++ molecular rotor presented previously [154]. For this study the fluorophore FITC was used as a background contrast agent due to its solubility in water and its increased lifetime with relation to that for BODIPY C10 in lipid bilayers. FITC is a highly fluorescent fluorophore with a large extinction coefficient, 75,000, and a quantum yield approaching unity. BODIPY rotors in fluid membranes, such as DOPC, experience a reduction in fluorescent lifetime and also quantum yield. The concentration for the BODIPY probe in the imaged bilayers was equivalent to 2 μM. Limitations are realised in this demonstration due to the relative brightness differences of the two dyes within the illuminated region. However, the presented system demonstrates exclusive lifetime imaging of a surface localised lipid bilayer against an increasing background solution of a highly fluorescent dye over a large range of concentrations.

For the case of a BODIPY ++ labelled cell the contributions of sub-cellular localised molecules would likely be from internalised lipid subject to thermally driven motion. As a result these particular molecules would contribute transiently to theobtained lifetime image. Other sources of fluorescent background arising from more aqueous cellular environments would likely exhibit shortened lifetimes and quantum yields compared with molecules located in the more viscous plasma membrane. As such the system would likely distinguish lifetimes of molecules residing in the membrane itself. Demonstrating this through the use of artificial bilayers offered the extreme case of a homogenous, highly fluorescent, longer lifetime background signal. These results suggest that the TIRF-FLIM system offers a means of improving the SNR for imaging the heterogenous nature of the plasma membrane at the substrate surface. As a result there is potential for increasing the reliability of information extracted from molecular rotors incorporated to cellular membranes against the ongoing internalisation of the probe.

5.4. Conclusions

A TIRF-FLIM system was constructed with the ability of resolving both fluorescence intensity and fluorescence lifetime images within a reduced 110 nm region above a substrate surface. The system was constructed to improve upon the resolution of conventional confocal based lifetime imaging systems to provide information on membrane dynamics, in particular membrane viscosity. The molecular rotor BODIPY was investigated in SLBs formed through the bursting of GUVs to a solid glass support. Substrate effects were found through the use of a combined FCS-lifetime spectroscopic approach. Measuring the lateral diffusion of the fluorophores in the bilayer revealed a hindrance upon mobility due to the glass support. This was qualified through the investigation of the difference in lifetime values measured at both the apical and bottom region of a GUV and within an SLB itself. Following this the TIRF-FLIM principle was demonstrated through the inclusion of a highly fluorescent background signal of FITC in water. The FITC background provided a significant difference in lifetime compared with the BODIPY rotor. This was seen when imaging was switched between TIRF and non-TIRF illumination where a clear pixel-wide lifetime shift was observed. In addition to this the limits of detection for the model system were determined through increasing the concentration of the fluorescent background. It was found that the lifetime of the imaged bilayer remained constant over a wide range of concentrations; up to 1 μM. Beyond this the lifetime value became distorted by the background fluorescence until a point where it became indistinguishable. The presented system shows promise for the difficult task of determining fluidity in the plasma membrane with molecular rotors. The difficulties faced with ensuring the retention of significant probe concentration at the membrane may be circumnavigated through the use of this alternative illumination scheme. It stands to reason that the system would be a useful tool for further investigating the use of the charged BODIPY ++ probe in live cell lifetime imaging studies. In addition the new BODIPY-cholesterol probe discussed in [164] may be of similar interest and the presented TIRF-FLIM system could be of great importance in determining its efficacy as a plasma membrane probe.

6. Chapter 6: Conclusions and future perspectives

6.1. TIRF investigation of insulin regulated glucose metabolism in HeLa and adipocyte cell lines

The insulin responsive recruitment of GLUT4 molecules was analysed in two different cell lines: adipocytes and a modified HeLa cell line. The primary objective was to compare the rates of recruitment of GLUT4 molecules to the plasma membrane in the HeLa cell line to that of the well characterised adipocyte cell line [92], [95], [100], [113], [114]. This was achieved through the construction of a TIRFM system capable of illuminating a selective region of 110 nm at the substrate-cell interface. The system was constructed based on a through objective illumination scheme where excitation light, provided through a 481 nm laser diode, and the resultant fluorescence emission was collected through the same 1.45 NA objective. The illuminated region was localised to include the plasma membrane and a small amount of intracellular signals. The technique was first used to analyse the recruitment of GLUT4 to the plasma membrane by measuring the time dependent fluorescence intensity within the footprint of a cell. By analysing discrete time points of intensity within the initial perimeter of the cell, a rise was observed upon stimulation with 100 nM insulin. In the adipocyte cell line the rise was found to be 2.15 ± 0.2 fold in intensity normalised against the average value prior to insulin stimulation. The HeLa cell line was analysed under the same condition and a subsequent 1.34 ± 0.1 fold rise in normalised intensity was observed. The comparative rise in the new HeLa cell line, while significantly lower, was significant enough to indicate a dynamic recruitment of GLUT4 to the plasma membrane under insulin stimulated conditions. In addition a significant difference was found in the rise times of measured intensity between the HeLa and adipocyte cell lines.

Following these preliminary results the dynamic recruitment of GLUT4 storage vesicles (GSVs) to the plasma membrane was analysed. This was achieved through time lapse imaging of both cell lines for 25 minutes upon insulin stimulation. Image analysis techniques, implemented through ImageJ, were employed to determine the relative abundance of mobile and stationary GSVs at the plasma membrane. These values were analysed within defined time windows of 1 minute after the initial stimulation. For the adipocyte cell line a rise in the

amount of mobile vesicles was observed within the first 5 minutes after stimulation. In addition to this a constant rise in stationary vesicles was noted within the illuminated membrane region. In comparison, under the same conditions in the HeLa cell line a similar level of increased activity, in terms of mobile GSVs, was observed over a time frame of 8 minutes post-insulin stimulation. However, the abundance of stationary vesicles at the membrane was seen to reduce over the time course of experimentation. These results suggest that, while insulin sensitivity and dynamic recruitment of GLUT4 to the plasma membrane are present in the modified HeLa cell line, the relative rates and quantities are lower than those found in adipocytes. These results suggest that the HeLa cell is responsive to insulin in a similar manner to the adipocyte model which indicates similar machinery involved in dynamic recruitment of GLUT4 to the membrane. However, the information provided through analysis of the GSV activity at the membrane suggests differing involvement at the point of GLUT4 dispersal from vesicles to the membrane.
Further experimentation is required to fully understand the apparent differences in the tethering and fusion processes involved in the recruitment of GSVs to the membrane of the HeLa cell line.

6.1.1. Future work for TIRFM imaging of novel HeLa cell line

The work presented in chapter 3 suggests that the robust HeLa cell model may be of use in determining factors influencing modifications to insulin mediated glucose metabolism. However, limitations are noted in the throughput of experimentation, dictated by the TIRFM setup itself. A through objective configured TIRF microscope is limited to high NA aperture objectives, and subsequently, high magnification lenses resulting in a small field of view, typically 100-200 μm wide. In the context of analysing the insulin stimulated increase in GLUT4-GFP signal at the membrane data sets are limited to 1 – 2 cells per image sequence. With each sequence observed for up to 30 minutes this greatly increases the time necessary for statistically significant data. Modifications to the optical system could be made to enable the use of lower magnification objective lenses through the use of either a prism or waveguide to couple excitation light to the sample via TIR. Simplified systems have be demonstrated previously using a glass prism as a light coupler to a light guide to

enable TIRF illumination [194]. Alternatively a simple LED based system has been shown to convert any inverted microscope to a TIRFM [195]. The LED based waveguide system couples light to a high refractive index substrate, SF11 glass, with light propagating below the critical angle absorbed by a black rubber seal. The system was shown to provide TIRF illumination compatible with all objective types without the requirement of any glass prisms. Such a system would provide a high throughput method for analysing the insulin dependent increase in GLUT4-GFP signal in both adipocytes and HeLa cells.

While increasing the field of view would be beneficial in investigating the average intensity within the footprint of the cell, lower NA objective lenses would be unable to resolve the diffraction limited GSV structures. Using the constructed objective based TIRFM system further analysis of the tethering and fusion of these GSVs in the HeLa cell line would be of great interest. Image analysis techniques have been presented previously [93], [196], [197] which report the ability to distinguish vesicle fusion at the plasma membrane when used with TIRFM generated image sequences. Applying similar image analysis methods through MATLAB implemented algorithms it would be possible to assess the rates of tethering and fusion of GSVs within the HeLa cell line. This would possibly illuminate the reasons for the observed differences in GSV activity seen in the HeLa cell line compared to the adipocyte cell line. The ability to distinguish between vesicles retaining and releasing their GLUT4 content upon fusion would enable experiments to investigate the machinery present in both cell lines related to endocytosis.

In addition to the purely intensity based TIRF system, the presented TIRF-FLIM system may be of interest in the analysis of insulin regulated glucose metabolism. A great deal of research in the area has focussed on the association of important endocytosis associated molecules with the spatial distribution of membrane dispersed GLUT4 [91], [92], [99]. Using the functional imaging capabilities of the TIRF-FLIM system it would be possible to assess colocalisation of important molecules through Forster Resonance Energy Transfer (FRET) analysis. FRET occurs when two spectrally overlapping fluorescent molecules are within a few nanometres of each other [27]. Energy from a donor fluorophore is coupled to an acceptor fluorophore non-radiatively resulting in a reduction in

the donor's fluorescent lifetime. By analysing the lifetime of the donor molecule with the TIRF-FLIM system the overall FRET efficiency within the region of the plasma membrane could be determined. This approach could be helpful in probing the seemingly different levels of vesicle activity at the membrane surface between the HeLa and adipocyte cell lines. It may also provide a novel approach for investigating the machinery involved in GLUT4 membrane dispersal and certain physiological parameters affecting this process.

6.2. FCS-Lifetime analysis of molecular rotors

A combined Fluorescence Correlation Spectroscopy (FCS) and Fluorescence Lifetime Imaging Microscopy (FLIM) system was optimised for combined FCS-Lifetime measurements of the molecular rotor BODIPY in artificial bilayers. Combining sensitive hybrid detection pulsed laser diodes simultaneous correlation and lifetime measurements were achieved with single photon sensitivity. The system was utilised to compare the lateral mobility of a small number of fluorescent molecules within a simplified bilayer system to the lifetime measured micro-viscosity values. Through implementation of the Saffman-Delbruck model for membrane viscosity, equivalent diffusion coefficients were determined for the lifetime inferred micro-viscosity values. This was to determine whether the solvent based calibration of these particular molecular rotors was truly representative of viscosity in more complex environments. The diffusion coefficients found through FCS measurements were in good agreement with previously reported molecular dynamic simulation values. The diffusion coefficients measured through spectroscopic lifetime analysis were comparable in magnitude to those from FCS but deviate slightly from both the FCS measurements and simulations. This was found to be consistent for three different variants of the BODIPY based molecular rotor suggesting that all three rotors respond similarly to viscosity. Inherent assumptions made through conversion of the measured viscosity to diffusion coefficient through the Saffman-Delbruck model may be a source for these deviations. The rotors were further analysed as indicators of membrane order through incorporation into bilayers made from phospholipids of varying degrees of saturation in the hydrocarbon tail region. Systems of pure DOPC, POPC, and DPPC represented systems of saturated, partially saturated and unsaturated

hydrocarbons respectively. An increase in diffusion coefficients measured by FCS was observed when incorporated to more rigid environments as indicated by decreasing degrees of saturation. An observed decrease in measured lifetime of the molecular rotor suggested that the probes were good indicators of membrane viscosity.

6.2.1. Future work with molecular rotors in artificial bilayers

To strengthen the argument that the rotors do in fact report on the viscosity of the bilayer environment an experiment could be constructed investigating the rotors in bilayers of varying hydrocarbon tail lengths. The length of the hydrocarbon tails comprising the hydrophobic core of a bilayer influences the fluidity of the environment with increasing tail length corresponding to an increase in diffusion [198–200]. By incorporating the rotors into bilayers of increasing tail lengths it would be reasonable to suggest that the lateral mobility would decrease measurable with FCS. If the probe is oriented as suggested in [164], with the head group of the probe positioned at the interface between the tail and head regions of the lipids, then any increase in lifetime would indicate a direct response to increasing viscosity.

The combined FCS-lifetime approach suggests that the measured lifetime values respond to changes in local viscosity within simplified lipid bilayers. One area of future research interest may focus on dynamic separation of phases in more complex bilayer systems. Cholesterol enriched lipid rafts are of increasing importance in the context of the model plasma membrane and GUVs represent interesting homologues for investigating the physical nature of membranes. Most current studies utilise multiple probes to spectrally separate coexisting domains of particular lipids in model membranes [52]. The BODIPY based molecular rotors present the possibility to not only image coexisting phases through separated lifetime values, but can simultaneously offer information on the differing physical environments. This can be seen from the preliminary lifetime image in Figure 81 of a ternary phase vesicle consisting of DOPC-DPPC-Cholesterol at a ratio of 35-35-30 respectively.

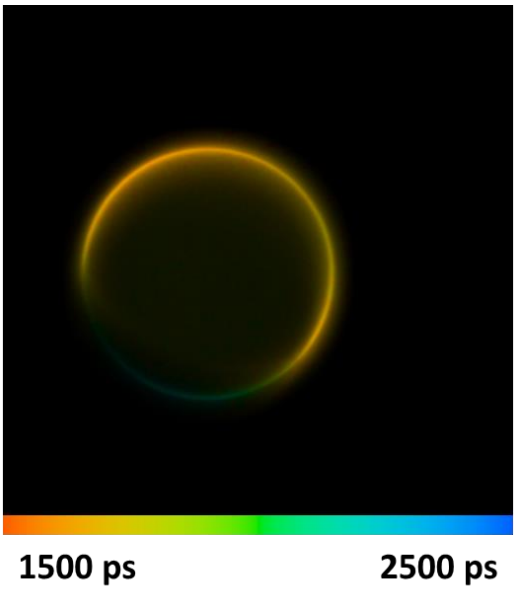

Figure 81: Confocal FLIM image of DOPC-DPPC-Cholesterol GUV with a lipid ratio of 35:35:30. Regions of varying lifetime correspond to liquid ordered and liquid disordered phases of ternary phase GUV.

It was shown in chapter 5 that when incorporated to supported lipid bilayer structures the reported lifetime increased from that of a free standing bilayer. SLBs represent systems similar to free standing bilayers but suffer through interactions with the substrate surface. There is interest in creating polymer based functional surfaces to act as tethered supports for bilayers creating systems with similar physical properties to free standing bilayers [201]. Lifetime constructed viscosity images could be useful in determining the efficacy of such supports with the ability to investigate any lateral heterogeneities within the supported bilayer. All current qualification methods for polymer supported bilayers rely on spectroscopic information with no information on any potential spatial differences. In addition the pixel distribution of lifetime values could be useful for investigating properties of the substrate surface, e.g. roughness and hydrophobicity.

6.3. TIRF-FLIM system for imaging membrane viscosity

A combined Total Internal Reflection Fluorescence Lifetime Imaging Microscopy (TIRF-FLIM) system was constructed for selective lifetime imaging of membrane dynamics, in particular viscosity using molecular rotors. The previously described through objective TIRFM system was modified to include a set of pulsed laser

diodes and image intensified CCD (ICCD) camera. The resulting system was capable of gated lifetime imaging within a TIRF illumination configuration. The system was combined with the lifetime image analysis software package FLIMfit, developed at Imperial College London, capable of multi-component exponential decay fitting to a recorded Instrument Response Function (IRF). To demonstrate the abilities of the system, Supported Lipid Bilayers (SLBs) were deposited to glass supports through the adhesion and bursting of Giant Unilamellar Vesicles (GUVs). It was found that the physical properties of the supporting substrate reduced the mobility within the bilayer as indicated by an increased diffusion coefficient measured by FCS. Analysing the lifetime for a low concentration of the BODIPY based molecular rotor revealed an increase in lifetime compared with that measured in a free standing bilayer. It is understood that frictional coupling between the substrate and bilayer can reduced the lateral diffusion of phospholipids, and as a results fluorophores, by a factor of 2-3 [191]. The increased lifetime suggests that this mechanism also alters the measured micro-viscosity, further suggesting that the recorded values are indicative of the viscosity of the bilayer itself. The TIRF-FLIM principle was demonstrated by imaging the SLBs against an increasing background concentration of FITC. The surface localised lifetime values of bilayer were distinguishable over a large range of concentrations, up to a ratio of 2:1 FITC molecules to BODIPY molecules. The basic demonstration suggests that the increased axial resolution should be able to distinguish membrane localised signals in a cellular environment where selective plasma membrane staining may be difficult or temporary.

6.3.1. Future work for TIRF-FLIM imaging of membrane viscosity

A TIRF-FLIM system was constructed and demonstrated to be able to selectively determine the viscosity of a surface localised signal through the use of supported lipid bilayers and cellular membranes. The future view for this system is to explore its abilities in more physiologically relevant scenarios by investigating fluidity changes in cellular membrane systems. Using the charged molecular rotor BODIPY ++ it would be of interest to determine precisely the time frame over which the system could effectively determine the membrane specific signal against an increasing background. In addition it would be of interest in

determining the cholesterol based BODIPY rotor's potential as a plasma membrane stain. Other fluorophores based on a cholesterol motif have been utilised to investigate changes to the environment of the cell plasma membrane. NBD-Cholesterol was previously imaged with FLIM to determine the effect of cholesterol depletion on the lifetime dependencies of the fluorescent probe [202]. Using the TIRF-FLIM system the BODIPY molecular rotors will provide an effective technique for assessing changes to the plasma membrane under certain stresses, such as lipid peroxidation [203] and shear stress [204]. Such a method will be useful for research into a wide range of illnesses associated with alterations to plasma membrane fluidity [119], [122], [124], [127], [129].

Bibliography

[1] M. Edidin, “Lipids on the frontier: a century of cell-membrane bilayers,” *Nature reviews. Molecular cell biology*, vol. 4, no. May, pp. 414-418, 2003.

[2] J. Lombard, “Once upon a time the cell membranes : 175 years of cell boundary research,” *Biology Direct*, vol. 32, pp. 1-35, 2014.

[3] E. Overton, “The probable origin and physiological significance of cellular osmotic properties,” *Trans. Park, R. B. in Biological Membrane Structure*, vol. 44, pp. 88-135, 1899.

[4] E. Overton, “Über die osmotischen Eigenschaften der lebenden Pflanzen-,” *Vierteljahrschr Naturf Ges Zurich*, vol. 40, pp. 159–184., 1895.

[5] E. Overton, “Ueber die allgemeinen osmotischen Eigenschaften der Zelle,” *Vierteljahrschr Naturf Ges Zurich*, vol. 44, pp. 88-135, 1899.

[6] E. Overton, “Studien uber die Narkose: zugleich ein Beitrag zur allgemeinen.,” *Pharmakologie. Fischer*, 1901.

[7] E. Gorter and F Grendel, “On bimolecular layers of lipoids on the chromocytes of the blood.,” *Journal of experimental medicine*, pp. 439-443, 1924.

[8] H. Davson, “A contribution to the theory of permeability of thin films,” *Journal of Cellular and Comparative Physiology*, vol. 5, pp. 495-508, 1935.

[9] J. D. Robertson, “The ultrastructure of cell membranes and their derivatives.,” *Biochem. Soc. Symp.*, vol. 16, pp. 3-43, 1959.

[10] S. J. Singer and G. L. Nicolson, “The fluid mosaic model of the structure of cell membranes.,” *Science (New York, N.Y.)*, vol. 175, no. 4023, pp. 720-31, Feb. 1972.

[11] D. Chapman, “Phase transitions and fluidity characteristics of lipids and cell membranes.,” *Quart. Rev. Biophys.*, vol. 8, pp. 185-235, 1975.

[12] J. Pietzsch, “Mind the membrane,” *Horizon Symposia: A living frontier*, no. October, pp. 1-4, 2004.

[13] H. B. White and M. K. Jain, “Long range order in biomembranes.,” *Adv. Lipid Res.*, vol. 15, pp. 1-60, 1977.

[14] K. Simons and E. Ikonen, “Functional rafts in cell membranes,” *Nature*, pp. 569-572, 1997.

[15] D. A. Brown and E. London, “Functions of lipid rafts in biological membranes.,” *Annu Rev Cell Dev Biol*, vol. 14, pp. 111-136, 1998.

[16] M. Edidin, “The State of Lipid Rafts : From Model Membranes to Cells,” *Annual review of biomolecular structure*, vol. 32, pp. 257-283, 2003.

[17] L. J. Pike, “report Rafts defined : a report on the Keystone symposium on lipid rafts and cell function,” *Journal of lipid research*, vol. 47, pp. 1597-1598, 2006.

[18] K. Simons and D. Toomre, “Lipid Rafts and Signal Transduction” *Nature reviews. Molecular cell biology*, vol. 1, no. October, pp. 31-41, 2000.

[19] G. Li , D. Citrin, K. Camphausen, B. Mueller, C. Burman, B. Mychalczak, R. Miller and Y. Song, “Advances in 4D Medical Imaging and 4D Radiation Therapy Department of Radiation Oncology,” *Technology in cancer and treatment*, vol. 7, no. 1, pp. 67-81, 2008.

[20] R. Weissleder and U. Mahmood, “Molecular Imaging,” *Radiology*, vol. 219, pp. 316-333, 2000.

[21] F. Chiti and C. M. Dobson, “Protein Misfolding , Functional Amyloid , and Human Disease,” *Annual review of biochemistry*, vol. 75, pp. 333-366, 2006.

[22] D. J. Taatjes, M. P. Wadsworth, A. S. Quinn, J. H. Rand, E. G. Bovill, and B. E. Sobel, “Imaging aspects of cardiovascular disease at the cell and molecular level,” *Histochemistry and cell biology*, vol. 130, pp. 235-245, 2008.

[23] X. Li, D.-T. Luu, C. Maurel, and J. Lin, “Probing plasma membrane dynamics at the single-molecule level.,” *Trends in plant science*, vol. 18, no. 11, pp. 617-24, Nov. 2013.

[24] J. Lakowicz, *Principles of Fluorescence Spectroscopy*. Springer. 2010.

[25] J. W. Lichtman and J.-angel Conchello, “Fluorescence microscopy,” *Nature protocols*, vol. 2, no. 12, 2005.

[26] B. Giepmans, S. Adams, M.Ellisman and R.Tsien, “The Fluorescent Toolbox for Assessing Protein Location and Function,” *Science*, no. April, pp. 217-224, 2006.

[27] M. Y. Berezin and S. Achilefu, “Fluorescence lifetime measurements and biological imaging.,” *Chemical reviews*, vol. 110, no. 5, pp. 2641-84, May 2010.

[28] P. Verveer, *Advanced Fluorescence Microscopy*. Springer New York, 2015.

[29] A. L. Mattheyses, S. M. Simon, and J. Z. Rappoport, “Imaging with total internal reflection fluorescence microscopy for the cell biologist.,” *Journal of cell science*, vol. 123, no. Pt 21, pp. 3621-8, Nov. 2010.

[30] C. J. Merrifield, M. E. Feldman, L. Wan, and W. Almers, “Imaging actin and dynamin recruitment during invagination of single clathrin-coated pits,” *Nature cell biology*, vol. 4, no. September 2002, 2003.

[31] C. J. Merrifield, D. Perrais, D. Zenisek, S. Saëns, and B. Cedex, “Coupling between Clathrin-Coated-Pit Invagination , Cortactin Recruitment , and Membrane Scission Observed in Live Cells,” *Cell*, vol. 121, pp. 593-606, 2005.

[32] J. Z. Rappoport, A. Benmerah, and S. M. Simon, “Analysis of the AP-2 Adaptor Complex and Cargo During Clathrin- Mediated Endocytosis,” *Traffic*, vol. 6, no. 7, pp. 539-547, 2006.

[33] J. Z. Rappoport and S. M. Simon, “Real-time analysis of clathrin-mediated endocytosis during cell migration,” *Journal of cell science*, pp. 847-855, 2003.

[34] I. Grigoriev, D. Splinter, N. Keijzer, P. Wulf, J. Demmers, T. Ohtsuka, M. Modesti, I. Maly, F. Grosveld, C. Hoogenraad and A. Akhmanova, “Rab6 Regulates Transport and Targeting of Exocytotic Carriers,” *Cell*, no. August, pp. 305-314, 2007.

[35] M. Fix, T. Mella, J. Jalswal, J. Rappoport, D. You, T. Sollner, J. Rothman and S. Simon , “Imaging single membrane fusion events mediated by SNARE proteins,” *PNAS*, vol. 101, no. 19, pp. 7311-7316, 2004.

[36] I. Akopova, S. Tatur, M. Grygorczyk, and R. Luchowski, “Imaging exocytosis of ATP-containing vesicles with TIRF microscopy in lung epithelial A549 cells,” *Purinergic Signalling*, pp. 59-70, 2012.

[37] F. E. Lock, K. R. Ryan, N. S. Poulter, M. Parsons, and N. A. Hotchin, “Differential Regulation of Adhesion Complex Turnover by ROCK1 and ROCK2,” *PloS one*, vol. 7, no. 2, 2012.

[38] S. J. Fletcher, N. S. Poulter, E. J. Haining, and J. Z. Rappoport, “Clathrin-mediated endocytosis regulates occludin , and not focal adhesion , distribution during epithelial wound healing,” *Biol. cell*, pp. 238-256, 2012.

[39] M. A. Partridge and E. E. Marcantonio, “Initiation of Attachment and Generation of Mature Focal Adhesions by Integrin-containing Filopodia in Cell Spreading,” *Molecular biology of the cell*, vol. 17, no. October, pp. 4237-4248, 2006.

[40] M. E. Berginski, E. A. Vitriol, K. M. Hahn, and S. M. Gomez, “High-Resolution Quantification of Focal Adhesion Spatiotemporal Dynamics in Living Cells,” *PloS one*, vol. 6, no. 7, 2011.

[41] J. Howard, A. J. Hunt, D. J. Odde, M. K. Gardner, B. D. Charlebois, and I. M. Ja, “Rapid Microtubule Self-Assembly Kinetics,” *Cell*, vol. 146, pp. 582-592, 2011.

[42] J.-B. Manneville, “Use of TIRF Microscopy to Visualize Actin and Microtubules in Migrating Cells,” *Methods in enzymology*, vol. 406, no. 2004, pp. 520-532, 2006.

[43] R. Webb, O. Rozov, S. Watkins, and B. McCartney, “Using Total Internal Reflection Fluorescence (TIRF) microscopy to visualize cortical actin and microtubules in the Drosophila syncytial embryo,” *Developmental dynamics*, vol. 238, no. 10, pp. 2622-2632, 2014.

[44] C. H. Li, L. Bai, D. D. Li, S. Xia, and T. Xu, “Dynamic tracking and mobility analysis of single GLUT4 storage vesicle in live 3T3-L1 cells,” *Cell research*, vol. 14, pp. 480-486, 2004.

[45] D. Sud, G. Mehta, K. Mehta, J. Linderman, S. Takayama, and M.-A. Mycek, “Optical imaging in microfluidic bioreactors enables oxygen monitoring for continuous cell culture.,” *Journal of biomedical optics*, vol. 11, no. 5, p. 050504, 2014.

[46] F.-J. Schmitt, B. Thaa, C. Junghans, M. Vitali, M. Veit, and T. Friedrich, “eGFP-pHsens as a highly sensitive fluorophore for cellular pH determination by fluorescence lifetime imaging microscopy (FLIM).,” *Biochimica et biophysica acta*, vol. 1837, no. 9, pp. 1581-93, Sep. 2014.

[47] M. A. M. J. V. Zandvoort et al., “Discrimination of DNA and RNA in Cells by a Vital Fluorescent Probe : Lifetime Imaging of SYTO13 in Healthy and Apoptotic Cells,” vol. 235, pp. 226-235, 2002.

[48] J. R. W. Conway, N. O. Carragher, and P. Timpson, “Developments in preclinical cancer imaging: innovating the discovery of therapeutics.,” *Nature reviews. Cancer*, vol. 14, no. 5, pp. 314-28, May 2014.

[49] J. Bec, M. Dinglong, D. Yankelevich, J. Liu, W. Ferrier, J. Southard and L. Marcu., “Multispectral fluorescence lifetime imaging system for intravascular diagnostics with ultrasound guidance: in vivo validation in swine arteries.,” *Journal of biophotonics*, vol. 7, no. 5, pp. 281-5, May 2014.

[50] Y. Ardeshirpour, V. Chernomordik, M. Hassan, R. Zielinski, J. Capala, and A. Gandjbakhche, “In vivo fluorescence lifetime imaging for monitoring the efficacy of the cancer treatment.,” *Clinical cancer research : an official journal of the American Association for Cancer Research*, vol. 20, no. 13, pp. 3531-9, Jul. 2014.

[51] Y. Ardeshirpour, V. Chernomordik, R. Zielinski, J. Capala, G. Griffiths, O. Vasalatiy, A. Smirnov, J. Knutson, I. Lyakhov, S. Achilefu, A. Gandjbakhche and M. Hassan, “In vivo fluorescence lifetime imaging monitors binding of specific probes to cancer biomarkers.,” *PloS one*, vol. 7, no. 2, p. e31881, Jan. 2012.

[52] R. F. M. D. Almeida, L. M. S. Loura, and M. Prieto, “Membrane lipid domains and rafts : current applications of fluorescence lifetime spectroscopy and imaging,” vol. 157, pp. 61-77, 2009.

[53] R. N. Day, “Measuring protein interactions using Förster resonance energy transfer and fluorescence lifetime imaging microscopy.,” *Methods (San Diego, Calif.)*, vol. 66, no. 2, pp. 200-7, Mar. 2014.

[54] A. Holt, R. Almeida, T. Nyholm, L. Loura, A. Daily, R. Staffhorst, D. Rijkers, R. Koeppe, M. Prieto and A. Killian, “Is There a Preferential Interaction between Cholesterol and Tryptophan Residues in Membrane Proteins?” *Biochemistry*, vol. 47, pp. 2638-2649, 2008.

[55] A. Fedorov and M. Prieto, “Quantification of Protein-Lipid Selectivity using FRET : Application to the M13 Major Coat Protein,” *Biophysical journal*, vol. 87, no. July, pp. 344-352, 2004.

[56] M. S. Loura, M. Prieto, A. Watts, A. Fedorov, R. F. M. D. Almeida, and F. J. Barrantes, “Cholesterol Modulates the Organization of the gM4 Transmembrane Domain of the Muscle Nicotinic Acetylcholine Receptor,” *Biophysical journal*, vol. 86, no. April, 2004.

[57] A. S. Klymchenko and R. Kreder, “Fluorescent Probes for Lipid Rafts: From Model Membranes to Living Cells.,” *Chemistry & biology*, pp. 1-17, Dec. 2013.

[58] Y. Wu, M. Stefl, A. Olzynska, M. Hof, G. Yahioglu, P. Yip, D. R. Casey, O. Ces, J. Humpolickova and M. K. Kuimova, “Molecular rheometry: direct determination of viscosity in Lo and Ld lipid phases via fluorescence lifetime imaging.,” *Physical chemistry chemical physics : PCCP*, vol. 15, no. 36, pp. 14986-93, Sep. 2013.

[59] M. K. Kuimova, G. Yahioglu, J. a Levitt, and K. Suhling, “Molecular rotor measures viscosity of live cells via fluorescence lifetime imaging.,” *Journal of the American Chemical Society*, vol. 130, no. 21, pp. 6672-3, May 2008.

[60] D. Magde, E. Elson, and W. Webb, “Thermodynamic fluctuations in a reacting system - Measurement by Fluorescence Correlation Spectroscopy,” *Physical Review Letters*, vol. 29, no. September, pp. 705-708, 1972.

[61] E. L. Elson and W. W. Webb, “Fluorescence correlation spectroscopy. II. An experimental realization,” *Biopolymers*, vol. 13, pp. 29-61, 1974.

[62] R. Rigler and P. Kask, “Fluorescence correlation spectroscopy with high count rate and low background: analysis of translational diffusion,” *Chemical Physics*, pp. 169-175, 1993.

[63] E. L. Elson, “Fluorescence correlation spectroscopy: past, present, future.,” *Biophysical journal*, vol. 101, no. 12, pp. 2855-70, Dec. 2011.

[64] P. Schwille, J. Korlach, and W. W. Webb, “With Single-Molecule Sensitivity on Cell and Model Membranes,” *Biophysical Journal*, vol. 182, pp. 176-182, 1999.

[65] J. Ries and P. Schwille, “New concepts for fluorescence correlation spectroscopy on membranes.,” *Physical chemistry chemical physics : PCCP*, vol. 10, no. 24, pp. 3487–97, Jun. 2008.

[66] D. Axelrod, T. P. Burghardt, and S. Francisco, “Total internal reflection fluorescence,” *Annual review of biophysics and bioengineering*, no. 17, pp. 247–268, 1984.

[67] L. Novotny and B. Hecht, *Principles of Nano-Optics*. 2012, pp. 35–37.

[68] D. Axelrod, “Total internal reflection fluorescence microscopy in cell biology.,” *Methods in enzymology*, vol. 361, no. 2, pp. 1–33, Jan. 2003.

[69] W. Becker, *The bh TCSPC Handbook*. Springer, 2015.

[70] W. Becker and K. Koenig, “Fluorescence lifetime imaging by time correlated single photon counting Fluorescence Lifetime Imaging by Time-Correlated Single-Photon Counting,” *Microscopy research and technique*, no. 63, pp. 58–66, 2004.

[71] K. Dowling, M. J. Dayel, M. J. Lever, P. M. W. French, and J. D. Hares, “Fluorescence lifetime imaging with picosecond resolution for biomedical applications,” *Optics Letters*, vol. 23, no. 10, pp. 810–812, 1998.

[72] A. Agronskaia, L. Tertoolen, and H. C. Gerritsen, “High frame rate fluorescence lifetime,” *Journal of Applied Physics*, vol. 1655, pp. 1655–1662, 2003.

[73] K. Suhling, M. W. French, and D. Phillips, “Time-resolved fluorescence microscopy,” *Photochemistry and photobiology*, vol. 4, pp. 13–22, 2005.

[74] H. Schneckenburger, M. Wagner, P. Weber, T. Bruns, V. Richter, W. S. L. Strauss and R. Wittig, “Multi-dimensional fluorescence microscopy of living cells.,” *Journal of biophotonics*, vol. 4, no. 3, pp. 143–9, Mar. 2011.

[75] H. Schneckenburger, “Total internal reflection fluorescence microscopy: technical innovations and novel applications.,” *Current opinion in biotechnology*, vol. 16, no. 1, pp. 13–8, Feb. 2005.

[76] J. Mcginty, J. Requejo-Isidro, I. Munro, D. S. Elson, N. P. Galletly, M. J. Lever, M. A. A. Neil, G. W. H. Stamp and P. M. W. French, “High-speed wide-field time-gated endoscopic fluorescence-lifetime imaging,” *Optics letters*, vol. 29, no. 19, pp. 2249–2251, 2004.

[77] M. J. Cole, J. Siegel, S. E. D. Webb, R. Jones, K. Dowling, M. J. Dayel, D. Parsons-Karavassilis, P. M. W. French, M. J. Lever, L. O. D. Sucharov, M. A. A. Neil, R. Justaitis and T. Wilson, “Time-domain whole-field fluorescence lifetime imaging with optical sectioning,” *Journal of Microscopy*, vol. 203, no. 3, pp. 246–257, 2001.

[78] J. Ries, “Fluorescence correlation spectroscopy,” in *Principles of Fluorescence Spectroscopy*, vol. 79, no. 5, 2012, pp. 4031–4368.

[79] S. Ruttinger, V. Buschmann, B. Kramer, R. ERdmann, R. Macdonald, and F. Koberling, “Comparison and accuracy of methods to determine the confocal,” *Journal of microscopy*, vol. 232, no. May, pp. 343-352, 2008.

[80] N. Altan-bonnet and G. Altan-Bonnet, “FCS in living cells a practical approach,” *Current protocols in Cell Biology*, pp. 1-15, 2013.

[81] D. Grünwald, M. C. Cardoso, H. Leonhardt, and V. Buschmann, “Diffusion and binding properties investigated by Fluorescence Correlation Spectroscopy (FCS).,” *Current pharmaceutical biotechnology*, vol. 6, no. 5, pp. 381-6, Oct. 2005.

[82] T. J. Arbour and J. Enderlein, “Application of dual-focus fluorescence correlation spectroscopy to microfluidic flow-velocity measurement.,” *Lab on a chip*, vol. 10, no. 10, pp. 1286-92, May 2010.

[83] S. Smyth and A. Heron, “Diabetes and obesity : the twin epidemics,” *Nature medicine*, vol. 12, no. 1, pp. 75-80, 2005.

[84] M. Y. Donath, “Targeting inflammation in the treatment of type 2 diabetes : time to start,” *Nature Reviews Drug Discovery*, vol. 13, no. 6, pp. 465-476, 2014.

[85] A. D. Association, “Economic Costs of Diabetes in the U.S. in 2012,” *Diabetes Care*, vol. 36, pp. 1033-1046, 2013.

[86] D. Daneman, “Type 1 diabetes,” *The Lancet*, vol. 367, pp. 847-858, 2006.

[87] D. I. M. Ellitus, “Report of the Expert Committee on the descriptions of diabetes categories of glucose,” *Diab*, vol. 25, pp. 5-20, 2002.

[88] P. Cryer, “Hypoglycemia in Diabetes,” *Diabetes Care*, vol. 26, no. 6, pp. 1902-1912, 2003.

[89] M. J. Birnbaum, “Identification of a Novel Gene Encoding an Insulin-Responsive G lucose Transporter Protein,” *Cell*, vol. 57, pp. 305-315, 1989.

[90] D. James, M. Strube, and M. Mueckler, “Molecular cloning and characterisation of an insulin-regulatable glucose transporter,” *Nature*, vol. 338, pp. 83-87, 1989.

[91] S. Huang, “Insulin stimulates membrane fusion and GLUT4 accumulation in clathrin coats on adipocyte plasma membranes.,” *Molecular and cellular biology*, vol. 27, no. 9, pp. 3456-69, May 2007.

[92] J. B. A. Sadler, N. J. Bryant, G. W. Gould, and C. R. Welburn, “Posttranslational Modifications of GLUT4 Affect Its Subcellular Localization and Translocation,” *International journal of molecular sciences*, vol. 14, pp. 9963-9978, 2013.

[93] K. G. Stenkula, V. A. Lizunov, S. W. Cushman, and J. Zimmerberg, “Insulin Controls the Spatial Distribution of GLUT4 on the Cell Surface through

Regulation of Its Postfusion Dispersal," *Cell Metabolism*, vol. 12, no. 3, pp. 250-259, 2010.

[94] D. Leto and A. R. Saltiel, "Regulation of glucose transport by insulin : traffic control of GLUT4," *Nature Reviews Molecular Cell Biology*, vol. 13, no. 6, pp. 383-396, 2012.

[95] N. J. Bryant and G. W. Gould, "SNARE Proteins Underpin Insulin-Regulated GLUT4 Traffic," *Traffic*, vol. 23, pp. 657-664, 2011.

[96] J. Stöckli, D. J. Fazakerley, and D. E. James, "GLUT4 exocytosis," *Journal of Cell Science*, vol. 124, no. 24, pp. 4147-4159, 2011.

[97] W. T. Garvey, T. P. Huecksteadt, S. Matthaei, and J. M. Olefsky, "Role of Glucose Transporters in the Cellular Insulin Resistance of Type 11 Non-Insulin-dependent Diabetes Mellitus," *Journal of clinical investigation*, vol. 81, no. May, pp. 1528-1536, 1988.

[98] V. a Lizunov, H. Matsumoto, J. Zimmerberg, S. W. Cushman, and V. a Frolov, "Insulin stimulates the halting, tethering, and fusion of mobile GLUT4 vesicles in rat adipose cells.," *The Journal of cell biology*, vol. 169, no. 3, pp. 481-9, May 2005.

[99] Y. Chen, Y. Wang, J. Zhang, Y. Deng, L. Jiagn, E. Song, X. S. Wu, J. A. Hammer, T. Xu, J. Lippincott-Schwartz, "Rab10 and myosin-Va mediate insulin-stimulated GLUT4 storage vesicle translocation in adipocytes.," *The Journal of cell biology*, vol. 198, no. 4, pp. 545-60, Aug. 2012.

[100] J. M. Dawicki-McKenna, Y. E. Goldman, and E. M. Ostap, "Sites of glucose transporter-4 vesicle fusion with the plasma membrane correlate spatially with microtubules.," *PloS one*, vol. 7, no. 8, p. e43662, Jan. 2012.

[101] S. Marshall, W. T. Garvey, and M. Geller, "Primary Culture of Isolated Adipocytes," *The Journal of biological chemistry*, vol. 259, no. 3, pp. 6376-6385, 1984.

[102] K. Zebisch, V. Voigt, M. Wabitsch, and M. Brandsch, "Protocol for effective differentiation of 3T3-L1 cells to adipocytes," *Analytical Biochemistry*, vol. 425, no. 1, pp. 88-90, 2012.

[103] M. J. Lopez and N. D. Spencer, "In vitro adult rat adipose tissue-derived stromal cell isolation and differentiation," in *Adipose-derived stem cells: Methods and Protocols*, vol. 702, 2011, pp. 37-46.

[104] H. Green and O. Kehinde, "An Established Preadipose Cell Line and its Differentiation in Culture II . Factors Affecting the Adipose Conversion," *Cell*, vol. 5, no. May, pp. 19-27, 1975.

[105] H. Green and M. Meuth, "An Established Pre-Adipose Cell Line and its Differentiation in Culture," *Cell*, vol. 3, no. October, pp. 127-133, 1974.

[106] S. Rubin, A. Hirsch, O. M. Rosen, and G. I. P. O. Am, “Development of Hormone Responsiveness in Vitro Receptors and Hormonal,” *The Journal of biological chemistry*, vol. 253, no. 20, pp. 7570-7578, 1978.

[107] T. R. Russell, “Conversion of 3T3 fibroblasts into adipose cells: Triggering of differentiation by prostaglandin F2a, and 1-methyl-3-isobutyl xanthine,” *PNAS*, vol. 73, no. 12, pp. 4516-4520, 1976.

[108] A. Mehra, I. Macdonald, and T. S. Pillay, “Variability in 3T3-L1 adipocyte differentiation depending on cell culture dish,” *Analytical Biochemistry*, vol. 362, pp. 281-283, 2007.

[109] G. Gey, “Studies on the propagation in vitro of poliomyelitis viruses,” *Journal of experimental medicine*, vol. 97, pp. 695-710, 1953.

[110] R. Rahbari, T. Sheahan, V. Modes, P. Collier, C. Macfarlane, and R. M. Badge, “A novel L1 retrotransposon marker for HeLa cell line identification,” *Biotechniques*, vol. 46, pp. 277-284, 2009.

[111] E. M. Stephenson, “Locomotory invasion of human cervical epithelium and avian fibroblasts by HeLa cells in vitro,” *Journal of cell science*, vol. 314, pp. 293-314, 1983.

[112] R. MacLeod, W. Dirks, Y. Matsuo, M. Kaufmann, H. Milch, and H. Drexler, “Widespread intraspecies cross-contamination of human tumor cell lines arising at source,” *International Journal of Cancer*, vol. 563, no. June, pp. 555-563, 1999.

[113] Y. Haga, K. Ishii, and T. Suzuki, “N-glycosylation is critical for the stability and intracellular trafficking of glucose transporter GLUT4.,” *The Journal of biological chemistry*, vol. 286, no. 36, pp. 31320-7, Sep. 2011.

[114] Y. Haga, K. Ishii, K. Hibino, Y. Sako, Y. Ito, N. Taniguchi and T. Suzuki, “Visualising specific protein glycoforms by transmembrane fluorescence resonance energy transfer,” *Nature Communications*, vol. 3, no. may, p. 907, 2012.

[115] V. A. Lizunov, I. Lisinski, K. Stenkula, J. Zimmerberg, and S. W. Cushman, “Insulin Regulates Fusion of GLUT4 Vesicles Independent of,” *The Journal of biological chemistry*, vol. 284, no. 12, pp. 7914-7919, 2009.

[116] S. R. Sternberg, “Biomedical Image Processing,” *IEEE computer*, pp. 22-34, 1983.

[117] A. D. Herbert, A. M. Carr, and E. Hoffmann, “FindFoci : A Focus Detection Algorithm with Automated Parameter Training That Closely Matches Human Assignments , Reduces Human Inconsistencies and Increases Speed of Analysis,” *PloS one*, pp. 1-33, 2014.

[118] J. J. García, L. Lopez-Pingarron, P. Almeida-Souza, A. Tres, P. Escudero, F. A. Garcia-Gil, D. X. Tan, R. J. Reiter, J. M. Ramirez and M. Bernal-Perez, “Protective effects of melatonin in reducing oxidative stress and in

preserving the fluidity of biological membranes: a review.," *Journal of pineal research*, vol. 56, no. 3, pp. 225-37, Apr. 2014.

[119] K. Tsuda and I. Nishio, "Membrane Fluidity and Hypertension," *The american journal of hypertension*, vol. 7061, no. 02, pp. 259-261, 2003.

[120] X. Tekpli, J. a Holme, O. Sergent, and D. Lagadic-Gossmann, "Role for membrane remodeling in cell death: implication for health and disease.," *Toxicology*, vol. 304, pp. 141-57, Feb. 2013.

[121] C. Klein, "Determination of plasma membrane fluidity with a fluorescent analogue of sphingomyelin by FRAP measurement using a standard confocal microscope," vol. 11, pp. 46-51, 2003.

[122] G. G. Ortiz et al., "Alzheimer Disease and Metabolism : Role of Cholesterol and Membrane Fluidity," *Alzheimer Disease and Metabolism: Role of Cholesterol and Membrane Fluidity, Understanding Alzheimer's Disease, Prof. Inga Zerr (Ed.)*, vol. Chapter 7, 2013.

[123] J. Zicha, "Abnormalities of Membrane Function and Lipid Metabolism in Hypertension," vol. 7061, no. 98, pp. 315-331, 1999.

[124] A. F. Dominiczak and D. F. Bohr, "The Primacy of Membrane Microviscosity in Genetic Hypertension," *The american journal of hypertension*, vol. 4, pp. 963-969, 1991.

[125] C. Stubbs and A. Smith, "The modification of mammalian membrane polyunsaturated fatty acid composition in relation to membrane fluidity and function," *Biochimica et biophysica acta*, vol. 779, pp. 89-137, 1984.

[126] I. Nakazawa and M. Iwaizumi, "A Role of the cancer cell membrane fluidity in the cancer metastases an ESR study," *Journal of experimental medicine*, no. 1973, pp. 193-198, 1989.

[127] M. Schara and M. Sok, "Membrane fluidity characteristics of human lung cancer," *Cancer letters*, vol. 139, pp. 215-220, 1999.

[128] Y. Komizu, H. Ueoka, and R. Ueoka, "Biochemical and Biophysical Research Communications Selective accumulation and growth inhibition of hybrid liposomes to human hepatocellular carcinoma cells in relation to fluidity of plasma membranes," *Biochemical and Biophysical Research Communications*, vol. 418, no. 1, pp. 81-86, 2012.

[129] P. Gillies and C. Robinson, "Decreased plasma membrane fluidity in the development of atherosclerosis in cholesterol-fed rabbits," *Atherosclerosis*, vol. 70, pp. 161-164, 1988.

[130] P. de Medina, "Tamoxifen and AEBS ligands induced apoptosis and autophagy in breast cancer cells through the stimulation of sterol accumulation," *Autophagy*, vol. 5, no. 7, pp. 1066-1067, 2009.

[131] S. Becker, V. Ardisson, N. Lepareur, and O. Sergent, “Increased Lipiodol uptake in hepatocellular carcinoma possibly due to increased membrane fluidity by dexamethasone and tamoxifen,” *Nuclear Medicine and Biology*, vol. 37, no. 7, pp. 777-784, 2010.

[132] N. Boubekeur, F. Terce, and M. Poirot, “Ligands of the antiestrogen-binding site induce active cell death and autophagy in human breast cancer cells through the modulation of cholesterol metabolism,” *Cell death and differentiation*, pp. 1372-1384, 2009.

[133] A. Ferretti, A. Knijn, E. Iorio, S. Pulciani, M. Giambenedetti, A. Molinari, S. MEschini, A. Stringaro, A. Calcabrini, I. Freitas, R. Strom, G. Arancia and F. Podo, “Biophysical and structural characterization of 1 H-NMR-detectable mobile lipid domains in NIH-3T3 fibroblasts,” *Biochimica et biophysica acta*, vol. 1438, pp. 329-348, 1999.

[134] M. Bouchard, N. Boudreau, and M. Auger, “Membrane fluidity response to odorants as seen by H-NMR and infrared spectroscopy,” *Biochimica et biophysica acta*, vol. 6, pp. 233-239, 1996.

[135] M. F. Brown, S. Lope-piedrafita, G. V. Martinez, and H. I. Petrache, “Solid-State Deuterium NMR Spectroscopy of Membranes,” in *Modern Magnetic Resonance*, 2006, pp. 1-12.

[136] G. Buech, W. Herrmann, and H. Borchert, “Measurement of Microviscosity in Vesicular Membranes by Electron Spin Resonance,” *Applied Magnetic Resonance*, pp. 269-283, 2008.

[137] L. Coderch, J. Fonollosa, M. D. Pera, J. Estelrich, and A. D. L. Maza, “Influence of cholesterol on liposome fluidity by EPR Relationship with percutaneous absorption,” *Journal of controlled release : official journal of the Controlled Release Society*, vol. 68, pp. 85-95, 2000.

[138] B. A. I. V. D. Bergh, P. W. Wertz, H. E. Junginger, and J. A. Bouwstra, “Elasticity of vesicles assessed by electron spin resonance , electron microscopy and extrusion measurements,” *International journal of pharmaceutics*, vol. 217, pp. 13-24, 2001.

[139] C. Day, L. Kraft, M. Kang, and A. Kenworthy, “Analysis of protein and lipid dynamics using confocal FRAP,” *Current protocols in cytometry*, pp. 1-32, 2013.

[140] C. Guzman, M. Solman, and D. Abankwa, “Nanoclustering and Heterogeneous Membrane Diffusion of Ras Studied by FRAP and RICS Analysis,” *Methods in molecular biology*, vol. 1120, pp. 307-326, 2014.

[141] K. C. Crosby, M. Postma, M. A. Hink, C. H. C. Zeelenberg, M. J. W. Adjobo-hermans, and T. W. J. Gadella, “Quantitative Analysis of Self-Association and Mobility of Annexin A4 at the Plasma Membrane,” *Biophysj*, vol. 104, no. 9, pp. 1875-1885, 2013.

[142] A. Benda, M. Benes, V. Marec, A. Lhotsky, W. T. Hermens, and J. Heyrovsky, “How To Determine Diffusion Coefficients in Planar Phospholipid Systems by Confocal Fluorescence Correlation Spectroscopy,” *Society*, vol. 9, no. 14, pp. 4120-4126, 2003.

[143] V. Mueller, A. Honigmann, C. Ringemann, R. Medda, G. Schwarzmann, and C. Eggeling, *FCS in STED microscopy: studying the nanoscale of lipid membrane dynamics.*, vol. 519. 2013, pp. 1-38.

[144] F. Heinemann, V. Betaneli, F. a Thomas, and P. Schwille, “Quantifying lipid diffusion by fluorescence correlation spectroscopy: a critical treatise.,” *Langmuir : the ACS journal of surfaces and colloids*, vol. 28, no. 37, pp. 13395-404, Sep. 2012.

[145] F. Heinemann, S. K. Vogel, and P. Schwille, “Lateral Membrane Diffusion Modulated by a Minimal Actin Cortex,” *Biophysical Journal*, vol. 104, no. 7, pp. 1465-1475, Apr. 2013.

[146] R. Machán and M. Hof, “Lipid diffusion in planar membranes investigated by fluorescence correlation spectroscopy.,” *Biochimica et biophysica acta*, vol. 1798, no. 7, pp. 1377-91, Jul. 2010.

[147] J. Ries, S. Chiantia, and P. Schwille, “Accurate determination of membrane dynamics with line-scan FCS.,” *Biophysical journal*, vol. 96, no. 5, pp. 1999-2008, Mar. 2009.

[148] M. K. Kuimova, “Mapping viscosity in cells using molecular rotors.,” *Physical chemistry chemical physics : PCCP*, vol. 14, no. 37, pp. 12671-86, Oct. 2012.

[149] T. Forster and G. Hoffmann, “Die Viskositatsabhängigkeit der Fluoreszenzquantenausbeuten einiger Farbstoffsysteme [Effect of viscosity on the fluorescence quantum yield of some dye systems,” *Journal of physical chemistry*, vol. 75, pp. 63-76, 1971.

[150] A. Singh and J. Das, “Liposome encapsulated vitamin A compounds exhibit greater stability and diminished toxicity,” *Biophysical chemistry*, pp. 155-162, 1998.

[151] R. K. P. Benninger et al., “Fluorescence-Lifetime Imaging of DNA – Dye Interactions within continuous-flow microfluidic systems,” *Microfluidics*, pp. 2228-2231, 2007.

[152] M. A. Haidekker, E. A. Theodorakis, and E. A. Theodorakis, “Molecular rotors — fluorescent biosensors for viscosity and flow,” pp. 1669-1678, 2007.

[153] D. M. Owen, P. M. P. Laniganm C. Dunsby, I. Munro, D. Grant, M. A. A. Neil, P. M. W. French and A. I. Magee, “Fluorescence Lifetime Imaging Provides Enhanced Contrast when Imaging the Phase-Sensitive Dye di-4-ANEPPDHQ in Model Membranes and Live Cells,” *Biophysical Journal*, vol. 90, no. 11, p. L80-L82, 2006.

[154] I. López-Duarte, T. T. Vu, M. A. Izquierdo, J. a Bull, and M. K. Kuimova, “A molecular rotor for measuring viscosity in plasma membranes of live cells.,” *Chemical communications (Cambridge, England)*, vol. 50, no. 40, pp. 5282-4, May 2014.

[155] R. Nayar, M. J. Hope, and P. R. Cullis, “Generation of large unilamellar vesicles from long-chain saturated phosphatidylcholines by extrusion technique,” *Biochimica et biophysica acta*, vol. 986, pp. 200-206, 1989.

[156] M. I. Angelova and D. S. Dimitrov, “Liposome Electro formation,” pp. 303-311, 1986.

[157] D. J. Estes and M. Mayer, “Electroformation of giant liposomes from spin-coated films of lipids.,” *Colloids and surfaces. B, Biointerfaces*, vol. 42, no. 2, pp. 115-23, May 2005.

[158] L. Liu, A. Viallat, and G. Jin, “Vesicle adhesion visualized with total internal reflection imaging ellipsometry biosensor,” *Sensors and Actuators B: Chemical*, vol. 190, pp. 221-226, Jan. 2014.

[159] M. Zhao, L. Jin, B. Chen, Y. Ding, and D. Chen, “Afterpulsing and its correction in fluorescence correlation spectroscopy measurements,” *Applied optics*, vol. 42, no. 19, pp. 4031-4036, 2003.

[160] O. Krichevsky and G. Bonnet, “Fluorescence correlation spectroscopy : the technique and its applications,” *Reports on progress in physics.*, vol. 65, pp. 251-297, 2002.

[161] J. Enderlein, I. Gregor, D. Patra, and J. Fitter, “Art and artefacts of fluorescence correlation spectroscopy.,” *Current pharmaceutical biotechnology*, vol. 5, no. 2, pp. 155-61, Apr. 2004.

[162] N. Boens et al., “Fluorescence lifetime standards for time and frequency domain fluorescence spectroscopy,” *Analytical chemistry*, vol. 79, no. 5, pp. 2137-2149, 2007.

[163] Y. Wu et al., “Molecular rheometry : direct determination of viscosity in L o and L d lipid phases via fluorescence lifetime imaging .,” pp. 1-9, 2013.

[164] M. Dent, I. Lopez-Duarte, C. J. Dickson, N. D. Geoghegan, J. M. Cooper, I. R. Gould, R. Krams, J. A. Bull, N. J. Brooks and M. K. Kuimova, “Imaging phase separation in model lipid membranes through the use of BODIPY based molecular rotors,” *Physical Chemistry Chemical Physics*, vol. 17, pp. 18393-18402, 2015.

[165] G. P. Saffman and M. Delbruck, “Brownian motion in biological membranes,” *PNAS*, vol. 72, no. 8, pp. 3111-3113, 1975.

[166] E. P. Petrov and P. Schwille, “Translational diffusion in lipid membranes beyond the Saffman-Delbruck approximation.,” *Biophysical journal*, vol. 94, no. 5, pp. L41-3, Mar. 2008.

[167] Y. F. Dufre, T. Boland, J. W. Schneider, W. R. Bargera, and U. Lee, “Characterization of the physical properties of model biomembranes at the nanometer scale with the atomic force microscope,” *Faraday Discussions*, pp. 79-94, 1998.

[168] P.-emmanuel Milhiet, F. Gubellini, A. Berquand, P. Dosset, J-L. Rigaud, C. L. Grimellec and D. Levy, “High-Resolution AFM of Membrane Proteins Directly Incorporated at High Density in Planar Lipid Bilayer,” *Biophysical journal*, vol. 91, no. November, pp. 3268-3275, 2006.

[169] S. J. Attwood, Y. Choi, and Z. Leonenko, “Preparation of DOPC and DPPC Supported Planar Lipid Bilayers for Atomic Force Microscopy and Atomic Force Spectroscopy,” *International journal of molecular sciences*, vol. 14, pp. 3514-3539, 2013.

[170] K. Akashi, H. Miyata, H. Itoh, and K. Kinosita, “Preparation of giant liposomes in physiological conditions and their characterization under an optical microscope.,” *Biophysical journal*, vol. 71, no. 6, pp. 3242-50, Dec. 1996.

[171] A. Vysniauskas, M. Qurashi, N. Gallop, M. Balaaz, H. L. Anderson, and M. K. Kuimova, “Unravelling the effect of temperature on viscosity sensitive fluorescent molecular rotors,” *Chemphysphyschem*, vol. 10, no. 1, pp. 1-6, 2015.

[172] T. M. Konyakhina, J. Wu, J. D. Mastroianni, F. a Heberle, and G. W. Feigenson, “Phase diagram of a 4-component lipid mixture: DSPC/DOPC/POPC/chol.,” *Biochimica et biophysica acta*, vol. 1828, no. 9, pp. 2204-14, Sep. 2013.

[173] J. A. Levitt, M. K. Kuimova, G. Yahioglu, P.-hua Chung, K. Suhling, and D. Phillips, “Membrane-bound molecular rotors measure viscosity in live cells via fluorescence lifetime imaging,” *Journal of physical chemistry*, vol. 113, pp. 11634-11642, 2009.

[174] M. A. Haidekker, T. Ling, M. Anglo, H. Y. Stevens, J. A. Frangos, and E. A. Theodorakis, “New fluorescent probes for the measurement of cell membrane viscosity,” *Chemistry & biology*, vol. 8, pp. 123-131, 2001.

[175] X. Peng, Z. Yang, J. Wang, J. Fan, Y. He, F. Song, B. Wang, S. Sun, J. Qu and M. Yan, “Fluorescence Ratiometry and Fluorescence Lifetime Imaging : Using a Single Molecular Sensor for Dual Mode Imaging of Cellular Viscosity,” *Journal of the American Chemical Society*, vol. 133, pp. 6626-6635, 2011.

[176] M. K. Kuimova, S. W. Potchway, A. W. Parker, M. Balaz, H. A. Collins, H. L. Anderson, K. Suhling and P. R. Ogilby, “Imaging intracellular viscosity of a single cell during photoinduced cell death,” *Nature Chemistry*, vol. 1, no. April, pp. 69-73, 2009.

[177] M. E. Nipper, M. Dakanali, E. Theodorakis, and M. A. Haidekker, “Detection of liposome membrane viscosity perturbations with ratiometric molecular rotors,” *Biochimie*, vol. 93, no. 6, pp. 988-994, 2011.

[178] M. A. Haidekker, M. Nipper, A. Mustafic, D. Lichlyter, M. Dakanali, and E. A. Theodorakis, *Dyes with Segmental Mobility : Molecular Rotors*. 2010, pp. 267-308.

[179] E. Betzig, G. H. Patterson, R. Sougrat, O. W. Lindwasser, S. Olenych, J. S. Bonifacino, M. W. Davidson, J. Lippincott-Schwartz and H. F. Hess, “Imaging intracellular fluorescent proteins at nanometer resolution,” *Science*, vol. 313, pp. 1642-1645, 2006.

[180] L. Schermelleh, R. Heintzmann, and H. Leonhardt, “A guide to super-resolution fluorescence microscopy,” vol. 190, no. 2, pp. 165-175, 2010.

[181] M. Fernández-suárez and A. Y. Ting, “Fluorescent probes for super-resolution imaging in living cells,” *Nature Reviews Molecular Cell Biology*, vol. 9, no. December, pp. 929-943, 2008.

[182] S. W. Hell and J. Wichmann, “Breaking the diffraction resolution limit by stimulated emission: stimulated-emission-depletion fluorescence microscopy.,” *Optics letters*, vol. 19, no. 11, pp. 780-2, Jun. 1994.

[183] S. W. Hell, E. H. K. Stelzer, S. Lindek, and C. Cremer, “Confocal microscopy with an increased detection aperture : type-B 4Pi confocal microscopy,” *Optics Letters*, vol. 19, no. 3, pp. 222-224, 1994.

[184] S. Glaschick, C. Rocker, K. Deuschle, J. Wiedenmann, F. Oswald, V. Mailander and G. U. Nienhaus, “Axial Resolution Enhancement by 4Pi Confocal Fluorescence Microscopy with Two-Photon Excitation,” *Journal of Biological Physics*, no. 2007, pp. 433-443, 2008.

[185] U. Dürig, D. W. Pohl, F. Rohner, D. W. Pohl, and F. Rohner, “Near-field optical-scanning microscopy,” *Journal of Applied Physics*, pp. 3318-3327, 1986.

[186] S. C. Warren, A. Margineanu, D. Alibhai, D. J. Kelly, C. Talbot, Y. Alexandrov, I. Munro, M. Katan, C. Dunsby and P. M. W. French, “Rapid Global Fitting of Large Fluorescence Lifetime Imaging Microscopy Datasets,” *PloS one*, vol. 8, no. 8, p. e70687, 2013.

[187] R. Tero, “Substrate Effects on the Formation Process, Structure and Physicochemical Properties of Supported Lipid Bilayers,” *Materials*, vol. 5, pp. 2658-2680, 2012.

[188] K. J. Seu, A. P. Pandey, F. Haque, E. A. Proctor, A. E. Ribbe, and J. S. Hovis, “Effect of Surface Treatment on Diffusion and Domain Formation in Supported Lipid Bilayers,” *Biophysical Journal*, vol. 92, no. April, pp. 2445-2450, 2007.

[189] T. Charitat and B. Tinland, “Diffusion in supported lipid bilayers : Influence of substrate and preparation technique on the internal dynamics Diffusion in supported lipid bilayers : Influence of substrate and preparation technique on the,” *The European Physical Journal E*, vol. 28, no. FEBRUARY, pp. 211-220, 2009.

[190] J. Schmitt, B. Danner, and T. M. Bayerl, “Polymer Cushions in Supported Phospholipid Bilayers Reduce Significantly the Frictional Drag between Bilayer and Solid Surface,” *Langmuir*, no. 10, pp. 982-984, 2001.

[191] M. Przybylo, J. Sýkora, J. Humpolíckova, A. Benda, A. Zan, and M. Hof, “Lipid diffusion in giant unilamellar vesicles is more than 2 times faster than in supported phospholipid bilayers under identical conditions.,” *Langmuir : the ACS journal of surfaces and colloids*, vol. 22, no. 22, pp. 9096-9, Oct. 2006.

[192] M. J. Dallman, C. L. Celso, and C. L. Celso, “From seeing to believing : labelling strategies for in vivo cell-tracking experiments,” *Interface Focus*, vol. 3, p. 0001, 2013.

[193] L. Spotl, A. Sarti, M. P. Dierich, J. Most, L. Franzens, and U. Innsbruck, “Cell Membrane Labeling With Fluorescent Dyes for the Demonstration of Cytokine-Induced Fusion Between Monocytes and Tumor Cells,” *Cytometry*, vol. 169, pp. 160-169, 1995.

[194] A. Asanov, A. Zepeda, and L. Vaca, “A novel form of Total Internal Reflection Fluorescence Microscopy (LG-TIRFM) reveals different and independent lipid raft domains in living cells.,” *Biochimica et biophysica acta*, vol. 1801, no. 2, pp. 147-55, Feb. 2010.

[195] S. Ramachandran, D. a Cohen, A. P. Quist, and R. Lal, “High performance, LED powered, waveguide based total internal reflection microscopy.,” *Scientific reports*, vol. 3, p. 2133, Jan. 2013.

[196] N. Deng, Y. Xu, D. Sun, P. Hua, X. Zheng, and H. Duan, “Image Processing for Fusion Identification Between the GLUT4 Storage Vesicles and the Plasma Membrane,” *Journal of Signal Processing Systems*, vol. 54, no. 1–3, pp. 115-125, May 2008.

[197] L. Bai, Y. Wang, J. Fan, Y. Chen, A. Qu, P. Xu, D. E. James and T. Xu, “Dissecting Multiple Steps of GLUT4 Trafficking and Identifying the Sites of Insulin Action,” *Cell Metabolism*, no. January 2007, pp. 47-57, 2010.

[198] K. J. Seu, L. R. Cambrea, R. M. Everly, and J. S. Hovis, “Influence of Lipid Chemistry on Membrane Fluidity : Tail and Headgroup Interactions,” *Biophysical Journal*, vol. 91, no. 10, pp. 3727-3735, 2006.

[199] W. K. D. Otter and S. A. Shkulipa, “Intermonolayer Friction and Surface Shear Viscosity of Lipid Bilayer Membranes,” *Biophysical Journal*, vol. 93, no. 2, pp. 423-433, 2007.

[200] P. Niemla, M. Hyvonen, and I. Vattulainen, “Influence of Chain Length and Unsaturation on Sphingomyelin Bilayers,” *Biophysical journal*, vol. 90, no. February, pp. 851-863, 2006.

[201] L. Renner, T. Osaki, S. Chiantia, P. Schwille, T. Pompe, and C. Werner, “Supported lipid bilayers on spacious and pH-responsive polymer cushions with varied hydrophilicity.,” *The journal of physical chemistry. B*, vol. 112, no. 20, pp. 6373-8, May 2008.

[202] P. Ostaˇ, S. Jan, J. Brejchová, A. Ol, M. Hof, and P. Svoboda, “FLIM studies of 22- and 25-NBD-cholesterol in living HEK293 cells : Plasma membrane change induced by cholesterol depletion,” *Chemistry and physics of lipids*, vol. 168, pp. 62-69, 2013.

[203] J. Wong-ekkabut, Z. Xu, W. Triampo, I.-ming Tang, and D. P. Tieleman, “Effect of Lipid Peroxidation on the Properties of Lipid Bilayers : A Molecular Dynamics Study,” *Biophysical journal*, vol. 93, no. December, pp. 4225-4236, 2007.

[204] B. Liu, S. Lu, Y.-li Hu, X. Liao, M. Ouyang, and Y. Wang, “RhoA and Membrane Fluidity Mediates the Spatially Polarized Src / FAK Activation in Response to Shear Stress,” *Scientific reports*, pp. 4-11, 2014.